
Fatigue life estimation of steel half-pipes bolted connections for onshore wind towers applications

Rita Gonçalves Reis Dantas

Dissertation submitted to
Faculdade de Engenharia da Universidade do Porto
for the degree of:

Mestre em Engenharia Mecânica

Advisor:

Prof. José António Fonseca de Oliveira Correia
(University of Porto)

Co-Advisors:

Prof. Grzegorz Lesiuk
(Wrocław University of Science and Technology)

Prof. Abílio de Jesus
(University of Porto)

Prof. Carlos Rebelo
(University of Coimbra)

Departamento de Engenharia Mecânica
Faculdade de Engenharia da Universidade do Porto

Porto, 2019

The work presented in this dissertation was performed at the
Department of Mechanical Engineering
Faculty of Engineering
University of Porto
Porto, Portugal.

Rita Gonçalves Reis Dantas
E-mail: up201403351@fe.up.pt

Faculdade de Engenharia da Universidade do Porto
Departamento de Engenharia Mecânica
Rua Dr. Roberto Frias s/n,
4200-465 Porto
Portugal

Abstract

Nowadays, an evolution and development of renewable energies sector is observed, in order to reduce the consume of fuel fossils which are responsible for the emission of greenhouse effect gases. Wind is the largest renewable resource and every day new and larger wind turbines are installed around the world. The increasing of power production is obtained by achieving faster winds, which implies higher and larger wind turbine towers. Consequently, new design solutions are proposed to overcome transportation and assembly issues, which arise due to the large size of towers and respective section diameters.

Therefore, the SHOWTIME project proposed a hybrid turbine tower, formed by a lattice and a tubular part, which is presented throughout this work. Usually, the lattice towers show some fatigue problems, because of the bolted connections present in the lattice part. Thus, this master thesis proposes to estimate the fatigue life of a steel half-pipes bolted connection of the tower proposed by SHOWTIME project.

Hence, uniaxial and multiaxial fatigue tests for S355 steel and different stress ratios in high cycle region were conducted and the results analysed. Besides, different multiaxial fatigue models were applied to this fatigue data and evaluated. The Dang Van model was selected as the most suitable model to multiaxial fatigue data of S355 steel. The experimental fatigue curves were obtained for multiaxial and uniaxial fatigue in high cycle regime.

Moreover, fatigue crack growth rate tests were conducted for mode I under different stress ratios as well as the Paris law constants were estimated for S355 steel. The fatigue crack growth rate for tests carried out under mode I was compared with the values obtained for mixed mode (I+II), through experimental tests conducted by other authors.

Finally, it was performed the fatigue analysis of the steel half-pipes bolted connection and the numerical fatigue curves were estimated, considering uniaxial and multiaxial fatigue stress states. At the end of this master thesis, the importance of a multiaxial fatigue analysis was demonstrated.

Keywords: fatigue, fracture, S355 steel, multiaxial, wind turbines, structures

Resumo

Atualmente, é observada uma evolução e desenvolvimento do sector das energias renováveis, de modo a reduzir o consumo de combustíveis fósseis, que são responsável pela emissão de gases efeito de estufa. O vento é a maior fonte de energia renovável e todos os dias são instaladas novas turbinas eólicas de maior potência. O aumento da potência produzida é conseguida através do alcance de ventos mais rápidos, que só se encontram a elevadas altitudes, e como tal implicam a produção de torres eólicas maiores e mais altas. Consequentemente, são propostas novas soluções de design, com o objetivo de superar os problemas de transporte e montagem, que surgem devido aos maiores tamanhos de torres e respetivos diâmetros das secções.

Deste modo, o projeto SHOWTIME propôs uma torre eólica híbrida, ou seja, formada por uma parte treliçada e outra tubular, que é apresentada ao longo deste trabalho. Geralmente, as torres treliçadas manifestam alguns problemas de fadiga, devido às ligações aparafusadas usadas para ligar os diferentes elementos. Assim, esta dissertação pretende estimar a vida à fadiga de ligações aparafusadas formadas por duas meias peças conformadas plasticamente a frio. Esta ligação foi elaborada pelo projeto SHOWTIME e utiliza o aço S355.

Por isso, foram realizados testes de fadiga uniaxial e multiaxial em provetes de aço S355, utilizando diferentes razões de tensões, para a região de longas vidas à fadiga. Para além disto, foram avaliados e aplicados diferentes modelos de fadiga multiaxial aos dados experimentais obtidos. Desta análise, foi concluído que modelo multiaxial elaborado por Dang Van é o mais adequado para descrever o fenómeno de fadiga em aço S355. A partir destes ensaios foram também obtidas as curvas experimentais de fadiga para os estados uniaxiais e multiaxiais na região de vidas longas.

Ademais, foram executados testes de taxa de propagação de fenda em fadiga para modo I e diferentes razões de tensão, assim como também foram obtidas as constantes da lei de Paris para o aço S355. As curvas obtidas para a taxa de propagação em função do fator de intensidade de tensões para modo I são também comparadas às obtidas para modo misto (I+II) por outros autores.

Finalmente, a análise à fadiga da ligação proposta no âmbito do projeto SOWTIME foi analisada à fadiga. As curvas numéricas de fadiga para a ligação em estudo foram estimadas considerando tanto um estado de tensões uniaxial como multiaxial. No final desta tese é evidenciada a importância de realizar uma análise multiaxial.

Keywords: fatigue, fracture, S355 steel, multiaxial, wind turbines, structures

To my family.

“Eles não sabem, nem sonham,
Que o sonho comanda a vida,
Que sempre que um homem sonha
O mundo pula e avança
Como bola colorida
Entre as mãos de uma criança.”

António Gedeão, “Pedra Filosofal”

Acknowledgements

First of all, I would like to express my deep gratitude to my parents and sister for all the support, for the infinite patient and for never stop to believe in me.

Besides, I could not forget to mention my boyfriend, who was always present to make me believe in myself and put a smile on my face during the hardest moments.

I am also very grateful for all amazing friends that Porto gave me. Without all of them, these 5 years would be less colourful.

I also owe a huge “thank you” to Professor Grzegorz Lesiuk, my supervisor in Wroclaw, who was always available during my time in Poland, not only with knowledge but also as human being. I would also like to address a special acknowledgement to Monika Duda, PhD student, who kindly taught me how to prepare a sample to perform a microstructure analysis.

Furthermore, I would like to express my acknowledgements to all my co-advisors, Professor Abílio de Jesus and Professor Carlos Rebelo, who also gave crucial contributes to this master thesis. Besides, I am also in debt to Bruno Pedrosa, PhD student and almost a fourth co-advisor, who supported and helped me during the elaboration of this master thesis.

Last but not least, I would like express my gratitude to Professor José Correia, my supervisor, who was so patient with all my doubts and insecurities. He taught to see the world through the eyes of an engineer and not be afraid of being creative and innovator.

Additionally, I would like to express my acknowledgements to FCT - Fundação para a Ciência e a Tecnologia which supported this work through national funds; UID/ECI/047 08/2019 - CONSTRUCT - Instituto de I& D em Estruturas e Construções funded by national funds through the FCT/MCTES (PIDDAC); European Commission’s Framework Program “Horizon 2020”, through the Marie Skłodowska-Curie Innovative Training Networks (ITN) “AEOLUS4FUTURE – Efficient harvesting of the wind energy” (H2020-MSCA-ITN-2014: Grant agreement no. 643167); and ERASMUS+ program. Besides, I would like to acknowledge Wroclaw University of Science and Technology for providing the laboratory facilities, where the experimental work of this master thesis was developed.



Contents

Abstract	i
Resumo	iii
Acknowledgements	ix
1 Introduction	1
1.1 Motivation	1
1.2 Objectives	1
1.3 Content of the Thesis	2
2 State of the Art	3
2.1 A Review on Wind Turbine Towers	3
2.1.1 The Value of Wind Energy	3
2.1.2 Wind Energy Conversion Systems and Working Principle	4
2.1.3 Wind Turbine Towers	5
2.1.4 SOWTIME Proposal	7
2.2 A Review on Fatigue	9
2.2.1 Definition	9
2.2.2 Fatigue stages, influencing factors and regimes	10
2.2.3 Conventional Approaches	12
2.2.3.1 S-N curves	13
2.2.3.2 Fatigue Diagrams	14
2.2.4 Multiaxial Fatigue State	16
2.2.5 Multiaxial Fatigue Models	17
2.2.5.1 Stress Based Multiaxial Fatigue Models	17
2.2.6 Estimation of fatigue life based on multiaxial criterion	24
2.3 A review on Fracture Mechanics	25
2.3.1 Definition	25
2.3.2 Stress Intensity Factor	26
2.3.3 Fatigue Crack Propagation: Paris Law	27
2.4 A review on Basis of Design	28
3 Experimental Programme	31
3.1 Introduction	31
3.1.1 S355 Steel Composition and Properties	31
3.2 Uni- and Multi-axial fatigue Assessment of the S355 steel	32
3.2.1 Uniaxial Fatigue Assessment: Axial load	33
3.2.2 Multiaxial Fatigue Assessment: Axial and Torsional loads	38

3.3	Pure-mode I and Mixed-mode Fatigue Crack Growth Characterization of S355 steel	43
3.3.1	Fatigue Crack Growth Tests - Mode I	43
3.3.2	Fatigue Crack Growth tests- Mixed Mode (Mode I+II)	51
3.3.3	Comparison Between Pure-mode I and Mixed-mode (Mode I+II) Fatigue Crack Growth of S355 Steel	60
4	Application and Evaluation of Multiaxial Fatigue Models	63
4.1	Introduction	63
4.2	Uniaxial Stress Fatigue State Analysis	65
4.3	Multiaxial Stress Fatigue State Analysis	68
4.3.1	Sines Model	68
4.3.2	Findley Model	72
4.3.3	McDiarmid Model	80
4.3.4	Dang Van Model	82
4.4	Conclusions	87
5	Fatigue Numerical Modelling of a Steel Half-pipes Bolted Connection	91
5.1	Finite Element Model	91
5.1.1	Description	92
5.1.2	Materials under Consideration	95
5.2	Monotonic Characterization	95
5.3	Fatigue Modelling Based on Local Stress approaches for High Cycles Regimes	98
5.3.1	Uniaxial Fatigue Stress Analysis	98
5.3.2	Multiaxial Fatigue Stress Analysis	99
5.3.3	Proposed Approaches for Fatigue Life Prediction of Structural Components	100
5.4	Linear Elastic Stress Analysis	102
5.5	Results and Discussion	108
5.5.1	Uniaxial Fatigue Evaluation based on Basquin Law	108
5.5.2	Multiaxial Fatigue Evaluation based on Dang Van Model	110
5.5.3	Multiaxial Fatigue Evaluation based on Findley Model	113
5.6	Conclusions	114
6	Conclusion	117
6.1	Conclusions	117
6.2	Future Work	118
	References	119
A	Experimental Fatigue Data	123
B	Damage Parameters of Sines, Findley, McDiarmid and Dang Van models	127
C	Publications	135

List of Figures

2.1	Total power generation capacity in the European Union from 2008 until 2018 [WindEurope, 2018]	4
2.2	Traditional wind turbine components [Navigant Consulting, 2012]	5
2.3	Large Diameter Steel Tower developed by Vestas [Bauer, Lucas and Matysik, Silvio, 2019b]	6
2.4	Nordex N43 Lattice model [Bauer, Lucas and Matysik, Silvio, 2019a]	6
2.5	Hybrid wind tower proposed by Suzlon [North American Windpower, 2019]	7
2.6	Hybrid tower proposed by [Jovasevic et al., 2019] within the scope of SHOW-TIME project	8
2.7	Cyclic loading	9
2.8	Different stress ratios	10
2.9	Fatigue stages	10
2.10	Main fatigue life domains	12
2.11	S-N curve	13
2.12	Conversion of S-N curves to a fatigue diagram	14
2.13	Gerber fatigue diagram	14
2.14	Goodman fatigue diagrams	15
2.15	Soderberg fatigue diagram	16
2.16	Non-proportional and proportional loading [Lee et al., 2012]	16
2.17	Mesoscopic and macroscopic scales	22
2.18	The three basic modes of fracture [Suresh, 1998]	25
2.19	Stress state around the crack tip [Fernandes et al., 1999]	27
2.20	Fatigue crack growth rate as function of stress intensity factor range [Fernandes et al., 1999]	28
3.1	Microstructure of S355 steel (Magn.400x)	32
3.2	hourglass specimen	33
3.3	Axial loading	33
3.4	MTS 810 testing system	34
3.5	Specimens after axial fatigue tests	35
3.6	Fracture surface of specimens tested under axial loading for $R=0.01$	36
3.7	Specimens tested under axial loading for $R=0.01$	37
3.8	Specimens tested under axial loading for $R=-1$	38
3.9	Biaxial loading applied over time	39
3.10	MTS 809 Axial/torsional test system	39
3.11	Specimens after biaxial tests	41
3.12	Specimens tested under proportional loading for $R=-1$	41
3.13	Fracture surfaces of specimens tested under proportional loading for $R=-1$.	42
3.14	Specimens tested under proportional loading for $R=-1$	43

3.15	CT Specimen geometry	44
3.16	CT specimens used in pure mode I fatigue crack growth rate tests	44
3.17	Apparatus of fatigue crack growth rate test conducted under pure mode I: 1-MTS clip gage (extensometer); 2-MTS clevis grip for fracture mechanics; 3-specimen.	45
3.18	Computer screen during test	46
3.19	Kinetic fatigue fracture diagram for S355 steel for $R=0.1$	47
3.20	Kinetic fatigue fracture diagram for S355 steel for $R=0.5$	48
3.21	Kinetic fatigue fracture diagram for S355 steel for $R=0.7$	48
3.22	Kinetic fatigue fracture diagram for S355 steel for $R=0.1$, $R=0.5$ and $R=0.7$	49
3.23	Broken CT specimens used in pure mode I fatigue crack growth tests	50
3.24	CTS specimen tested under mixed mode	51
3.25	CTS specimen holder [Richard and Benitz, 1983]	52
3.26	Apparatus of FCGR tests performed for mixed-mode: 1-MTS clevis grip for fracture mechanics; 2- CTS specimen holder; 3-CTS specimen 4-DinoLite microscope	53
3.27	Broken CTS specimens (for $\alpha = 30^\circ$, $\alpha = 45^\circ$ and $\alpha = 60^\circ$) [Rozumek et al., 2018]	54
3.28	Macroview on the fracture surface of specimen tested for 30° (initial crack length – notch+precrack=20.675 mm /max 20.895)	54
3.29	Crack initiation angle ($\alpha = 30^\circ$)	55
3.30	Macroview on the fracture surface of specimen tested for 30° (initial crack length – notch+precrack=20.023 mm /max 20.032)	55
3.31	Crack initiation angle ($\alpha = 45^\circ$)	55
3.32	Macroview on the fracture surface of specimen tested for 30° (initial crack length – notch+precrack=20.678 mm /max 20.877)	56
3.33	Crack initiation angle ($\alpha = 60^\circ$)	56
3.34	Fatigue crack growth versus number of cycles under mixed mode	57
3.35	Fatigue crack growth rate versus stress intensity factor for mode I and mode II ($\alpha = 30^\circ$)	58
3.36	Fatigue crack growth rate versus stress intensity factor for mode I and mode II ($\alpha = 45^\circ$)	58
3.37	Fatigue crack growth rate versus stress intensity factor for mode I and mode II ($\alpha = 60^\circ$)	59
3.38	Fatigue crack growth rate versus equivalent stress intensity factor	59
3.39	Fatigue crack growth rate versus stress intensity factor for mode I / equiv- alent stress intensity factor curves and experimental points	60
3.40	Fatigue crack growth rate versus stress intensity factor for mode I / equiv- alent stress intensity factor curves	61
4.1	Stress state and field for tensile, bending, torsional and biaxial loading	64
4.2	Design curves for axial loading for $R = 0.01$ and $R = -1$	65
4.3	Design curves for bending loading for $R = 0$, $R = -0.5$ $R = -1$	66
4.4	Design curves for torsional loading for $R = 0$, $R = -0.5$ $R = -1$	67
4.5	Comparison between design curves for bending and axial stresses	67
4.6	Comparison between design curves for axial and torsional stresses	68
4.7	Sines damage parameter versus fatigue life graph for axial and axial com- bined with torsional stresses (for $k_s = 0.095$)	69
4.8	Sines damage parameter versus fatigue life graph for bending, torsional and bending combined with torsional stresses (for $k_s = 0.095$)	70

4.9	Graph of octahedral shear amplitude versus hydrostatic mean stress	70
4.10	Sines damage parameter versus fatigue life graph for axial and axial combined with torsional stresses (for $k_s = 0.125$)	71
4.11	Sines damage parameter versus fatigue life graph for bending, torsional and bending combined with torsional stresses (for $k_s = 0.125$)	72
4.12	Representation of θ and the normal and shear stress on the <i>theta</i> plane . .	73
4.13	Findley damage parameter versus fatigue life graph for axial and axial combined with torsional stresses (for $k_f = 0.192$)	74
4.14	Findley damage parameter versus fatigue life graph for torsional, bending and bending combined with torsional stresses (for $k_f = 0.192$)	74
4.15	Findley damage parameter versus fatigue life graph for axial and axial combined with torsional stresses (for $k_f = 0.228$)	75
4.16	Findley damage parameter versus fatigue life graph for torsional, bending and bending combined with torsional stresses (for $k_f = 0.228$)	75
4.17	Findley damage parameter versus fatigue life graph for axial and axial combined with torsional stresses (for $k_f = 0.425$)	76
4.18	Findley damage parameter versus fatigue life graph for torsional, bending and bending combined with torsional stresses (for $k_f = 0.425$)	77
4.19	Representation of a new approach to determine k_f	79
4.20	Findley damage parameter versus fatigue life graph for axial and axial combined with torsional stresses (for $k_f = 0.304$)	79
4.21	Findley damage parameter versus fatigue life graph for torsional, bending and bending combined with torsional stresses (for $k_f = 0.304$)	80
4.22	McDiarmid damage parameter versus fatigue life graph for axial and axial combined with torsional stresses	81
4.23	McDiarmid damage parameter versus fatigue life graph for bending, torsional and bending combined with torsional stresses	81
4.24	Experimental fatigue limit points for axial loading and the respective linear regression plotted in a maximum shear stress amplitude versus maximum hydrostatic normal stress graph	82
4.25	Dang Van damage parameter versus fatigue life graph for axial and axial combined with torsional stresses (for $k_d = 0.367$)	83
4.26	Dang Van damage parameter versus fatigue life graph for axial and axial combined with torsional stresses (for $k_d = 0.367$)	83
4.27	Experimental fatigue limit points loading and the respective linear regression plotted in a maximum shear stress amplitude versus maximum hydrostatic normal stress graph	84
4.28	Dang Van damage parameter versus fatigue life graph for axial and axial combined with torsional stresses (for $k_d = 0.341$)	85
4.29	Dang Van damage parameter versus fatigue life graph for bending, torsional and bending combined with torsional stresses (for $k_d = 0.341$)	85
4.30	Dang Van damage parameter versus fatigue life graph for axial and axial combined with torsional stresses (for $k_d = 0.587$)	86
4.31	Dang Van damage parameter versus fatigue life graph for bending, torsional and bending combined with torsional stresses (for $k_d = 0.587$)	87
4.32	Dang Van calculated number of cycles versus experimental number of cycles until failure graph for axial and axial combined with torsional stresses . . .	88

4.33	Dang Van calculated number of cycles versus experimental number of cycles until failure graph for bending, torsional and bending combined with torsional stresses	88
5.1	Gusset plate bolted connection between a brace and a pylon with a diagonal angle of 90°	91
5.2	Numerical model of the gusset plate bolted connection with a pylon to diagonal angle of 90°	93
5.3	Solid bolt model	93
5.4	Numerical model geometry	94
5.5	Assembly and preparation of specimen	96
5.6	Test description	96
5.7	Experimental results	96
5.8	Comparison between the finite element model values with the experimental results [Jovasevic et al., 2019] [SHOWTIME, 2018]	97
5.9	Multiaxial fatigue stress assessment based on Findley criterion and finite element method proposed by Takahashi [2014]	100
5.10	Overview of von Mises stress for a displacement of $20mm$	102
5.11	Overview of maximum principal stress for a displacement of $20mm$	102
5.12	σ_{11} on the gusset plate for a displacement of $20mm$	103
5.13	σ_{22} on gusset plate for a displacement of $20mm$	103
5.14	σ_{33} on the gusset plate for a displacement of $20mm$	104
5.15	τ_{12} on the gusset plate for a displacement of $20mm$	104
5.16	τ_{23} on the gusset plate for a displacement of $20mm$	104
5.17	τ_{13} on the gusset plate for a displacement of $20mm$	105
5.18	σ_{11} on brace for a displacement of $20mm$	105
5.19	σ_{22} on the brace for a displacement of $20mm$	105
5.20	σ_{33} on the brace for a displacement of $20mm$	106
5.21	τ_{12} on the brace for a displacement of $20mm$	106
5.22	τ_{23} on the brace for a displacement of $20mm$	106
5.23	σ_{13} on the brace for a displacement of $20mm$	107
5.24	Numerical fatigue curve considering uniaxial fatigue data and applying the Basquin Law for high cycle regime	110
5.25	Overview of Dang Van damage parameter field for a displacement of $20mm$	111
5.26	Dang Van damage parameter field on the gusset plate for a displacement of $20mm$	111
5.27	Dang Van damage parameter field on the brace for a displacement of $20mm$	112
5.28	Numerical fatigue curve considering multiaxial fatigue data and applying the Dang van model for high cycle region	113
5.29	Comparison between numerical fatigue curves obtained considering uniaxial fatigue data (Basquin law) and multiaxial fatigue data (Dang van model)	115

List of Tables

3.1	Mechanical properties	31
3.2	Chemical composition	31
3.3	Axial tests	35
3.4	Biaxial tests	40
3.5	Dimensions of CT specimens (in <i>mm</i>)	43
3.6	Values of $\frac{da}{dN}$ versus ΔK curves parameters(C, m) for R=0.1, R=0.5 and R=0.7	47
3.7	Experimental programme for mixed mode FCGR tests	52
3.8	Results of mixed mode FCGR tests obtained by Rozumek et al. [2018]	54
3.9	Values of $\frac{da}{dN}$ versus ΔK curves parameters(C, m) for mixed mode	60
3.10	Values of $\frac{da}{dN}$ versus ΔK curves parameters(C, m) for pure mode I and mixed mode(I+II)	60
4.1	Experimental fatigue limit points expressed in $\sigma_{h,mean}$ and $\tau_{a,oct}$ (for $N_f = 5 \cdot 10^6$)	71
4.2	Critical plane for each loading, stress ratio and k_f	78
4.3	Experimental fatigue limit points expressed in $\sigma_{h,max}$ and $\tau_{a,max}$ (for $N_f = 5 \cdot 10^6$)	84
5.1	Key dimensions of B90 connection	94
5.2	Comparison of response characteristics between numerical models and experimental results	98
5.3	Stress levels obtained for each displacement and cross-section properties of the gusset plate	107
5.4	Stress levels obtained for each displacement and cross-section properties of the brace	108
5.5	Stress tensor components in the critical point of the gusset plate and brace for each displacement	108
5.6	Values of Basquin law applied to the gusset plate and brace, for each displacement under consideration	109
5.7	Values of Dang Van model applied to the gusset place and brace for each displacement under consideration	112
5.8	Values of Findley model applied to the gusset place and brace for each displacement under consideration	114
A.1	Fatigue data for pure torsion [Rozumek and Pawliczek, 2004]	123
A.2	Fatigue data for pure bending [Rozumek and Pawliczek, 2004]	124
A.3	Fatigue data for bending combined with torsion [Rozumek and Pawliczek, 2004]	125
A.4	Fatigue data for pure axial loading	126

A.5	Fatigue data for axial combined with torsional loading	126
B.1	Sines damage parameter for pure axial loading and axial combined with torsional loading (for $k_s = 0.125$)	127
B.2	Sines damage parameter for pure torsion, pure bending and torsion com- bined with bending (for $k_s = 0.125$)	128
B.3	Findley damage parameter for pure axial loading and axial combined with torsional loading (for $k_f = 0.304$)	129
B.4	Findley damage parameter for pure torsion, pure bending and torsion com- bined with bending (for $k_f = 0.304$)	130
B.5	McDiarmid damage parameter for pure axial loading and axial combined with torsional loading	131
B.6	McDiarmid damage parameter for pure torsion, pure bending and torsion combined with bending	132
B.7	Dang Van damage parameter for pure axial loading and axial combined with torsional loading	133
B.8	Dang Van damage parameter for pure torsion, pure bending and torsion combined with bending	134

Nomenclature

P	Power produced by a wind turbine
v_w	Wind velocity
r	Length of a wind turbine blade
R	Stress ratio
σ_a	Alternating normal stress
$\Delta\sigma$	Normal stress range
σ_{max}	Maximum normal stress
σ_{fo}	Fatigue limit
σ'_f	Fatigue strength at one cycle
N_f	Number of cycles until failure
σ_E	Maximum principal stress damage parameter
τ_E	Tresca damage parameter
b	Material constant of Basquin model
$\sigma_{VM,a}$	von Mises stress amplitude
$\sigma_{VM,m}$	von Mises mean stress
α_{VM}	Mean stress intensity factor
σ_{min}	Minimum normal stress
σ_{fo-1}	Fatigue limit for R=-1
σ_{bf-1}	Fatigue limit for R=-1 and pure bending/tensile test
$\tau_{a,R=-1}$	Fatigue limit for R=-1 and pure torsional test
$\sigma_{\theta min}$	Minimum normal stress on a θ plane
σ_{mean}	Mean normal stress
σ_1	First principal stress
σ_2	Second principal stress
σ_3	Third principal stress
$\sigma_{1,a}$	Amplitude of the first principal stress
$\sigma_{2,a}$	Amplitude of the second principal stress
$\sigma_{3,a}$	Amplitude of the third principal stress
$\sigma_{1,mean}$	First principal mean stress
$\sigma_{2,mean}$	Second principal mean stress
$\sigma_{3,mean}$	Third principal mean stress
σ_x	Normal stress in the direction of x axis
σ_y	Normal stress in the direction of y axis
τ_{xy}	Shear stress on the xy plane
τ_a	Alternating shear stress
τ_{max}	Maximum shear stress
τ_{min}	Minor normal stress
τ_{mean}	Mean shear stress
$\tau_{a,oct}$	Alternating octahedral stress
σ_{hmean}	Hydrostatic mean stress

s	Sines damage parameter
k_s	Sines constant
σ_{hmax}	Maximum hydrostatic stress
c	Crossland damage parameter
k_c	Crossland constant
f	Findley damage parameter
k_f	Findley constant
σ_θ	Normal stress on a θ plane
$\sigma_{\theta max}$	Maximum normal stress on a θ plane
$\tau_{\theta max}$	Maximum shear stress on a θ plane
$\tau_{\theta min}$	Minimum shear stress on a θ plane
$\tau_{\theta a}$	Alternating shear stress on a θ plane
θ	Angle between σ_x and σ_θ
$t_{A,B}$	Material constants of McDiarmid
$\bar{\sigma}_{macro}(t)$	Macroscopic stress tensor
$\bar{\epsilon}_{macro}(t)$	Macroscopic strain tensor
$\bar{\sigma}_{meso}(t)$	Mesoscopic stress tensor
$\bar{\epsilon}_{meso}(t)$	Mesoscopic strain tensor
$\bar{\epsilon}_{macro}^e(t)$	Elastic macroscopic strain tensor
$\bar{\epsilon}_{meso}^e(t)$	Elastic mesoscopic strain tensor
$\bar{\epsilon}_{meso}^p(t)$	Plastic mesoscopic strain tensor
E_{macro}	Macroscopic Young's modulus
E_{meso}	Mesoscopic Young's modulus
$\bar{\sigma}_{macro,h}(t)$	Macroscopic hydrostatic stress tensor
$\bar{\sigma}_{meso,h}(t)$	Mesoscopic hydrostatic stress tensor
$\bar{\sigma}_{macro,d}(t)$	Macroscopic deviatoric stress tensor
$\bar{\sigma}_{meso,d}(t)$	Mesoscopic deviatoric stress tensor
k_d	Dang Van constant
d	Dang Van damage parameter
K_I	Stress intensity factor for mode I
K_{II}	Stress intensity factor for mode II
K_{III}	Stress intensity factor for mode III
a	crack size length
$\frac{da}{dN}$	Fatigue crack growth rate
C	Paris law constant
m	Paris Law constant
ΔK	Stress intensity factor range
$\Delta\sigma_{nom}$	Nominal normal stress
$\Delta\tau_{nom}$	Nominal shear stress
$\Delta\sigma_{eq,nom}$	Equivalent normal stress
$\Delta\tau_{eq,nom}$	Equivalent shear stress
N_{ref}	Reference number of cycles until failure at a certain level of stress
E	Young modulus
f_y	Yield strength
f_u	Tensile strength
ASTM	American Society for Testing and Materials
F_{min}	Minimum force
F_{max}	Maximum force
M_{min}	Minimum torque
M_{max}	Maximum torque

LIST OF TABLES

FCGR	Fatigue crack growth rate
ΔF	Force range
B	CT and CTS thickness
W	CT and CTS width
ΔK_{eqq}	Equivalent stress intensity factor
δ	Imposed displacement
S_j	Initial stiffness
R_p	Plastic resistance
U_p	Plastic deformation
R_m	Ultimate resistance resistance
U_m	Ultimate deformation
M	Bending moment
I	Inertia of the section
σ_{11}	Normal stress component on 11 direction
σ_{22}	Normal stress component on 22 direction
σ_{33}	Normal stress component on 33 direction
σ_{12}	Shear stress component on 12 plane
σ_{13}	Shear stress component on 13 plane
σ_{23}	Shear stress component on 23 plane

Introduction

1.1 Motivation

Nowadays, the energetic dependency of fossil fuels is a real and critical problem, responsible not only for the exhaustion of natural resources, but also for the climate changes. One available solution is to reduce the energy consume and, consequently, abdicate of some quality life. However, it is easily conclude that this option is not feasible, and only another one is left: develop and increase the energy production from renewable sources.

On of the most emerging and promising renewable sources is the wind. Every year, the energy obtained from onshore and offshore wind turbines is increasing, as well as the number of new wind turbines. Besides, it is observed a tendency to install turbines with greater power capacity. In order to increase the power production, the turbine wind towers are becoming higher with the aim of achieving faster and less turbulent winds, since the power generated is influenced by the wind field.

The increase of tower heights brings some transportation problems, because of the public roads limitations, and additional assembly costs, since higher cranes are also required for erection purpose. Therefore, new design solutions were developed as an alternative to the widely used steel tubular wind tower.

The SHOWTIME project proposed a hybrid tower formed by a lattice lower part and a tubular upper part connected by a transition piece. The lattice part is built with sections produced by cold forming and bolted connected. Because of this, a fatigue assess of the bolted connections is required.

Therefore, uniaxial and biaxial fatigue tests of S355 steel, material used on the lattice structure, should be conducted for different kinds of loading and stress ratio, in order to obtain the experimental fatigue design curves and evaluate the fatigue initiation phase. The biaxial fatigue tests should be conducted under proportional loading, since multiaxial stress state in these structures is mainly a result of the complex geometry.

Besides, the fracture crack growth rate should also be evaluated in Paris law region for S355 steel through experimental tests, with the aim of evaluating the fatigue crack propagation region.

Furthermore, it is also desired to assess a numerical model of the connection steel half-pipes bolted connection, with the purpose of estimating a numerical fatigue design curve.

1.2 Objectives

This master thesis was developed in order to accomplish the following objectives:

- Perform uniaxial(axial) and biaxial(axial+torsional) fatigue experimental tests for different stress ratios, in order to assess the fatigue behaviour of S355 steel in high cycle region;
- Conduct fatigue crack growth tests in pure mode I and mixed mode (mode I+II) and determination of Paris law constants (C and m);
- Obtain uniaxial and multiaxial experimental fatigue curves of S355 steel for different stress ratios;
- Evaluate different multiaxial fatigue damage models and select the one which better describes the fatigue behaviour S355 steel;
- Estimate a numerical fatigue curve of a steel half-pipes bolted connections for onshore wind towers applications;
- Evaluate if a multiaxial fatigue analysis should be performed, instead of a uniaxial fatigue analysis for this kind of connections.

1.3 Content of the Thesis

The research work developed within the scope of this master thesis is described throughout five chapters.

The Chapter 2 aims to introduce some topics, concepts and issues related to the work developed in this master thesis. Thus, it is presented an overview on wind turbine towers, multiaxial fatigue, fracture mechanics and basis of fatigue design for a multiaxial stress state. It is important to keep in mind that this chapter is mainly focus on steel, and some of the behaviours and definitions stated can be different for other materials such as polymers.

In Chapter 3, it is described the experimental programme defined and carried out, in order to characterize the behaviour of S355 steel under a uniaxial and multiaxial fatigue stress state, as well as, the crack growth rate for a mode I and mixed mode(I+II) loading on the same material. Besides describing the experimental procedure, a brief description of the experimental results is also presented in this chapter.

On the other hand, the Chapter 4 includes an extensive and deep analysis of uniaxial and biaxial fatigue data through the application of four different multiaxial fatigue models: Sines, Findley, McDiarmid and Dang Van. The experimental fatigue curves for uniaxial stress states(Torsional, axial and bending loading) are also obtained through the classic basquin law. At the end of this chapter, the experimental fatigue curves for an uniaxial or multiaxial fatigue stress state, for different stress ratios, are determined.

Finally, in Chapter 5, the numerical fatigue curves of the half-pipes connection are estimated for $R = 0$, considering a uniaxial or multiaxial fatigue stress state. The uniaxial fatigue curve is obtained through the basquin law equation determined in Chapter 4, while the multiaxial fatigue curve is proposed based on Dang Van model equation described in the same chapter. The numerical curves considering different stress states are compared, and the relevance of a multiaxial analysis discussed.

Last but not the least, the main conclusions of the work developed and suggestion for future works are presented in Chapter 6.

Additionally, in Appendices can be founded: experimental fatigue data; estimated multiaxial fatigue damage parameters; and, a journal paper and a conference extended abstract, that were developed during the elaboration of this master thesis.

State of the Art

2.1 A Review on Wind Turbine Towers

2.1.1 The Value of Wind Energy

The global warming is a daily concern of modern society which every year is becoming more and more visible and intimidating. The world leaders have been promoting actions and establishing goals in order to reduce the greenhouse effect gases emissions and, consequently, slow down the climate changes.

The energy industry (transportation, electricity production, industry and heating) is responsible for more than half of the greenhouse effect gases produced to the atmosphere. Moreover, in 2014, 81% of the global energy and 65% of global electricity were obtained from fossil fuels [Letcher, 2017].

Since the reducing of energy consume implies a decrease in level of life, the solution for environmental issues relies on the development and investment on renewable energies. For this reason, the wind power industry is quickly growing throughout the last years.

Wind is the second largest source of energy in European Union and its power capacity is growing every year as can be seen in Figure 2.1. At the end of 2018, the total wind power installed capacity was 189 GW (170 GW from onshore and 19 GW from offshore) in Europe and 5.38 GW in Portugal. However, the highest value of wind power production belongs to Germany and 65 % of it was installed in four countries: the UK, Germany, France and Sweden [WindEurope, 2018]. In 2018, wind energy produced was enough to cover 14 % of European Union electricity demand, While in Portugal could cover 24 % [WindEurope, 2018].

Moreover, the financial investment of Europe in wind energy is increasing and in 2018 represented 63% of the total investment in renewable energies. Onshore wind turbines still the most popular way of wind energy conversion and achieved 39% of the total investment mentioned above [WindEurope, 2018].

Another observed trend is the progressive enlargement of wind turbines and the achievement of higher heights, in order to increase the energy production. The average rated capacity of the offshore which were installed in 2018 was 15% larger than the value registered at the end of 2017.

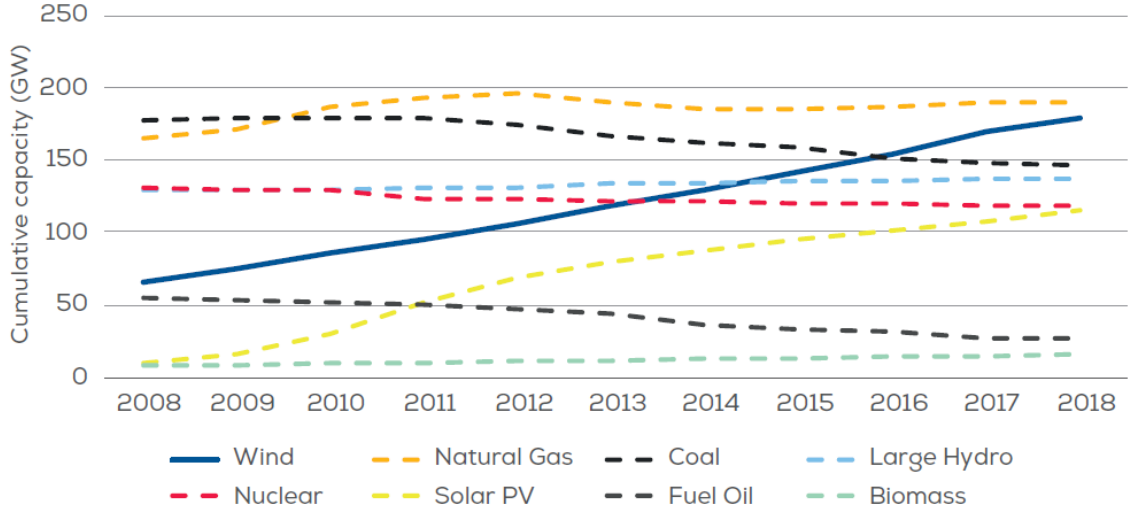


Figure 2.1: Total power generation capacity in the European Union from 2008 until 2018 [WindEurope, 2018]

Summarising, in last years, the investment in offshore wind is increasing and it is expected that the number of offshore installations will double by the end of 2020 [Global Wind Energy Council (GWEC), 2018] [WindEurope, 2018].

However, the increase of energy wind sector arises a few technical challenges related to assembly, transportation and structural safety. In the next sections, these challenges will be more deeply described as well as some solutions proposed.

2.1.2 Wind Energy Conversion Systems and Working Principle

A traditional onshore wind turbine is mainly formed by the foundation, tower, nacelle (where the gearbox and generator are located), hub and three blades (see Figure 2.2).

The wind energy is collect by the blades, which are forced to move into a low-pressure region caused by the air on the blades downside. This force, which is originated by the gradient of pressures, is known as lift, and when combined with another one named as draft, which is caused by the wind against the blade frontside, make the rotor spin. Consequently, the generator turns and electricity is produced [Letcher, 2017].

Therefore, the power generated by a wind turbine can be defined by the following equations:

$$P = av_w^3 \quad (2.1)$$

$$P = br^2 \quad (2.2)$$

where P is the power produced, a and b are constants, v_w is the wind velocity and r is the length of the blade [Letcher, 2017].

At looking for equations above, it is possible to conclude that the power capacity of a wind turbine is highly influenced by wind velocity. Because of this, the wind turbines are becoming higher, in order to achieve regions where the wind is faster and less turbulent [Jovasevic et al., 2019].

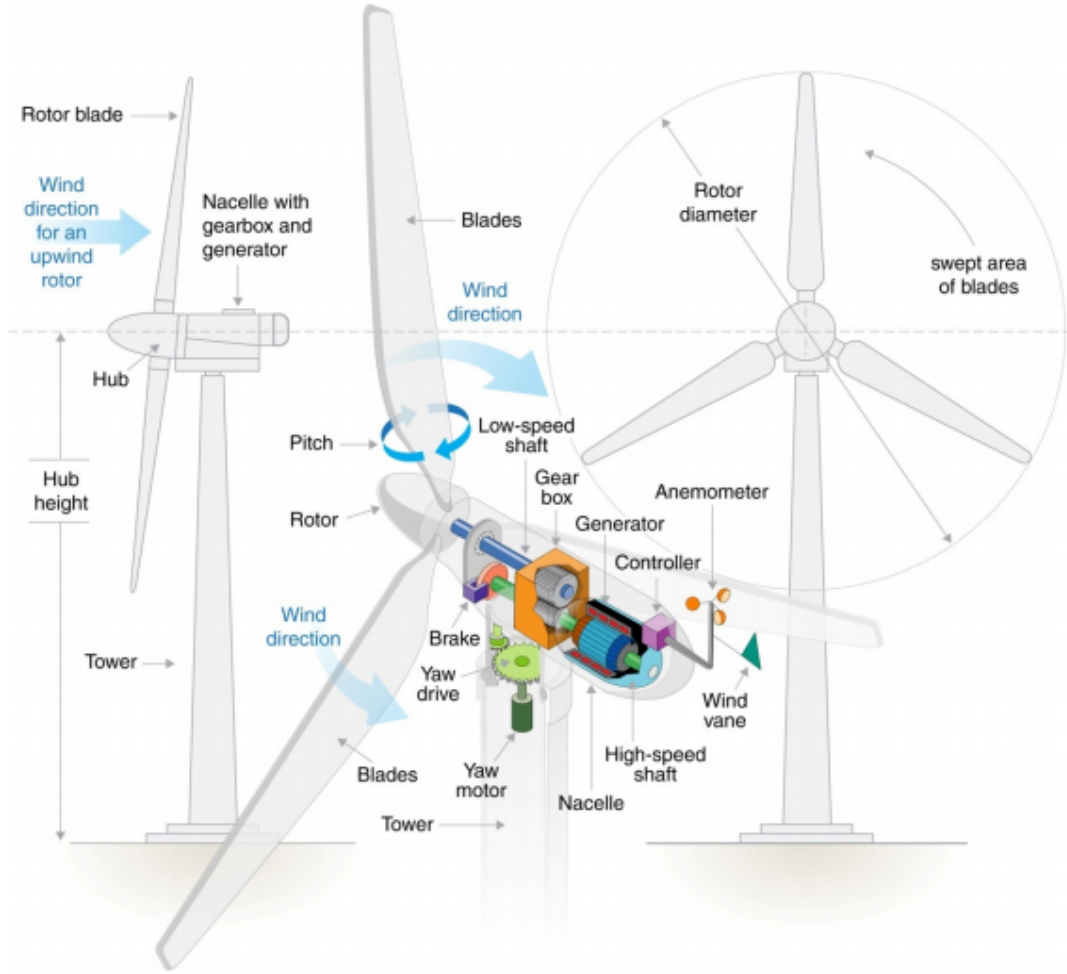


Figure 2.2: Traditional wind turbine components [Navigant Consulting, 2012]

However, the increase of wind turbine towers height is constrained by the following factors:

- Road transportation limits: higher towers require tubular sections of bigger diameter to withstand the buckling effect.
- Assembly cost: larger structures usually imply the use of higher cranes, and, subsequently, more expensive cranes [Jovasevic et al., 2019].

Thus, alternative design solutions for the tower component have been proposed by different authors, in order to overcome these problems and continue to increase the wind energy production.

2.1.3 Wind Turbine Towers

Since the beginning of wind energy industry until now, different wind tower configurations appear, but the most popular were lattice, steel tubular, concrete and hybrid towers.

The lattice towers were widely used in the first decades of the last century, but were progressively replaced by the tubular steel structures, which nowadays is the predominant design solution. The tubular towers have some advantages such as the higher stiffness and easier maintenance and access to different components provided by the tubular sections which constitutes itself a protective structure [Muskulus, 2012].



Figure 2.3: Large Diameter Steel Tower developed by Vestas [Bauer, Lucas and Matysik, Silvio, 2019b]

However, the increase of tower height requires sections of larger diameter and result in a more expensive transportation and assembly. An example of this is the largest world turbine tower which was developed by Vestas and produces 3MW. It has a hub height of $166m$ and a tower bottom section diameter of $6.5m$ (Fig. 2.3), which has to be divided into three parts and assembled on site [Jovasevic et al., 2019] [Vestas Wind Systems A/S, 2013], in order to overcome the transportation road limitations.

Therefore, the lattice and hybrid towers have attracted the interest of some companies and research projects as a solution for these issues, since the structure can be divided in smaller parts for transportation propose.



Figure 2.4: Nordex N43 Lattice model [Bauer, Lucas and Matysik, Silvio, 2019a]

The lattice structures, as can be seen in Figure 2.4, are usually formed by metal profiles connected through bolted connections. These structures provide a reduce on weight, material and cost, as well as, are easily integrated with the environment. Besides, the global vibration are usually not a concern in this structures as in the tubular towers. On the other hand, the manufacturing and maintenance are more difficult and require more attention [Muskulus, 2012]. However, the joints are the critical point of this structures, because of the stress concentration and fatigue phenomenons [Alvarez-Anton et al., 2016].

The hybrid towers are formed by a lower lattice part and a tubular upper part connected by a transition piece (Fig. 2.5), which is usually a critical component since it is responsible for loads transmission between the parts. This design solution combines advantages of tubular and lattice towers, while overcomes the transportation problems [SHOWTIME, 2014].



Figure 2.5: Hybrid wind tower proposed by Suzlon [North American Windpower, 2019]

2.1.4 SOWTIME Proposal

The SHOWTIME project (Steel Hybrid Onshore Wind Towers Installed with Minimal Effort) was one of the research projects which emerged with the aim of developing a new design solution, in order to overcome the transportation and assembly issues.

This project proposed and developed an hybrid wind turbine tower with the lowest number of joints, in order to avoid maintenance issues. Therefore, the project aims to accomplish the following topics:

- Design and optimize the wind tower, taking into account transportation and erection;
- Design and simulate the erection process;
- Develop very high strength steel for preloaded bolts used on the connections of lattice part;

- Design and evaluate through experimental tests the lattice cross sections;
- Describe the construction states and foundation;
- Study the tower life cycle;
- Elaborate design rules for the new wind tower solution proposed, with the aim of including them in design standards [Institute for Sustainability and Innovation in Structural Engineering, 2018];

Thus, the lattice tower sections proposed are formed by three or two elements bolted connected and produced by cold forming. These sections are very thin, but they have a large diameter and, consequently, a high inertia, with the purpose of increasing the resistance to global buckling [Jovasevic et al., 2019].

A large number of studies were conducted to optimize the lattice geometry, which defined several variables such as the number of legs and the spatial distribution of brace members. These analysis were based on the lattice structure weight, number of joints, number of bolts and reaction forces on the foundation. From these studies, a hybrid tower was selected as shown in Figure 2.6.

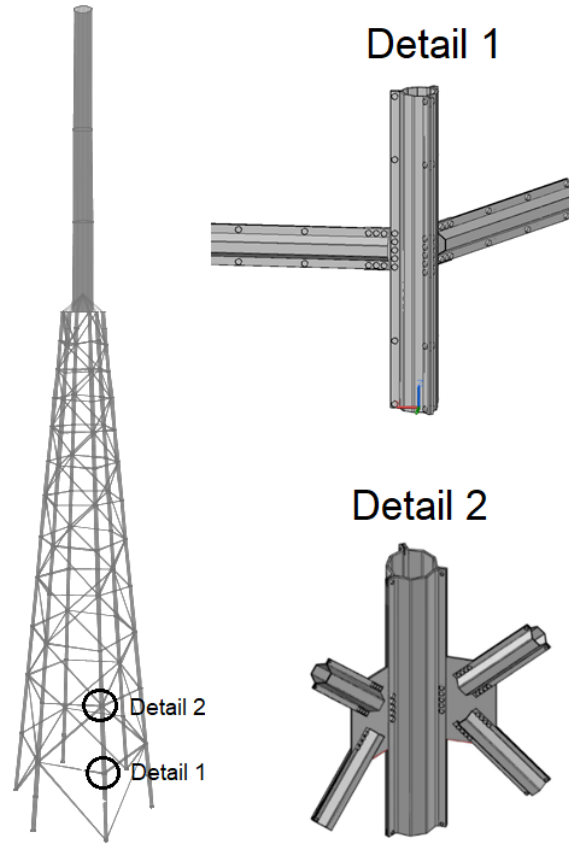


Figure 2.6: Hybrid tower proposed by [Jovasevic et al., 2019] within the scope of SHOW-TIME project

This master thesis is focused on fatigue life assessment of the joint portrayed in detail 1 of Figure 2.6. This steel half-pipes bolted connection is described, in more detail, in Chapter 5.

2.2 A Review on Fatigue

2.2.1 Definition

Fatigue can be easily defined as a failure caused by a repeated load that is lower than the load level that is needed to induce a static failure and it can be from mechanical, thermal or other nature [Kamal and Rahman, 2018]. Searching for a more conventional definition, the American Society for testing and materials defines fatigue as:

“The process of progressive localized permanent structural change occurring in a material subjected to conditions that produce fluctuating stresses and strains at some point or points and that may culminate in cracks or complete fracture after a sufficient number of fluctuations” [ASTM International, 2013]

Regarding to this phenomenon, there are some variables and parameters relevant to mention with the aim to characterize it. One of them, it is the fatigue life that is expressed in the number of cycles until the material failure. Another one is the stress ratio (R) that is calculated by the algebraic ratio of two loading parameters correlated to each cycle. Because of this last variable, it is required to define a couple of loading parameters such as: maximum stress (σ_{max}), minimum stress (σ_{min}), mean stress (σ_{mean}) and stress amplitude (σ_a) [Lee et al., 2012][ASTM International, 2013]. These parameters are represented in Figure 2.7 and related to each other through the Equations (2.3), (2.4) and (2.5).

$$R = \frac{\sigma_{min}}{\sigma_{max}} \quad (2.3)$$

$$\sigma_a = \frac{\sigma_{max} + \sigma_{min}}{2} \quad (2.4)$$

$$\sigma_{mean} = \frac{\sigma_{max} - \sigma_{min}}{2} \quad (2.5)$$

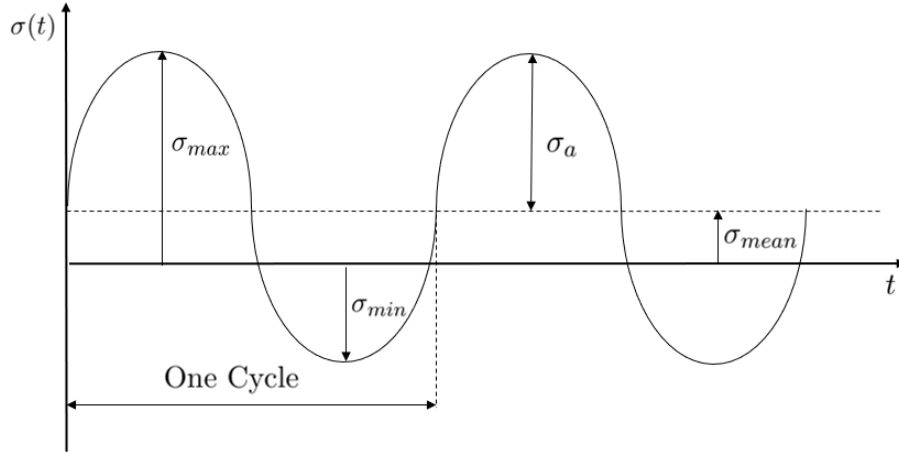


Figure 2.7: Cyclic loading

Hence, a stress fatigue cycle can be defined three different couples of parameters: maximum stress and minimum stress; mean stress and stress amplitude; or stress amplitude and ratio stress. However, in order to characterize the fatigue stress cycle, it is also required the definition of the loading wave shape. In the Figures 2.7 and 2.8, the loading

spectrum is represented as a sinusoidal wave, but it can be of different and more complex shapes. In the case of phenomenons dependent of time such as creep or corrosion, the shape wave and frequency can highly affect the fatigue life [Schijve, 2001].

The loading can be classified according to the mean stress value as: fluctuating ($R > 0$), fully reversed ($R = -1$), repeated ($R = 0$) and reversed ($R < 0$) (Fig. 2.8) [Fernandes et al., 1999].

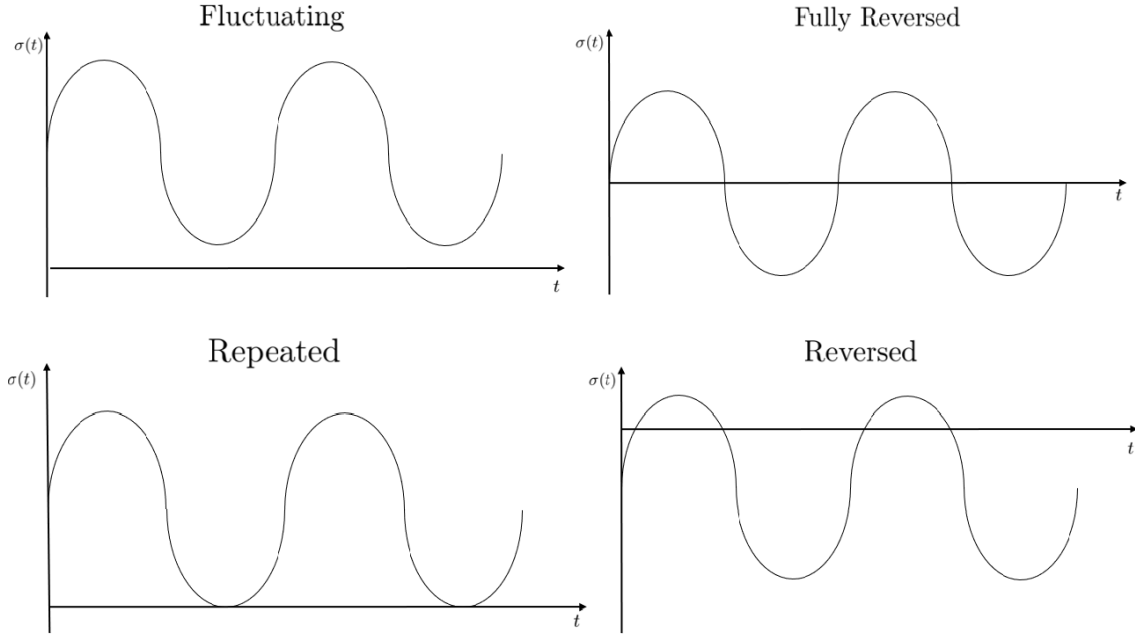


Figure 2.8: Different stress ratios

The fatigue limit (σ_{fo}) can be defined as the limit cyclic loading that does not originate a fatigue failure [Schijve, 2001]

2.2.2 Fatigue stages, influencing factors and regimes

The fatigue life is divided in three phases: initiation/nucleation, crack growth and final failure (Fig. 2.9). These fatigue stages are affected by different factors, for example, the surface condition only influences the first stage and the corrosion affects both of crack initiation and propagation stages, but in different ways and degrees. Therefore, the methodology used to predict the fatigue life of initiation and crack growth should be different [Schijve, 2001].

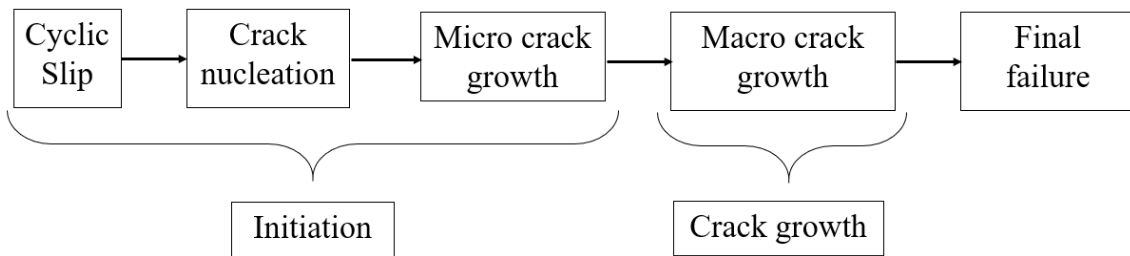


Figure 2.9: Fatigue stages

Nevertheless, most part of fatigue life belongs to the initiation phase. The initiation is

expected to include some microcracks that are not seen by naked eye until a stage near to the failure. The crack initiates at the material surface because of a great number of factors such as: surface roughness, corrosion pits and lower restriction to the movement of slip bands. Concerning to the last factor, it is important to mention that fatigue damage is seen as a consequence of the slip bands dislocations and, as well, the microcracks initiate along them. Usually, after the initiation stage, the crack deviates from the slip band direction and grows perpendicular to the loading direction [Schijve, 2001].

Besides the surface state, there are some material properties that also affect the initiation phase and need to be taken into account, such as: grain size and shape, type of lattice crystal, anisotropy, variation of crystal orientation, composition and presence of inclusions [Schijve, 2001].

The residual stresses have also a huge impact in the fatigue life that is positive when they are compressive and mainly undesirable in the tensile case. Generally, the ultimate tensile strength is also a decisive factor in the material fatigue behaviour. Moreover, concerning the component characteristics, the geometry requires attention since it can originate a concentration of stresses that implies the application of some kind of corrective factors such as the stress concentration factor (K_f) [Boardman et al., 1990].

There are two main regimes of fatigue: low cycle fatigue (LCF) and high cycle fatigue (HCF), which one with different characteristics. These two regimes are represented through a S-N curve in Figure 2.10, which is a graphic way to represent the fatigue life of a component or material that will be explained in the future sections. In the last years, other fatigue regimes started to be focus of research, such as very-high cycle fatigue or ultra low cycle fatigue [Lee et al., 2012].

Low cycle fatigue regime is characterized by high loads and a short fatigue life, that is usually less than 10^4 cycles. In this regime, the material suffers a macroplastic deformation since the first cycle. On the other hand, for a high cycle fatigue regime, a elastic deformation state is present and is observed a longer life between 10^4 and 10^7 number of cycles. Hence, the crack initiation occupies major part of the fatigue life in high cycle regime.

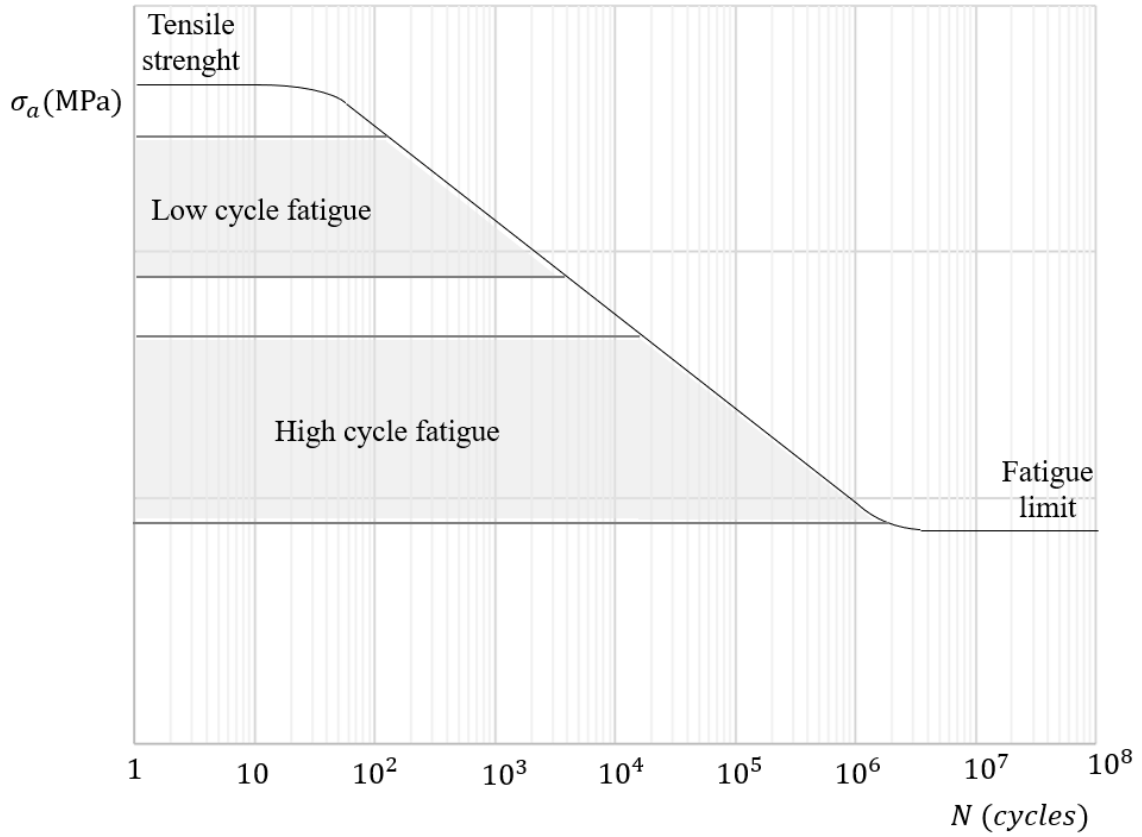


Figure 2.10: Main fatigue life domains

The turning point from one regime to the other is not well established and the main difference relies on the types of deformation that were mention before. Thus, because of these differences, the approaches more suitable and used to evaluate the fatigue life are distinct and based on different parameters for each regime. For example, the major part of LCF models use a strain approach, while the HCF models prefer a stress approach [Schijve, 2001] [Socie, 1993].

The stress amplitude highly affects the fatigue damage and the mean stress is a factor that requires same attention in the high cycle fatigue regime since it influences the opening or the closing of microcracks. For example, a compressive mean normal stress helps the closing of microcracks which increases the resistance to fatigue, while a tensile mean stress has the opposite effect. Hence, there are a large number of models that account for the mean stress effect as it is explained in the next sections [Lee et al., 2012].

Since the main focus of this work is the high cycle fatigue regime, from here to beyond the approaches and models suitable to it will be explained and presented .

2.2.3 Conventional Approaches

The first identification of fatigue phenomenon occurred in the end of nineteenth century and August Wöhler was one of the first ones to describe it. He had not only published the results of some fatigue tests, but also stated important conclusions about them such as: the main parameter of influence in fatigue life is the stress amplitude, while the mean stress has a secondary important role. A few years later, Basquin completed Wöhler's work with a way to represent and evaluate fatigue life that even nowadays is of great relevance. In

this section, Basquin's work and other pertinent fatigue approaches that were developed during the last century will be presented and explained [Schütz, 1996].

The models discussed in this chapter assume that the initial material is perfect and without defects or cracks. If it is desired to analyse the behaviour of a material to the presence of a defect or the crack growth stage in detail should be applied a mechanic fracture approach [Fernandes et al., 1999].

2.2.3.1 S-N curves

Basquin suggested to plot the fatigue data points for different level of loading as stress amplitude (σ_a) versus number of cycles until failure (N_f), selecting a logarithmic scale for the number of cycles axis and a logarithmic or linear scale for the stress amplitude axis (Fig. 2.11). Hence, it is possible to obtain a linear curve that is known as S-N curve or Wöhler curve. Since a S-N curve is a mean curve, it represents each combination of stress amplitude and number of cycles for which half of the specimens fail. It is important to notice that there is a S-N curves for each value of mean stress and for higher values of mean stress this curve will be located lower on the graph [Boardman et al., 1990] [Lee et al., 2012].

The S-N curve can be written as:

$$\sigma_a = \sigma_{f'}(2N_f)^b \quad (2.6)$$

where, b is a material constant and slope of the linear regression and $\sigma_{f'}$ is the fatigue strength at one cycle [Lee et al., 2012].

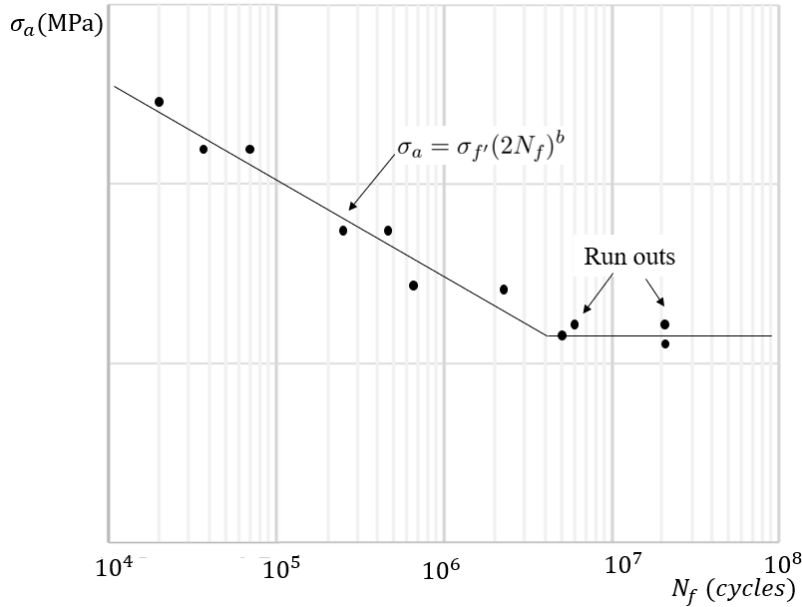


Figure 2.11: S-N curve

A material S-N curve can be determined by carrying out an experimental campaign with unnotched specimens. Since about 90 % of the fatigue life of each specimen is covered by the initiation stage, this curve can be used to predict the initiation crack stage of a notched element [Schijve, 2001].

2.2.3.2 Fatigue Diagrams

Fatigue diagrams plot fatigue data for a certain number of cycles or for the fatigue limit in a single curve. This curve usually represents the amplitude stress, the maximum or minimum stress as function of the mean stress and it can be compared to the S-N curves (Fig. 2.12). Moreover, for an amplitude stress equal to zero, all curves generally converge to the ultimate tensile strength or yield strength [Schijve, 2001].

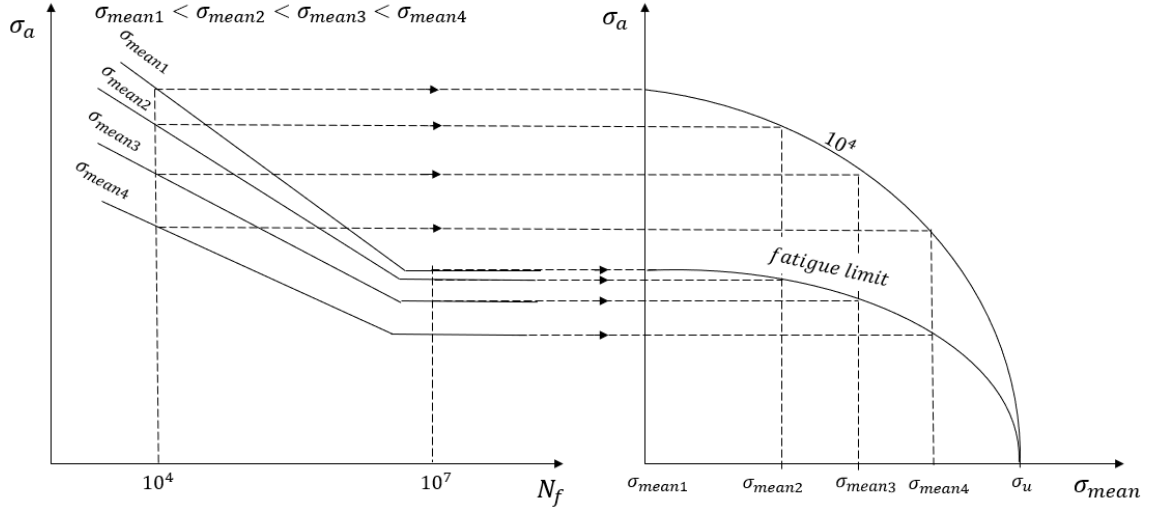


Figure 2.12: Conversion of S-N curves to a fatigue diagram

This is a general description of this kind of representation, and, obviously, there are some variations between each diagram type. The most relevant fatigue diagrams will be presented in the following sections.

Gerber

Around 1880, Gerber proposed the following equation as fatigue criterion:

$$\sigma_a = \sigma_{fo-1} \left(1 - \left(\frac{\sigma_{mean}}{\sigma_u} \right)^2 \right) \quad (2.7)$$

where σ_{fo-1} is the fatigue limit for $R = -1$

As can be seen in the Figure 2.13, this diagram is a parable and has in consideration the fatigue limit and the ultimate strength.

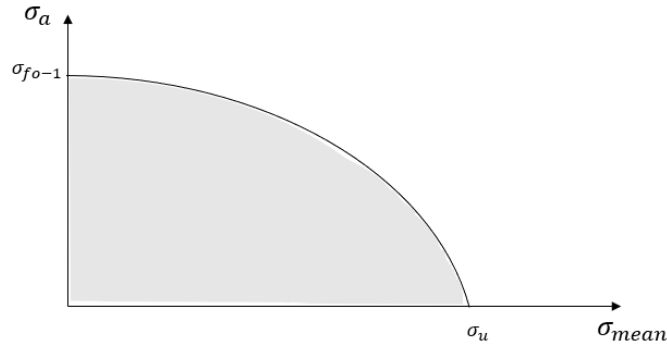


Figure 2.13: Gerber fatigue diagram

Goodman

Some years later, around 1900, Goodman proposed as criterion the expression from Equation 2.8. However, this diagram was modified through the addition of a second condition in order to avoid the plastic deformation zone. This pair of equations is known as “modified Goodman ” and it is expressed through the system Equation (2.9).

The original Goodman and modified Goodman diagrams are depicted in Figure 2.14. Thus, it is possible to observe that the safety area is reduced from the first diagram to the modified one since it results from the intersection of areas below the two lines defined.

$$\sigma_a = \sigma_{fo-1} \left(1 - \frac{\sigma_{mean}}{\sigma_u} \right) \quad (2.8)$$

$$\begin{cases} \sigma_a = \sigma_{fo-1} \left(1 - \frac{\sigma_{mean}}{\sigma_u} \right) \\ \sigma_{mean} + \sigma_a = \sigma_y \end{cases} \quad (2.9)$$

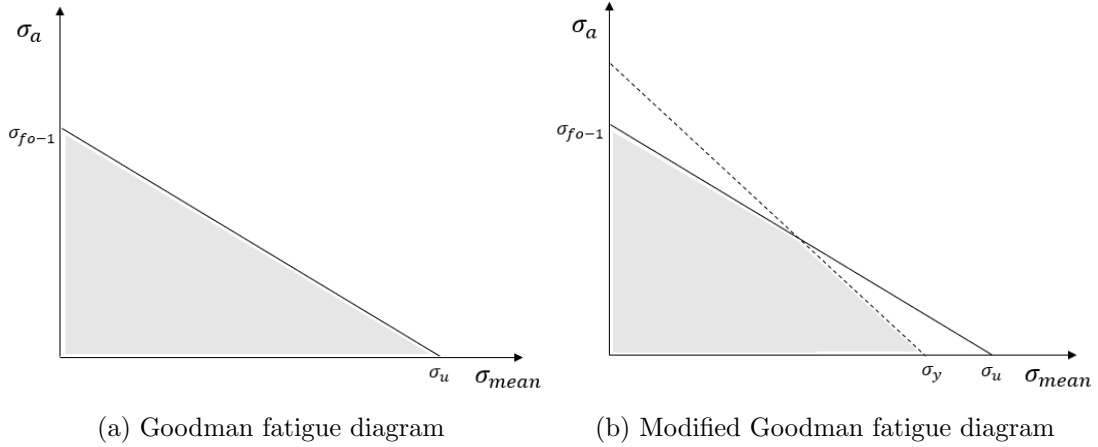


Figure 2.14: Goodman fatigue diagrams

Soderberg

The Soderberg diagram was elaborated around 1930 and is the most safe and conservative one since limits the maximum mean stress value to the yield strength. Hence, it proposes the following linear relation as fatigue criterion:

$$\sigma_a = \sigma_{fo-1} \left(1 - \frac{\sigma_{mean}}{\sigma_y} \right) \quad (2.10)$$

Through the Soderberg representation in Figure 2.15, it is possible to verify the linear relation that is established between σ_a and σ_{mean} .

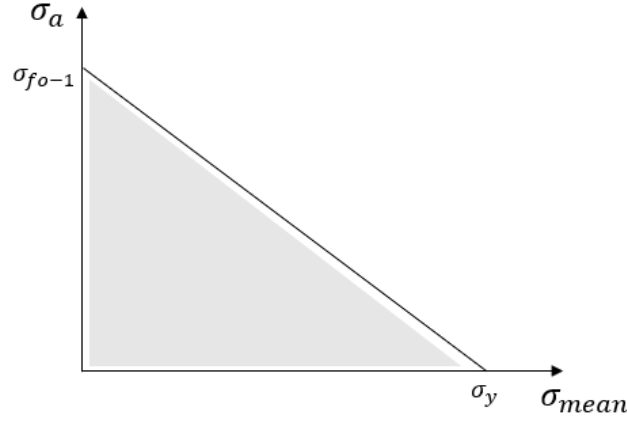


Figure 2.15: Soderberg fatigue diagram

2.2.4 Multiaxial Fatigue State

Until now, the fatigue state was perceived as a uniaxial state and all the approaches mention above are elaborated for that stress state. However, the reality is far from a uniaxial state: most of the time, it is, in fact, a complex multiaxial stress state. A large number of engineering structures such as wind turbine towers, bridges or offshore structures suffer of this fatigue state. Unfortunately, the damage caused by a multiaxial fatigue stress state and the way to assess it have remained not well known. Hence, it is a completely open topic and, nowadays, continues to be focus of investigation [Ellyin and Kujawski, 1993] [Dang-Van, 1994].

The multiaxial loading can be divided into two types: proportional and non-proportional. During the first type, the principal stress directions do not change since the loads are in-phase, while in a non-proportional loading these directions are always changing as result of out-of-phase loads (Fig. 2.16). These types of loading will result in distinguish fatigue behaviours, and, as consequence, the models suitable to proportional loading sometimes are not appropriate to the second one. Besides, usually, a non-proportional loading is more damaging and implies a more complex interpretation and prediction of fatigue life [Kamal and Rahman, 2018] [Lee et al., 2012].

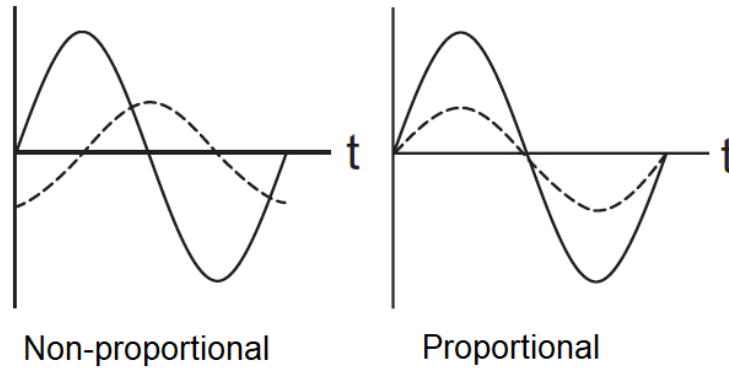


Figure 2.16: Non-proportional and proportional loading [Lee et al., 2012]

The main scope of this thesis is to analyse a proportional fatigue loading, for this reason hardening and other material phenomenons related with out-of-phase loads will not be mentioned.

2.2.5 Multiaxial Fatigue Models

As stated before, multiaxial fatigue is a complex phenomenon, then it should not be turned into an equivalent uniaxial fatigue state through a simple static hypotheses. In fact, a large number of variables need to be considered such as the material cyclic properties and the different effects of a shear stress and normal stress [Margetin et al., 2016]. Therefore, since the last century, a large number of multiaxial fatigue models which account for different factors have appeared. Generally, each models try to reflect the multiaxial fatigue process and damage in a mathematics condition.

The development of multiaxial fatigue models is a quite recent and open topic, for this reason, a large number of models and different point of views can be easily founded in the literature. Frequently, even contradictory ideas are stated, which makes establishing a solid idea about multiaxial fatigue a hard task. Thus, it was decided to approach this topic based on the most frequently accepted and mentioned points of view.

Hence, as expected, there are no consensual classification of the multiaxial models, but they can be generally divided into three major groups: stress, strain or energy based models. Actually, the last ones mentioned are also known as strain-energy models and, sometimes, are even suppressed and included in the strain approaches [Lee et al., 2012].

The stress based models are based on the stress tensor and are suitable for the high cycle regime since it is seen as an elastic deformation state. On the other hand, stain models are related to the strain tensor and usually applied to the low cycle regime. However, they are also appropriated for the high cycle fatigue regime, what makes them a good choice when it is desired to asses both of the regimes. Finally, the energy models rely on energy quantities and are associated to plastic deformation energy. As consequence of this, they are also more suitable and applied to low cycle regime [Maktouf et al., 2016].

In the next sections will be presented some of the most relevant and important models established during the last decades. Since the focus of this thesis and the experimental program develop is to assess the high cycle fatigue regime, only the stress based models will be mention.

2.2.5.1 Stress Based Multiaxial Fatigue Models

Besides the classification established above, the stress based models can be divided into: empirical formula, equivalent stress and critical plane models [Lee et al., 2012]. Each of these categories has distinguish characteristics that will be explained.

Empirical Formula Models

The empirical models were the first ones to appear and are strongly related to experimental fatigue data. The main drawback of these models is the limited applicability to biaxial fully reversed stress state [Lee et al., 2012].

Gough and Pollard

Around 1930, Gough and Pollard had conducted a large number of in-phase fatigue tests under bending and torsional loads, that in 1950 allowed the formulation of an empirical model. The proposed hypotheses establishes different failure conditions to brittle and ductile materials:

$$\begin{cases} \left(\frac{\sigma_a}{\sigma_{a,R=-1}}\right)^2 + \left(\frac{\tau_a}{\tau_{a,R=-1}}\right)^2 = 1 & \text{for ductile materials} \\ \left(\frac{\sigma_a}{\sigma_{a,R=-1}}\right) + \left(\frac{\tau_a}{\tau_{a,R=-1}}\right)^2 = 1 & \text{for brittle materials} \end{cases} \quad (2.11)$$

where $\sigma_{a,R=-1}$ is the fully reversed fatigue limit for pure bending and $\tau_{a,R=-1}$ is the fully reversed fatigue limit for pure torsion [Lee et al., 2012].

Equivalent Stress Models

The equivalent stress models are based on static yield criteria and consist on the transformation of a multiaxial state into a equivalent uniaxial fatigue stress state. A great part of these models can not be applied to a non-proportional loading and are not very effective to incorporate the fatigue phenomenon. However, they are frequently used because of the simple and easy application [Kallmeyer et al., 2002].

Maximum Principal Stress

The maximum principal stress model states that fatigue crack initiation starts when the maximum principal stress amplitude ($\sigma_{1,a}$) is equal or greater than normal stress fatigue limit of a uniaxial fully reversed test ($\sigma_{a,R=-1}$) [Lee et al., 2012]:

$$\sigma_E = \sigma_{1,a} \geq \sigma_{a,R=-1} \quad (2.12)$$

Maximum Shear Stress (Tresca)

The tresca criterion can be also extended to fatigue and it considers that initiation crack happens when the following condition is verified.

$$\tau_E = \tau_{a,max} = \frac{\sigma_{1,a} - \sigma_{3,a}}{2} \geq \tau_{a,R=-1} \quad (2.13)$$

where $\sigma_{1,a}$ is the maximum principal amplitude and σ_3 is the minimum principal amplitude [Lee et al., 2012].

von Mises

Accordingly to the von Mises model extended to fatigue, the crack initiation occurs when the Equation (2.14) is verified.

$$\sigma_{VM,a} + \alpha_{VM} \cdot \sigma_{VM,m} \geq \sigma_{a,R=-1} \quad (2.14)$$

where α_{VM} is the mean stress sensitivity factor, $\sigma_{VM,a}$ is the von Mises stress amplitude and $\sigma_{VM,m}$ is the von Mises mean stress.

The last two variables are calculated through the following equations:

$$\sigma_{VM,m} = \sigma_{1,mean} + \sigma_{2,mean} + \sigma_{3,mean} \quad (2.15)$$

$$\sigma_{VM,a} = \frac{1}{\sqrt{2}} \sqrt{(\sigma_{1,a} - \sigma_{2,a})^2 + (\sigma_{2,a} - \sigma_{3,a})^2 + (\sigma_{1,a} - \sigma_{3,a})^2} \quad (2.16)$$

where $\sigma_{1,a}$, $\sigma_{2,a}$ and $\sigma_{3,a}$ are the principal stresses amplitudes and $\sigma_{1,mean}$, $\sigma_{2,mean}$ and $\sigma_{3,mean}$ are the principal mean stresses [Lee et al., 2012].

Sines

Sines [1955] and Sines [1959] conducted an extensive study around experimental fatigue data for bending, torsional and combined torsional and bending that resulted in the equation 2.17. The failure happens when the left side of the equation is larger than the constant s .

$$\tau_{a,oct} + k_s \cdot (3\sigma_{hmean}) = s \quad (2.17)$$

where s is a constant material proportional to the fatigue limit, k_s is another material constant that represents the allowed value of static stress, σ_{hmean} is the hydrostatic stress for mean stresses defined as:

$$\sigma_{hmean} = \frac{\sigma_{1mean} + \sigma_{2mean} + \sigma_{3mean}}{3} \quad (2.18)$$

and $\tau_{a,oct}$ is the octahedral shear stress amplitude calculated through the following equation:

$$\tau_{a,oct} = \frac{1}{3} \sqrt{(\sigma_{1,a} - \sigma_{2,a})^2 + (\sigma_{2,a} - \sigma_{3,a})^2 + (\sigma_{1,a} - \sigma_{3,a})^2} \quad (2.19)$$

Both of the constants can be calculated with two tensile fatigue tests: one for $R = -1$ and another for $R = 0$ [Sines, 1959].

Hence, the octahedral shear stress amplitude and hydrostatic mean stress were calculated for $R = -1$:

$$\tau_{a,oct,R=-1} = \frac{\sqrt{2}}{3} \sigma_{1,a} = \frac{\sqrt{2}}{3} \sigma_{a,R=-1} \quad (2.20)$$

$$\sigma_{hmean,R=-1} = 0 \quad (2.21)$$

then, it is obtained:

$$s = \tau_{a,oct,R=-1} = \frac{\sqrt{2}}{3} \sigma_{a,R=-1} \quad (2.22)$$

Now, calculating the same parameters for $R = 0$:

$$\tau_{a,oct,R=0} = \frac{\sqrt{2}}{3} \sigma_{1,a} = \frac{\sqrt{2}}{3} \sigma_{a,R=0} \quad (2.23)$$

$$\sigma_{hmean,R=0} = \sigma_{1,mean} = \sigma_{1,a} \quad (2.24)$$

substituting in the equation 2.17:

$$k_s = \frac{\sqrt{2}}{3} \left(\frac{\sigma_{a,R=-1} - \sigma_{a,R=0}}{\sigma_{a,R=0}} \right) \quad (2.25)$$

Although this model includes the effect of mean stress, it can not be applied to non-proportional loading [Lee et al., 2012].

Crossland

The Crossland model is identical to the one proposed by Sines, but instead of hydrostatic mean stress is included the maximum hydrostatic stress (σ_{hmax}) as can be seen in Equation (2.26). Hence, this model can be applied to non-proportional loading [Lee et al., 2012].

$$\tau_{a,oct} + k_c \cdot (3\sigma_{hmax}) = c \quad (2.26)$$

where c and k_c are material constants and σ_{hmax} is the maximum hydrostatic stress that can be calculated through the following equation:

$$\sigma_{hmax} = \frac{\sigma_{1max} + \sigma_{2max} + \sigma_{3max}}{3} \quad (2.27)$$

Critical Plane Models

The critical plane approach introduces the concept of critical plane where the probability of crack initiation is higher. This kind of models should take into account the physical mechanism of fatigue damage and microcracking and each model is characterized by the definition of critical plane [McDowell and Ellis, 1994] [Kallmeyer et al., 2002].

Findley

Findley [1958] proposed, for the first time, a critical plane approach. This criterion states that shear stress is the primary mechanism of fatigue damage and normal stress behaves as a secondary mechanism. Therefore, nucleation and initiation of small cracks is responsibility of shear stress, while normal stress affects the capability of a material withstand cyclic loadings. This model takes in account the effect of mean stress, and states that, in ductile metals, this variable is not very relevant for torsion, but it has a great influence on bending [Findley, 1958].

According to this criterion, the critical plane is defined as the plane where a certain damage parameter achieves the maximum value. The damage parameter is the maximum value of a linear relation between alternating shear stress on a θ plane ($\tau_{\theta a}$) and maximum normal stress ($\sigma_{\theta a}$) on that same plane multiplied by a k_f factor that manages the influence of this kind of stress on fatigue life. The failure will happen when the damage parameter is equal to a material constant f as can be seen in the following equation [Findley, 1958]:

$$(\tau_{\theta a} + k_f \cdot \sigma_{\theta max})_{max} = f \quad (2.28)$$

It is important to mention that f and k_f are constants for a certain number of cycles until failure.

This theory can be applied only to proportional loadings, which means that the following condition need to be verified:

$$\frac{\tau_a}{\sigma_a} = \frac{\tau_{max}}{\sigma_{max}} = a \quad (2.29)$$

Besides, Findley defined other equations to determine f in particular cases of combined torsional and bending/axial load, pure torsion and pure bending/axial load. For the first case:

$$f = \sqrt{\left(\left(\frac{\sigma_a}{2} \right)^2 + \tau_a^2 + k_f^2 \cdot \left(\left(\frac{\sigma_{max}}{2} \right)^2 + \tau_{max}^2 \right) \right)} + k_f \cdot \frac{\sigma_{max}}{2} \quad (2.30)$$

For pure torsion, it is known that $\sigma_{max} = \sigma_a = 0$:

$$f = \sqrt{\tau_a^2 + k_f^2 \cdot \tau_{max}^2} \quad (2.31)$$

as $\tau_{max} = \tau_a + \tau_{mean}$, equation (2.31) can be redefined:

$$f = \sqrt{\tau_a^2 + k_f^2 \cdot (\tau_a + \tau_{mean})^2} \quad (2.32)$$

As stated before, mean shear stress is almost irrelevant for fatigue life in case of torsion loads. For this reason, it can be ignored in Equation (2.32):

$$f = \sqrt{1 + k_f^2} \cdot \tau_a \quad (2.33)$$

For axial load or pure bending, $\tau_{max} = \tau_a = 0$, then f is defined as :

$$f = \sqrt{\left(\frac{\sigma_a}{2}\right)^2 + k_f^2 \cdot \left(\frac{\sigma_{max}}{2}\right)^2} + k_f \cdot \frac{\sigma_{max}}{2} \quad (2.34)$$

The value of k_f constant or the method to determine it is not well establish neither by Findley nor other authors. However, some expressions related with stress fatigue limit in case of pure bending, axial or pure torsion loads, were developed [Socie, 2018]:

$$\frac{\sigma_{a,R=-1}}{\tau_{a,R=-1}} = \frac{2}{1 + \frac{k_f}{\sqrt{1+k_f^2}}} \quad (2.35)$$

$$\frac{\sigma_{a,R=0}}{\sigma_{a,R=-1}} = \frac{k_f + \sqrt{1+k_f^2}}{2k_f + \sqrt{1+(2k_f)^2}} \quad (2.36)$$

$$\frac{\sigma_{a,R=0.5}}{\sigma_{a,R=-1}} = \frac{k_f + \sqrt{1+k_f^2}}{4k_f + \sqrt{1+(4k_f)^2}} \quad (2.37)$$

In the equations above (Eqs. (2.35),(2.36) and(2.37)), $\sigma_{a,R=-1}$ is the fatigue limit in a axial or bending fatigue test performed with stress ratio equal to -1; $\sigma_{a,R=0}$ is the fatigue limit in a axial or bending fatigue test performed with stress ratio equal to 0; $\sigma_{a,R=0.5}$ is the fatigue limit in a axial or bending fatigue test performed with stress ratio equal to 0; and $\tau_{a,R=-1}$ is the fatigue limit in a torsion fatigue test performed with stress ratio equal to -1. Hence, It is only necessary to conduct two different types of uniaxial tests to determine fatigue limit, and, as consequence, be able to calculate k_f [Socie, 2018].

However, in chapter 3, this subject will be discussed again and a another method used to calculated this constant is presented.

McDiarmid

McDiarmid [1994] and McDiarmid [1991] presented a critical plane approach for multi-axial high-cycle fatigue that can be applied to non-proportional loading and includes the mean stress effect. According to this criterion, the critical plane is the plane where shear stress amplitude achieves the maximum value. This model defines two different cases: a case A characterized by cracks growing along the surface and a case B when the cracks grow inwards from the surface.

Hence, it is stated that fatigue failure is achieved when the following condition is verified:

$$\frac{\tau_{\theta a}}{t_{A,B}} + \frac{\sigma_{\theta max}}{2\sigma_u} = 1 \quad (2.38)$$

where $t_{A,B}$ is a material constant defined as:

$$\begin{cases} t_{A,B} = t_A & \text{for case A} \\ t_{A,B} = t_B & \text{for case B} \end{cases} \quad (2.39)$$

where t_A and t_b are the reversed shear fatigue limit for case A and case B, respectively.

This criterion can be rewritten and expressed by the Equation (2.40).

$$\tau_{\theta a} + \frac{t_{A,B}}{2\sigma_u} \sigma_{\theta max} = t_{A,B} \quad (2.40)$$

Dang Van's Multi-scale Approach

Dang-Van [1994] defined an approach based on a "micro-macro" scale analysis and local variables. Hence, two scales are defined:

- Macroscopic scale: used by engineers and characterized by an elementary volume $V(M)$ surrounding the point M where the fatigue analysis is made. The macroscopic stress ($\bar{\sigma}_{macro}(t)$) and strain ($\bar{\epsilon}_{macro}(t)$) are assumed to be homogeneous in the elementary volume at any time t (Fig. 2.17).
- Mesoscopic scale: is a subdivision of $V(M)$ and of the order of grain size. The mesoscopic stress ($\bar{\sigma}_{meso}(t)$) and strain ($\bar{\epsilon}_{meso}(t)$) are not homogeneous and different from macroscopic variables (Fig. 2.17).

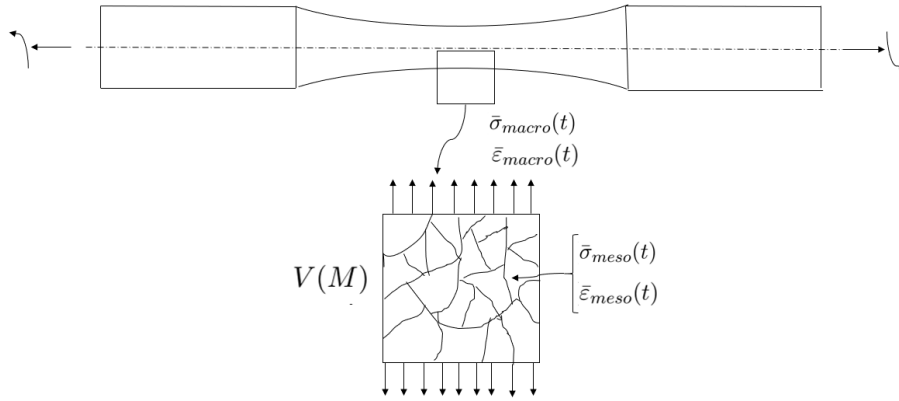


Figure 2.17: Mesoscopic and macroscopic scales

This criterion applies the elastic shakedown principles to the mesoscopic scale and assumes that an elastic shakedown occurs before crack initiation [Desimone et al., 2006]. This phenomenon is associated to high cycle fatigue since it represents a stabilized elastic response which only occurs when the yield strength is not achieved [Lee et al., 2012]. Due to the principles mentioned above, the following conditions between macroscopic and mesoscopic variables can be established:

$$\bar{\epsilon}_{macro}^e(t) = \bar{\epsilon}_{meso}^e(t) + \bar{\epsilon}_{meso}^p(t) \quad (2.41)$$

where $\bar{\epsilon}_{meso}^e(t)$ is the elastic mesoscopic strain tensor and $\bar{\epsilon}_{meso}^p(t)$ is the plastic mesoscopic strain tensor.

Applying Hooke's law:

$$\bar{\epsilon}_{macro}^e(t) = \frac{\bar{\sigma}_{macro}(t)}{E_{macro}} \quad (2.42)$$

$$\bar{\epsilon}_{meso}^e(t) = \frac{\bar{\sigma}_{meso}(t)}{E_{meso}} \quad (2.43)$$

where E_{macro} is the macroscopic Young's modulus and E_{meso} is the mesoscopic Young's modulus.

Besides, after a certain number of cycles, the mesoscopic plastic strain stabilizes and turns independent of time. Thus, the mesoscopic stress tensor can be defined by rewriting the Equation (2.41):

$$\bar{\sigma}_{meso}(t) = \frac{E_{meso}}{E} \bar{\sigma}_{macro}(t) - E_{meso} \bar{\varepsilon}_{meso}^p \quad (2.44)$$

Assuming $\frac{E_{meso}}{E_{macro}} = 1$:

$$\bar{\sigma}_{meso}(t) = \bar{\sigma}_{macro}(t) - E_{meso} \bar{\varepsilon}_{meso}^p = \bar{\sigma}_{macro}(t) + \rho \quad (2.45)$$

where ρ is a mesoscopic residual stress and a deviatoric tensor.

Both macroscopic and mesoscopic stress tensors can be divided into a deviatoric stress tensor ($\bar{\sigma}_{macro,d}(t)$ or $\bar{\sigma}_{meso,d}(t)$) and hydrostatic stress tensor ($\bar{\sigma}_{macro,h}(t)$ or $\bar{\sigma}_{meso,h}(t)$). For the first scale mentioned:

$$\bar{\sigma}_{macro}(t) = \bar{\sigma}_{macro,h}(t) + \bar{\sigma}_{macro,d}(t) \quad (2.46)$$

where the hydrostatic tensor is defined as:

$$\bar{\sigma}_{macro,H}(t) = \begin{bmatrix} \sigma_h(t) & 0 & 0 \\ 0 & \sigma_h(t) & 0 \\ 0 & 0 & \sigma_h(t) \end{bmatrix} \quad (2.47)$$

$$\sigma_h(t) = \frac{\sigma_1(t) + \sigma_2(t) + \sigma_3(t)}{3} \quad (2.48)$$

and for the mesoscopic stress tensor:

$$\bar{\sigma}_{meso}(t) = \bar{\sigma}_{meso,h}(t) + \bar{\sigma}_{meso,d}(t) \quad (2.49)$$

The mesoscopic and macroscopic hydrostatic stresses are equal:

$$\bar{\sigma}_{meso,h}(t) = \bar{\sigma}_{macro,h}(t) \quad (2.50)$$

On the other hand, the mesoscopic deviatoric stress is defined as:

$$\bar{\sigma}_{meso,d}(t) = \bar{\sigma}_{macro,d}(t) + \rho \quad (2.51)$$

For the case of proportional loading:

$$\rho = \text{average}(\bar{\sigma}_{macro,d}(t)) \quad (2.52)$$

Then, this model states that failure occurs when the following condition is verified:

$$\max(\bar{\tau}(t)_{meso,max,d} + k_d \cdot \bar{\sigma}(t)_{meso,h}) = d \quad (2.53)$$

where:

$$\bar{\tau}(t)_{meso,max,d} = \frac{\bar{\sigma}(t)_{meso,1,d} - \bar{\sigma}(t)_{meso,3,d}}{2} \quad (2.54)$$

Accordingly to Dang-Van [1994], the cracks initiate in transgranular slip bands, mainly due to the local shear stress and influenced by the hydrostatic tension [Desimone et al., 2006].

However, some years later, a simplified version of this model was proposed for engineering applications [Dang-Van and Maitournam, 2003]. This approach establishes that the fatigue failure will happen if the following condition is verified:

$$\tau_{a,max} + k_d \sigma_{h,max} = d \quad (2.55)$$

where k_f and d are material constants.

It is important to highlight that the value of $\tau_{a,max}$ is not affected in the presence of mean stresses, while the hydrostatic stress value includes the effect of mean stress.

The material constants k_f and f can be calculated by performing two fatigue tests at different stress ratio. If the fully reversed and torsional is applied to the Equation (2.55), the value of d is obtained:

$$d = \tau_{a,max} = \tau_{a,R=-1} \quad (2.56)$$

And combining with a fully reversed axial test the value of k_d is:

$$k_d = 3 \left(\frac{\tau_{a,R=-1}}{\sigma_{a,R=-1}} - \frac{1}{2} \right) \quad (2.57)$$

Moreover, these constants can also be calculated through two random tests at fatigue limit by plotting the test data and applying a linear regression [van Lieshout et al., 2017].

2.2.6 Estimation of fatigue life based on multiaxial criterion

Some of the models described above can be easily combined with basquin model, with the aim to determine fatigue damage in the finite life region, as can be seen in the following equations:

- Tresca

$$\frac{\sigma_{1,a} - \sigma_{2,a}}{2} = \tau'_f(2N_f)^b \quad (2.58)$$

- von Mises

$$\sigma_{VM,a} + \alpha_{VM}\sigma_{VM,m} = \tau'_f(2N_f)^b \quad (2.59)$$

- Sines

$$\tau_{a,oct} + k_s(3\sigma_{h,mean}) = \tau'_f(2N_f)^b \quad (2.60)$$

- Crossland

$$\tau_{a,oct} + k_c(3\sigma_{h,max}) = \tau'_f(2N_f)^b \quad (2.61)$$

- Findley

$$(\tau_{\theta a} + k_f\sigma_{\theta max})_{max} = \tau'_f(2N_f)^b \quad (2.62)$$

- McDiarmid

$$\tau_{\theta a} + \frac{t_{A,B}}{2\sigma_u}\sigma_{\theta max} = \tau'_f(2N_f)^b \quad (2.63)$$

- Dang Van

$$\tau_{a,max} + k_d\sigma_{h,max} = \tau'_f(2N_f)^b \quad (2.64)$$

In this way, it is possible to obtain a design curve and theoretically calculate fatigue life at a certain loading state [Socie, 1993].

2.3 A review on Fracture Mechanics

2.3.1 Definition

The fracture mechanics approaches assume that all structural elements have defects and cracks, and, consequently, the design is based on the tolerance to the presence of defects. Thus, the fracture mechanics is focused on calculate the number of cycles which a certain critical crack takes to achieve the final failure, in order to evaluate how long a structure or component can operate without having to be fixed [Suresh, 1998] [Fernandes et al., 1999].

This approach was mentioned for the first time in 1921, by Griffith, who studied the unstable growth of cracks and proposed an energetic approach. However, the analyse and characterization of fatigue crack growth became a concern only in the middle of the 20th century, mainly, because of the works developed by Irwin, which were based on Wastergaard analytic considerations [Fernandes et al., 1999]. After Irwin, a large number of fracture mechanics approaches and models were formulated and proposed. Hence, throughout this section, it will be mentioned the most pertinent and within scope of this master thesis.

The fracture mechanics can be divided into linear elastic fracture mechanics (LEFM) and elastic plastic fracture mechanics (EPFM). The first one can only be applied if the plastic region is very small and surrounded by an elastic region. When this condition is not verified, the analyse of crack growth requires an elastic plastic approach [Fernandes et al., 1999]. Since this master thesis is mainly focused on damage mechanisms related to elastic deformation, it will be only described the LEFM principles.

Besides, all fracture approaches usually distinguish three basic modes of fracture:

- Mode I: is the tensile opening mode and is characterized by the separation of crack faces in the direction perpendicular to the crack plane (Fig.2.18a);
- Mode II: is the in-plane shear mode and is the mode in which the crack faces are sheared in the direction parallel to the crack front face (Fig.2.18b);
- Mode III: is the transverse shear mode and, similarly to mode II, in this mode, the crack faces are sheared, but this time in the direction perpendicular to the crack front face (Fig.2.18c).

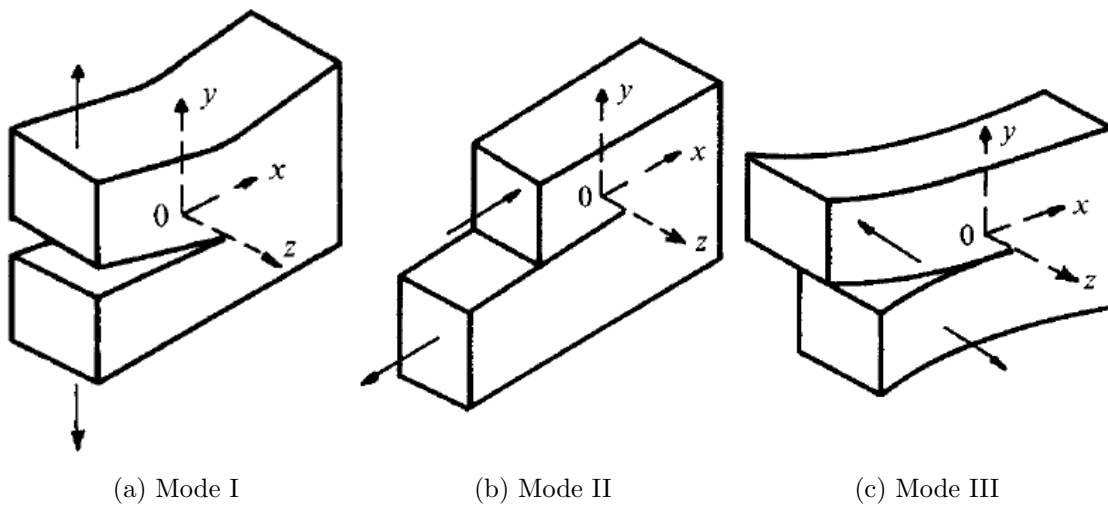


Figure 2.18: The three basic modes of fracture [Suresh, 1998]

The mode I of fracture is the most well known and studied, since it is the one of greater importance and relevance in engineering applications [Suresh, 1998].

2.3.2 Stress Intensity Factor

Irwin introduced an approach based on a new concept: the stress intensity factor(K), with the aim of expressing and quantifying the stress field on the crack tip through a scalar variable [Suresh, 1998].

Therefore, a stress intensity factor is defined for each mode of fracture (K_I , K_{II} and K_{III}) and Irwin describes the stress state around the crack tip through the following equations for:

- Mode I:

$$\sigma_x = \frac{K_I}{\sqrt{2\pi r}} \cos \frac{\theta}{2} \left(1 - \sin \frac{\theta}{2} + \sin \frac{3\theta}{2} \right) \quad (2.65)$$

$$\sigma_y = \frac{K_I}{\sqrt{2\pi r}} \cos \frac{\theta}{2} \left(1 + \sin \frac{\theta}{2} + \sin \frac{3\theta}{2} \right) \quad (2.66)$$

$$\tau_{xy} = \frac{K_I}{\sqrt{2\pi r}} \cos \frac{\theta}{2} \sin \frac{\theta}{2} \cos \frac{3\theta}{2} \quad (2.67)$$

- Mode II:

$$\sigma_x = \frac{-K_{II}}{\sqrt{2\pi r}} \sin \frac{\theta}{2} \left(2 + \cos \frac{\theta}{2} + \cos \frac{3\theta}{2} \right) \quad (2.68)$$

$$\sigma_y = \frac{K_{II}}{\sqrt{2\pi r}} \sin \frac{\theta}{2} \cos \frac{\theta}{2} \cos \frac{3\theta}{2} \quad (2.69)$$

$$\tau_{xy} = \frac{K_{II}}{\sqrt{2\pi r}} \cos \frac{\theta}{2} \left(1 - \sin \frac{\theta}{2} \sin \frac{3\theta}{2} \right) \quad (2.70)$$

- Mode III:

$$\tau_{xz} = \frac{-K_{III}}{\sqrt{2\pi r}} \sin \frac{\theta}{2} \quad (2.71)$$

$$\tau_{yz} = \frac{-K_{III}}{\sqrt{2\pi r}} \cos \frac{\theta}{2} \quad (2.72)$$

where θ and r are the coordinates defined by the axes define in Figure 2.19 [Fernandes et al., 1999].

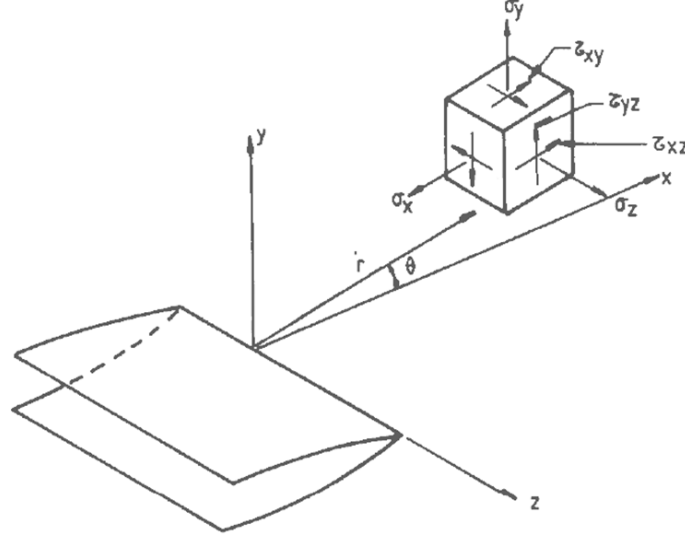


Figure 2.19: Stress state around the crack tip [Fernandes et al., 1999]

Subsequently, a new challenge arises from this stress state characterization: the definition of stress intensity factor for each case. Hence, it is easily founded in the literature, some solutions for a large number of cases formulated not only by Irwin, but also by other authors. However, the stress intensity factor can be, in a general way, defined as:

$$K = Y\sigma\sqrt{\pi a} \quad (2.73)$$

where Y is a dimensionless function related to the geometry and kind of load, σ is the stress remotely applied and a is the crack characteristic dimension [Suresh, 1998].

Thus, when the stress intensity factor achieves the material fracture toughness (K_c), the crack grows unstable, and, as consequence, the final failure occurs. The fracture toughness is defined as the critical value of stress intensity factor and is influenced by the mode of loading, chemical environment, material microstructure, temperature, strain rate and stress state. There are a fracture toughness for each fracture mode: K_I (mode I), K_{II} (mode II) and K_{III} (mode III).

2.3.3 Fatigue Crack Propagation: Paris Law

A large part of fracture mechanics was developed in order to analyse the behaviour of a crack under a cyclic loading. Therefore, if a structure is not perfect and without defects, instead of the classical fatigue approaches described above, a fracture mechanics approach is required. Besides, the macro crack growth phase mentioned in Figure 2.9, is explained and studied on detailed by fracture mechanics [Fernandes et al., 1999].

As can be seen in Figure 2.20, the fatigue crack growth is divided into three phases:

- I: is characterized by considerable low crack growth rates and in this region can be identified a value, known as threshold, above which there are no crack growth;
- II: is the region known as “Paris region”, because the crack growth as function of stress intensity can be defined by the following expression, which was proposed by Paul Paris in 1961:

$$\frac{da}{dN} = C(\Delta K)^m \quad (2.74)$$

where $\frac{da}{dN}$ is the fatigue crack growth rate, C and m are constants obtained through experimental tests and ΔK is the stress intensity factor range given by the following equation:

$$\Delta K = K_{max} - K_{min} \quad (2.75)$$

K_{max} is the maximum stress intensity factor and K_{min} is the minimum stress intensity factor.

- III: is the last phase and is characterized by an unstable crack growth since it ends when ΔK is equal to ΔK_c [Fernandes et al., 1999].

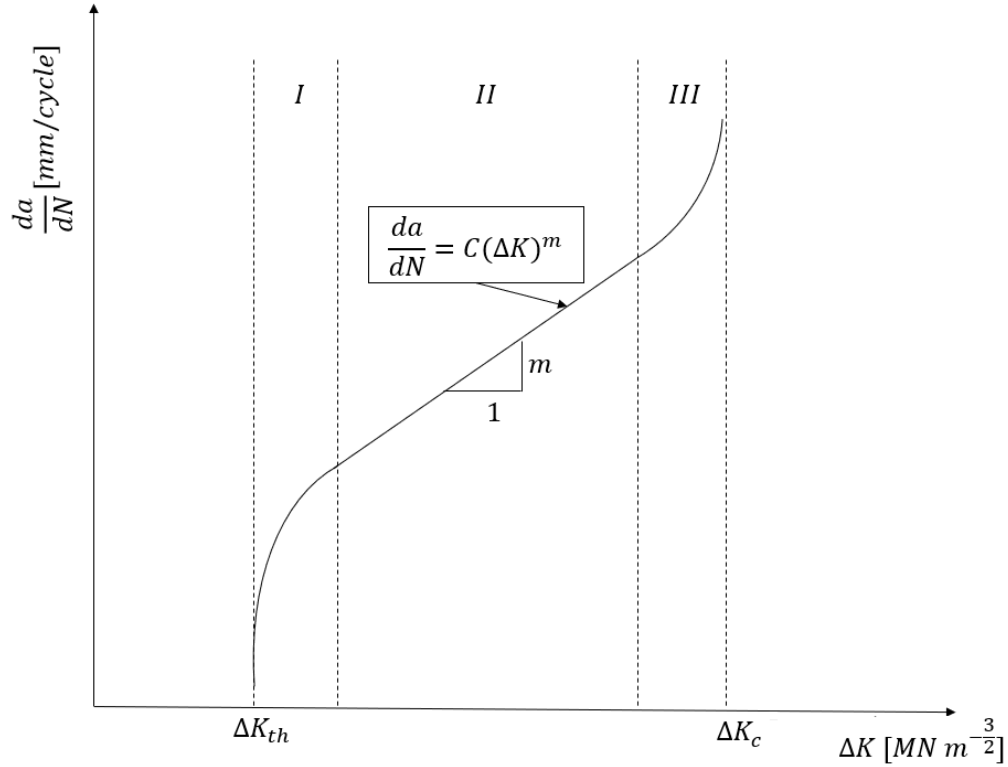


Figure 2.20: Fatigue crack growth rate as function of stress intensity factor range [Fernandes et al., 1999]

2.4 A review on Basis of Design

Usually, the design rules evaluate the fatigue life of a structure or component based on nominal normal ($\Delta\sigma_{nom}$) and shear ($\Delta\tau_{nom}$) stress ranges calculated through the theory of elasticity [Öztürk et al., 2016]. Moreover, the relation between nominal normal and shear stress ranges and number of cycles until failure is established by the following equations, which come from the classical fatigue approaches described in sections above:

$$N_f(\Delta\sigma_{nom})^m = C \quad (2.76)$$

$$N_f(\Delta\tau_{nom})^{m_\tau} = C_\tau \quad (2.77)$$

where C , C_τ , m and m_τ are material constants and N_f is the number of cycles until failure [Öztürk et al., 2016].

However, in the case of multiaxial loading is required the combination of shear and normal stress effects. The eurocode 3 part 1-9 proposes, for different cases, the following Eurocode approaches [European Committee for Standardization, 2010b]:

- The effect of shear stress can be ignored when the following condition is verified:

$$\Delta\tau_{nom} \leq 0.15\Delta\tau_{nominal} \quad (2.78)$$

- The maximum principal stress range may be used for fatigue design propose in case of proportional loading;
- In the case of non-proportional loading, the following condition may be verified:

$$\left(\frac{\Delta\sigma_{eq,nom}}{\Delta\sigma_c}\right)^3 + \left(\frac{\Delta\tau_{eq,nom}}{\Delta\tau_c}\right)^5 \leq 1 \quad (2.79)$$

where σ_C and τ_C are the fatigue strength reference values for $2 \cdot 10^6$ number of cycles; and $\Delta\sigma_{eq,nom}$ and $\Delta\tau_{eq,nom}$ are the equivalent normal and shear stresses given by the following equations:

$$\Delta\sigma_{eq,nom} = \sqrt[m]{\left(\frac{\sum_{i=1}^k (\Delta\sigma_{nom,i}^m n_i)}{N_{ref}}\right)} \quad (2.80)$$

$$\Delta\tau_{eq,nom} = \sqrt[m]{\left(\frac{\sum_{i=1}^k (\Delta\tau_{nom,i}^m n_i)}{N_{ref}}\right)} \quad (2.81)$$

where n_i is number of cycles at $\Delta\sigma_{nom,i}$ and N_{ref} is the reference number of cycles until failure at a certain level of stress [European Committee for Standardization, 2010b].

Experimental Programme

3.1 Introduction

The experimental programme was performed in the facilities of Wrocław University of Science and Technology, in Poland. This experimental work aims to assess the fatigue behaviour of S355 steel, in order to characterize and study the joint that will be mention in the next chapters.

Thus, uniaxial and biaxial fatigue tests were conducted in smooth specimens of S355 steel. Moreover, pure mode I and mixed mode fatigue crack growth tests were also carried out.

3.1.1 S355 Steel Composition and Properties

Besides performing experimental fatigue and fracture tests, the main mechanical properties and the chemical composition of S355 steel have to be determined and defined.

Most of the information present in Tables 3.1 and 3.2 was given by the material provider company. However, young modulus and hardness were not supplied. Therefore, in the case of young modulus, it was assumed the value stablish by Correia et al. [2015], while the hardness was determined.

In order to evaluate this property, it was cut and polished a piece of material obtained from a specimen. Then, there were executed five measurements, using the vickers hardness tester FV 800 from the company *Future Tech*, and obtained the following results: 150.9 HV10, 152.6 HV10, 147.4 HV10, 152.2HV10 and 153.3HV10. An average value was calculated from these measurements and is present in Table 3.1.

Table 3.1: Mechanical properties

Young Modulus (E) <i>GPa</i>	Yield Strength (f_y) <i>MPa</i>	Tensile Strength (f_u) <i>MPa</i>	Hardness <i>HV10</i>
211.60	367	579	151.28

Table 3.2: Chemical composition

C	Cu	Mn	N	P	S	Si
%	%	%	%	%	%	%
0.16	0.2	1.28	0.009	0.03	0.02	0.3

Besides mechanical and chemical description, it is important to observe and analyse the material microstructure. Therefore, a piece of material was polished and also etched with nitric acid to allow the microstructure observation. The result from this procedure can be found in Figure 3.1. Hence, as it is expected from a S355 steel, pearlite and ferrite are present on the microstructure, but the grains edges are sharp which indicates the material was not normalized. In spite of not being a standard process, it should not affect the fatigue behaviour.

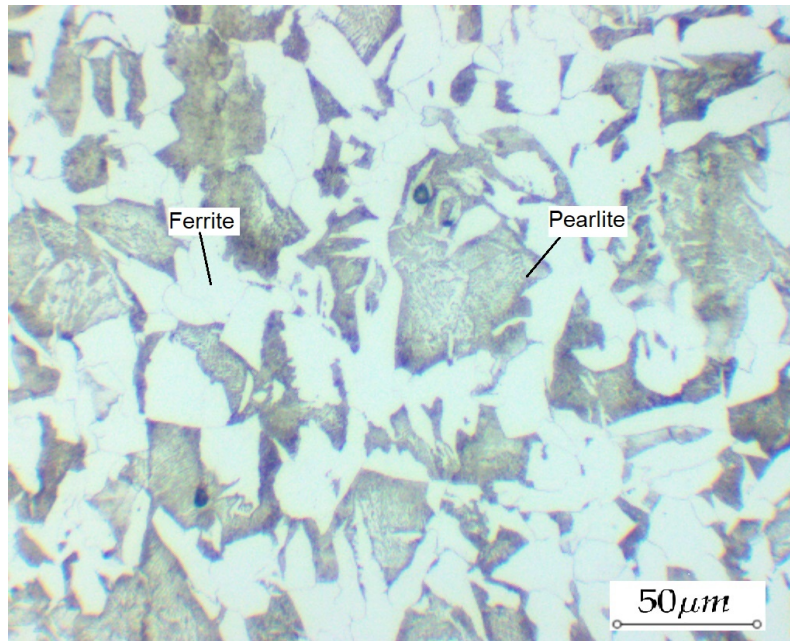


Figure 3.1: Microstructure of S355 steel (Magn.400x)

3.2 Uni- and Multi-axial fatigue Assessment of the S355 steel

Firstly, uniaxial and biaxial high-cycle fatigue tests were carried out. During the first ones an cyclic axial force was applied, while during the biaxial tests two different loads were applied: a cyclic torsional torque and a cyclic axial force. Since it is desired to assess high-cycle fatigue domain, the tests were conducted in force control which means that in the beginning were established the maximum and minimum values of force and torque applied by the test machine, and, as output, the number of cycles until failure were obtained.

For both uniaxial and biaxial tests was chosen an hourglass shape specimen with a minimum section area of 44.18mm^2 . In Figure 3.2 is represented the geometry of this specimen and an image of it before performing the tests.

These tests aim to determine experimental fatigue curves of S355 steel for an axial and biaxial stress state. Moreover, it is important to evaluate the effect of stress ratio (R) and different kinds of loading on the fatigue life of this steel. The impact of a biaxial state will also be evaluate and the fatigue curves obtained will be compared with some curves for other kinds of loading that can be found on literature.

Last but not least, the results of these tests will be used to study the accuracy and ability of some multiaxial models, which were mentioned in the preview chapter, to portray different stress fatigue states, in particular multiaxial ones.

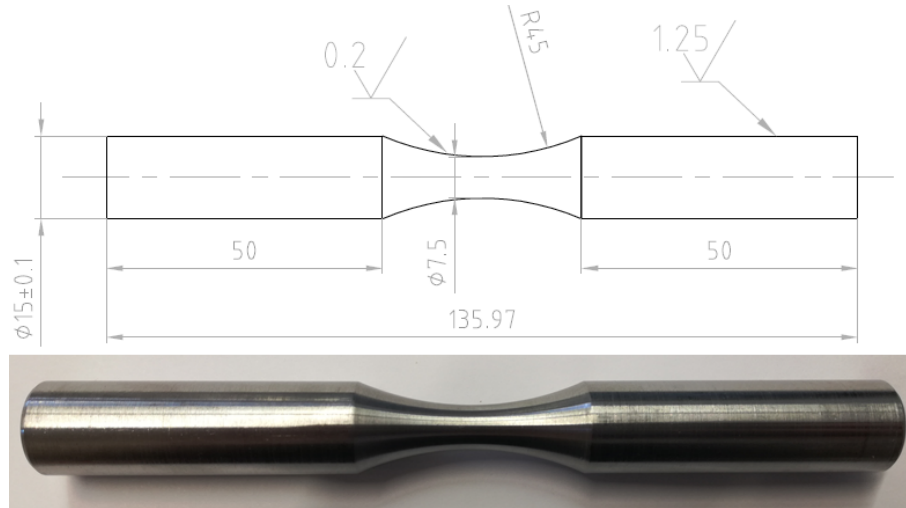


Figure 3.2: hourglass specimen

3.2.1 Uniaxial Fatigue Assessment: Axial load

The axial tests were performed by an MTS 810 testing system which is a servo hydraulic system characterized by a maximum capacity of 100 kN (Fig. 3.4).

The specimen is fixed at the bottom and top by the machine gripping system and during the fatigue test the hydraulic actuator applies, through the bottom grip, a cyclic axial load. This load is applied on a 10 Hz frequency and is characterized by sinusoidal shape signal and constant amplitude over time (Fig. 3.3).

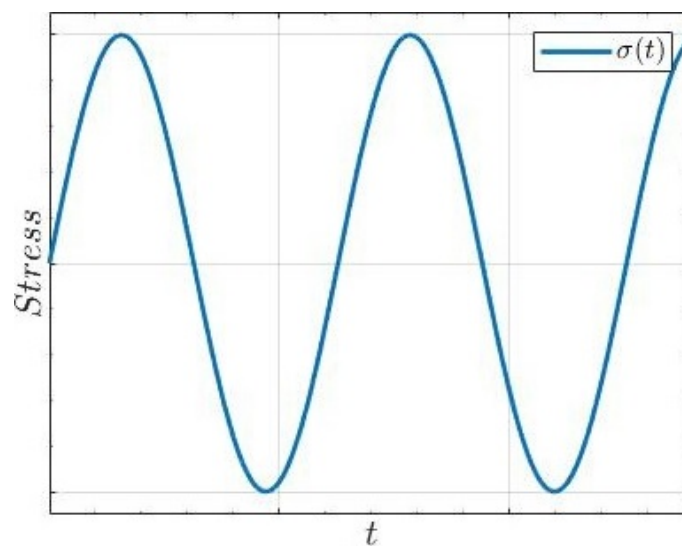


Figure 3.3: Axial loading

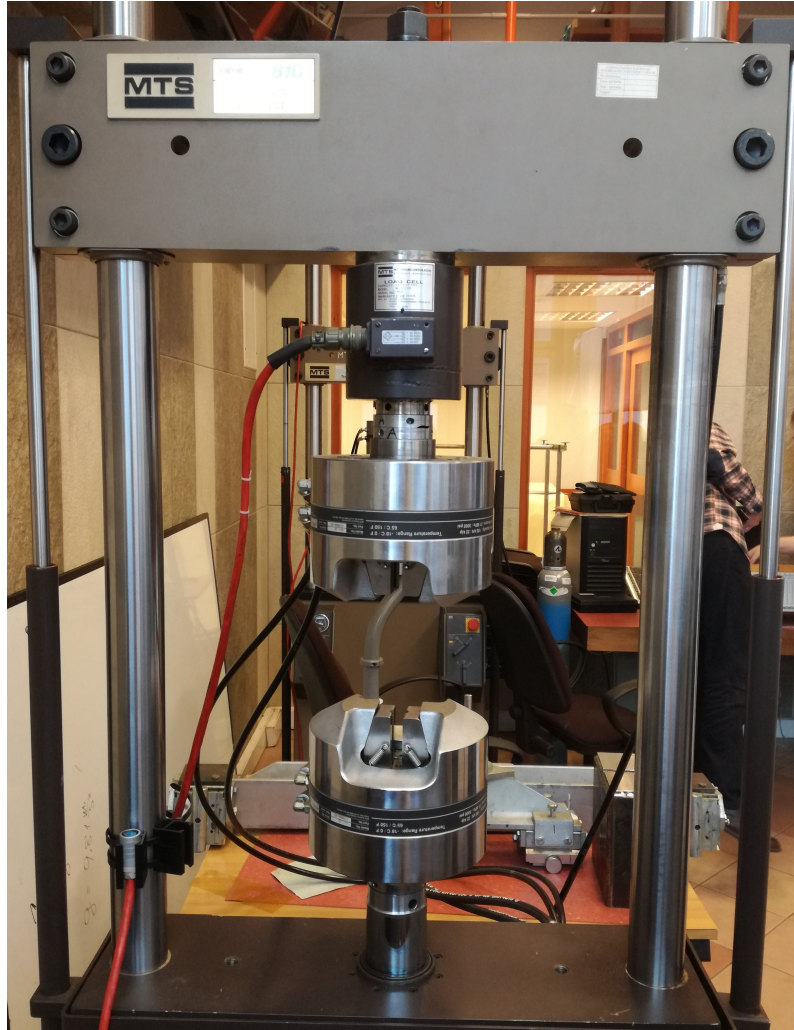


Figure 3.4: MTS 810 testing system

Twenty-two axial fatigue tests were conducted for two different stress ratios: -1 and 0.01. The last ratio is quite close to zero, then, in the next chapters, it will be considered as that. The infinite life was established at 5000000 number of cycles, which means that when a specimen achieved this value the test was stopped and assumed infinite fatigue life for the respectively test level of loading.

In Table 3.3, there are only listed the tests which were considered valid. Moreover, in future chapters, for the tests which achieved infinite life it will be only considered the upper limit.

Firstly, as can be seen in table of results, it was applied a level of loading bellow yield strength, since the focus of this experimental work is the high cycle region, and after that the level was increased or decreased, depending on the number of cycles until failure achieved.

The loading level performed and respective number of cycles until failure obtained in each test originate a experimental point in a S-N curve graph. Thus, the goal of these experiments is to obtain enough points to draw a design curve between 10^4 and $5 \cdot 10^6$ number of cycles. Ideally, three experimental points for three different loading levels would be obtained. However, only two experimental points were obtained for each loading level, because of the lack of time and specimens to perform the desired number of tests.

Table 3.3: Axial tests

Specimen Number -	Ratio -	σ_a MPa	σ_{max} MPa	σ_{min} MPa	F_{max} N	F_{min} N	Number of cycles -
1	0.01	168	340	3.40	15000	150	5000000(∞)
6	0.01	182	368	3.68	16250	162.50	5000000(∞)
7	0.01	188	379	3.79	16750	167.50	5000000(∞)
8	0.01	190	385	3.85	17000	170	5000000(∞)
9	0.01	193	390	3.90	17250	172.50	5000000(∞)
4	0.01	196	396	3.96	17500	175	324373
5	0.01	196	396	3.96	17500	175	281589
11	0.01	202	407	4.07	18000	180	621182
12	0.01	202	407	4.07	18000	180	131064
21	0.01	207	419	4.19	18500	185	247161
22	0.01	207	419	4.19	18500	185	315639
19	0.01	216	436	4.36	19250	192.50	122047
20	0.01	216	436	4.36	19250	192.50	76082
18	-1	232	232	-232	10250	-10250	5000000(∞)
17	-1	232	232	-232	10250	-10250	2147377
14	-1	249	249	-249	11000	-11000	561786
16	-1	249	249	-249	11000	-11000	406826
13	-1	272	272	-272	12000	-12000	157983
15	-1	272	272	-272	12000	-12000	98626

In Figure 3.5, there are represented all the specimens which were tested under an axial cyclic loading.



Figure 3.5: Specimens after axial fatigue tests

Furthermore, the specimens fracture surfaces were observed and some pictures were took using a optical microscope, in order to find some relation with loading level and type.

Thus, Figures 3.6a to 3.6d show the fracture surface of some specimens tested at different loading levels for $R=0.01$. In these surfaces, the crack origin, fatigue zone and overload zone are easily identified, particularly, in figures 3.6c and 3.6d where ratchet marks can be seen. The transition from fatigue zone to overload zone is mainly characterized by an increase in roughness. By looking at the different surfaces, it is noticeable that the overload region increases with the level loading, as well as the fracture becomes more brittle.

3. Experimental Programme

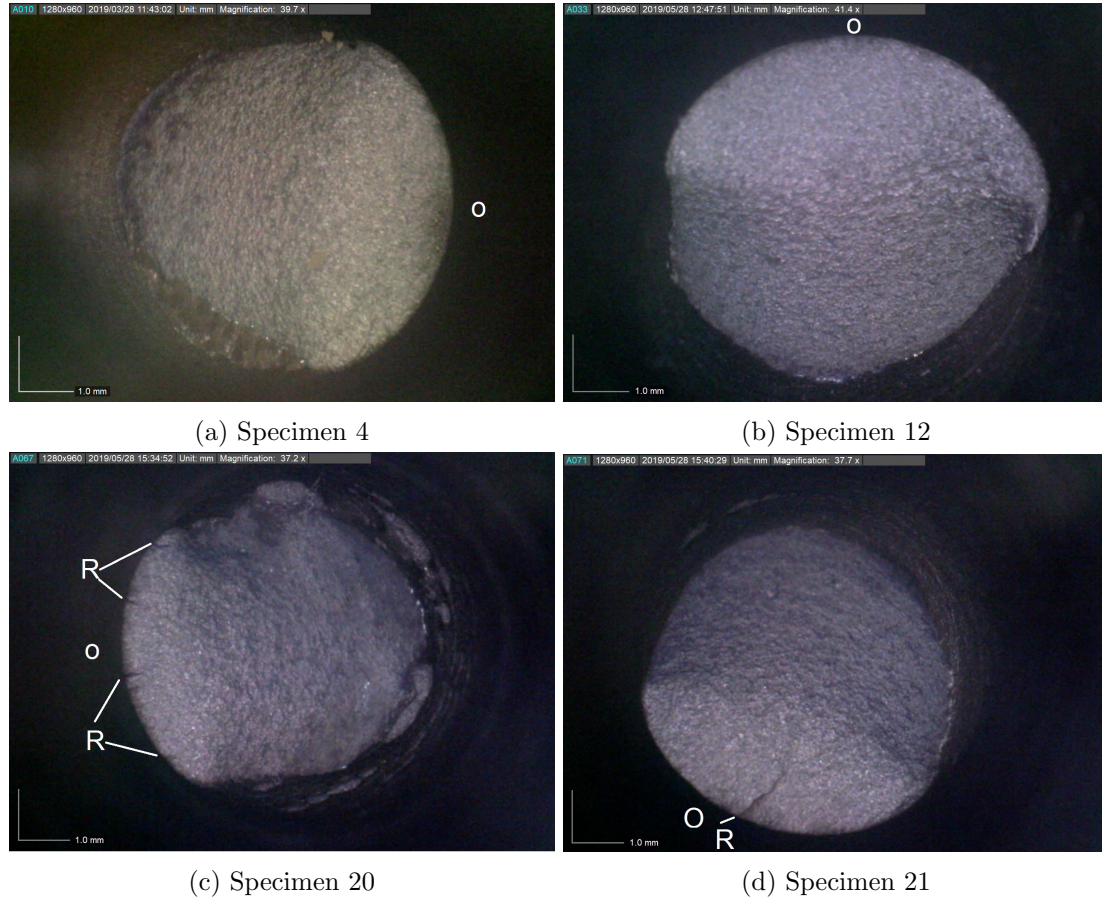


Figure 3.6: Fracture surface of specimens tested under axial loading for $R=0.01$

The ratchet marks are identified by letter R, while letter O marks the face where the origin of crack is located.

Besides, in Figures 3.7a to 3.7d, there are represented the fracture surfaces of the same specimens, which can be seen in figure above, but this time in the perpendicular direction. In specimens 4, 12 and 20, the fracture seems a bit ductile and shows some plastic deformation. On the other hand, the fracture of specimen 20 is almost completely brittle without plastic deformation and surrounded by little brittle cracks.



Figure 3.7: Specimens tested under axial loading for $R=0.01$

In the case of fully reversed axial loading, the presence of compression stresses is visible: none of the specimens suffered elongation and the fracture is brittle and remains closed after the test (Fig. 3.8a, 3.8b, 3.8d and 3.8).

Therefore, for this stress ratio, it was only observed the fracture surface of Figure 3.8a, where is more difficult to distinguish the different fracture zones. However, the river marks, which are identified by letter M, show the origin and direction of propagation.

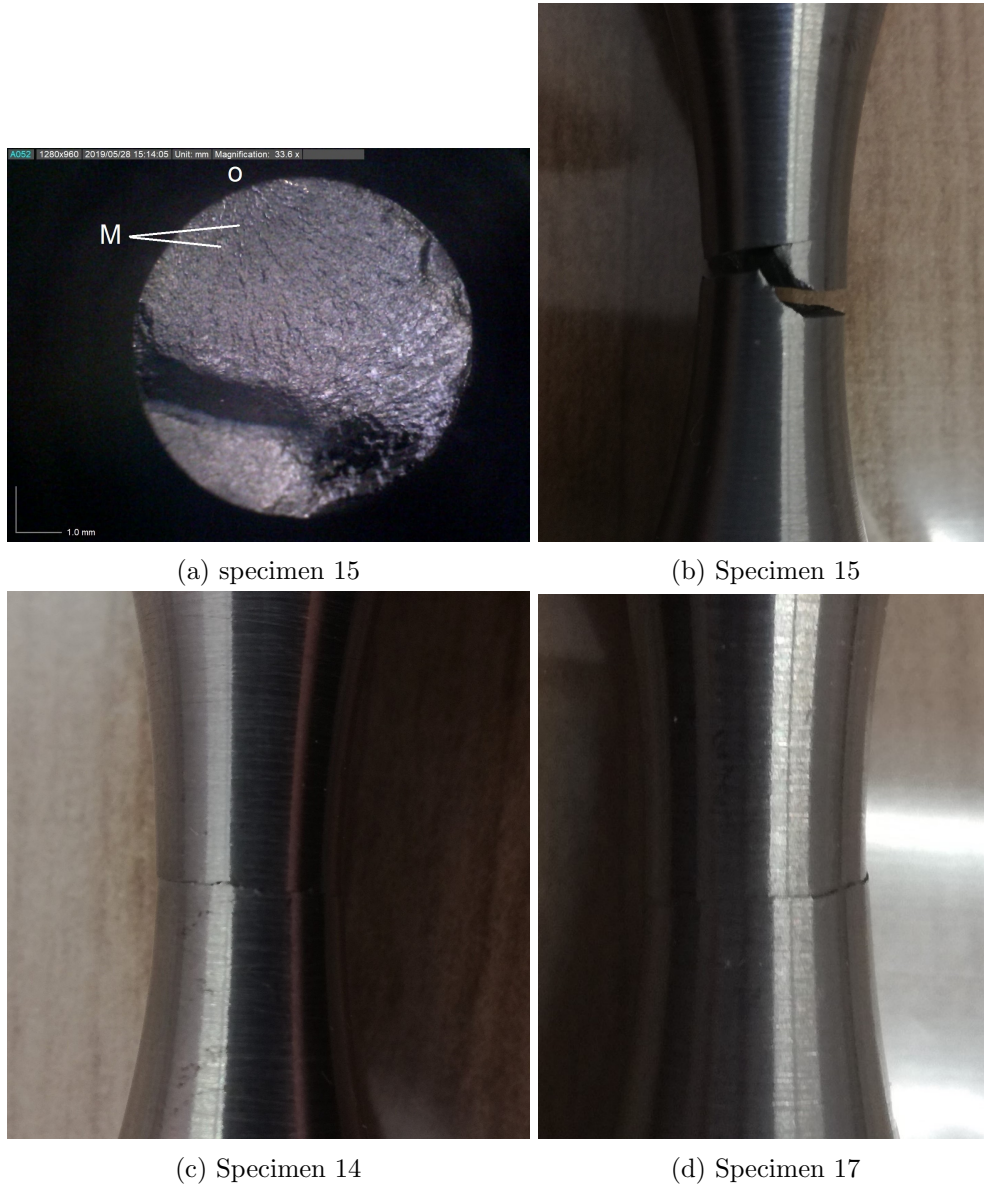


Figure 3.8: Specimens tested under axial loading for $R=-1$

These tests were mainly performed to explain and understand the influence of a multi-axial stress state on fatigue life. Furthermore, it is easy to find in literature data of torsional and bending tests of S355 steel, although there are no data of axial tests in high cycle fatigue regime of this steel.

3.2.2 Multiaxial Fatigue Assessment: Axial and Torsional loads

Within the scope of evaluate and comprehend a multi-axial fatigue state, the biaxial tests were performed, in which are applied an axial force and a torsional torque.

The normal stress originated by the force and the shear stress caused by the torque are in phase which means that, as was explained before, these tests are conducted under a proportional loading. Besides, the shear and normal stress are sinusoidal functions over time of constant amplitude (Fig.3.9).

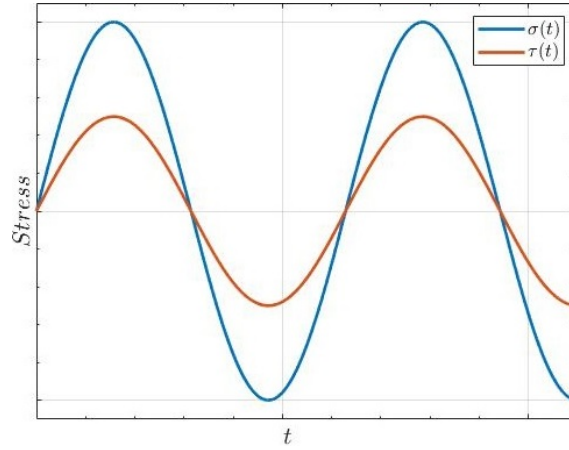


Figure 3.9: Biaxial loading applied over time

For these tests was used a MTS 809 Axial/torsional test system with an axial maximum capacity of 50kN and torsional maximum capacity of 0.5 kN.m (Fig.3.10).

Similarly to the previews tests, before starting the biaxial fatigue test, the hourglass specimen is fixed at the bottom and top by a gripping system as can be seen in Figure 3.10. Then, during the fatigue test, the bottom grip applies a cyclic torsional torque and a cyclic axial force at the same time.



Figure 3.10: MTS 809 Axial/torsional test system

3. Experimental Programme

Nineteen specimens were tested under proportional loading for -1 and 0.01 stress ratios, and, once again, the ratio 0.01 will be approximated to zero. Moreover, from the biaxial test number one until the seventeen, the shear stress value was defined as half of the normal stress value, while on the seventeen and eighteen tests the shear stress and normal stress were settled with the same value. The last tests were performed in these conditions, with the aim of evaluating the impact of shear stress in biaxial fatigue life.

In Table 3.4, the results of tests, which were considered valid, are listed and characterized by the applied loading and number of cycles until failure. Each experimental test originates a point on a graph where a certain damage parameter is function of the number of cycles until failure. Thus, the biaxial test will be used not only to determine a design curve to a complex stress state but also to evaluate some multiaxial damage parameter models.

Table 3.4: Biaxial tests

Specimen Number	Ratio	σ_a MPa	τ_a MPa	F_{max} N	F_{min} N	M_{max} N.m	M_{min} N.m	Number of cycles
-	-							-
3	0.01	151	75	13500	135	12.6	0.13	5000000(∞)
5	0.01	160	79	14250	142.5	13.30	0.13	5000000(∞)
6	0.01	165	82	14750	147.5	13.75	0.14	5000000(∞)
1	0.01	168	84	15000	150	14	0.14	332151
2	0.01	168	84	15000	150	14	0.14	256955
7	0.01	174	87	15500	155	14.5	0.15	313815
8	0.01	174	87	15500	155	14.5	0.15	656534
9	0.01	174	87	15500	155	14.5	0.15	181536
12	-1	164	82	7250	-7250	6.80	-6.80	5000000(∞)
13	-1	181	90	7975	-7975	7.48	-7.48	5000000(∞)
14	-1	194	99	8550	-8550	8.19	-8.19	2546156
15	-1	194	99	8550	-8550	8.19	-8.19	2040566
10	-1	204	104	9000	-9000	8.62	-8.62	133962
11	-1	204	104	9000	-9000	8.62	-8.62	835602
16	-1	204	104	9000	-9000	8.62	-8.62	390101
17	-1	204	104	9000	-9000	8.62	-8.62	383422
18	-1	164	164	7250	-7250	13.60	-13.60	88165
19	-1	164	164	7250	-7250	13.60	-13.60	44152

All the specimens tested under biaxial loading can be seen in Figure 3.11.

For these tests, some pictures of the surface fracture were also took, with the objective of more deeply describe and comprehend the biaxial fatigue.

Figures 3.12a to 3.12c show the fracture of the specimens tested for R=0.01. The fracture surface is identical to the one observed in the axial tests and the influence of torsional stresses is almost not noticed. However, the first specimen is the only one which shows a small plastic deformation.



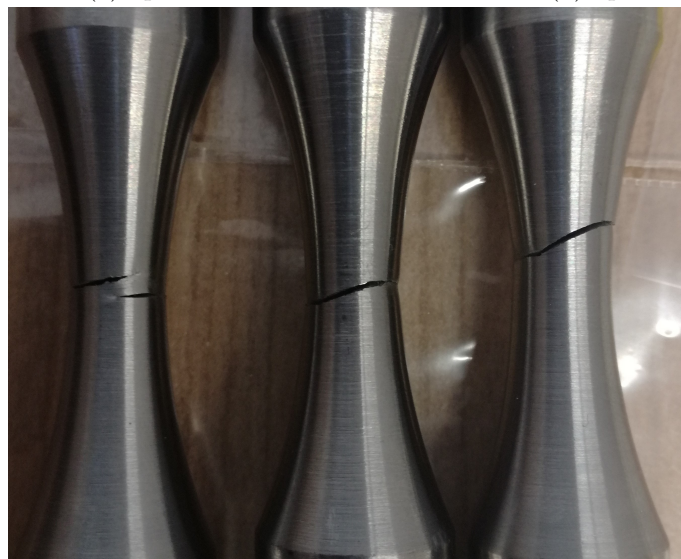
Figure 3.11: Specimens after biaxial tests



(a) Specimen 1



(b) Specimen 1



(c) From left to right: specimen 7, 8 and 9

Figure 3.12: Specimens tested under proportional loading for $R=-1$

3. Experimental Programme

On the other hand, as can be seen in figures 3.13a and 3.13b, for $R=-1$ the fracture surface is quite different from the axial ones since there are more than one area of fracture nucleation.

The surface fracture of Figure 3.13c shows the increase of torsional stresses influence through the ratchet marks present all around the cross section.

Finally, the fracture surfaces observed in the perpendicular direction, which are portrayed in figures 3.13a to 3.13c, do not show any plastic deformation.

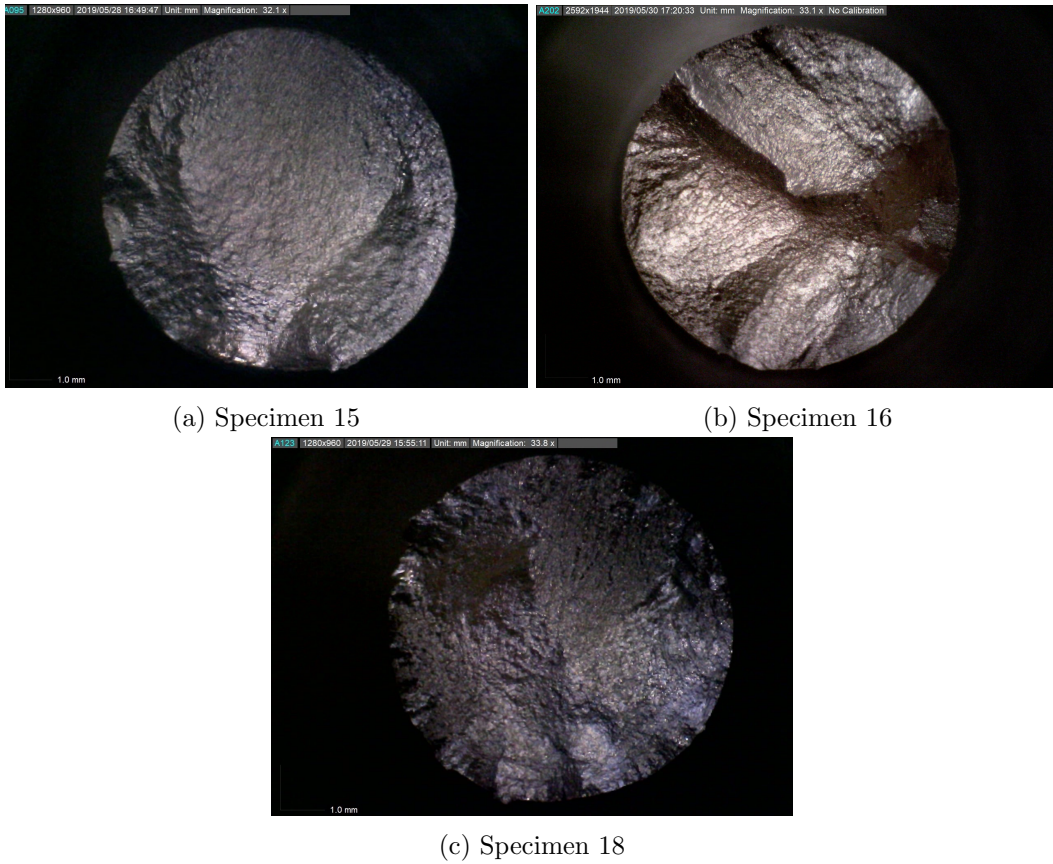


Figure 3.13: Fracture surfaces of specimens tested under proportional loading for $R=-1$

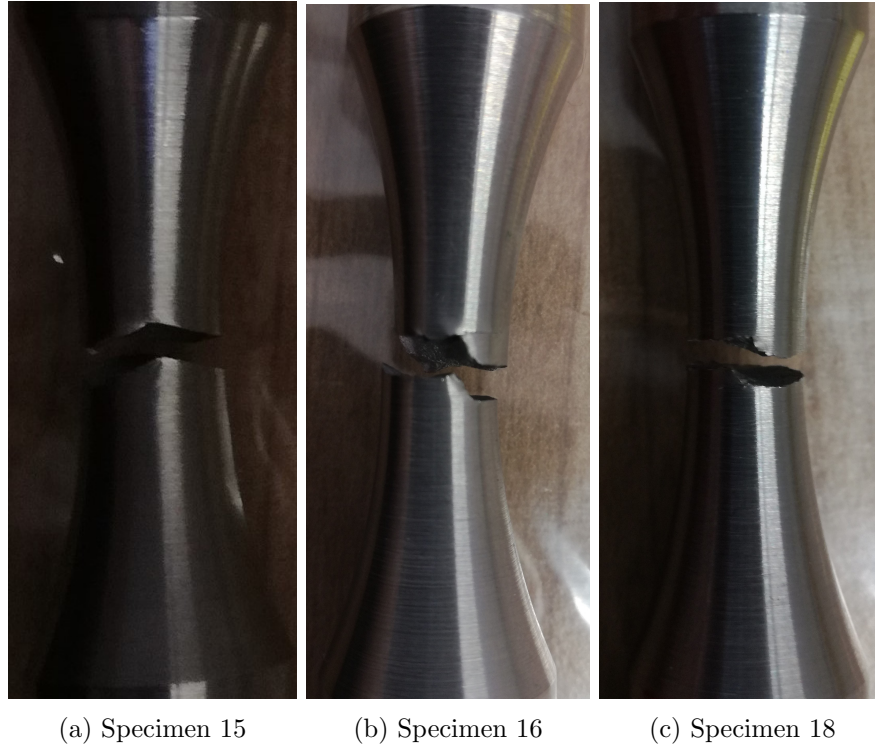


Figure 3.14: Specimens tested under proportional loading for $R=-1$

3.3 Pure-mode I and Mixed-mode Fatigue Crack Growth Characterization of S355 steel

3.3.1 Fatigue Crack Growth Tests - Mode I

The main goal of fatigue crack growth rate tests is to determine the crack growth ($\frac{da}{dN}$) as function of the stress intensity factor (ΔK) in Paris law region. Thus, these tests were performed according to ASTM E647, in order to study pure-mode I fatigue crack growth rate in S355 steel [ASTM International, 2015].

Two fatigue crack growth rate (FCGR) tests were carried out in pure mode I, each one under different stress ratios: $R=0.5$ and $R=0.7$. Ideally, at least two tests should be performed for each stress ratio, which was not possible due to lack of time and specimens.

For these tests were used compact tension specimens (CT), which geometry was defined according to ASTM E647 and is described in Figure 3.15 and Table 3.5. Figures 3.16a and 3.16b show the two specimens before before being tested.

Table 3.5: Dimensions of CT specimens (in mm)

Specimen	R	W	L	H	A	B	b	an	h	t/2
1	0.5	50	62.50	60.00	12.50	11.30	9.40	11.70	2.75	13.75
2	0.7	49.84	62.30	59.80	12.50	10.27	9.40	11.80	2.94	13.71

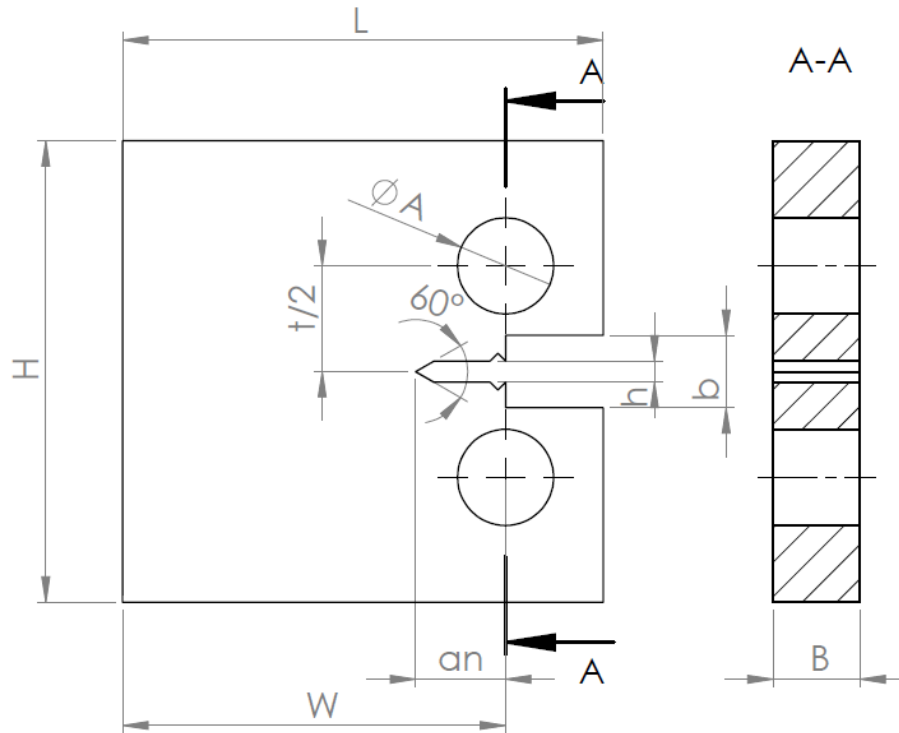


Figure 3.15: CT Specimen geometry

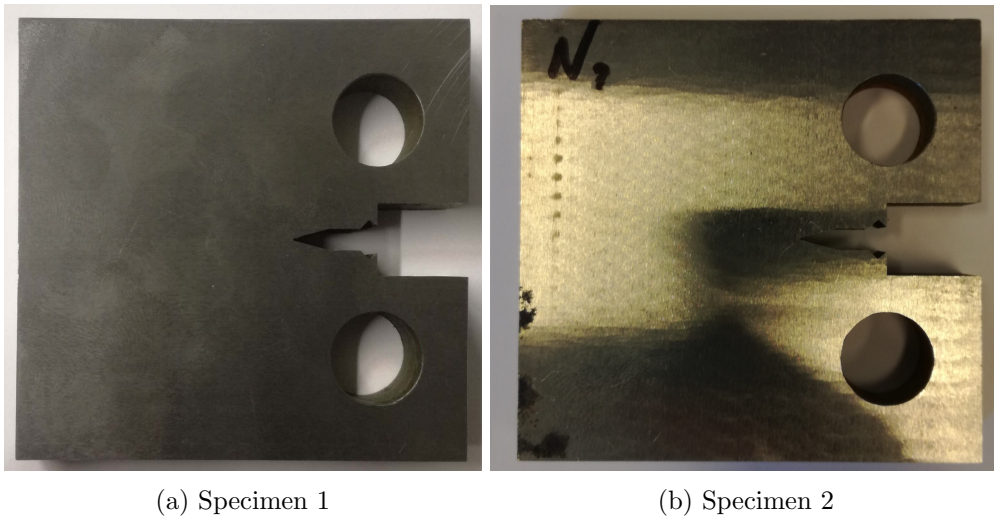


Figure 3.16: CT specimens used in pure mode I fatigue crack growth rate tests

Before starting the proper FCFGR tests, the specimens had to be precracked in fatigue conditions, since it is desired to evaluate the crack growth rate under fatigue loads without initiation phase. Thus, the precracking induces a small initial crack of a fixed final length, that for this case was defined as a_i in the notched specimen, through an experimental process similar to the proper test, but without achieving the final failure.

Hence, it was predefined a final precrack length of 14.5 mm , and established that ΔK can not be greater than $15 \text{ MPa} \cdot \text{m}^{0.5}$ during this process.

The apparatus used is represented in Figures 3.17a and 3.17b, where can also be seen that these tests were performed in a MTS 810 test machine identical to the one used

3.3. Pure-mode I and Mixed-mode Fatigue Crack Growth Characterization of S355 steel

for axial tests, but with an additional gripping system. During test apparatus preparation, the alignment of MTS clevis gripping system for fracture mechanics tests has to be assured, because any slightly misalignment can originate non-symmetric cracking and, as consequence, invalidate a fracture test.

The precrack procedure was performed in force control with $R=0.1$ and under a sinusoidal waveform cyclic loading characterized by a frequency of 10 Hz.

Finally, the proper tests were carried out until the final failure using the same apparatus and two different measurement techniques: constant force amplitude and controlled increasing ΔK amplitude. For both of experimental tests, a sinusoidal cyclic loading was applied with a frequency of 12 Hz.

These tests are controlled from a laboratory computer with a FCGR software which is integrated with MTS machine and managed by a FlexTest console (Fig. 3.18). Therefore, in the beginning of fracture test, some relevant geometrical and mechanical properties related to the specimen are introduced in the computer software. Because of this, the incorporated software will be able to calculate important variables such as crack length, ΔK and $\frac{da}{dN}$, from the applied force, crack opening displacement and number of cycles that are registered and directly measured during the test.

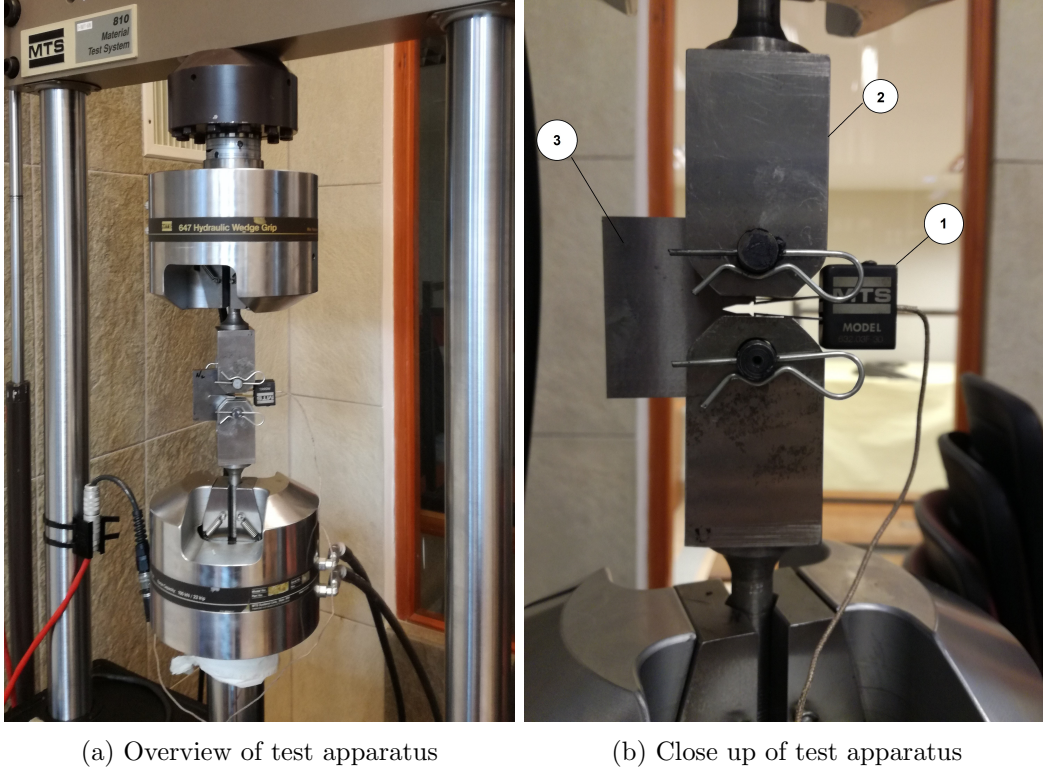


Figure 3.17: Apparatus of fatigue crack growth rate test conducted under pure mode I: 1-MTS clip gage (extensometer); 2-MTS clevis grip for fracture mechanics; 3-specimen.

During FCGR tests, the crack length is determined by the compliance method applied to the CT specimen elastic plane stress state. This method can be summarized by the following equations:

$$\frac{a}{W} = C_o + C_1 u_x + C_2 u_x^2 + C_3 u_x^3 + C_4 u_x^4 + C_5 u_x^5 \quad (3.1)$$

where a is the crack size (mm), W is the specimen width (mm), C_1 , C_2 , C_3 , C_4 and C_5 are

3. Experimental Programme

coefficients defined by ASTM Standard depending on the localization of clip gage; and u_x is:

$$u_x = \left(\left(\frac{EvB}{F} \right)^{1/2} + 1 \right)^{-1}, \text{ for } 0.2 \leq \frac{a}{W} \leq 0.975 \quad (3.2)$$

where E is the elastic modulus (MPa), B is the specimen thickness(mm), v is the displacement between measurement points (mm), $\frac{v}{F}$ is the slope of displacement versus force curve obtained during the experimental tests (mm/N).

Regarding stress-intensity factor range, ASTM E6447 states that for CT specimen geometry:

$$\Delta K = \frac{\Delta F}{B\sqrt{W}} \frac{2 + \alpha}{(1 - \alpha)(3/2)} (0.886 + 4.64\alpha - 13.32\alpha^2 + 14.72\alpha^3 - 5.6\alpha^4) \quad (3.3)$$

where $\alpha = \frac{a}{W}$.

Last but not least, the fatigue crack growth rate was determined by applying the incremental polynomial method to crack length and number of cycles data registered during fracture tests.

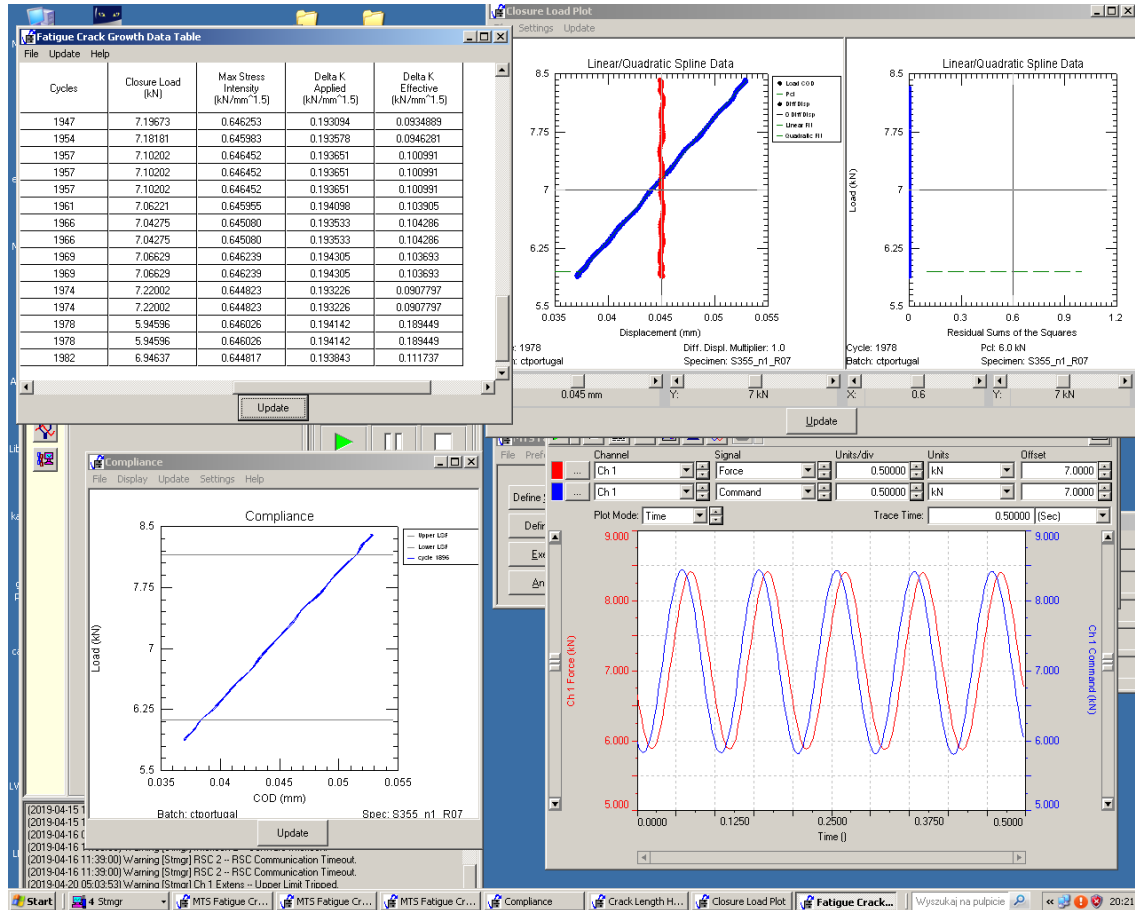


Figure 3.18: Computer screen during test

In order to better describe and characterize fatigue crack growth on S355 steel, besides the experimental data collected from FCGR tests described above, additional experimental data for $R=0.1$, which was previews obtained from two FCGR tests carried out within

3.3. Pure-mode I and Mixed-mode Fatigue Crack Growth Characterization of S355 steel

scopes of another experimental programme, was also evaluated. The FCGR tests for $R=0$ had followed an experimental procedure similar to the one described and CT specimen tested was also designed according to ASTM standards but with a thickness of 18 mm.

Hence, the results obtained for each stress ratio were plotted in a fatigue crack growth rate versus stress intensity factor range graph (Fig. 3.19 to 3.22). Then, a power regression was applied in order to calculate C and m parameters which characterize the fatigue growth rate curve in Paris region. These values are listed in Table 3.6 for $R=0.1$, $R=0.5$ and $R=0.7$.

Table 3.6: Values of $\frac{da}{dN}$ versus ΔK curves parameters (C , m) for $R=0.1$, $R=0.5$ and $R=0.7$

Specimen	R	C	m
1	0.5	$2 \cdot 10^{-8}$	2.619
2	0.7	$8 \cdot 10^{-9}$	2.869
3+4	0.1	$6 \cdot 10^{-10}$	3.642

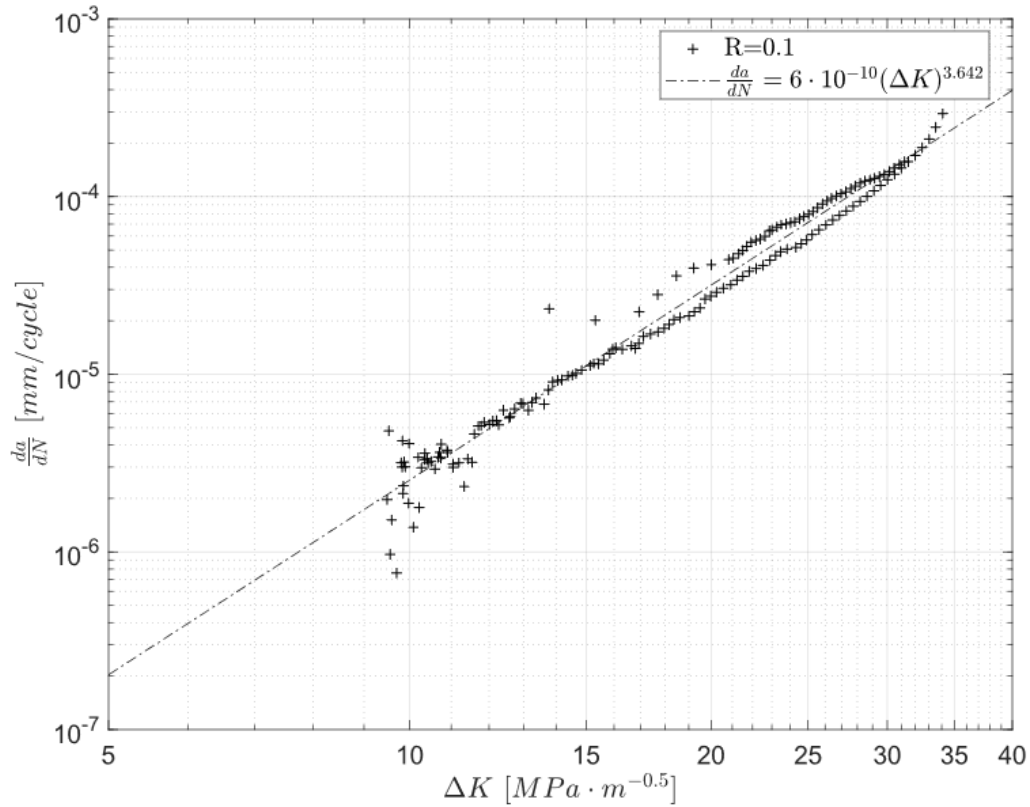


Figure 3.19: Kinetic fatigue fracture diagram for S355 steel for $R=0.1$

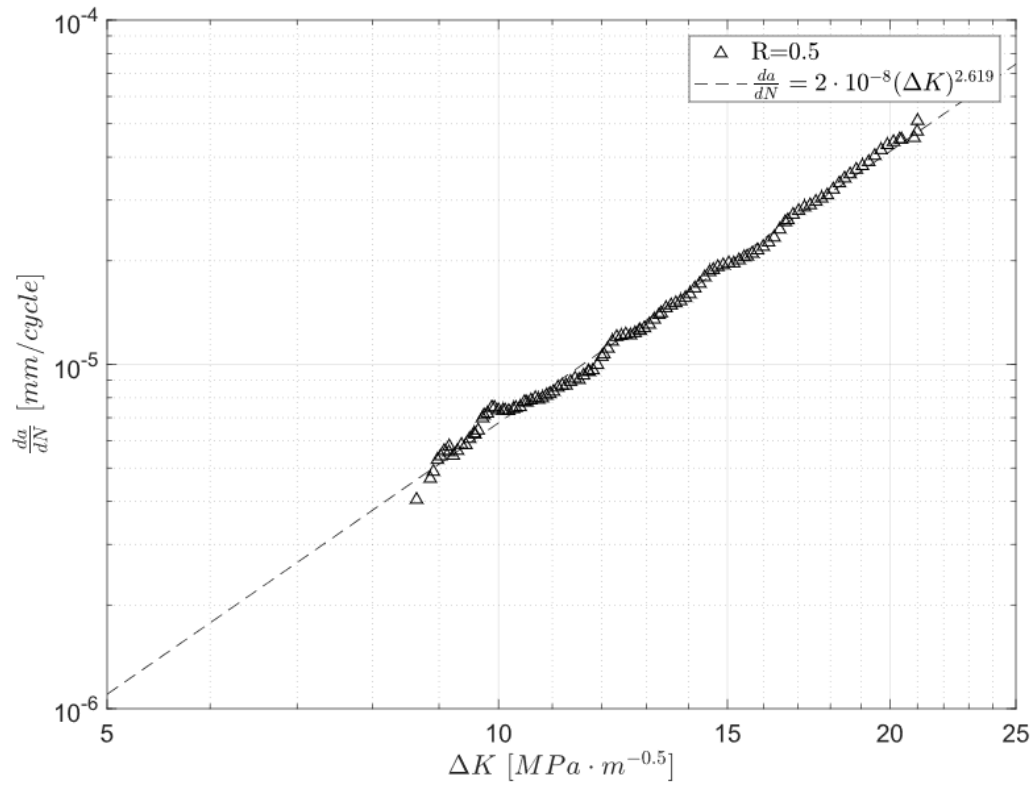


Figure 3.20: Kinetic fatigue fracture diagram for S355 steel for $R=0.5$

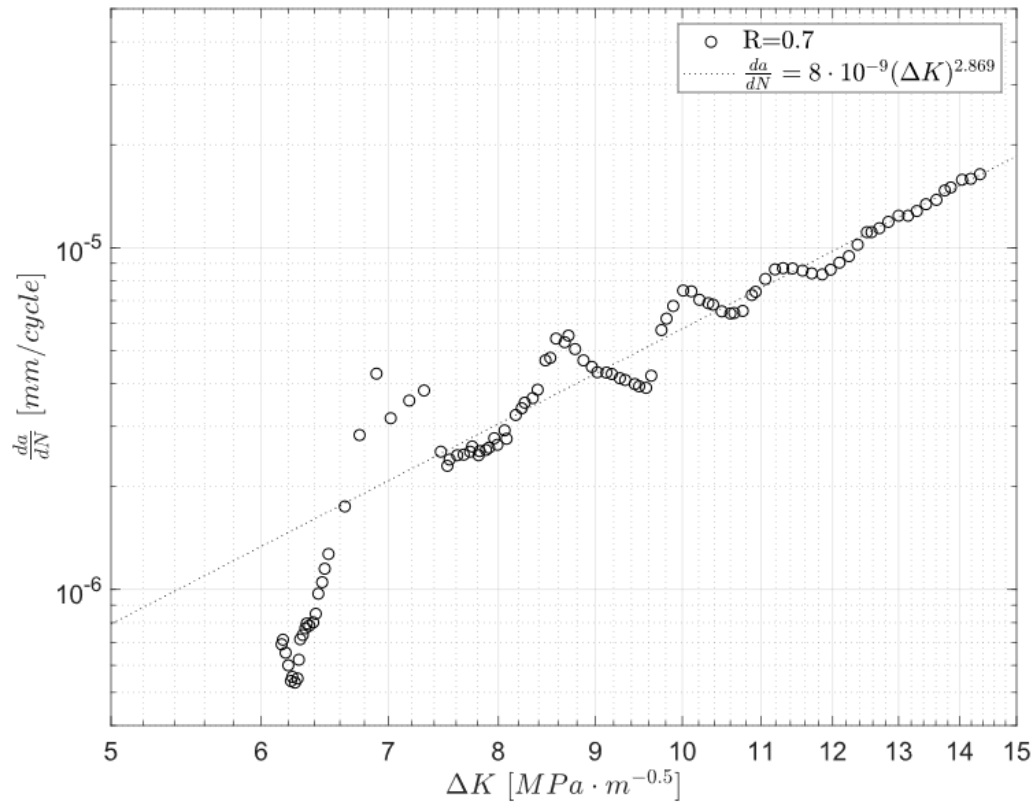


Figure 3.21: Kinetic fatigue fracture diagram for S355 steel for $R=0.7$

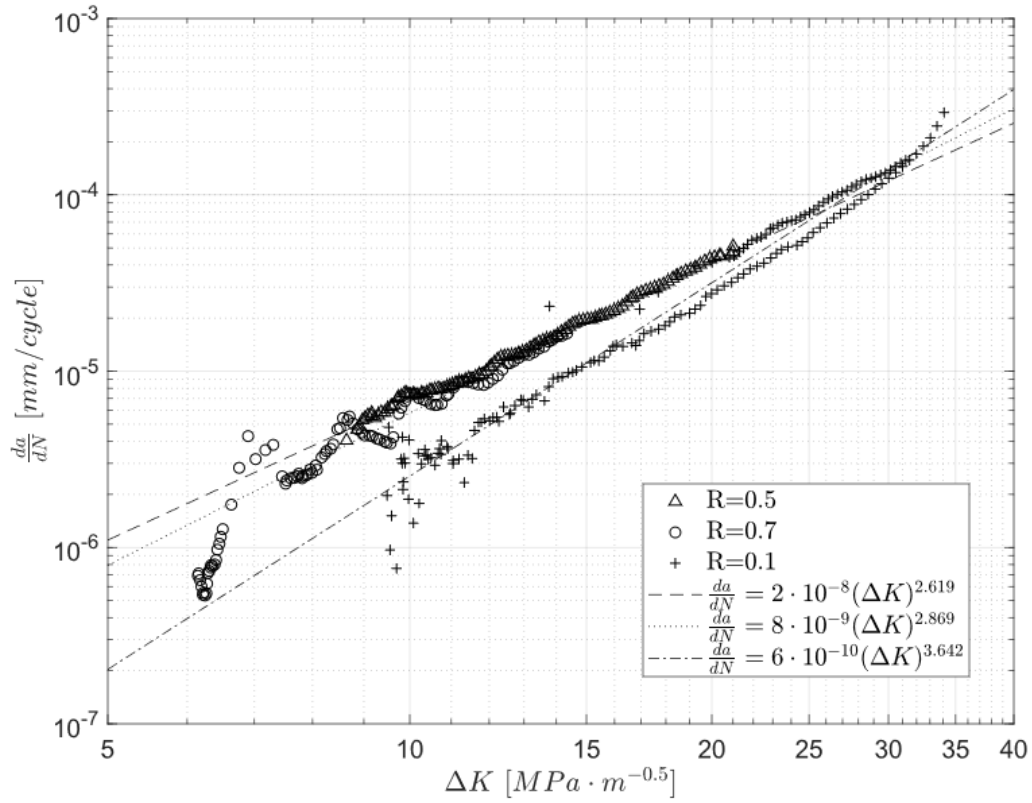
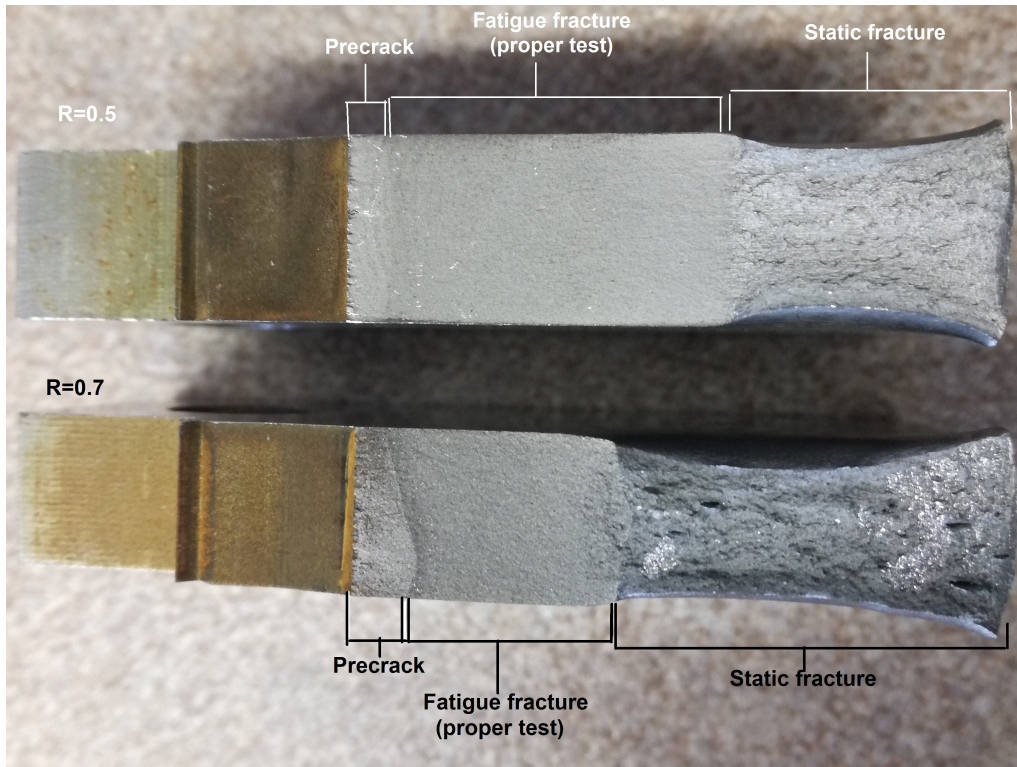
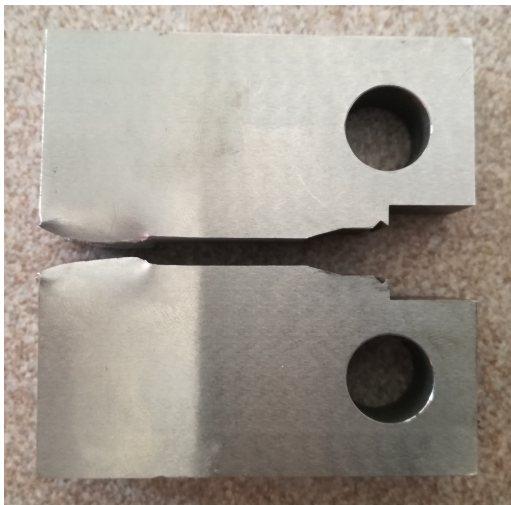


Figure 3.22: Kinetic fatigue fracture diagram for S355 steel for $R=0.1$, $R=0.5$ and $R=0.7$

Moreover, the fracture surfaces of CT broken specimens were observed and three different regions were easily distinguished: precrack, proper test and static failure (Fig. 3.23a). Figures 3.23b and 3.23c show the CT broken specimens after FCGR test and confirm the regularity and symmetry of fracture path.



(a) Fracture surfaces of broken CT specimens



(b) Specimen 1 ($R=0.5$)



(c) Specimen 2 ($R=0.7$)

Figure 3.23: Broken CT specimens used in pure mode I fatigue crack growth tests

3.3.2 Fatigue Crack Growth tests- Mixed Mode (Mode I+II)

In order to fulfil the analysis and description of fatigue crack growth on S355 steel, FCGR tests for mixed mode (mode I+II) were also conducted. Unfortunately, mixed mode tests are not standardized. Therefore, there was followed the experimental methodology proposed by Richard [1985].

Once again, these tests were performed with the aim of defining fatigue crack growth rate ($\frac{da}{dN}$) as function of stress intensity factor range (ΔK). In this case, three different stress intensity factor will be calculated: stress intensity factor in mode I (K_I), stress intensity factor in mode II (K_{II}) and equivalent stress intensity factor (K_{eqq}), which includes mode I and mode II.

For these tests, CTS (Compact Tension Shear) specimen, which geometry and dimensions can be observed in Figures 3.24a and 3.24b, a CTS specimen holder, identical to the one suggested by Richard [1985], were used (Fig. 3.25). This holder is formed by two plates and each plate have seven circular holes that attach to the MTS clevis system and another three elongated holes that connect to the specimen by rigid pins (Figures 3.26a and 3.26b).

The seven holes, which are separated for 15° , allow different positions of the CTS holder and, as consequence, different loading conditions by changing α angle (Fig. 3.25b). Hence, for $\alpha = 0^\circ$, the test is performed under pure mode I, while for $\alpha = 90^\circ$ is obtained pure mode II loading conditions.

As was mentioned before, the internal holes of the holder are elongated and the holes in CTS specimens are circular. So, all loads perpendicular to the machined notch are transmitted to the holes number 4, 6, 7 and 9, while holes number 5 and 8 handle the loads applied on the notch direction.

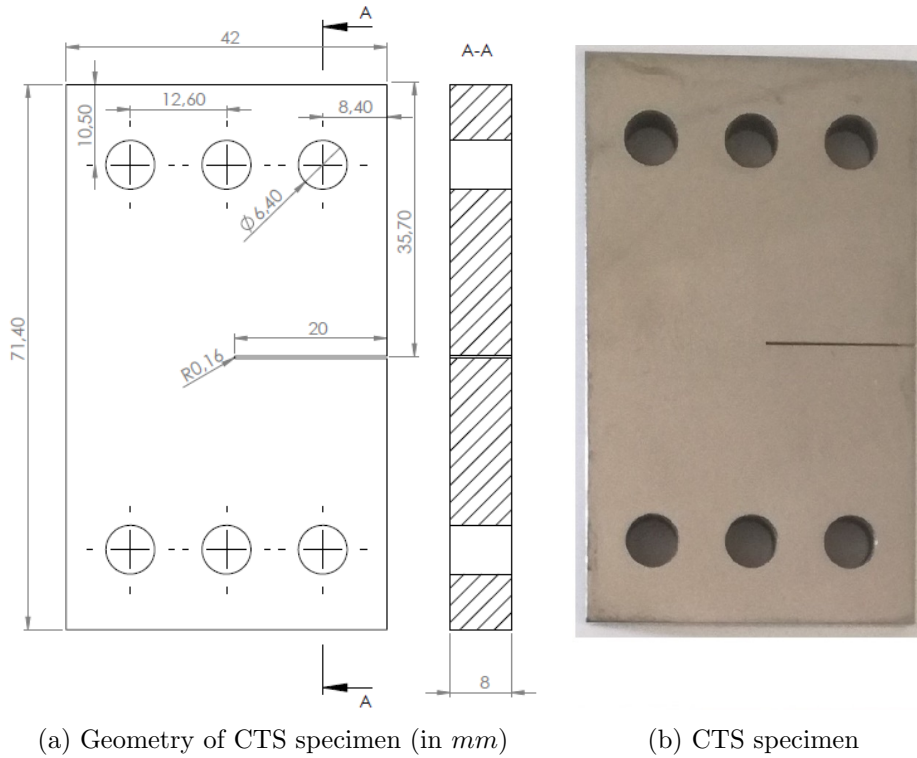


Figure 3.24: CTS specimen tested under mixed mode

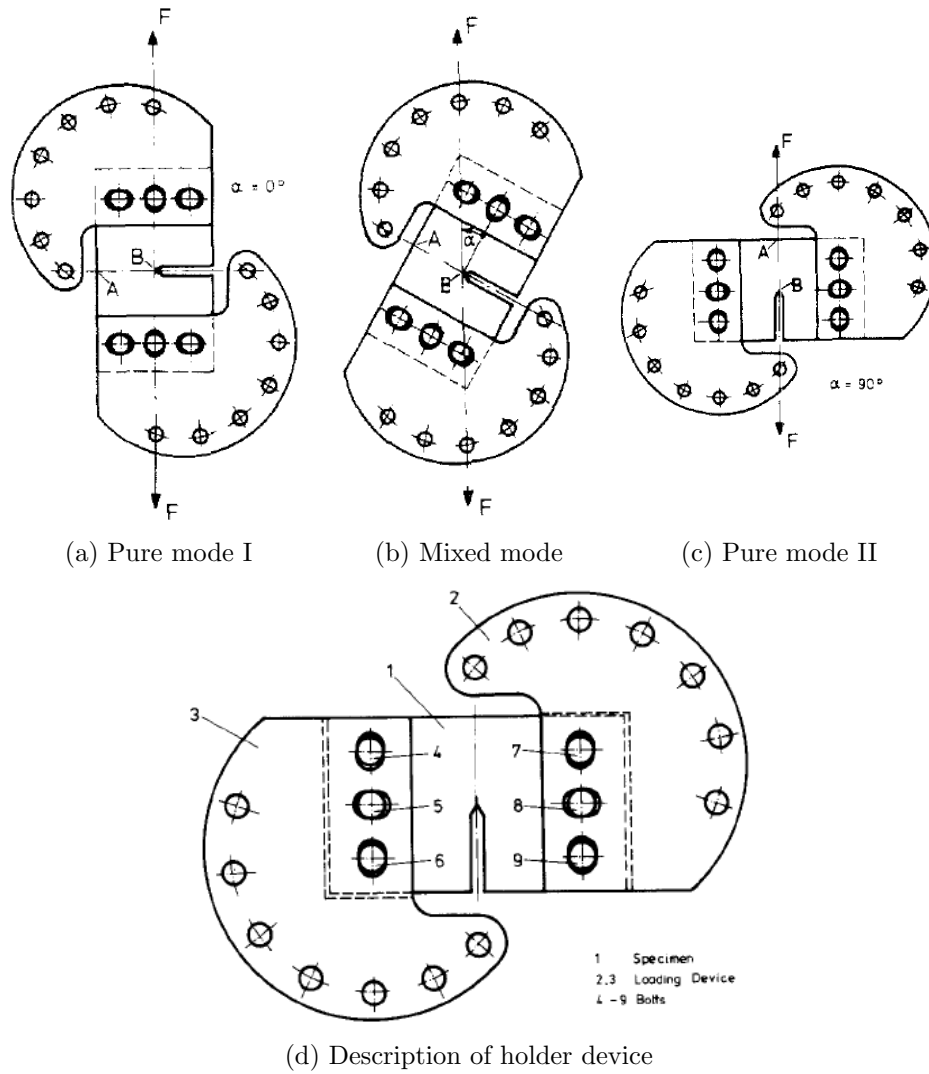


Figure 3.25: CTS specimen holder [Richard and Benitz, 1983]

The experimental programme defined for mixed mode FCGR tests can be seen in Table 3.7.

Table 3.7: Experimental programme for mixed mode FCGR tests

R	α	Number of Specimens
-	$^{\circ}$	-
0.01	30	3
0.5	30	3
0.01	45	3
0.5	45	3
0.01	60	3
0.5	60	3

As can be seen in Figures 3.26a and 3.26b, the mixed mode tests were performed in the MTS 810 tensile testing machine, which has already been characterized some sections above. An experimental apparatus very similar to the one used in previous fracture tests,

was used, but with the additional CTS holder and a digital microscope.

The microscope captures images of the crack evolution during the experimental test, in order to measure the crack length at certain number of cycles and so calculate the crack growth rate. This methodology is necessary since the acquisition system only registers the applied force and number of cycle.

However, before the proper tests, it was introduced a precrack, under mode I (with $\alpha = 0$), on all CTS specimens.

Both the precracking and the proper test were carried out in force control and under a cyclic tensile loading of sinusoidal waveform with a frequency of 10 Hz .

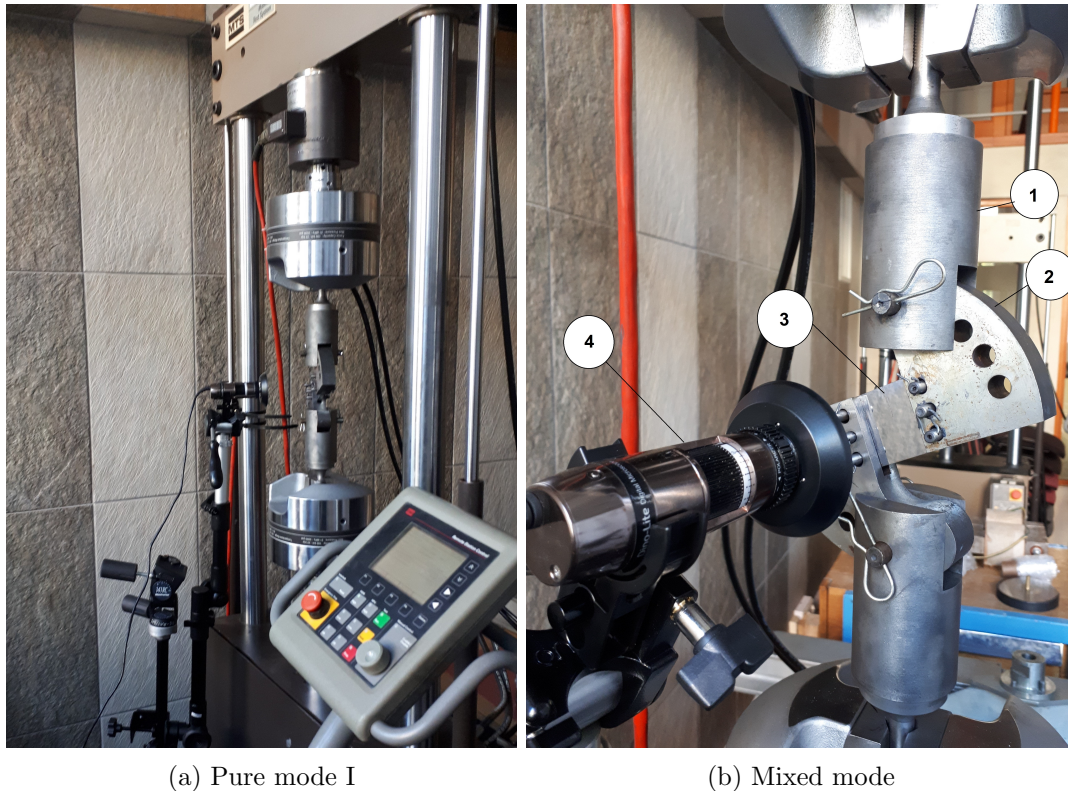


Figure 3.26: Apparatus of FCGR tests performed for mixed-mode: 1-MTS clevis grip for fracture mechanics; 2- CTS specimen holder; 3-CTS specimen 4-DinoLite microscope

Unfortunately, the experimental programme settled were not completed and finished on time to analyse and include the experimental results in this master thesis. Because of this, the experimental data obtained by Rozumek et al. [2018] was collected and analysed.

Rozumek et al. [2018] conducted three FCGR tests under mixed mode loading for stress ratio equal to 0.1, but each of them for different values of α : 30° , 45° and 60° .

The fracture surfaces of specimens were observed and evaluated, in order to measure the initial crack length (mechanical notch+precrack) and the crack initiation angles. In Table 3.8, there are summarized the results of these tests, and from Figure 3.27 to 3.33 are portrayed the fracture surfaces of each specimen. All macroviews were obtained with Dinolite microscope.

As can be seen in Table 3.8, for the same stress ratio and loading, the number of cycles increases with the loading angle, as well as, the crack initiation angle.

3. Experimental Programme

Table 3.8: Results of mixed mode FCGR tests obtained by Rozumek et al. [2018]

α $^{\circ}$	R	F_{max} N	F_{min} N	Number of cycles -	Notch+precrack length mm	Crack initiation angle $^{\circ}$
30	0.1	7500	750	335800	20.675(avg)/20.895(max)	29.4 (L)/23.6(R)
45	0.1	7500	750	428450	20.023(avg)/20.0 (max)	37.7(L)/36.1(R)
60	0.1	7500	750	496953	20.678(avg)/20.877(max)	56.2(L)/49.7(R)



Figure 3.27: Broken CTS specimens (for $\alpha = 30^{\circ}$, $\alpha = 45^{\circ}$ and $\alpha = 60^{\circ}$) [Rozumek et al., 2018]

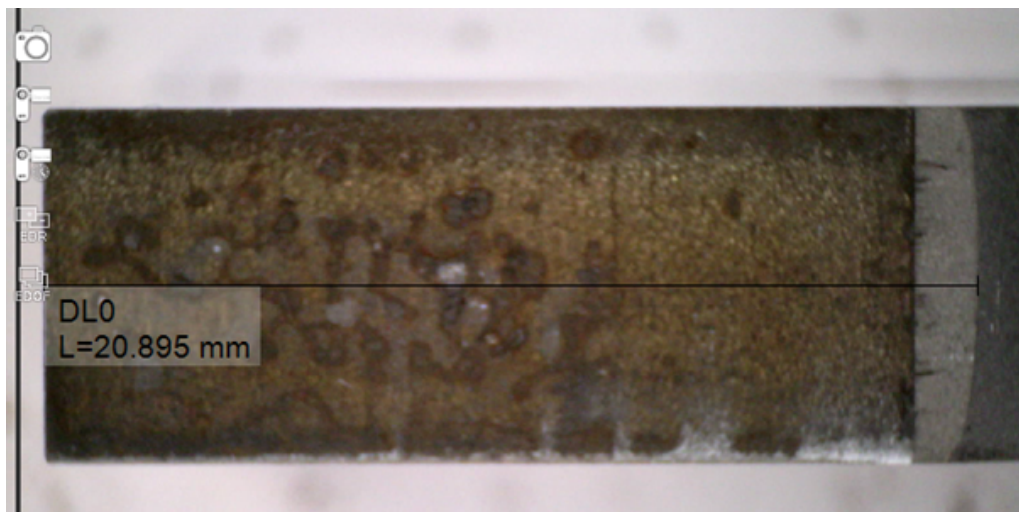
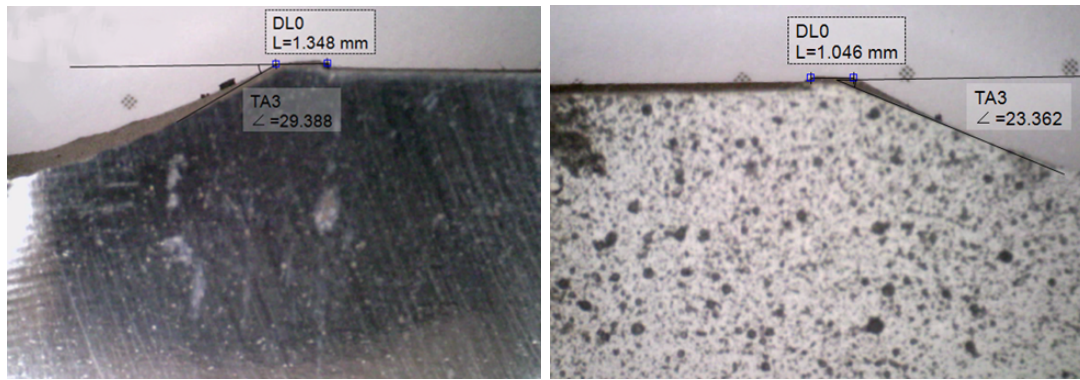


Figure 3.28: Macroview on the fracture surface of specimen tested for 30° (initial crack length – notch+precrack=20.675 mm /max 20.895)

3.3. Pure-mode I and Mixed-mode Fatigue Crack Growth Characterization of S355 steel



(a) Left side

(b) Right side

Figure 3.29: Crack initiation angle ($\alpha = 30^\circ$)

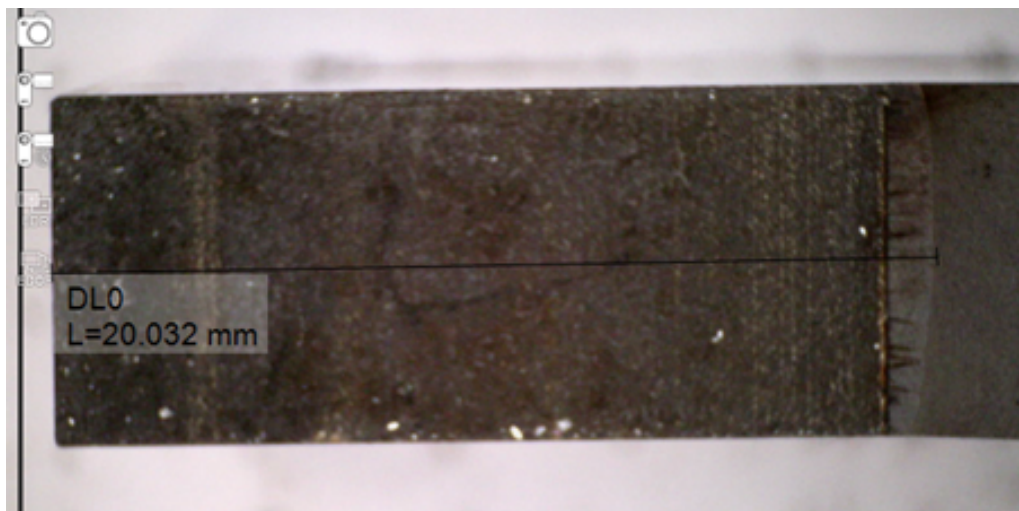
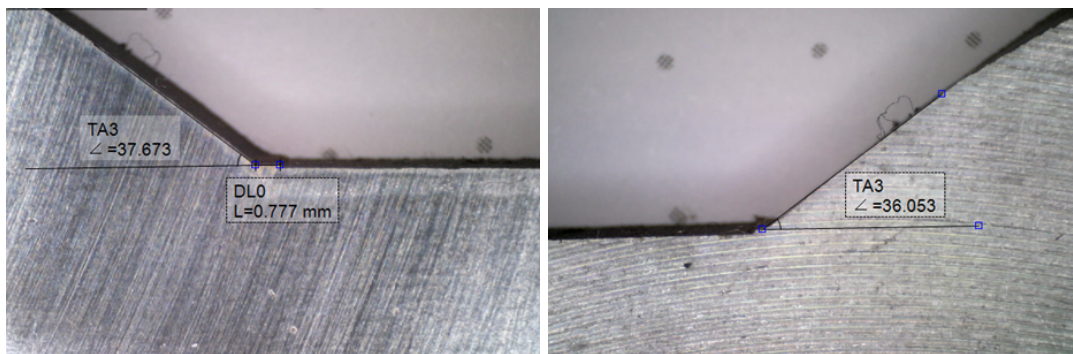


Figure 3.30: Macroview on the fracture surface of specimen tested for 30° (initial crack length – notch+precrack=20.023 mm /max 20.032)



(a) Left side

(b) Right side

Figure 3.31: Crack initiation angle ($\alpha = 45^\circ$)

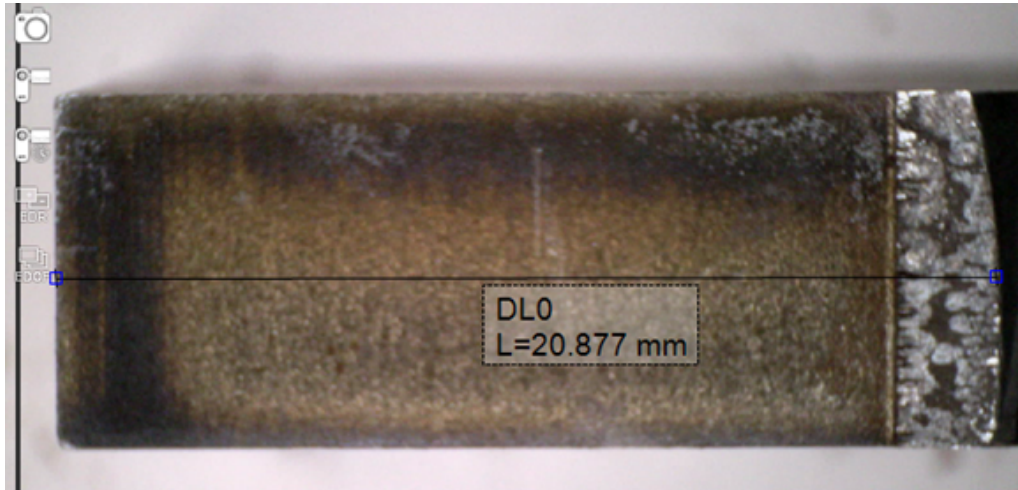
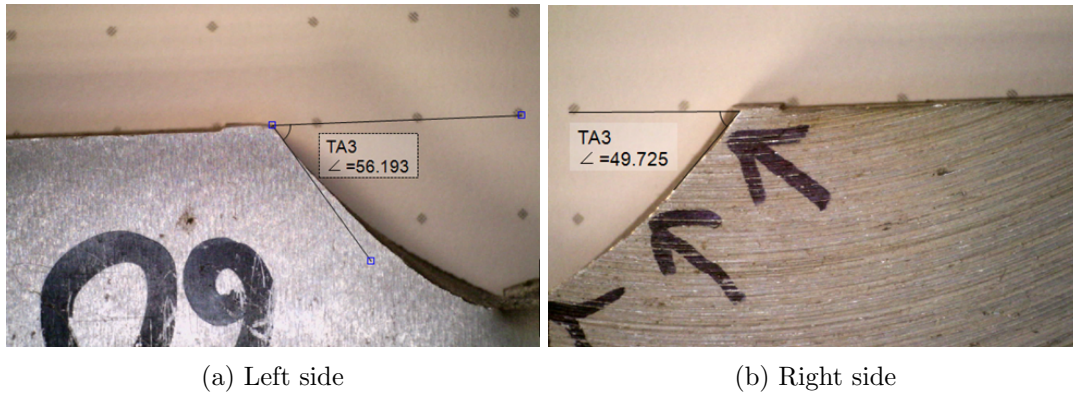


Figure 3.32: Macroview on the fracture surface of specimen tested for 30° (initial crack length – notch+precrack=20.678 mm /max 20.877)



(a) Left side

(b) Right side

Figure 3.33: Crack initiation angle ($\alpha = 60^\circ$)

Figure 3.34 shows the fatigue crack length and number of cycles data for each specimen plotted in a graph. The crack length was measure from the end of prepack and results from the combination of measurements in the direction along and perpendicular to notch.

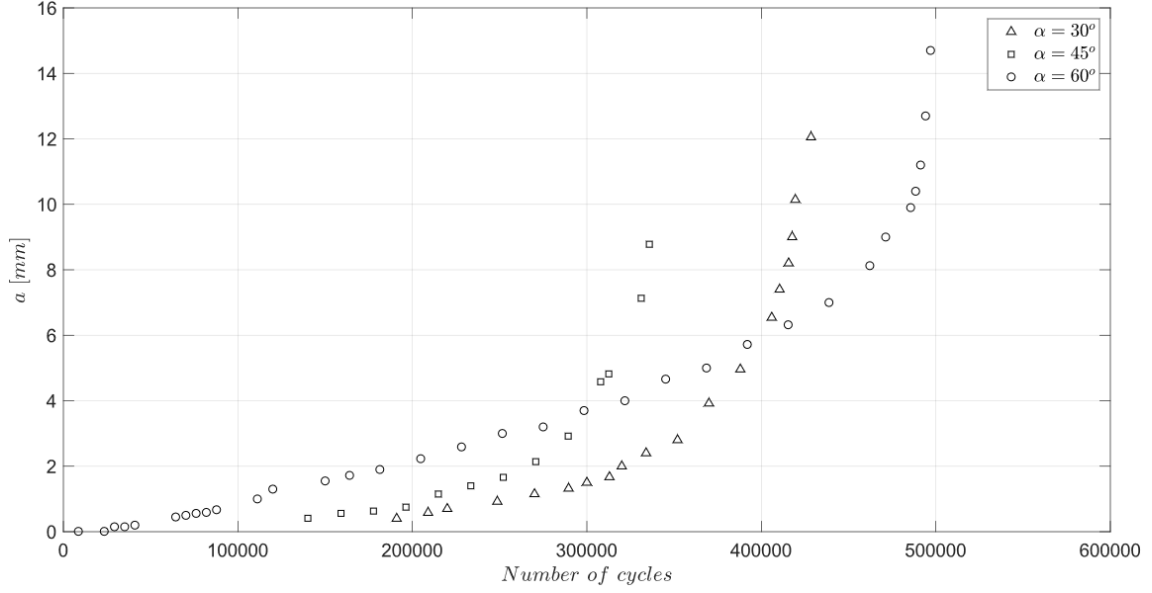


Figure 3.34: Fatigue crack growth versus number of cycles under mixed mode

Regarding the stress intensity factor, Richard [1985] proposed for CTS geometry and a crack straight and perpendicular to the specimens lateral faces, the following equations for K_I and K_{II} :

$$K_I = \frac{F\sqrt{\pi a}\cos(\alpha)}{WB(1 - \frac{W}{a})} \sqrt{\frac{0.26 + 2.65\frac{a}{W-a}}{1 + 0.55(\frac{a}{W-a}) - 0.08(\frac{a}{W-a})^2}} \quad (3.4)$$

$$K_{II} = \frac{F\sqrt{\pi a}\sin(\alpha)}{WB(1 - \frac{W}{a})} \sqrt{\frac{-0.23 + 1.40\frac{a}{W-a}}{1 - 0.67(\frac{a}{W-a}) + 2.08(\frac{a}{W-a})^2}} \quad (3.5)$$

where F is the applied force(N), W is the specimen width(mm), B is the specimen thickness(mm), a is the crack length(mm) and α is the loading angle

However, these equations are only valid for the initial crack (notch+precrack), since the crack becomes kinked during the mixed mode test. Hence, the stress intensity factor during the FCGR test was calculated through boundary element methods (BEM). The numerical procedure will be not described since it is not the main focus of this thesis, but a detailed description of it can be found in [Rozumek et al., 2018].

Figures 3.35 to 3.37 illustrate the graphs of fatigue crack growth rate versus stress intensity factor for mode I and mode II.

3. Experimental Programme

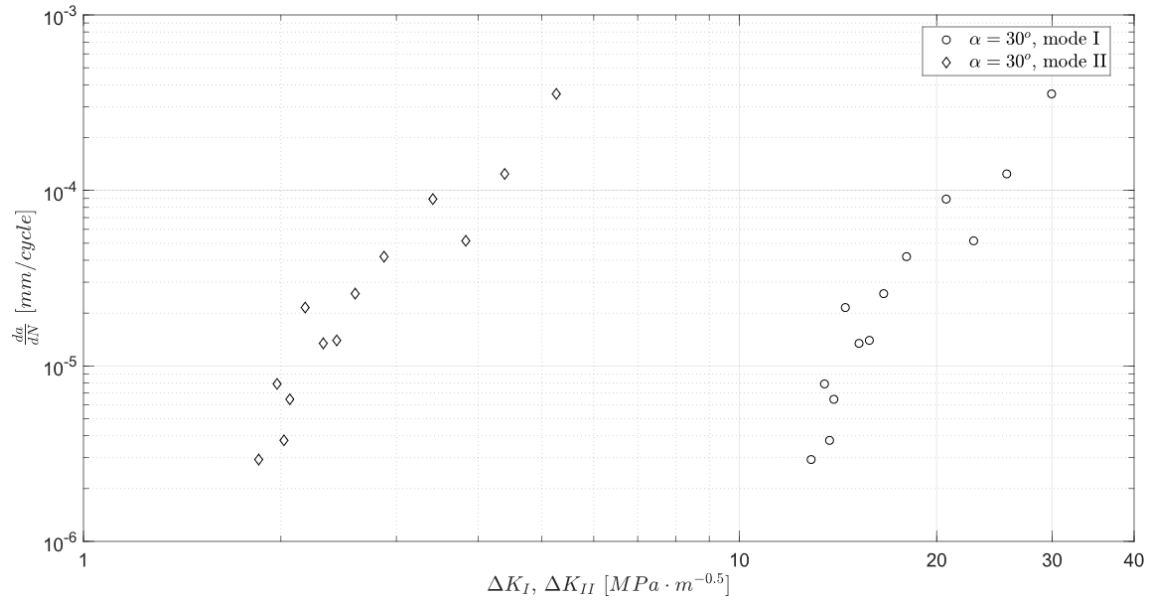


Figure 3.35: Fatigue crack growth rate versus stress intensity factor for mode I and mode II ($\alpha = 30^\circ$)

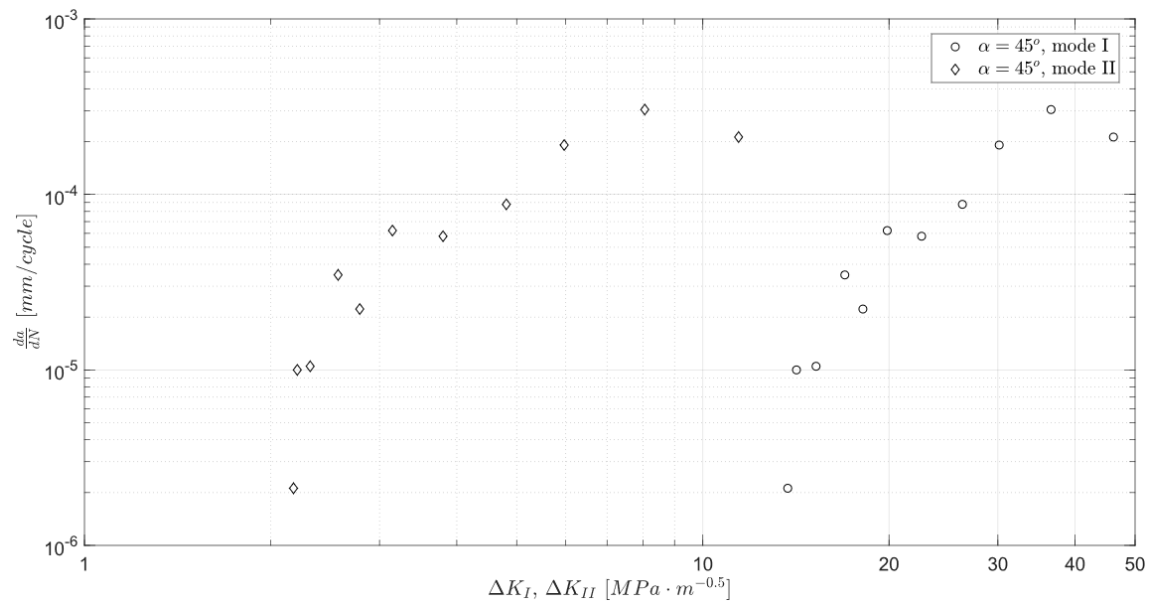


Figure 3.36: Fatigue crack growth rate versus stress intensity factor for mode I and mode II ($\alpha = 45^\circ$)

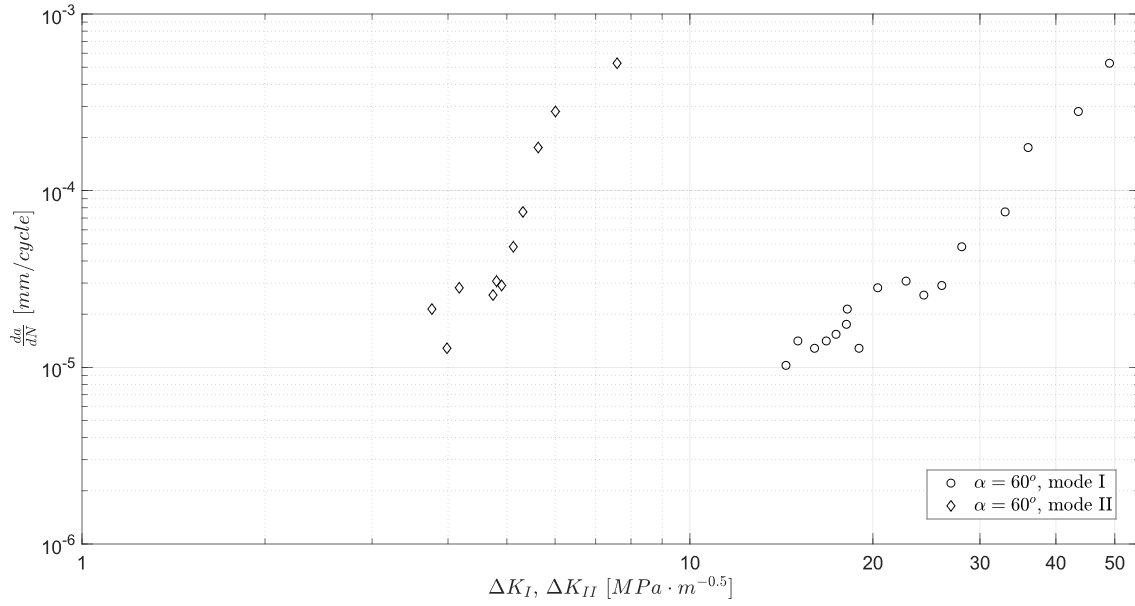


Figure 3.37: Fatigue crack growth rate versus stress intensity factor for mode I and mode II ($\alpha = 60^\circ$)

Finally, the equivalent stress intensity factor range (ΔK_{eqq}) was calculated using the Huber-Mises criterion for proportional loading:

$$\Delta K_{eqq} = \sqrt{\Delta K_I^2 + 3\Delta K_{II}^2} \quad (3.6)$$

Thus, the fatigue crack growth rate was replotted as function of equivalent stress intensity factor and fitted to a power function as can be seen in Figure 3.38. The Paris law constants (C,m), which are obtained through the power regression, are listed in Table 3.9.

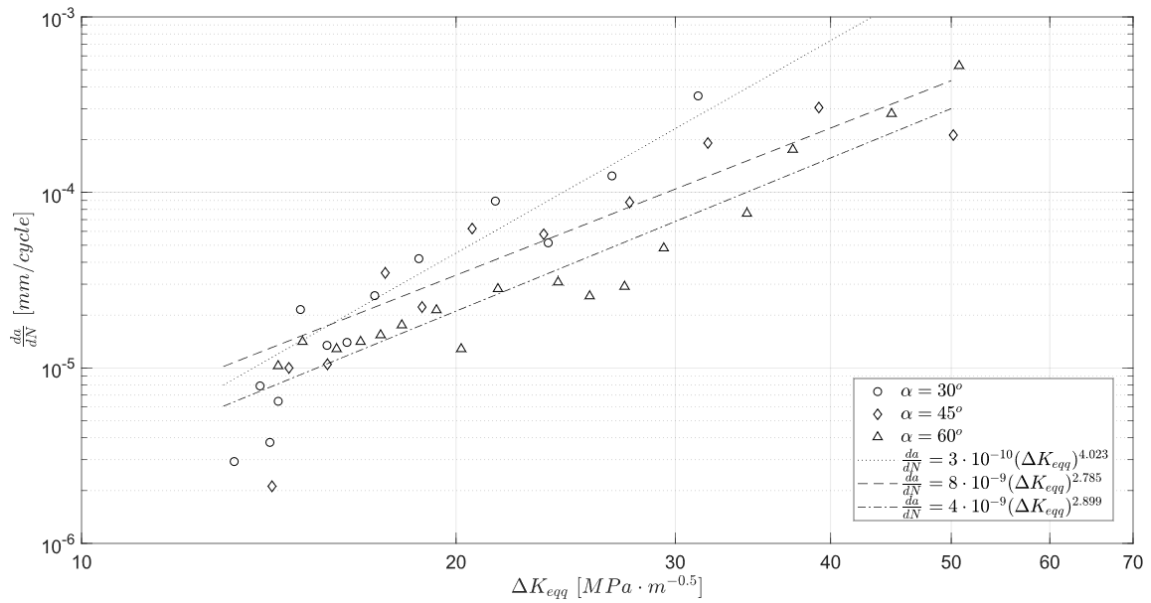


Figure 3.38: Fatigue crack growth rate versus equivalent stress intensity factor

Table 3.9: Values of $\frac{da}{dN}$ versus ΔK curves parameters(C, m) for mixed mode

α	R	C	m
30	0.1	$3 \cdot 10^{-10}$	4.023
45	0.1	$8 \cdot 10^{-9}$	2.785
60	0.1	$4 \cdot 10^{-9}$	2.899

3.3.3 Comparison Between Pure-mode I and Mixed-mode (Mode I+II) Fatigue Crack Growth of S355 Steel

In order to comprehend the effect of pure mode I and mixed mode on fatigue crack growth, all experimental points and respective power functions were plotted in the same graph (Figures 3.39 and 3.40). Besides, all constants of Paris law are summarized in Table 3.10.

Table 3.10: Values of $\frac{da}{dN}$ versus ΔK curves parameters(C, m) for pure mode I and mixed mode(I+II)

Type of test	α	R	C	m
Pure mode I	0	0.5	$2 \cdot 10^{-8}$	2.619
Pure mode I	0	0.7	$8 \cdot 10^{-9}$	2.869
Pure mode I	0	0.1	$6 \cdot 10^{-10}$	3.642
Mixed mode(I+II)	30	0.1	$3 \cdot 10^{-10}$	4.023
Mixed mode(I+II)	45	0.1	$8 \cdot 10^{-9}$	2.785
Mixed mode(I+II)	60	0.1	$4 \cdot 10^{-9}$	2.899

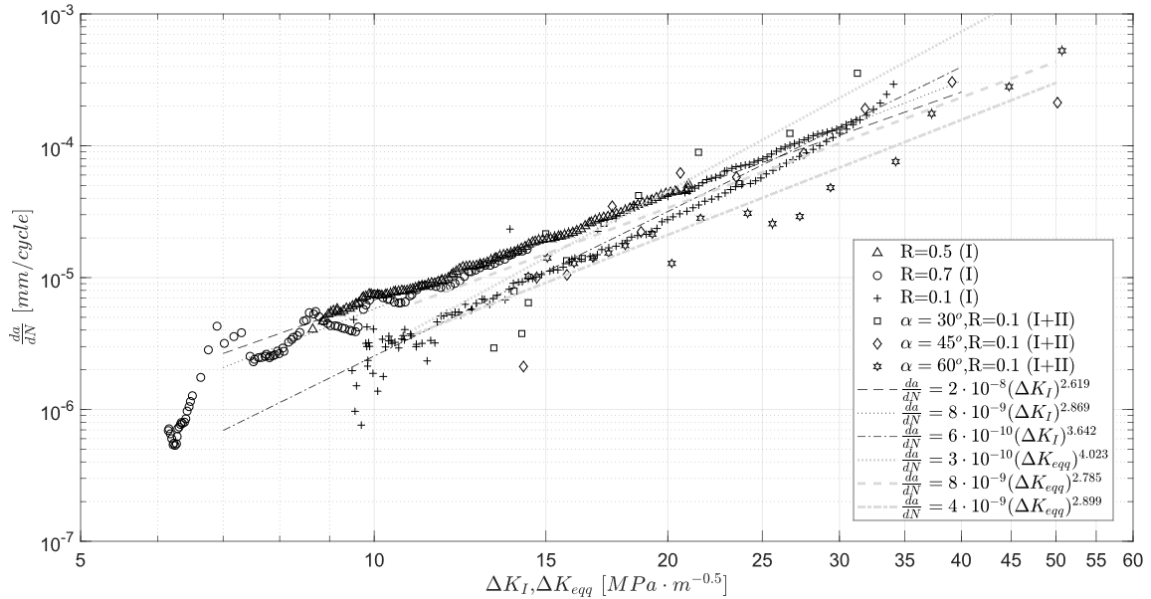


Figure 3.39: Fatigue crack growth rate versus stress intensity factor for mode I / equivalent stress intensity factor curves and experimental points

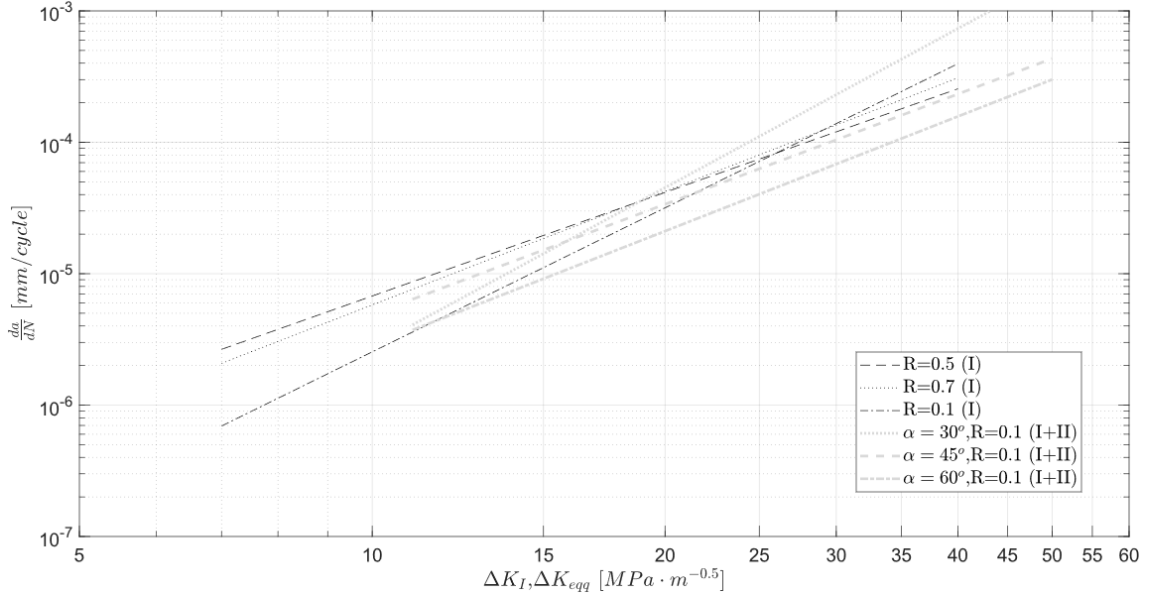


Figure 3.40: Fatigue crack growth rate versus stress intensity factor for mode I / equivalent stress intensity factor curves

For pure mode I, the effect of stress ratio originated by crack closure effects is almost not noticeable for $R = 0.5$ and $R = 0.7$, and even for $R = 0.1$ is not much significant. This observation is in accordance with same authors, such as Correia et al. [2016], who state that crack closure effects can be neglected for higher stress ratios.

Regarding the mixed mode tests, the fatigue crack growth rate is higher for $\alpha = 30^\circ$ and $\alpha = 45^\circ$, than for pure mode I carried out for the same stress ratio ($R = 0$). On the other hand, for $\alpha = 60^\circ$ is observed the lowest fatigue crack growth. For this reason, it is conclude that for S355 steel the mixed mode is more damaging when mode I is the mode of dominance.

However, all curves are distributed around a very narrow region. For this reason, it is conclude that the FCG tests conducted under mixed mode (mode I+II) are not crucial and for design propose is enough to evaluate the behaviour of this material under pure mode I.

Application and Evaluation of Multiaxial Fatigue Models

4.1 Introduction

The main idea of this chapter is to analyse and evaluate some multiaxial models by applying them to the fatigue data obtained from the experimental tests conducted. This analysis pretends to choose the most suitable model to S355 steel and assess the damage caused by a biaxial fatigue stress state. Then, a design curve will be obtained for a more complex fatigue state and applied to the joint described in Chapter 5. Therefore, four relevant multiaxial damage models were chosen and combined with the Basquin law. These choice was based on the idea of analysing models from different natures: Sines is an equivalent stress approach, Findley and McDiarmid are critical plane approaches but with different definitions for the critical plane, and, finally, Dang Van is a recent multiscale approach.

In order to more deeply evaluate the multiaxial case, the fatigue data for pure torsion, pure bending and combined torsion with bending at high cycle fatigue regime obtained by Rozumek and Pawliczek [2004] was added to this analysis. The biaxial tests were also conducted under a constant proportional loading, but shear stress and normal stress were established with the same value. This fatigue data is listed in tables A.1, A.2 and A.3 allocated in Appendix A.

One of the main goals of this chapter is not only to find a damage parameter that can incisively describe the multiaxial fatigue state, but also to describe the different levels of damage originated by each kind of loading. Thus, firstly, the uniaxial data for torsional, bending and tensile loading are studied and then, in the forward sections, the multiaxial fatigue data is added and evaluated.

However, before starting the analysis described, it is important to explain some assumptions made and describe the stress states that are evaluated.

Five different cases of loading - torsional, bending, tensile, combined torsional and bending and combined torsional and tensile - are studied and, as consequence, five different stress states are also analysed. In Figure 4.1 are represented the stress fatigue states and fields assumed for each of the loading cases.

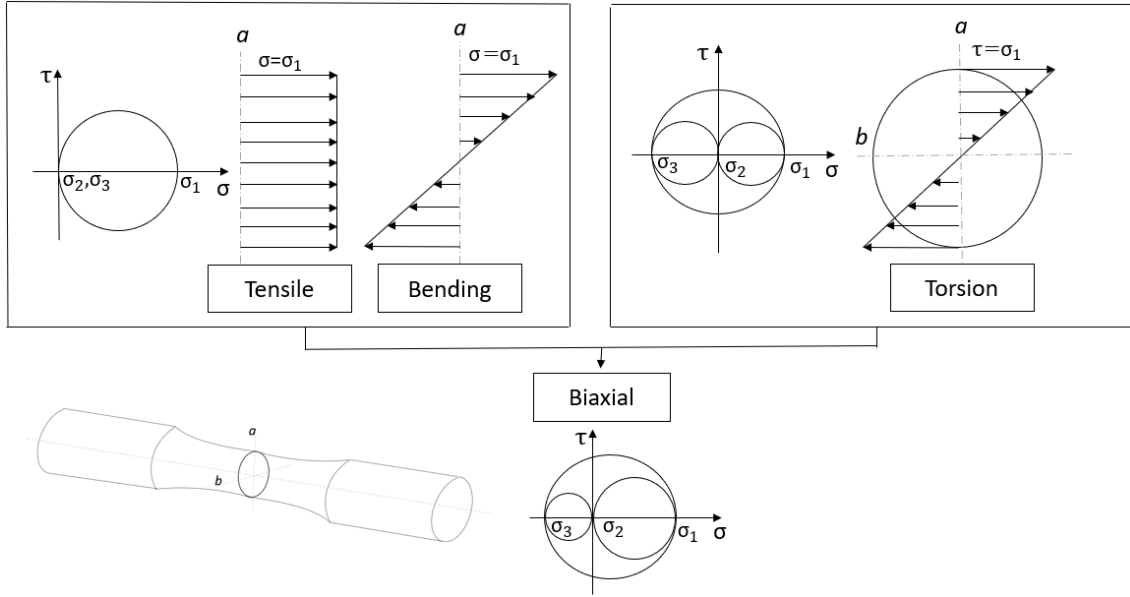


Figure 4.1: Stress state and field for tensile, bending, torsional and biaxial loading

The tensile stress state is easily understood and explained since the stress field is constant along the cross section thickness. However, in the case of bending the stress field changes throughout the thickness: decreases from the surface to the centre line, which in the specimen coincides with the neutral line where stress due to bending is null. Thus, for this stress analyses is only considered, as simplification, the critical point where the normal stress achieves the maximum value. Because of this, for the same specimen and stress level, a bending loading is less damaging and the fatigue lives are longer than in a axial loading.

Regarding the torsional loading, the stress field also decreases from the surface to the centre point of the circular cross-section. Once again, the critical external point, where the shear stress is maximum, is assessed.

Therefore, the bending and axial stress states can be represented by the same Mohr's circle (Fig. 4.1) where the principal stresses are:

$$\begin{cases} \sigma_1 = \sigma \\ \sigma_2 = \sigma_3 = 0 \end{cases} \quad (4.1)$$

where σ is the applied bending or axial stress

The torsional stress state can be also represented by an Mohr's circle (Fig. 4.1) and the respectively principal stress states are:

$$\begin{cases} \sigma_1 = \tau \\ \sigma_2 = 0 \\ \sigma_3 = -\tau \end{cases} \quad (4.2)$$

where τ is the maximum applied torsional stress.

Finally, for the biaxial state (combined torsional and bending or axial loading) can be assumed the fatigue stress state portrayed by the Mohr's circle in Figure 4.1 which principal stresses are:

$$\begin{cases} \sigma_1 = \frac{\sigma}{2} + \sqrt{\left(\frac{\sigma}{2}\right)^2 + \tau^2} \\ \sigma_2 = 0 \\ \sigma_3 = \frac{\sigma}{2} - \sqrt{\left(\frac{\sigma}{2}\right)^2 + \tau^2} \end{cases} \quad (4.3)$$

4.2 Uniaxial Stress Fatigue State Analysis

The uniaxial fatigue data described in the preview chapter and the one obtained by Rozumek and Pawliczek [2004] were plotted in a stress amplitude versus number of cycles until failure graph, using a logarithmic scale for both of the axes (Figures 4.2 to 4.4). The design curves were determined by applying a power regression, as it had been proposed by basquin.

Hence, the design curves for axial stress for different stress ratios are determined and defined by the following equations:

- For $R = 0$:

$$\sigma_a = 274.49 N_f^{-0.024} \quad (4.4)$$

- For $R = -1$

$$\sigma_a = 456.46 N_f^{-0.045} \quad (4.5)$$

From the observation of Figure 4.2 is confirmed the influence of mean normal stress on fatigue life.

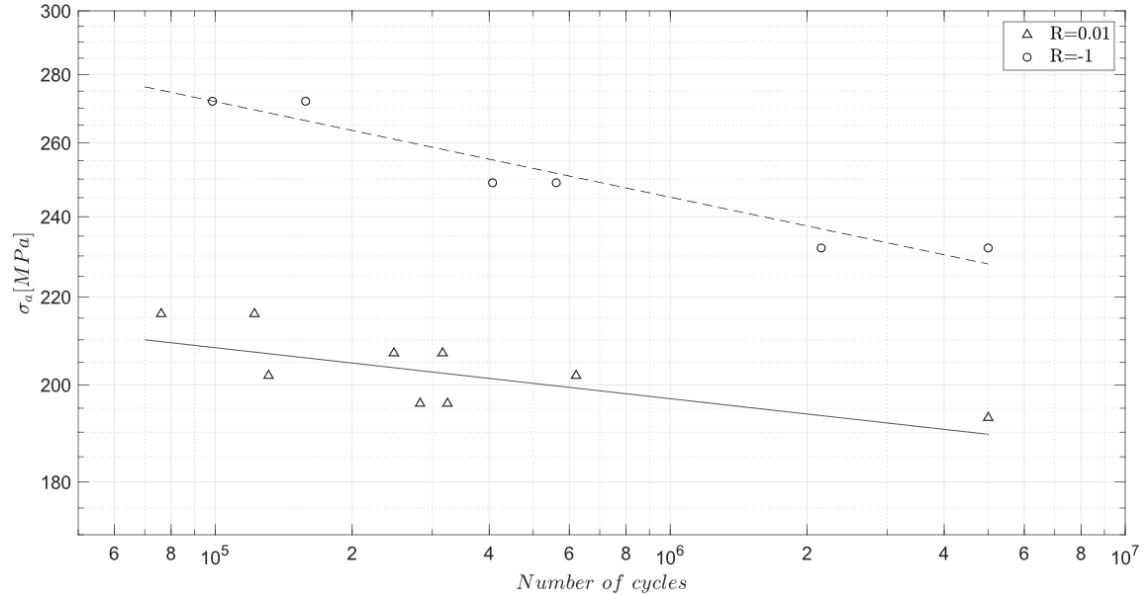


Figure 4.2: Design curves for axial loading for $R = 0.01$ and $R = -1$

The fatigue design curves for bending are represented in Figure 4.3 and defined by the Equations (4.6), (4.7) and (4.8):

- For $R = -0.5$:

$$\sigma_a = 1414 N_f^{-0.126} \quad (4.6)$$

- For $R = 0$:

$$\sigma_a = 764.55N_f^{-0.086} \quad (4.7)$$

- For $R = -1$:

$$\sigma_a = 1880N_f^{-0.13} \quad (4.8)$$

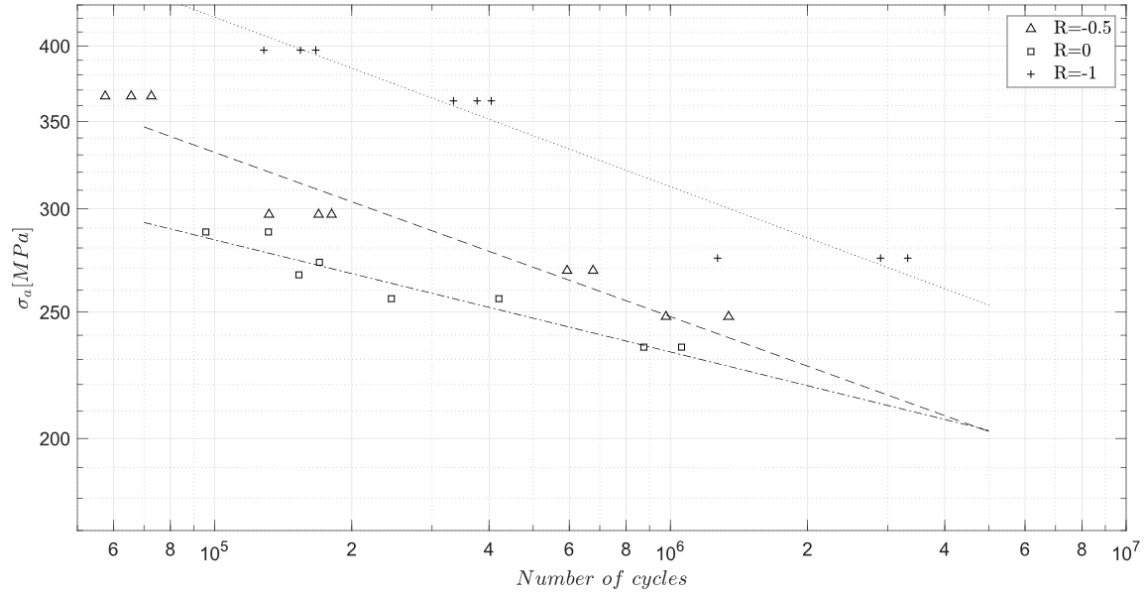


Figure 4.3: Design curves for bending loading for $R = 0$, $R = -0.5$, $R = -1$

Finally, for torsional loading are obtained the following power equations, which can be checked in Figure 4.4:

- For $R = -0.5$

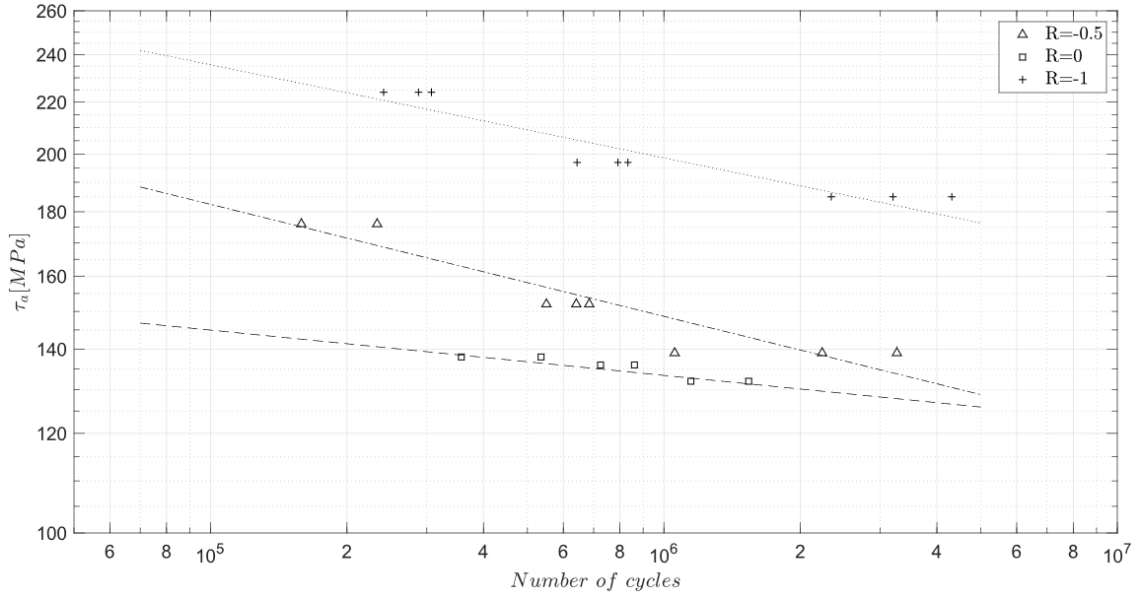
$$\tau_a = 508.38N_f^{-0.089} \quad (4.9)$$

- For $R = 0$:

$$\tau_a = 219.41N_f^{-0.036} \quad (4.10)$$

- For $R = -1$

$$\tau_a = 552.24N_f^{-0.074} \quad (4.11)$$

Figure 4.4: Design curves for torsional loading for $R = 0$, $R = -0.5$, $R = -1$

In order to enhance the difference between the fatigue damage originated by each kind of loading, the S-N curves were combined in two graphs (Figures 4.5 and 4.6).

In the first one, it is compared bending with axial loading and verified an idea stated before: bending is less damaging for the same level of loading and stress ratio since it is only included the bending stress present in critical point and ignored the stress field gradient. Because of this, in the next sections the fatigue data for bending and axial stress will be evaluated separately.

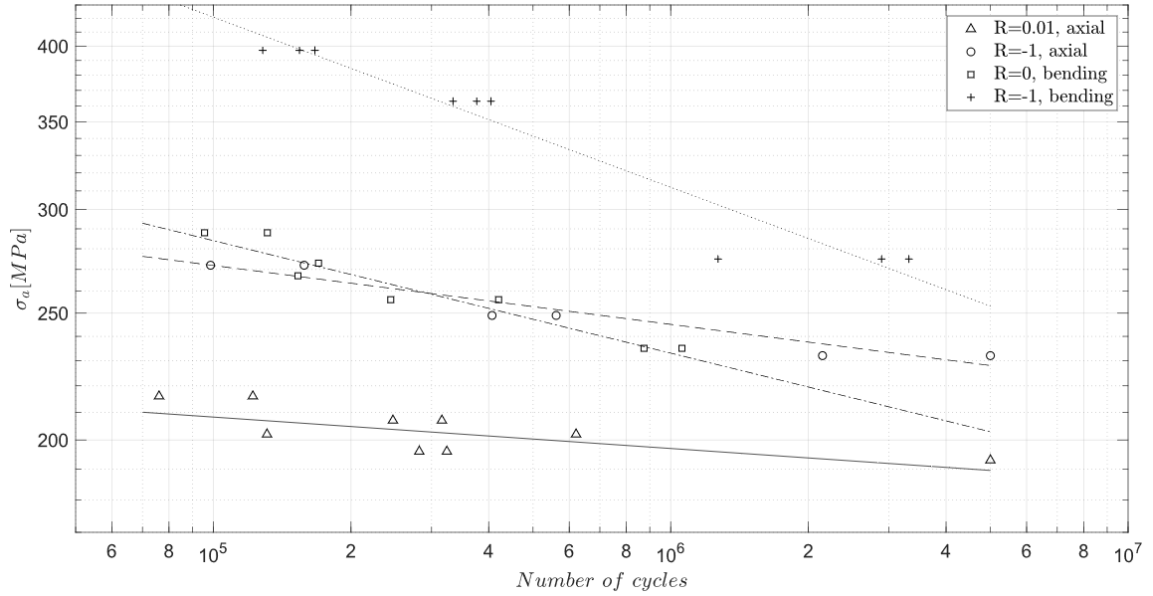


Figure 4.5: Comparison between design curves for bending and axial stresses

In the same way, curves for torsional and axial loading were plotted in the graph of Figure 4.6 for $R = 0$ and $R = -1$. In this Figure, it is observed that, for the same ratio, the torsion curves are lower than the axial curves, which means that a torsional loading

is more damaging. This conclusion agrees with the idea of shear stress being the main mechanism of fatigue initiation.

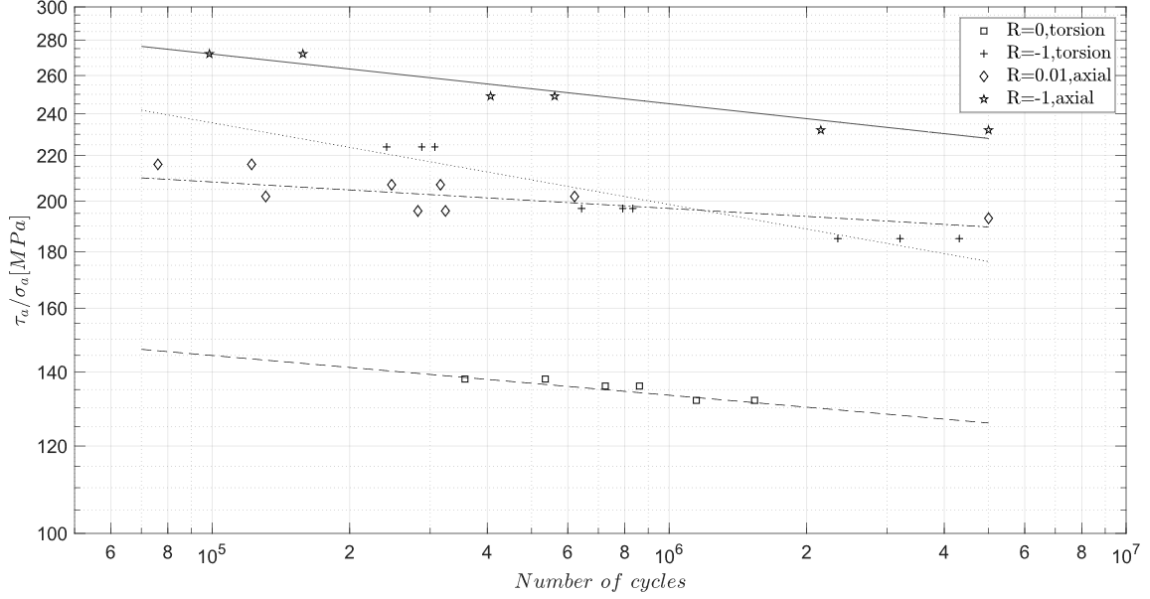


Figure 4.6: Comparison between design curves for axial and torsional stresses

4.3 Multiaxial Stress Fatigue State Analysis

The biaxial fatigue data can not be represented in the same way as the uniaxial data since it implies a more complex stress state with a normal and a shear stress component. Therefore, the application of a damage parameter to the experimental data is required in order to evaluate the fatigue behaviour of S355 steel. Then, four different damage parameters will be applied throughout this section.

An ideal model should “collapse” all the experimental data around a single curve with a small dispersion. This curve is obtained through a power regression fitted to all data and represents the design curve for a multiaxial state. Ideally, this power regression is really close to the one obtained for uniaxial data which allows to evaluate a multiaxial state with uniaxial data.

The fatigue data obtained during this work will be evaluated separately from the one presented by Rozumek and Pawliczek [2004].

4.3.1 Sines Model

First, it was applied the most simple approach: the equivalent stress model proposed by Sines which equation extended to finite life is mention at the end of Chapter 2, but can be reminded to the reader:

$$\tau_{a,oct} + k_s(3\sigma_{h,mean}) = \tau'_f(2N_f)^b \quad (4.12)$$

Thus, from a quick observation, it is concluded that the equation above has, until now, three constants not known: k_s , τ'_f and b . The last two are usually determined by a power regression, but the first one, related to the damage model, implies some considerations and it is not so easily calculated. Sines [1959] developed an expression for the value of k_s (see Chapter 2, Eq. (2.25)), which has a problem: is only based on experimental fatigue

limits of a kind of loading. However, this definition constitutes a practical solutions since allows the calibration of this model through a couple of easy tests.

Hence, the k_s constant was calculated with the limit stress values obtained through the axial tests: $\sigma_{a,R=-1} = 232MPa$ and $\sigma_{a,R=0} = 193MPa$, and, as result, was obtained that k_s is equal to 0.095. Finally, the left side of the Equation (4.12) was determined, represented in a damage parameter versus fatigue life graph and, after that, a power regression was applied.

In this way, the design curve graphs and equations are obtained for:

- Axial and axial combined with torsional stresses:

$$\begin{cases} s = 195.38N_f^{-0.036} \\ R^2 = 0.349 \end{cases} \quad (4.13)$$

where R^2 is the coefficient of determination and describes the regression accuracy. In the case of a perfect regression, this variable takes the value one [Guimarães and Cabral, 1997].

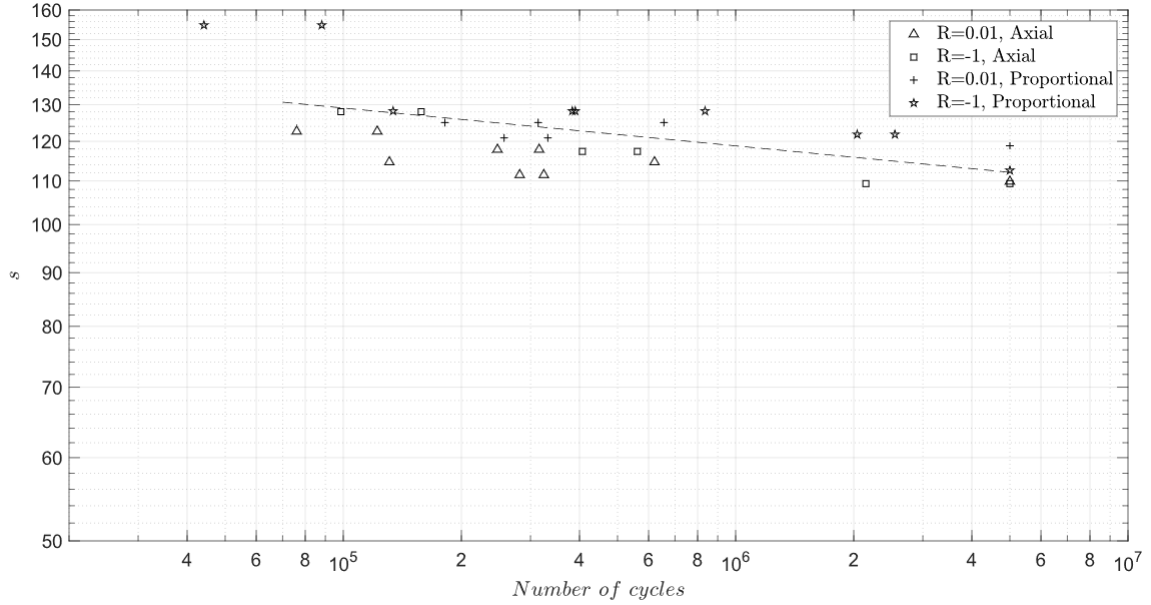


Figure 4.7: Sines damage parameter versus fatigue life graph for axial and axial combined with torsional stresses (for $k_s = 0.095$)

- Bending, torsion and bending combined with torsional data:

$$\begin{cases} s = 471.29N_f^{-0.093} \\ R^2 = 0.316 \end{cases} \quad (4.14)$$

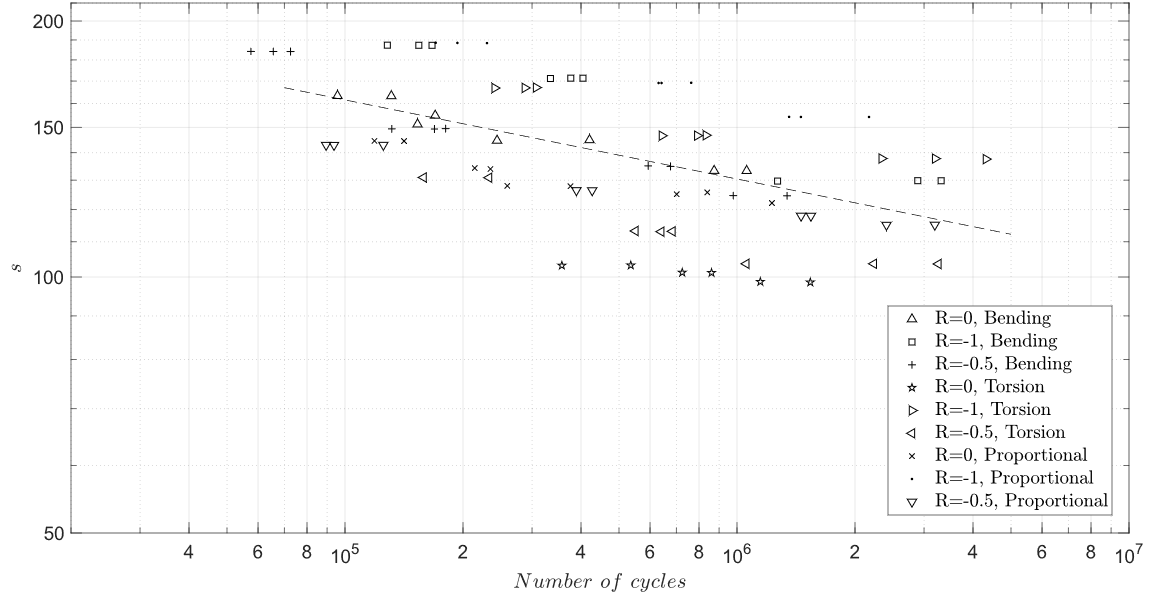


Figure 4.8: Sines damage parameter versus fatigue life graph for bending, torsional and bending combined with torsional stresses (for $k_s = 0.095$)

Moreover, another problem was found in the definition of k_s : if the same expression is applied in case of bending, the value obtained is a bit different since the fatigue limits are also different. Besides, the experimental points dispersion is high and the coefficient of determination low, for both of the cases described above.

Because of these problems, it was applied another method: to plot all the fatigue limit experimental points in an octahedral shear stress amplitude versus hydrostatic mean stress graph, apply a linear regression and, then, conclude that $3k_s$ is the slope of this line.

Thus, the fatigue limits points for the different stress states evaluated throughout this study were plotted and the respectively linear regression obtained as can be seen in Figure 4.9.

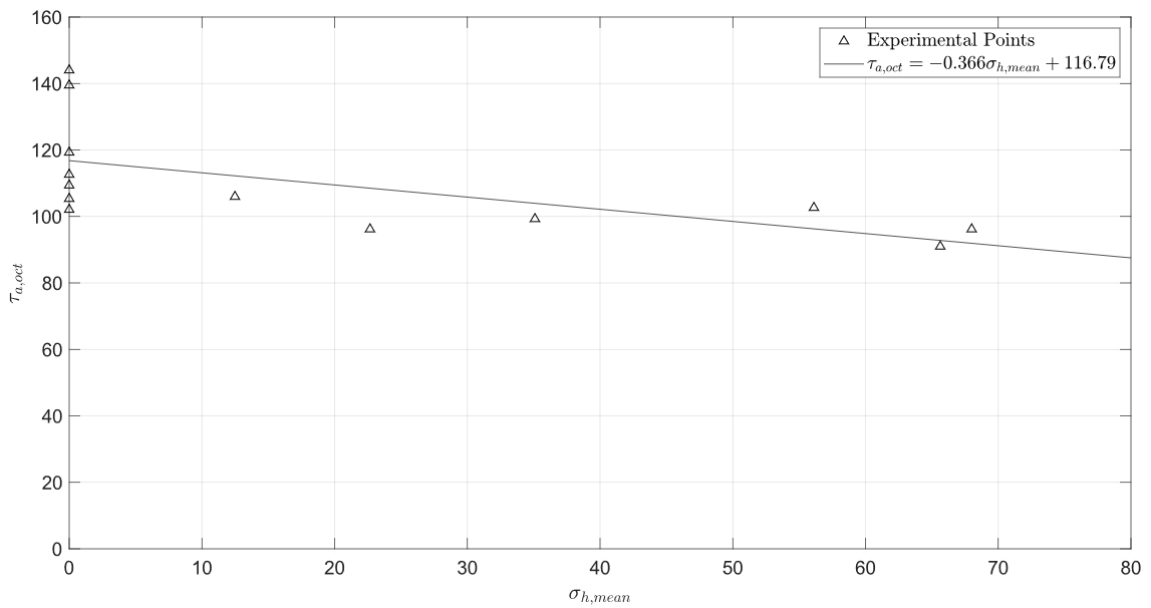


Figure 4.9: Graph of octahedral shear amplitude versus hydrostatic mean stress

The experimental points represented in the graph above are listed in Table 4.1.

Table 4.1: Experimental fatigue limit points expressed in $\sigma_{h,mean}$ and $\tau_{a,oct}$ (for $N_f = 5 \cdot 10^6$)

Loading	R	$\sigma_{h,mean}$ <i>MPa</i>	$\tau_{a,oct}$ <i>MPa</i>
-	-		
Axial	0.01	66	91
Axial	-1	0	109
Axial+Torsion	0.01	56	103
Axial+Torsion	-1	0	113
Torsion	-1	0	144
Torsion	-0.5	0	105
Torsion	0	0	102
Bending	0	68	96
Bending	-0.5	23	96
Bending	-1	0	119
Bending+Torsion	0	35	99
Bending+Torsion	-0.5	12	106
Bending+Torsion	-1	0	139

Finally, the damage parameter versus fatigue life graphs were plotted again and the respectively power regressions calculated, but this time for $3k_f = \frac{0.376}{3} = 0.125$.

- Axial and axial combined with torsional stresses:

$$\begin{cases} s = 205.81N_f^{-0.039} \\ R^2 = 0.452 \end{cases} \quad (4.15)$$

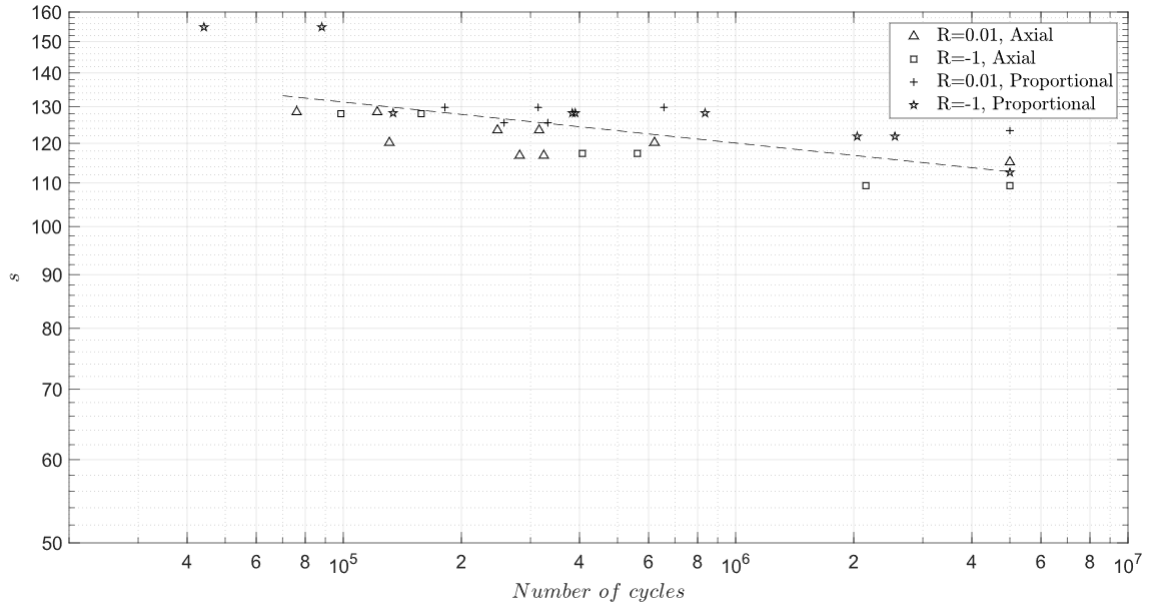


Figure 4.10: Sines damage parameter versus fatigue life graph for axial and axial combined with torsional stresses (for $k_s = 0.125$)

- Bending, torsional and bending combined with torsional stresses:

$$\begin{cases} s = 505.11N_f^{-0.098} \\ R^2 = 0.341 \end{cases} \quad (4.16)$$

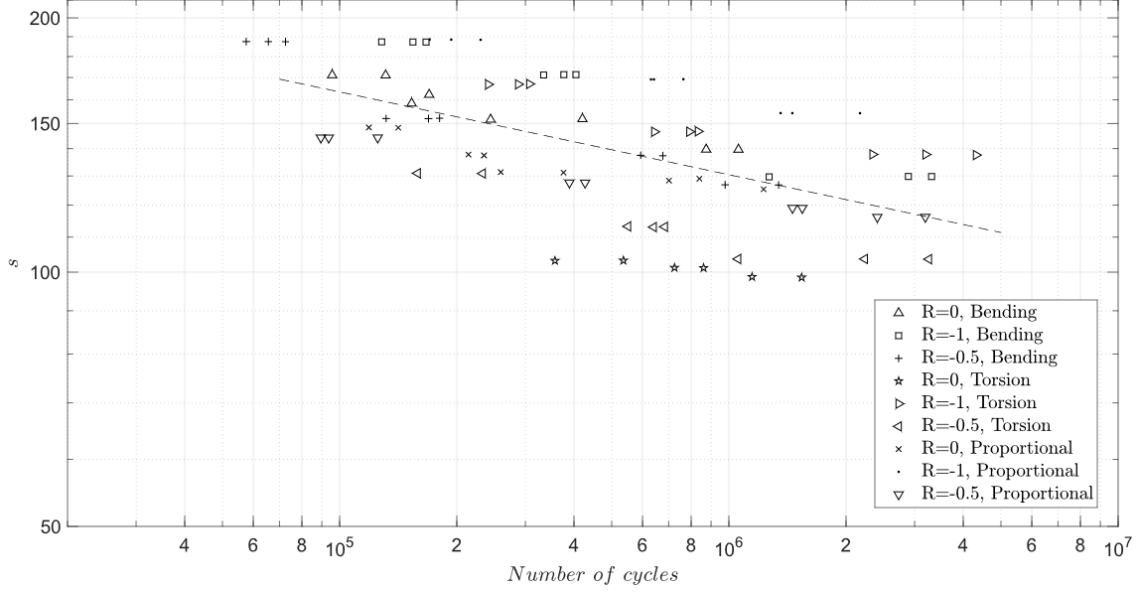


Figure 4.11: Sines damage parameter versus fatigue life graph for bending, torsional and bending combined with torsional stresses (for $k_s = 0.125$)

As can be seen in Figures 4.10 and 4.11, the dispersion of points slightly decreased and the coefficient of determination improved, which shows that this method is better for the k_s determination.

4.3.2 Findley Model

The application of the model proposed by Findley also implies some considerations and thoughts. Firstly, looking again to the combination of this model with Basquin law:

$$(\tau_{\theta a} + k_f \sigma_{\theta max})_{max} = \tau'_f (2N_f)^b \quad (4.17)$$

it is noticeable that an undetermined constant is present again. However, this time the problem is more complex since the critical plane changes with the constant value. Moreover, the critical plane and the shear and normal stress in this plane have to be determined.

Therefore, the shear stress amplitude and maximum normal stress were calculated for each plane using the Morh's circle principle and the following equations:

$$\sigma_{\theta} = \frac{\sigma_x + \sigma_y}{2} + \frac{\sigma_x - \sigma_y}{2} \cos(2\theta) + \tau_{xy} \sin(2\theta) \quad (4.18)$$

$$\tau_{\theta} = \frac{\sigma_x - \sigma_y}{2} \sin(2\theta) - \tau_{xy} \cos(2\theta) \quad (4.19)$$

where σ_x and σ_y are the applied normal stresses in x and y axis direction, τ_{xy} is the shear stress on the xy plane and θ is the angle between σ_x and σ_{θ} (Fig. 4.12).

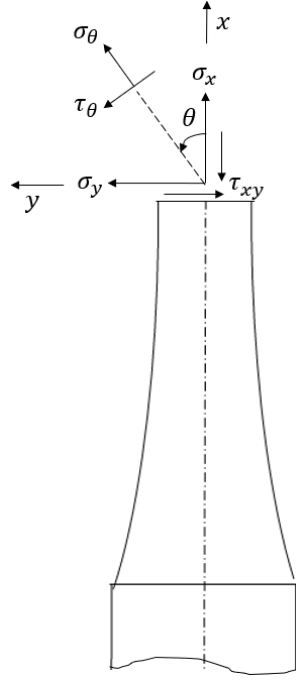


Figure 4.12: Representation of θ and the normal and shear stress on the θ plane

Later, the damage parameter for each plane was obtained and, finally, it was selected the maximum value and the plane where it happens.

Regarding the findley model constant k_f , as a first approach, different constants values were calculated, using the Equations (2.35) and (2.36) defined in chapter 2. Once again, this expressions do not specifies the kind of loading that should be considered in each expression. Because of this, different fatigue limits values were applied to these expressions:

- For bending and torsional fatigue limits ($\sigma_{a,R=-1} = 253MPa$; $\tau_{a,R=-1} = 176MPa$):

$$k_f = 0.425 \quad (4.20)$$

- For bending fatigue limits ($\sigma_{a,R=-1} = 253MPa$; $\sigma_{a,R=0} = 204MPa$):

$$k_f = 0.228 \quad (4.21)$$

- For axial fatigue limits ($\sigma_{a,R=-1} = 232MPa$; $\sigma_{a,R=0} = 193MPa$):

$$k_f = 0.192 \quad (4.22)$$

Subsequently, the damage parameter was calculated and the design curves were obtained for each value of k_f calculated, in order to evaluate which of them would fit better the fatigue data:

- For $k_f = 0.192$:
 - Axial and axial combined with torsional stresses:

$$\begin{cases} f = 251.65 N_f^{-0.036} \\ R^2 = 0.296 \end{cases} \quad (4.23)$$

4. Application and Evaluation of Multiaxial Fatigue Models

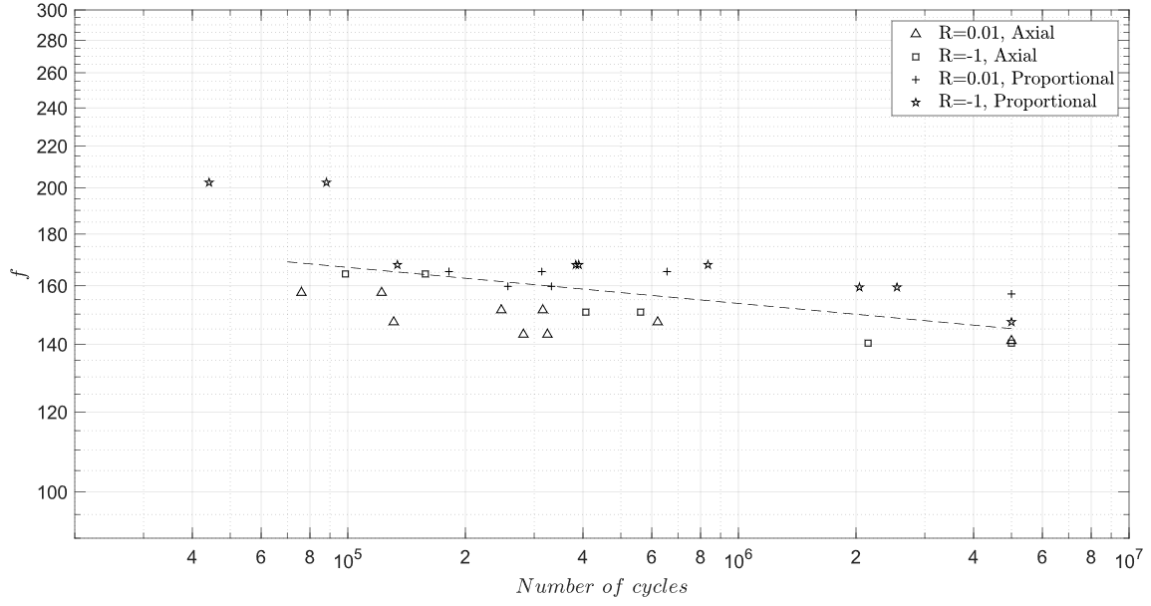


Figure 4.13: Findley damage parameter versus fatigue life graph for axial and axial combined with torsional stresses (for $k_f = 0.192$)

– Bending, torsional and bending combined with torsional stresses:

$$\begin{cases} f = 566.85N_f^{-0.086} \\ R^2 = 0.310 \end{cases} \quad (4.24)$$

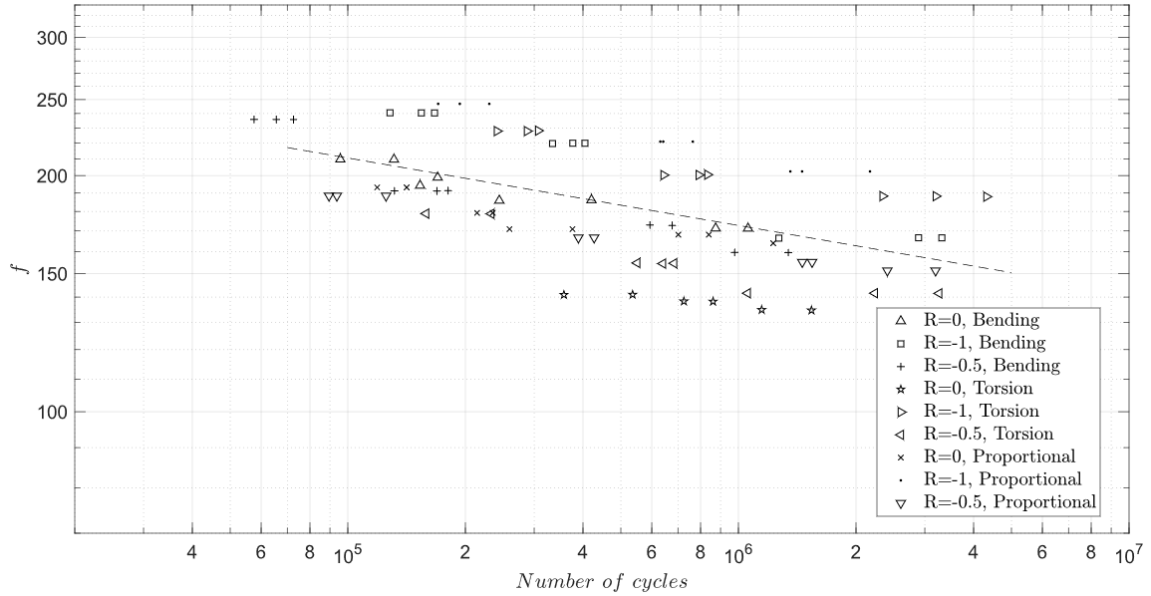


Figure 4.14: Findley damage parameter versus fatigue life graph for torsional, bending and bending combined with torsional stresses (for $k_f = 0.192$)

- For $k_f = 0.228$:

- Axial and axial combined with torsional stresses:

$$\begin{cases} f = 267.79 N_f^{-0.037} \\ R^2 = 0.378 \end{cases} \quad (4.25)$$

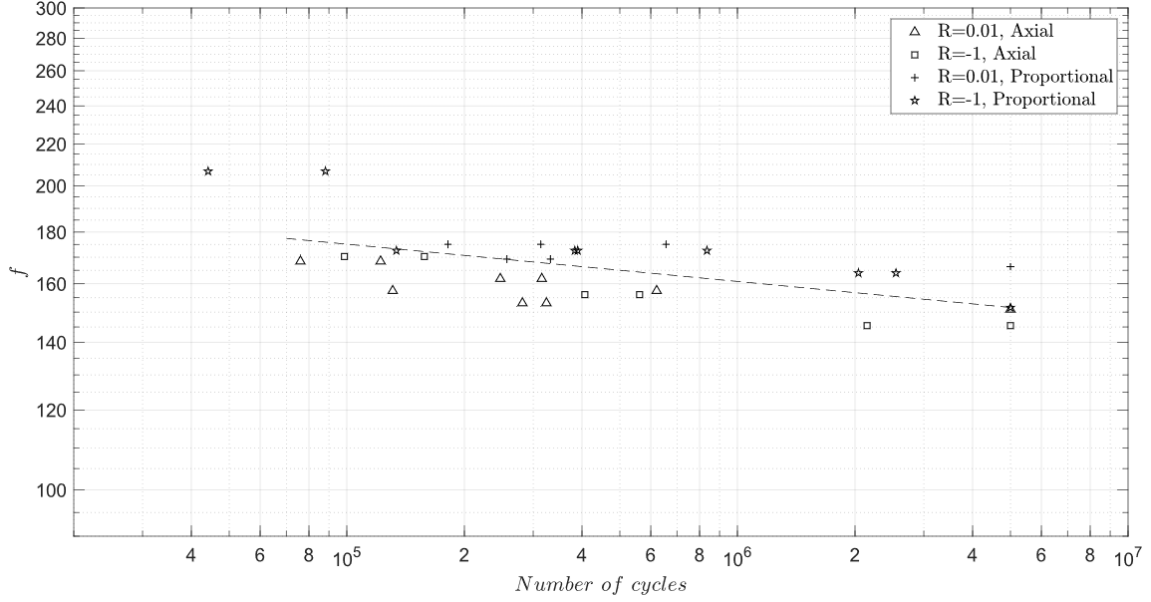


Figure 4.15: Findley damage parameter versus fatigue life graph for axial and axial combined with torsional stresses (for $k_f = 0.228$)

- Bending, torsional and bending combined with torsional stresses:

$$\begin{cases} f = 637.4 N_f^{-0.093} \\ R^2 = 0.340 \end{cases} \quad (4.26)$$

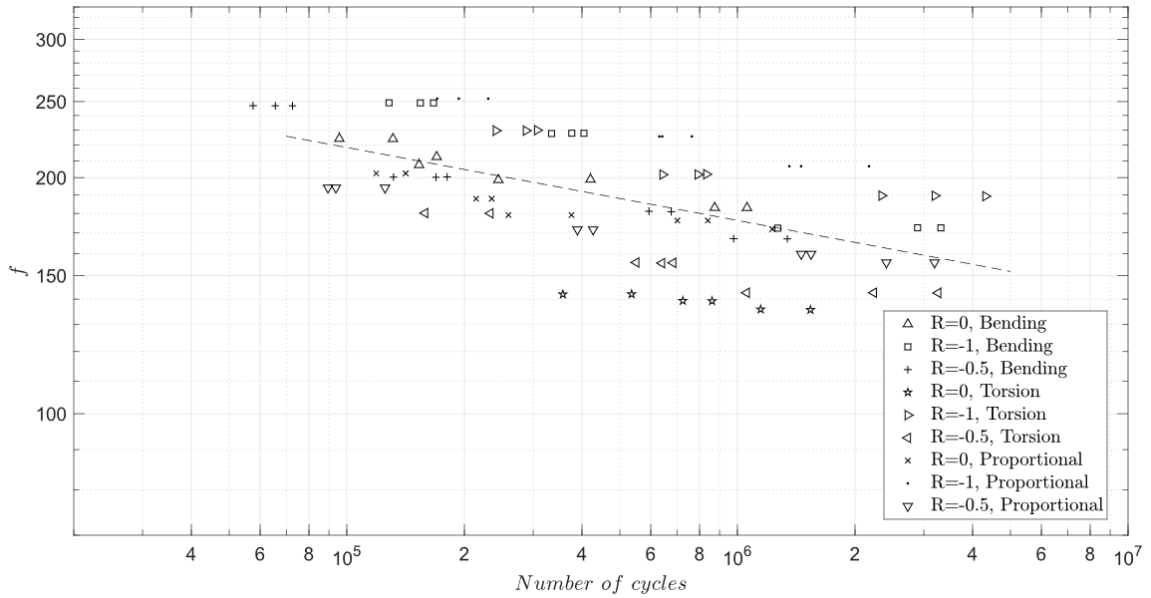


Figure 4.16: Findley damage parameter versus fatigue life graph for torsional, bending and bending combined with torsional stresses (for $k_f = 0.228$)

4. Application and Evaluation of Multiaxial Fatigue Models

- For $k_f = 0.425$:

– Axial and axial combined with torsional stresses:

$$\begin{cases} f = 365.42N_f^{-0.042} \\ R^2 = 0.359 \end{cases} \quad (4.27)$$

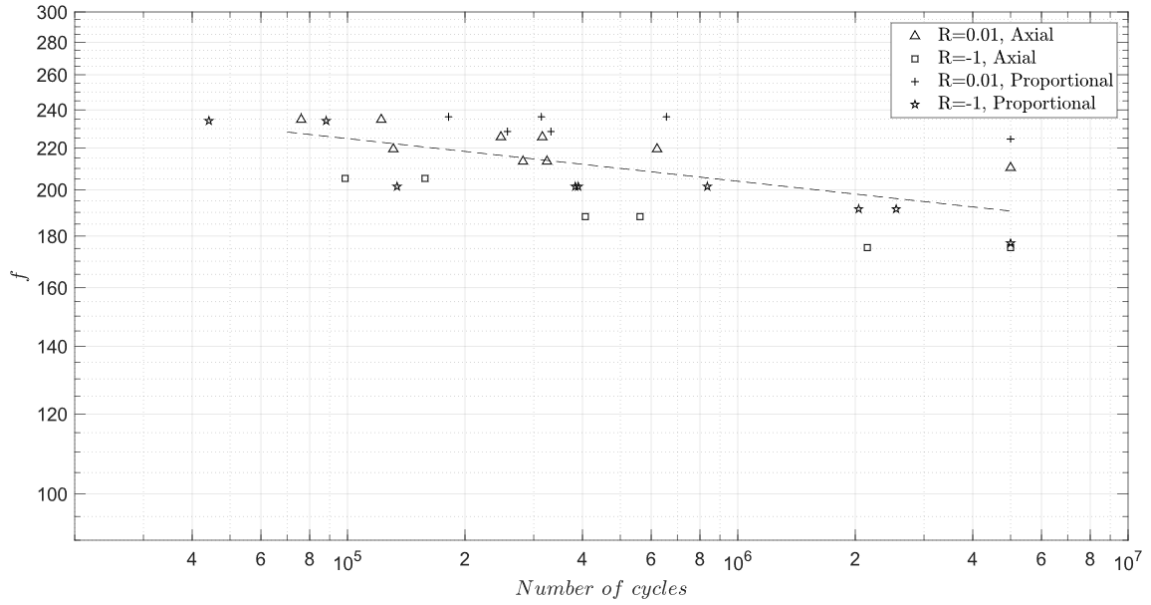


Figure 4.17: Findley damage parameter versus fatigue life graph for axial and axial combined with torsional stresses (for $k_f = 0.425$)

– Bending, torsional and bending combined with torsional stresses:

$$\begin{cases} f = 1137.1N_f^{-0.124} \\ R^2 = 0.385 \end{cases} \quad (4.28)$$

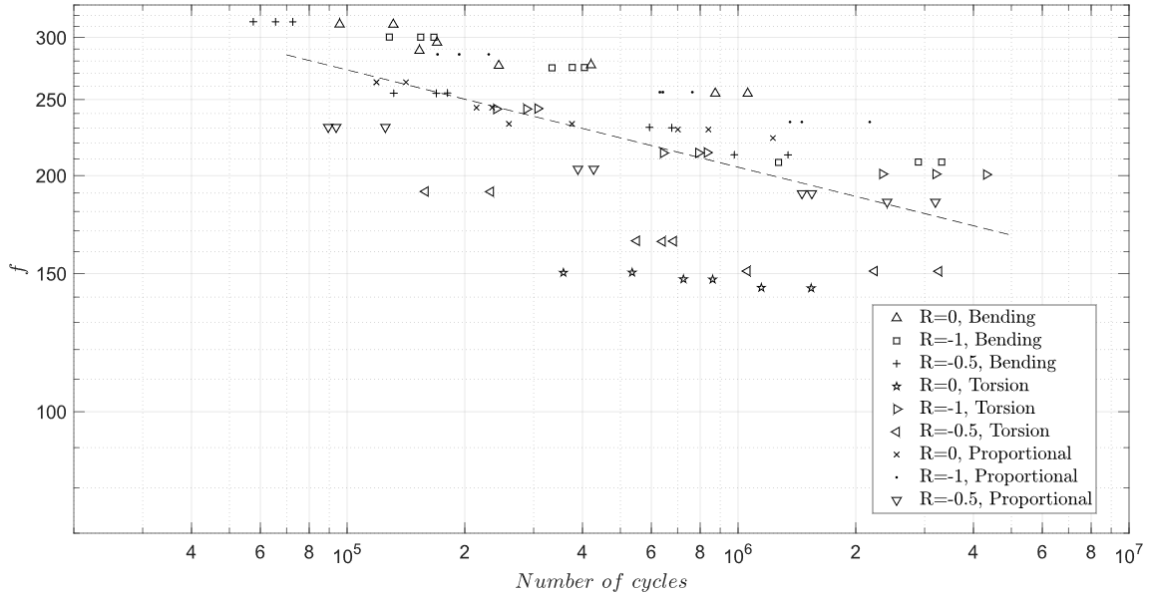


Figure 4.18: Findley damage parameter versus fatigue life graph for torsional, bending and bending combined with torsional stresses (for $k_f = 0.425$)

Hence, as can be seen in curves of Figures 4.13 to 4.18, the value of k_f takes an important rule in the capacity of this model to portrair a fatigue stress state. In the case of $k_f = 0.192$, the coefficient of determenation is very low and the dispersion too high. Fortunately, $k_f = 0.228$ and $k_f = 0.425$ the dispersion looks better, but it remains not so low as would be desired.

Consequently, a different approach was applied with the aim of finding a more suitable value for k_f . This approach defines k_f as a mean value to all fatigue data and tries to include the critical plane angle, since it is known that these variables are related to each other.

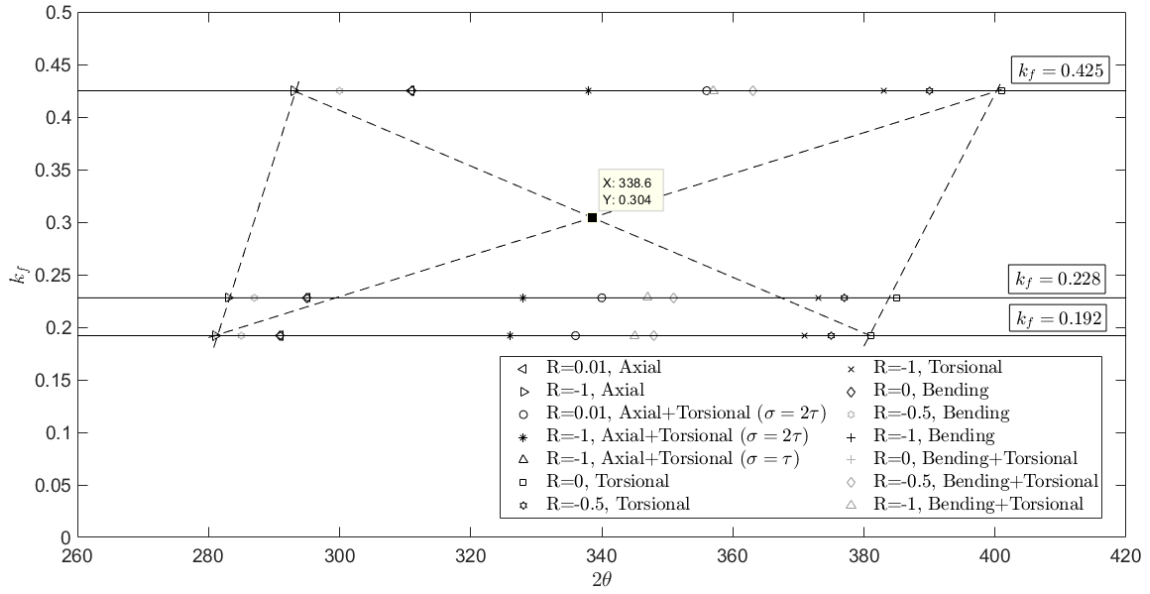
From the calculation of damage parameters for each k_f , it is conclude that the critical plane is constant for the same kind of loading and value of k_f . The critical planes (θ_c) for each loading and k_f are listed in Table 4.2. In order to underline and more easily comprehend the angles variation with k_f , 360° were added to the ones which achieved a full rotation.

Thus, for each k_f and type of loading, it is plotted a point in the k_f versus 2θ graph depicted in Figure 4.19. The points for each kind of loading are aligned and it is possible to define a shape very similar to a parallelogram, within they are all confined. Since the diagonals of a parallelogram intersect each other at the middle point, the value of k_f in this point can be seen as a mean value.

Table 4.2: Critical plane for each loading, stress ratio and k_f

Loading	R	$2\theta_c$ $^\circ$	k_f
-	-	-	-
Axial	0.01	291	0.192
		295	0.228
		311	0.425
Axial	-1	281	0.192
		283	0.228
		293	0.425
Axial+Torsional $\sigma = 2\tau$	0.01	336	0.192
		340	0.228
		356	0.425
Axial+Torsional $\sigma = 2\tau$	-1	326	0.192
		328	0.228
		338	0.425
Axial+Torsional $\sigma = \tau$	-1	345	0.192
		347	0.228
		357	0.425
Torsional	0	381	0.192
		385	0.228
		401	0.425
Torsional	-0.5	375	0.192
		377	0.228
		390	0.425
Torsional	-1	371	0.192
		373	0.228
		383	0.425
Bending	0	291	0.192
		295	0.228
		311	0.425
Bending	-0.5	285	0.192
		287	0.228
		300	0.425
Bending	-1	281	0.192
		283	0.228
		293	0.425
Bending+Torsional	0	355	0.192
		358	0.228
		374	0.425
Bending+Torsional	-0.5	348	0.192
		351	0.228
		363	0.425
Bending+Torsional	-1	345	0.192
		347	0.228
		357	0.425

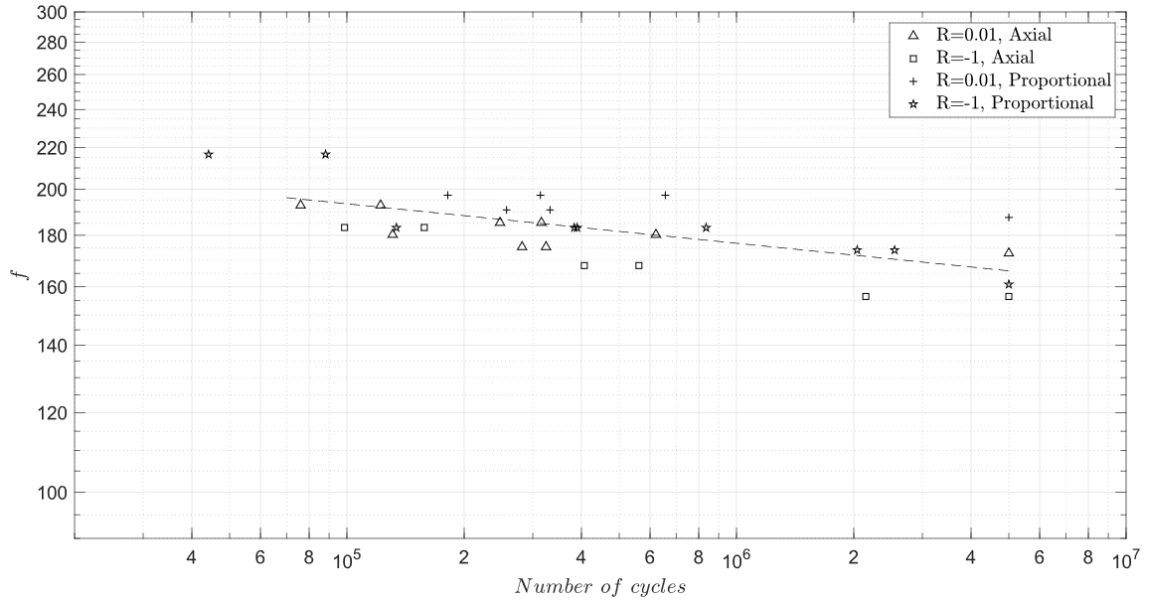
Hence, for S355 steel and accordingly to this new approach, the ideal value of k_f is 0.304.


 Figure 4.19: Representation of a new approach to determine k_f

Subsequently, the damage parameter graphs were replotted for $k_f = 0.304$ and the power regression equations recalculated:

- For axial and axial combined with torsional stresses:

$$\begin{cases} f = 303.78N_f^{-0.039} \\ R^2 = 0.466 \end{cases} \quad (4.29)$$


 Figure 4.20: Findley damage parameter versus fatigue life graph for axial and axial combined with torsional stresses (for $k_f = 0.304$)

- For torsional, bending and bending combined with torsional stresses:

$$\begin{cases} f = 807.66 N_f^{-0.106} \\ R^2 = 0.376 \end{cases} \quad (4.30)$$

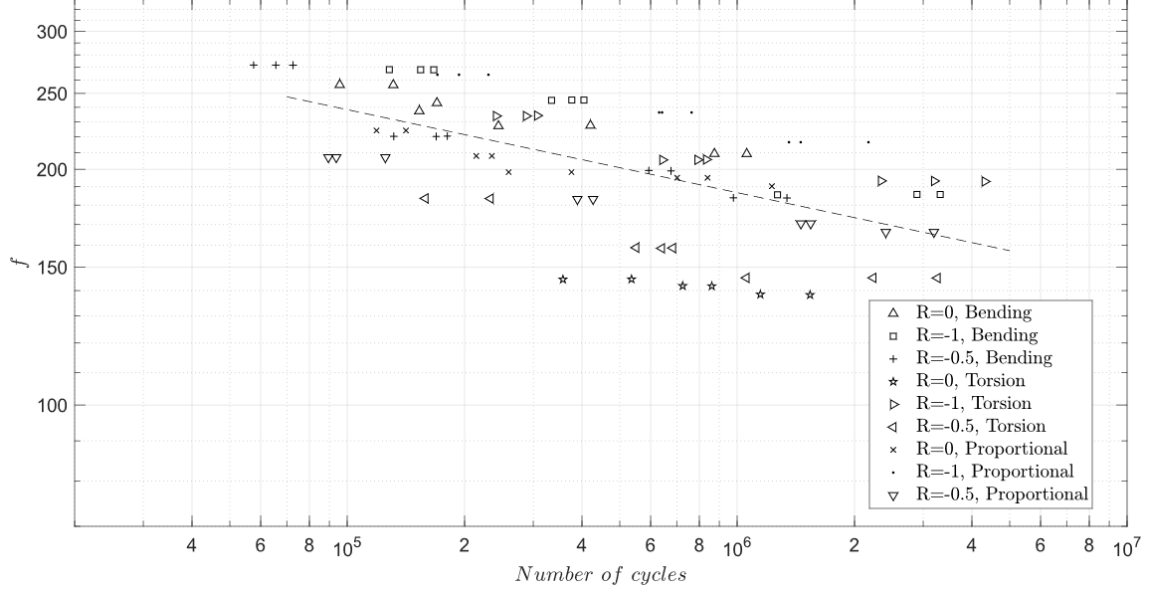


Figure 4.21: Findley damage parameter versus fatigue life graph for torsional, bending and bending combined with torsional stresses (for $k_f = 0.304$)

Overall, this value of k_f provides the lowest dispersion and a quite acceptable capacity to portray and summarize all the fatigue stress states into a design curve.

4.3.3 McDiarmid Model

The model formulated by McDiarmid is also a critical plane approach, but it has an advantage against the model described above: the critical plane is the one where shear stress amplitude achieves the highest value. Because of this, McDiarmid model is easily applied and the damage parameter is obtained from the determination of the left side of the following equation which results from the combination with Basquin law:

$$\tau_{\theta a} + \frac{t_{A,B}}{2\sigma_u} \sigma_{\theta max} = \tau'_f (2N_f)^b \quad (4.31)$$

For the fatigue tests conducted, it is assumed that $t_{A,B}$ is the torsional fatigue limit and, consequently:

$$\frac{t_{A,B}}{2\sigma_u} = \frac{176}{2 \cdot 579} = 0.152 \quad (4.32)$$

Hence, the damage parameter defined by this model for each level and kind of loading was calculated, the experimental points plotted in a graph damage parameter versus number of cycles until failure and, finally, a power regression was applied and the respective equations obtained for:

- Axial and axial combined with torsional stresses:

$$\begin{cases} m = 225.61 N_f^{-0.033} \\ R^2 = 0.173 \end{cases} \quad (4.33)$$

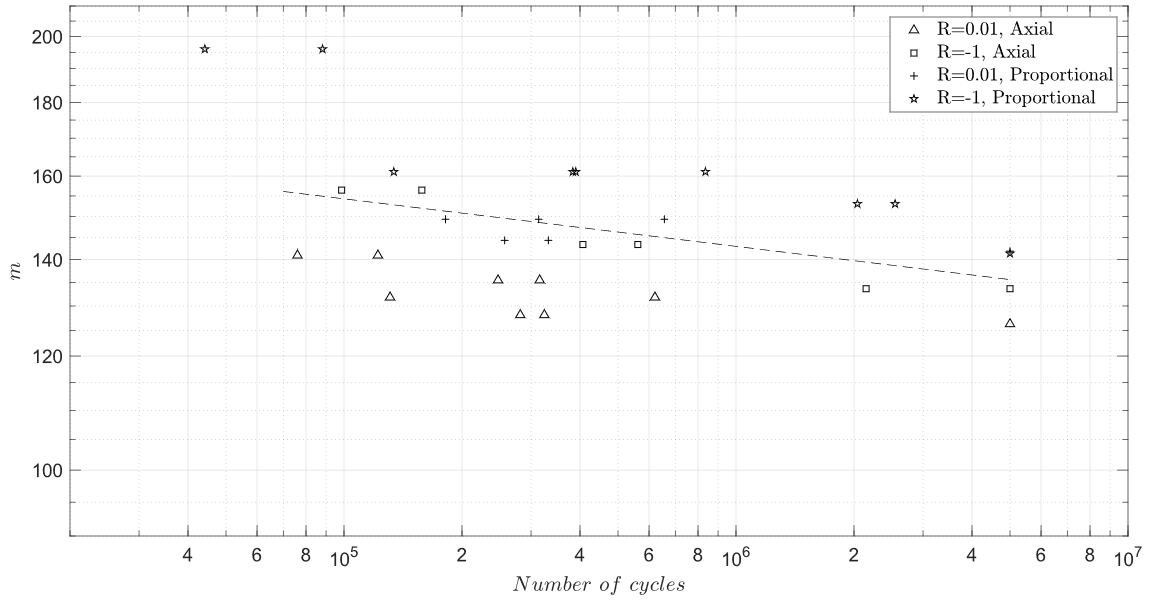


Figure 4.22: McDiarmid damage parameter versus fatigue life graph for axial and axial combined with torsional stresses

- Bending, torsional and bending combined with torsional stresses:

$$\begin{cases} m = 449.38N_f^{-0.073} \\ R^2 = 0.232 \end{cases} \quad (4.34)$$

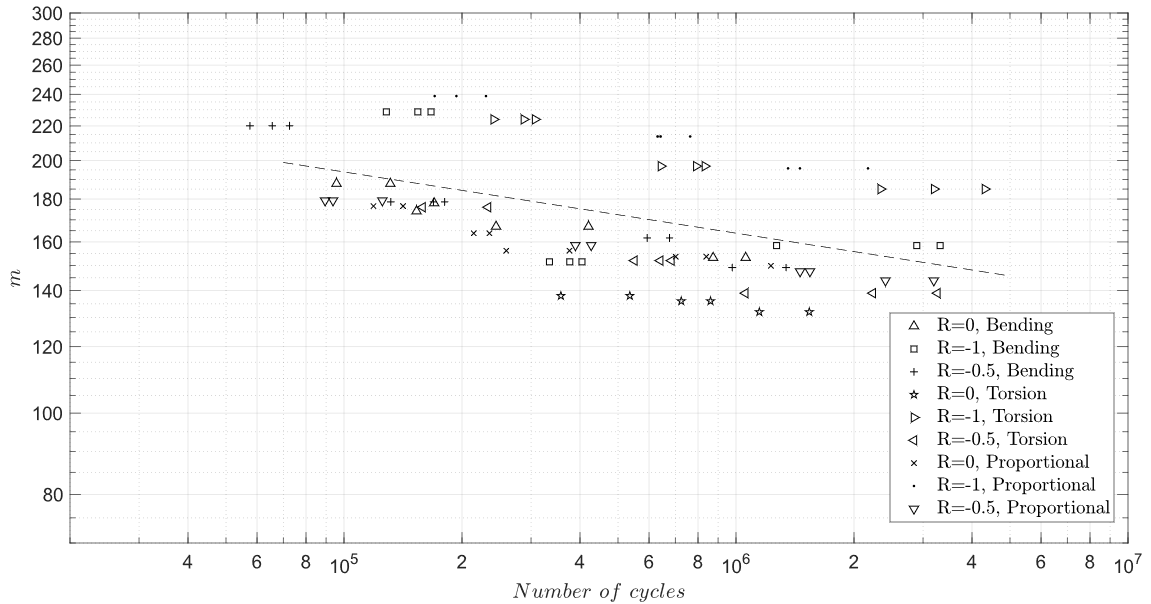


Figure 4.23: McDiarmid damage parameter versus fatigue life graph for bending, torsional and bending combined with torsional stresses

Unfortunately, this model shows a really high dispersion, as can be seen in the graphs of Figures 4.22 and 4.23.

4.3.4 Dang Van Model

Regarding the multiscale model proposed by Dang Van, it was applied the simplified version combined with Basquin law expressed by the following equation:

$$\tau_{a,max} + k_d \sigma_{h,max} = \tau'_f (2N_f)^b \quad (4.35)$$

Once again, this model includes a constant (k_d) which has to be calculated for each material. There are some definitions that were mentioned in the Chapter 2, but none of them is consensual. Thus, different values of this constant were obtained by the application of three distinguish methods.

Firstly, the fatigue limits for axial loading with $R = -1$ and $R = 0$ were plotted in a shear stress amplitude versus maximum hydrostatic normal stress graph and, then, a linear regression was applied. The slope of this line is the value of k_d .

The points represented in the graph bellow can be consulted in Table 4.3.

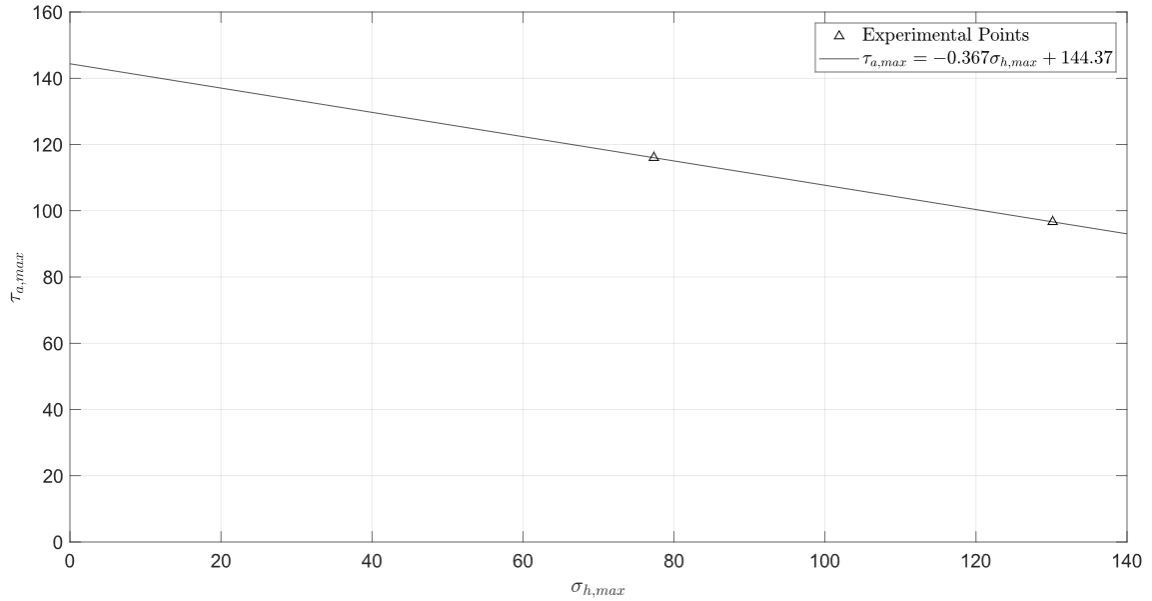


Figure 4.24: Experimental fatigue limit points for axial loading and the respective linear regression plotted in a maximum shear stress amplitude versus maximum hydrostatic normal stress graph

Hence, as can be seen in Figure 4.24, it is estimated that $k_d = 0.367$ and this model is applied using this value for:

- Axial and axial combined with torsional stresses:

$$\begin{cases} d = 253.93 N_f^{-0.035} \\ R^2 = 0.319 \end{cases} \quad (4.36)$$

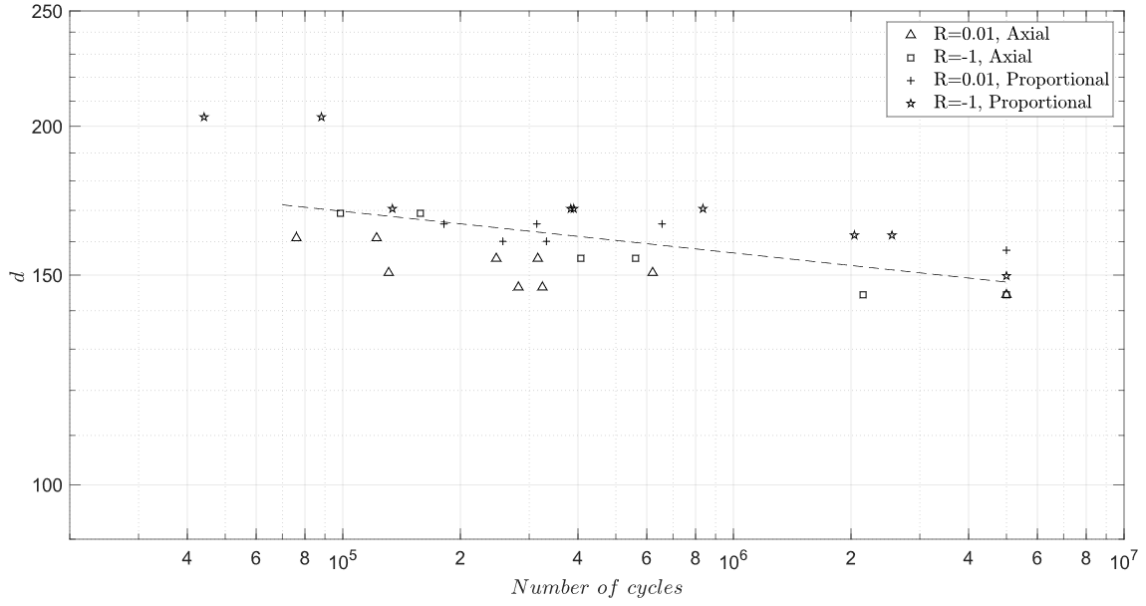


Figure 4.25: Dang Van damage parameter versus fatigue life graph for axial and axial combined with torsional stresses (for $k_d = 0.367$)

- Bending, torsional and bending combined with torsional stresses:

$$\begin{cases} d = 604.54N_f^{-0.091} \\ R^2 = 0.312 \end{cases} \quad (4.37)$$

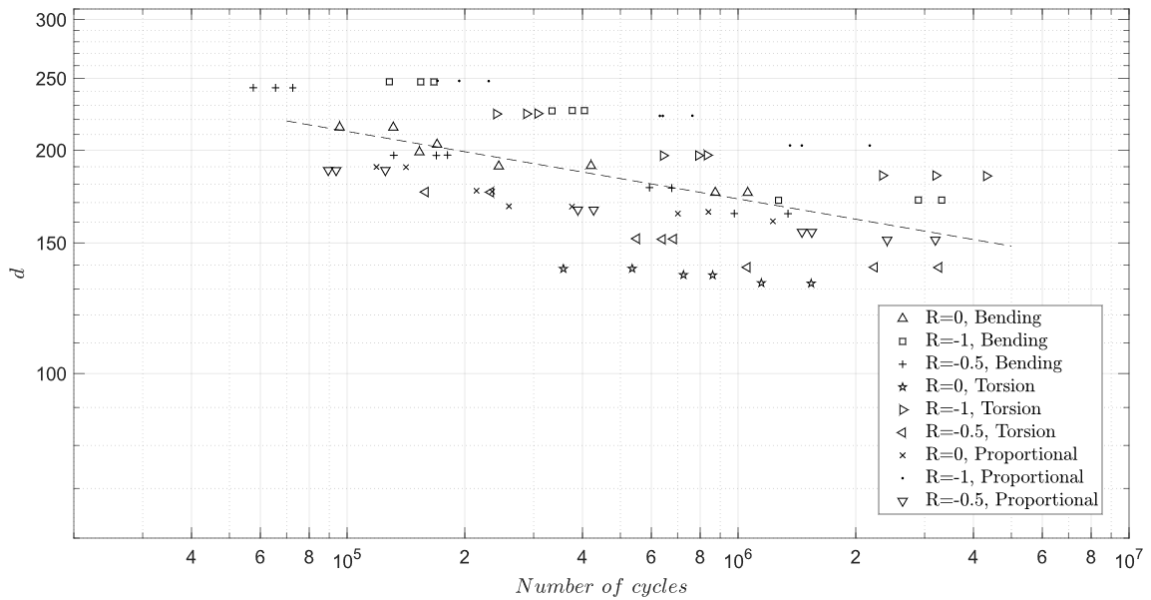


Figure 4.26: Dang Van damage parameter versus fatigue life graph for axial and axial combined with torsional stresses (for $k_d = 0.367$)

Since these graphs show a high dispersion, this method was repeated but with a small change: instead of plotting two experimental points, the fatigue limits for all kinds of loading and stress ratios were plotted. These experimental points are listed in Table 4.3.

4. Application and Evaluation of Multiaxial Fatigue Models

Table 4.3: Experimental fatigue limit points expressed in $\sigma_{h,max}$ and $\tau_{a,max}$ (for $N_f = 5 \cdot 10^6$)

Loading	R	$\sigma_{h,max}$ <i>MPa</i>	$\tau_{a,max}$ <i>MPa</i>
-	-		
Axial	0.01	130	97
Axial	-1	77	116
Axial+Torsional	0.01	111	116.5314094
Axial+Torsional	-1	60	128
Torsional	0	0	125
Torsional	-0.5	0	129
Torsional	-1	0	176
Bending	0	136	102
Bending	-0.5	91	102
Bending	-1	84	127
Bending+Torsional	0	70	118
Bending+Torsional	-0.5	50	126
Bending+Torsional	-1	49	165

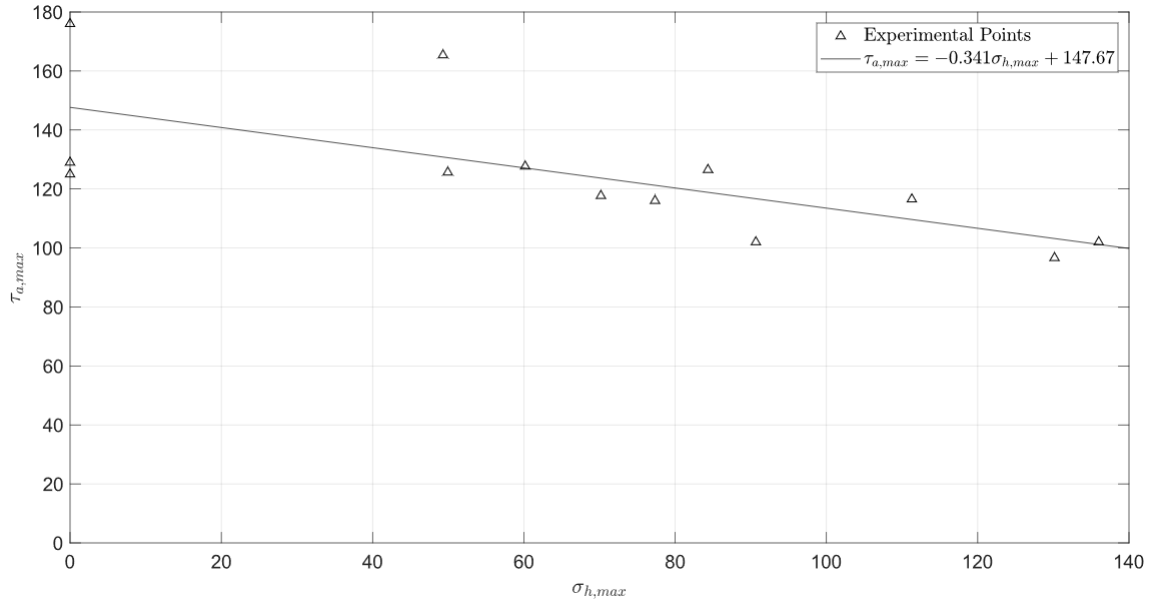


Figure 4.27: Experimental fatigue limit points loading and the respective linear regression plotted in a maximum shear stress amplitude versus maximum hydrostatic normal stress graph

Therefore, according to the linear regression obtained and plotted in the graph of Figure 4.27, the new value of k_d is 0.341, which it is not very different from the previous value. At this point, it can be already presumed that for Dang Van, this methodology is not very efficient, but the graph were replotted again for:

- Axial and axial combined with torsional stresses:

$$\begin{cases} d = 248.69N_f^{-0.035} \\ R^2 = 0.288 \end{cases} \quad (4.38)$$

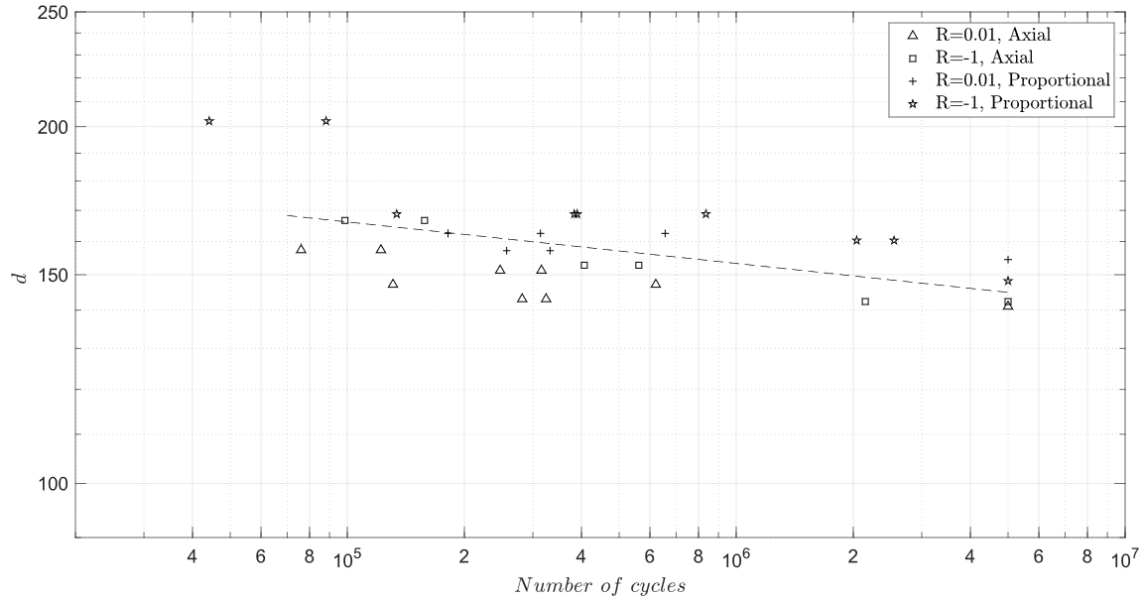


Figure 4.28: Dang Van damage parameter versus fatigue life graph for axial and axial combined with torsional stresses (for $k_d = 0.341$)

- Bending, torsional and bending combined with torsional stresses:

$$\begin{cases} d = 578.33N_f^{-0.088} \\ R^2 = 0.302 \end{cases} \quad (4.39)$$

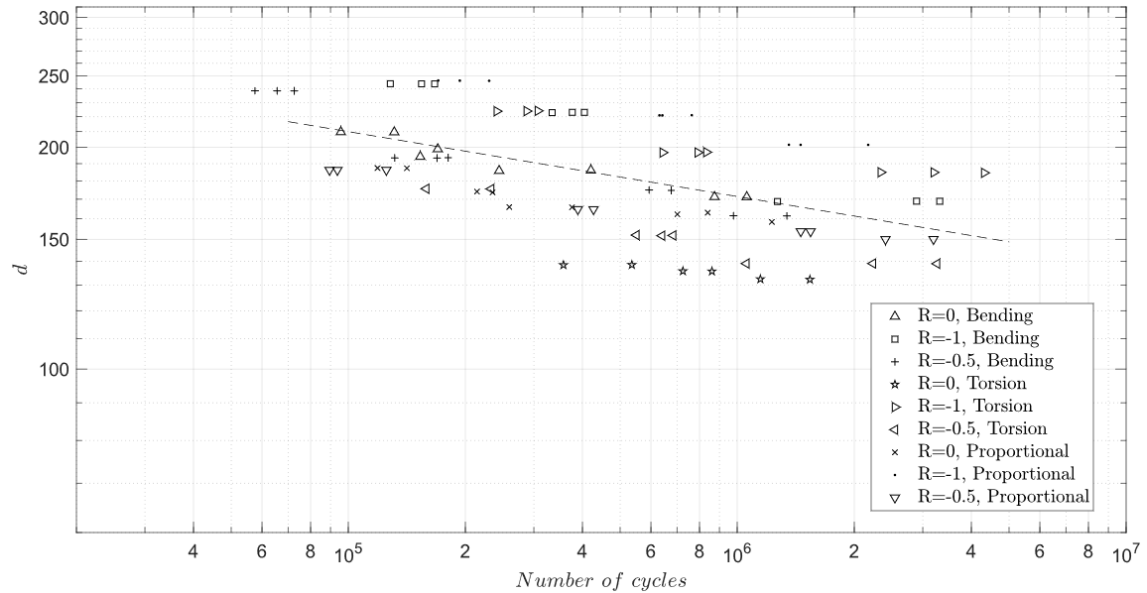


Figure 4.29: Dang Van damage parameter versus fatigue life graph for bending, torsional and bending combined with torsional stresses (for $k_d = 0.341$)

The graphs and equations obtained above confirmed that this approach was not worth, since the dispersion increased.

4. Application and Evaluation of Multiaxial Fatigue Models

Last but not least, it was analysed the value of k_d given by the following equation:

$$k_d = 3 \left(\frac{\tau_{a,R=-1}}{\sigma_{a,R=-1}} - \frac{1}{2} \right) = 3 \left(\frac{176}{253} - \frac{1}{2} \right) = 0.587 \quad (4.40)$$

where $\tau_{a,R=-1}$ is the torsional fatigue limit for $R = -1$ and $\sigma_{a,R=-1}$ is the bending fatigue limit for $R = -1$.

At first sight, the value obtained for k_d seems too high, but surprisingly it shows the lowest dispersion as can be seen in the following graphs and coefficient of determination for:

- Axial and axial combined with torsional stresses:

$$\begin{cases} d = 297.41 N_f^{-0.037} \\ R^2 = 0.570 \end{cases} \quad (4.41)$$

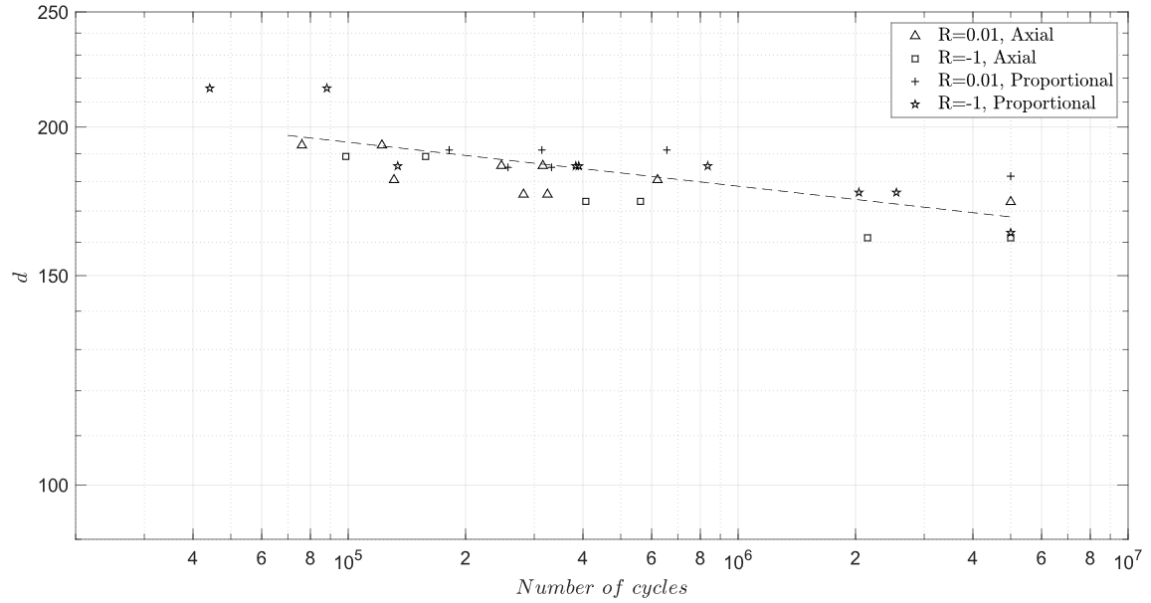


Figure 4.30: Dang Van damage parameter versus fatigue life graph for axial and axial combined with torsional stresses (for $k_d = 0.587$)

- Bending, torsional and bending combined with torsional stresses:

$$\begin{cases} d = 852.95 N_f^{-0.111} \\ R^2 = 0.346 \end{cases} \quad (4.42)$$

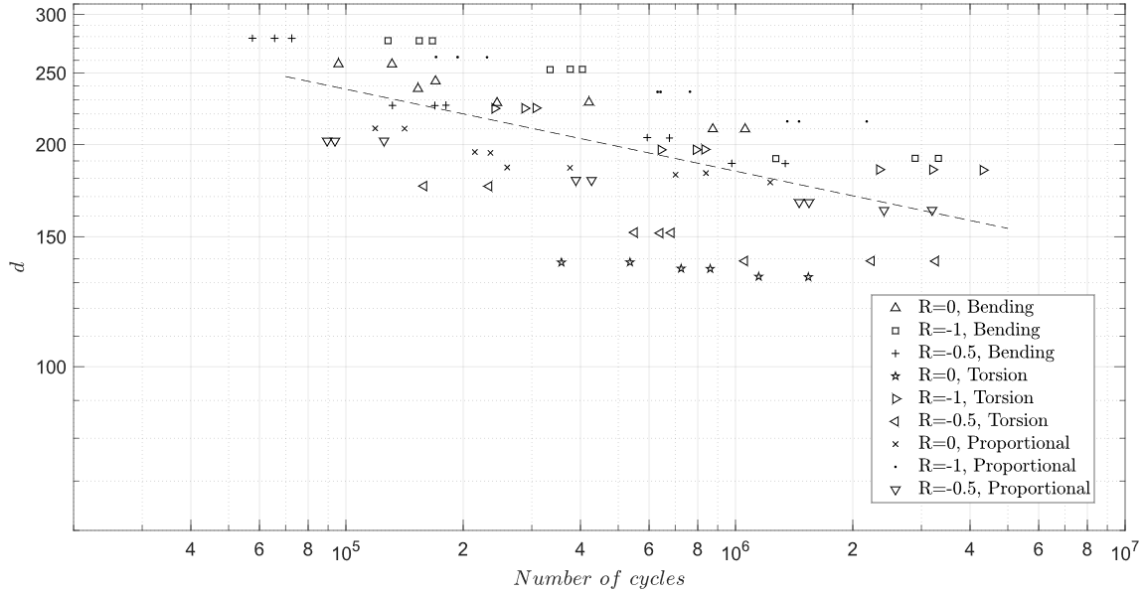


Figure 4.31: Dang Van damage parameter versus fatigue life graph for bending, torsional and bending combined with torsional stresses (for $k_d = 0.587$)

To summarize, for S355 steel, the Dang Van model should be applied with $k_d = 0.587$.

4.4 Conclusions

Throughout this chapter, four different multiaxial fatigue models were evaluated concerning the ability to describe and assess multiaxial fatigue stress states in the high cycle fatigue region. The main idea is to find a model that collapses all experimental data around a curve with lowest dispersion as possible.

The multiaxial models were not only applied to the fatigue data obtained from axial and biaxial tests conducted during this master thesis development, but also to Rozumek and Pawliczek [2004] fatigue data for bending, torsional and biaxial fatigue. The last data mention was added to this study only with the aim to strengthen and validate conclusions which would be formulated.

Thus, at this point, it is possible to take a overlook to the results obtained to each model and make some comments about them. First, it is not risky to say that McDiarmid model shows a really high dispersion and is not suitable to S355 steel. On the other hand, Findley and Sines models demonstrate to be quite reasonable choices to assess and portray the multiaxial fatigue behaviour of S355 steel in high cycle fatigue regime.

Regarding Findley model, it is important to highlight the new methodology elaborated and applied showed to provide the best estimation of k_f .

However, Dang Van model has the best results for this steel: the dispersion of experimental points is low, in particular for axial and axial combined with torsional stress, and the coefficients of determination are high in comparison with another models.

In order to prove the ability of Dang Van model to assess the multiaxial fatigue behaviour of S355 steel, the graphs present in Figures 4.32 and 4.33 were plotted. These graphs compare the theoretical fatigue life that is calculated, through the power regression obtained, with the experimental fatigue life for a certain level of damage.

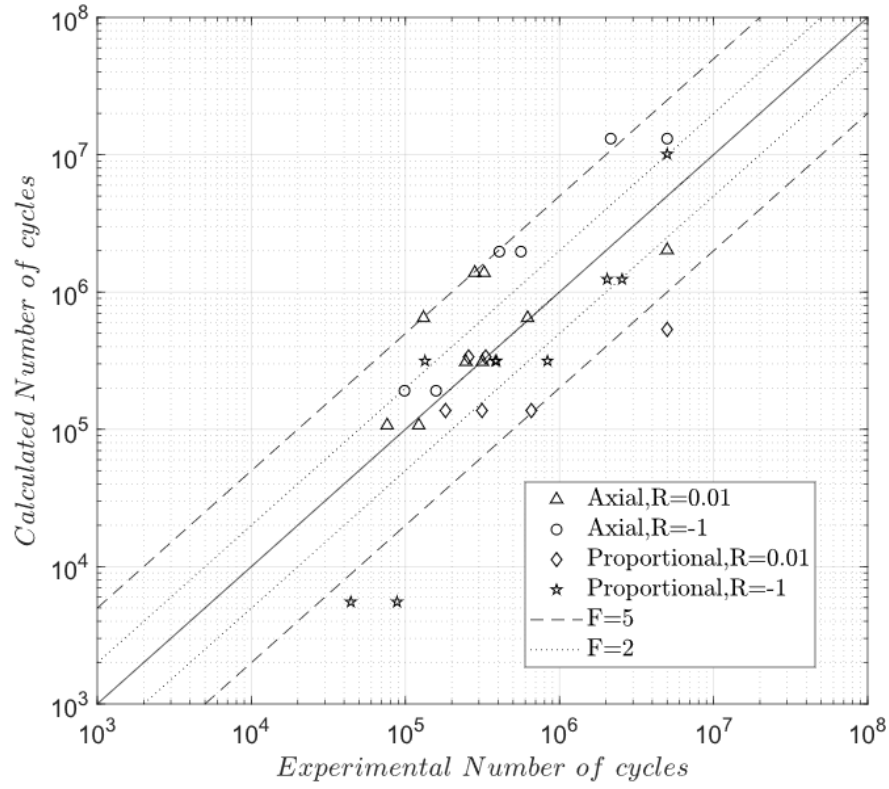


Figure 4.32: Dang Van calculated number of cycles versus experimental number of cycles until failure graph for axial and axial combined with torsional stresses

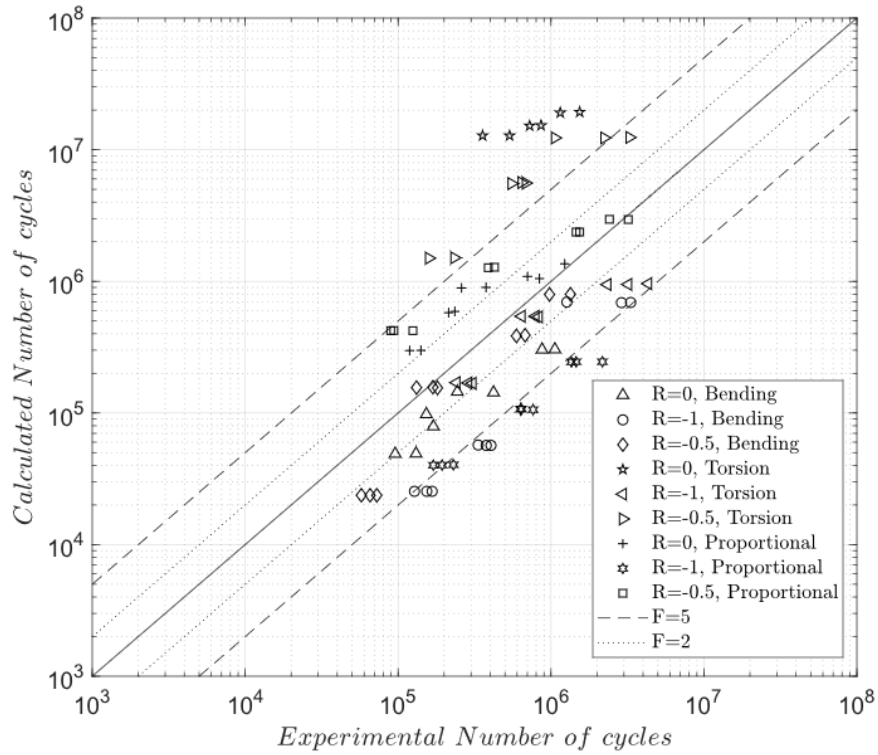


Figure 4.33: Dang Van calculated number of cycles versus experimental number of cycles until failure graph for bending, torsional and bending combined with torsional stresses

The most part of the experimental points, in both of the graphs, are located between lines of multiplicity five and, even a great part of them, are actually between lines of multiplicity two. Nevertheless, the experimental points for pure torsional stresses demonstrate some lack of accuracy since the theoretical values deviate more from the experimental ones. Moreover, the dispersion observed on the damage parameter graphs is not so great as desired, in particular to Rozumek and Pawliczek [2004] fatigue data.

These problems can be related to some experimental factors such as geometry defects, surface roughness or material anisotropies; or maybe a linear relation is not enough to describe multiaxial fatigue behaviour of S355 steel. However, non linear multiaxial models are beyond the scope of this master thesis.

The experimental damage parameters calculated which provide the lowest graphic dispersion, for each model, are listed in Appendix B.

Fatigue Numerical Modelling of a Steel Half-pipes Bolted Connection

5.1 Finite Element Model

In SHOWTIME [2014] several types of gusset plate bolted and welded connections were proposed and studied for hybrid wind turbine towers. Within the scope of this project, Jovasevic et al. [2019] proposed and studied a steel half-pipe bolted connection. Therefore, this chapter aims to perform a fatigue analysis of this connection. Consequently, a numerical model developed by Jovasevic et al. [2019] is analysed and studied.

The joint is formed by a gusset plate and preloaded bolts which connect a horizontal brace to a vertical pylon. The brace and the pylon make a 90° degrees angle between each other (Fig. 5.1a). The cross sections throughout the vertical and horizontal elements are portrayed in Figure 5.1b. In the joint region, the cross section is slightly different, in order to strengthen this critical region.

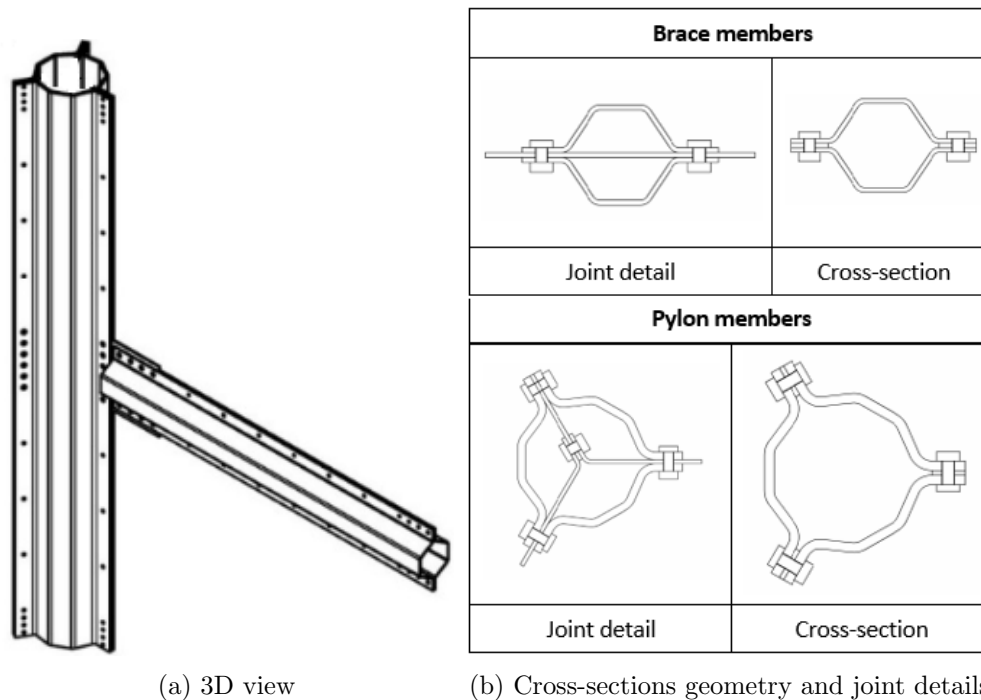


Figure 5.1: Gusset plate bolted connection between a brace and a pylon with a diagonal angle of 90°

5.1.1 Description

The numerical model studied was built in ABAQUS software package [Hibbit, D.K.B. and Karlsson, B.I. and Sorenson, P., 2001] and it can be seen in Figure 5.2.

This model uses and combines two different types of models: C3D8R (solid 8-node brick element with reduced integration) and SC8R (continuum shell 8-node hexahedron). The shell elements are applied at the end regions of members (pylon and brace), while the solid elements are present around the joint region (bolts, gusset plate and some parts of the pylon and brace) (see Figures 5.2 and 5.3). The shell-to-solid elements combination was implemented, according to Jovasevic et al. [2019], using a surface-based technique for coupling this different elements available in ABAQUS software [Hibbit, D.K.B. and Karlsson, B.I. and Sorenson, P., 2001].

Moreover, a mesh refinement was performed around the bolt holes, in order to increase the accuracy of stress values calculated in this region, where the higher stresses are more likely to occur [Jovasevic et al., 2019].

The boundary conditions were defined to portray the real structural interactions, which were verified during the experimental tests described in SHOWTIME [2018], and are applied through three reference points (RP). In sum, the pylon is pinned at the bottom and at the top, while a vertical displacement is applied to the reference point located at the end of the brace (Fig. 5.2)

Besides, three types of interaction [Jovasevic et al., 2019] were implemented:

- Tie constraint: which connects two surfaces, so that there is no relative displacement between them. This interaction was used to connect parts with different element types;
- Rigid body constraint: which simulates the planar behaviour of a cross-section and integrates the global mechanic response of the whole section (end of the members);
- Contact: which accounts for the interaction between surfaces that can not penetrate and are characterized by friction sliding. “Coulomb friction” was used with a friction coefficient equal to 0.4, in order to describe the tangential behaviour, while “Hard contact” is selected to characterize the normal behaviour.

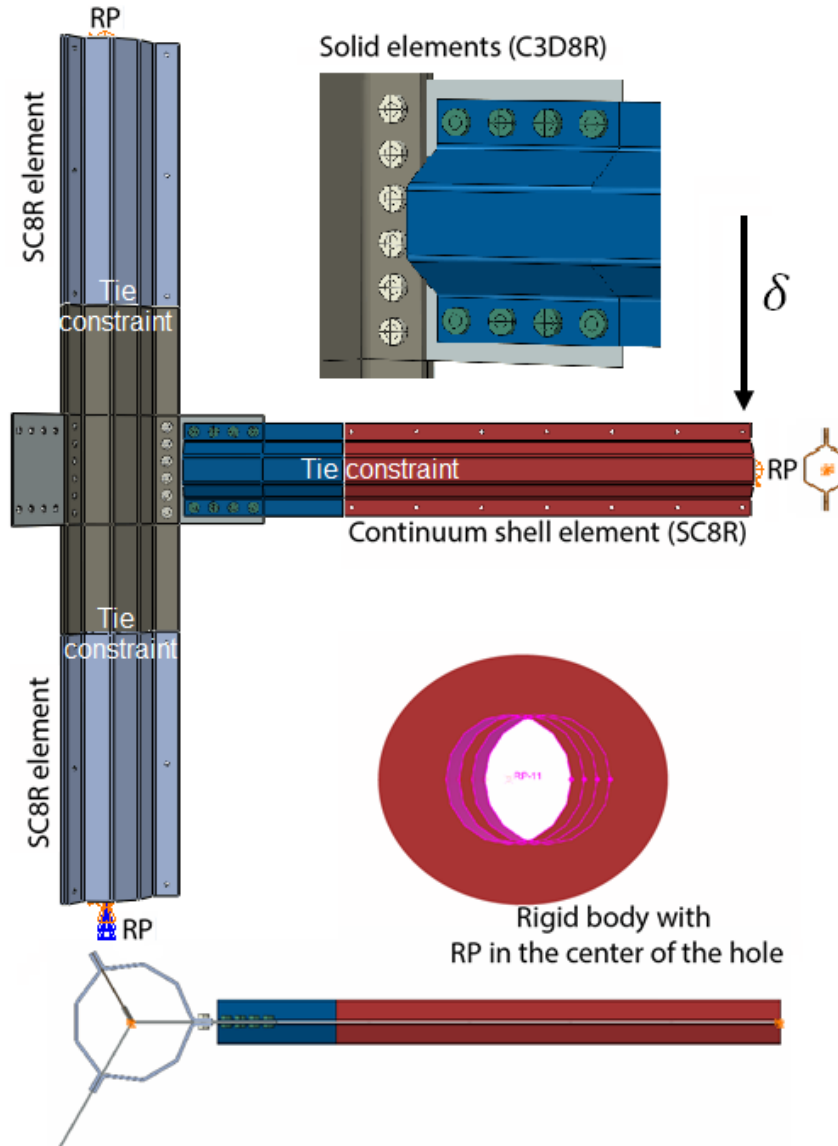


Figure 5.2: Numerical model of the gusset plate bolted connection with a pylon to diagonal angle of 90°

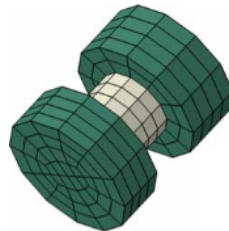


Figure 5.3: Solid bolt model

The key dimensions of the bolted connection are detailed in Table 5.1 and Figure 5.4.

Table 5.1: Key dimensions of B90 connection

	Pylon	Brace
Inner diameter[mm]	296	170
Thickness [mm]	12	5
Length [mm]	3000	2000
Bolt size	M20	M20
Number of bolts	6	4
Gusset plate thickness	6	6

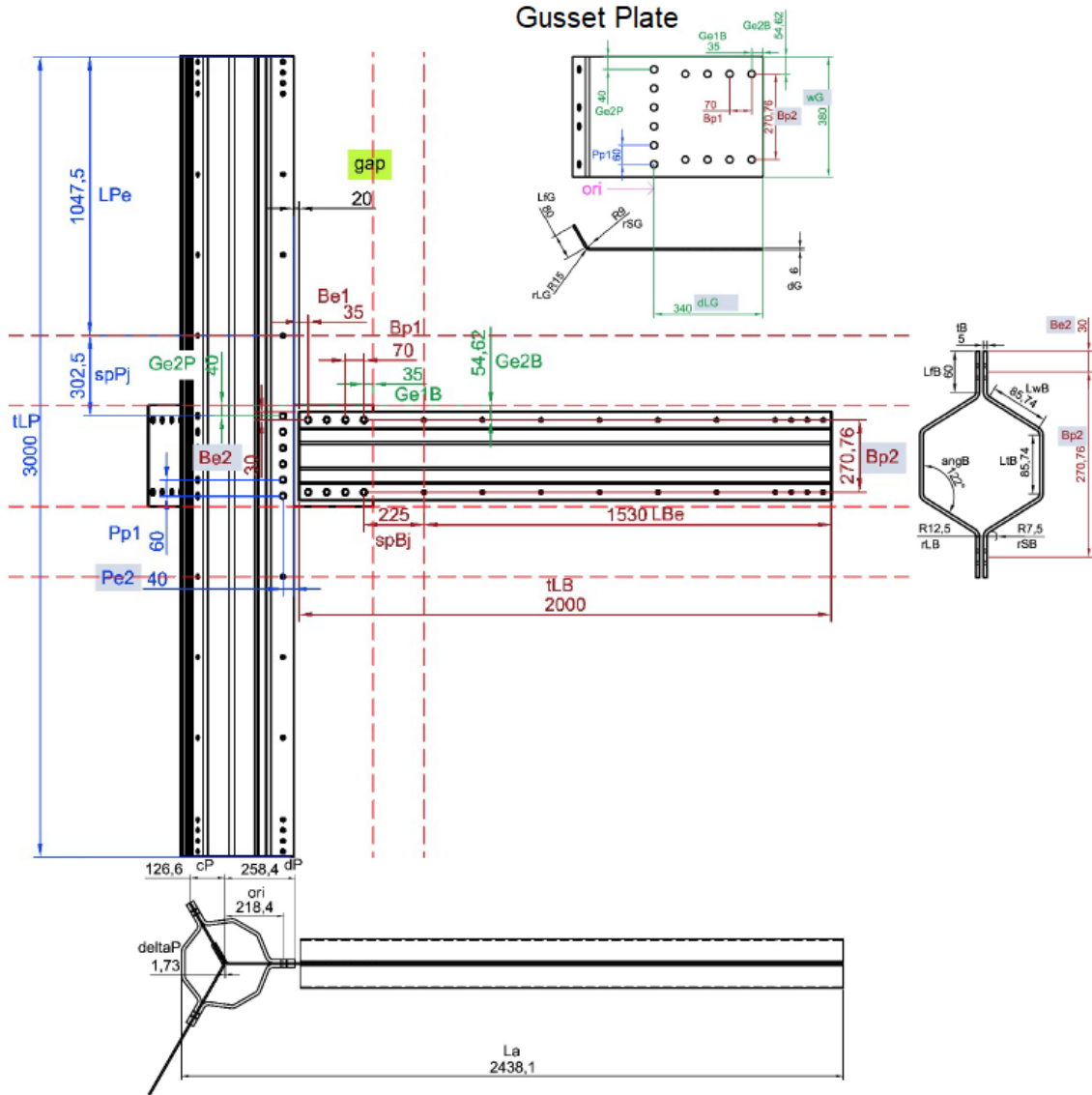


Figure 5.4: Numerical model geometry

An ABAQUS/explicit dynamic analysis is conducted and the loading is applied in two steps:

- First step: a load is applied on the bolts through a thermal shrink of the shanks, over

a period of 50s. In the material properties, shank expansion is defined as orthotropic, with $\alpha_{11} = \alpha_{22} = 0$ and $\alpha_{33} = \alpha = 1 \cdot 10^{-5}$.

- Second step: a monotonic load is applied through an imposed vertical displacement (δ) (as shown in Figure 5.2), over a period of 500s. This displacement is smoothly applied to withdraw the excitation of the model due to inertia forces.

As it was mentioned above, the steps are applied using the “Explicit Dynamic” method, and also including the non-linear effects of large displacements.

The numerical model was calibrated using the experimental tests presented in section 5.2, which were conducted by Jovasevic et al. [2019] and SHOWTIME [2018].

5.1.2 Materials under Consideration

The material of brace, pylon and gusset plate is defined as S355 steel with an elastic modulus of $210GPa$, Poisson ratio of 0.3, yield stress of $355MPa$ and ultimate strength of $510MPa$. On the other hand, all bolts are high strength steel of grade 10.9 with Poisson’s ratio of 0.3 and Young’s modulus of $210GPa$.

A true stress-strain material model, which is defined by the following equations, was used:

$$\varepsilon_{true} = \ln(1 + \varepsilon_{nom}) \quad (5.1)$$

$$\sigma_{true} = \sigma_{nom}(1 + \varepsilon_{nom}) \quad (5.2)$$

where ε_{true} is true strain, σ_{true} is true stress, ε_{nom} is engineering strain and σ_{nom} is engineering stress

5.2 Monotonic Characterization

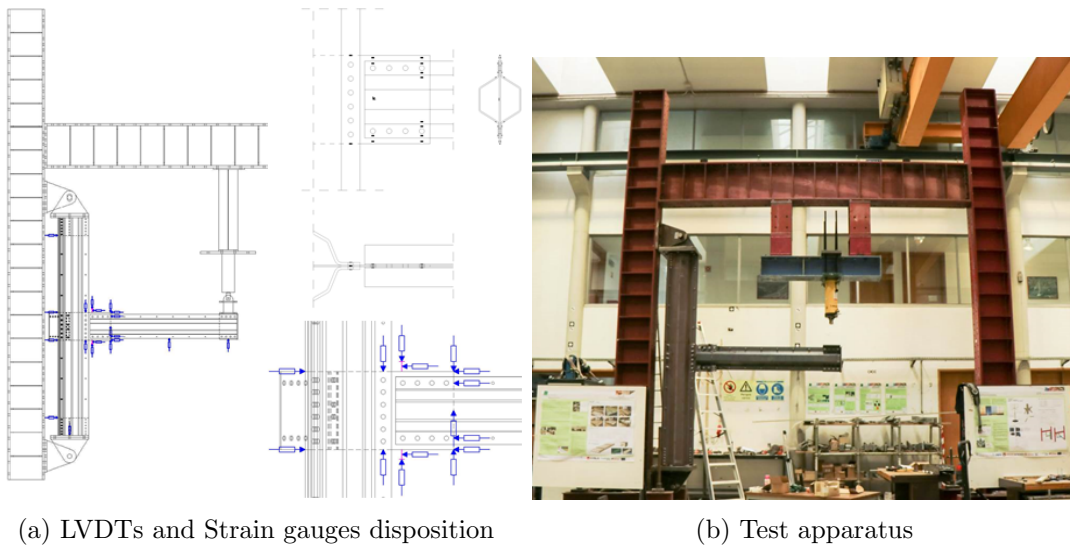
In this section, a monotonic characterization of the bolted connection is presented and collected from the Jovasevic et al. [2019] and SHOWTIME [2018]. This characterization was validated through experimental tests, as well as, numerically analysed and evaluated by Jovasevic et al. [2019].

The experimental specimen was built with the aim of reproducing the geometry of numerical model described above. The pylon is formed by three cold-formed segments of 3m length, which gaps every 120° . The brace is 2 m long and composed of 2 segments, which provides openings every 180° (see Figure 5.5). The joint is located in the middle of the pylon. The bolts used in the connection are M20 grade 10.9, while along the pylon and brace, for connection of segments, are used bolts M12.

The loading is applied monotonically, in the vertical direction, at the end of brace. The experiments are conducted in displacement control and with a constant speed of $0.02mm/s$. The maximal displacement applied is $200mm$. In order to extract the relevant experimental information, the specimens were instrumented according to the scheme shown in Figure 5.6. The displacements were measured through displacement transducers, while strain gauges were used to measure surface deformation.



Figure 5.5: Assembly and preparation of specimen

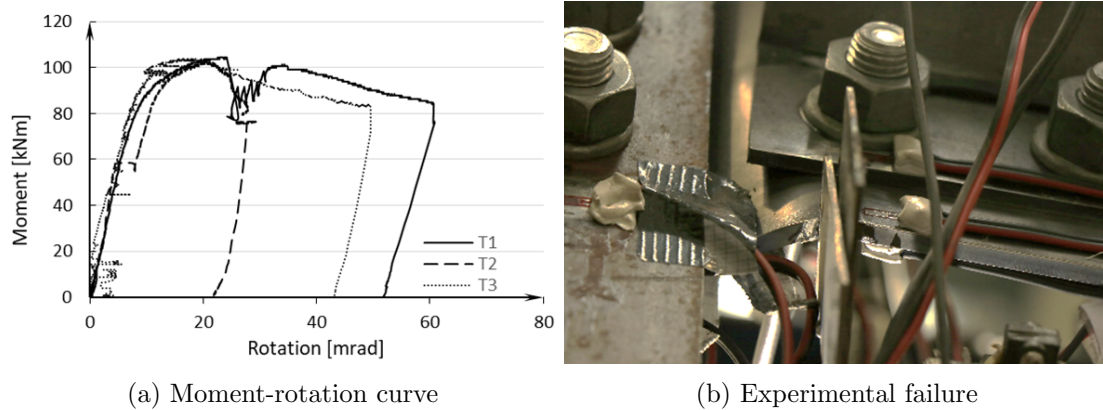


(a) LVDTs and Strain gauges disposition

(b) Test apparatus

Figure 5.6: Test description

The connection behaviour is represented by a moment-rotation curve (as exhibited in Figure 5.7a). The bending moment acting on the connection is result of the applied load (at the end of the brace) multiplied by the distance between the pylon axis and the loading application point. The joint failure is showed in Figure 5.7b.



(a) Moment-rotation curve

(b) Experimental failure

Figure 5.7: Experimental results

The experimental tests demonstrated a global and local behaviour in line with the numerical predictions. The same failure mode was observed in the experiments and numerical analysis: the buckling of gusset plate in the compression zone, and the gusset plate net section failure in tension zone.

The behaviour of joints can be described using either load-displacement or moment-rotation curves, as illustrated in Figure 5.7a. Therefore, there are three critical characteristics for checking the resistance of the joints: stiffness, plastic resistance and ultimate resistance. In order to systematically calculate the resistance values from the experimental and numerical results, a bi-linear curve fitting is used to determine the stiffness and plastic resistance according to EN1993-1-8 standard [European Committee for Standardization, 2010a]. The fitting procedure produces three sets of characteristic values:

- Initial stiffness (S_j);
- Plastic resistance and deformation (R_p and U_p);
- Ultimate resistance and deformation (R_m and U_m).

Moreover, stress-strain curves based on coupon tests were also obtained, as part of the experimental programme, and were used in the finite element model for validation and calibration purpose. Nominal values of yield and ultimate strength according to EN1991-1-15 standard [European Committee for Standardization, 2008] were used in subsequent parametric studies.

The load-displacement curves predicted by finite model are compared with test data in Figure 5.8, while the response characteristic values are compared in Table 5.2.

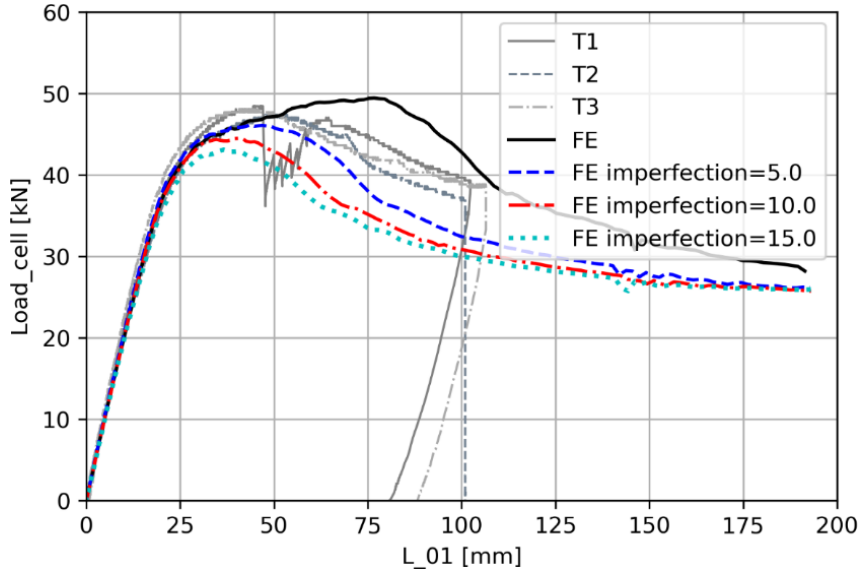


Figure 5.8: Comparison between the finite element model values with the experimental results [Jovasevic et al., 2019] [SHOWTIME, 2018]

The first numerical attempt was made without considering imperfections. Although the initial stiffness, obtained through the FE model, being similar to the experimental one, the plastic resistance and, particularly, the ultimate resistance are higher than the experimental values.

Therefore, three levels of imperfection (measured at the end of the brace) were used: 5mm, 10mm and 15mm. The inclusion of imperfection clearly improved the accuracy of

numerical model, as shown in Figure 5.8. Hence, it is conclude that an imperfection of $5mm$ ($5/3000$, considering the brace length is $3m$) gives an accurate joint stiffness and resistances.

Table 5.2: Comparison of response characteristics between numerical models and experimental results

	Numerical model				Experimental Tests		
	Without Imperf.	Imperf.5	Imperf.10	Imperf.15	T1	T2	T3
S_j [kN/mm]	2.2	2.0	1.9	1.9	1.8	1.7	2.1
R_p [kN]	42.2	39.7	38.4	35.5	40.4	40.1	40.2
U_p [mm]	19.3	19.9	19.7	18.6	21.0	21.7	19.0
R_m [kN]	69.6	46.2	44.5	43.1	48.5	47.4	48.1
U_m [mm]	87.7	43.7	40.6	36.6	44.5	47.7	40.7

5.3 Fatigue Modelling Based on Local Stress approaches for High Cycles Regimes

Numerous studies have been developed in order to comprehend the cyclic behaviour of structural members and to formulate reliable fatigue-resistant designs. Fatigue problems are complex in nature and not easily understandable or feasible to be precisely modelled, since a multitude of factors, which are not always independent, control the structural response to cyclic loading [Correia, 2014].

The fatigue curves, plotted as straight lines (when stress range or stress amplitude, and fatigue life are expressed in a logarithmic scale) are traditionally used to describe the cyclic response of a given structural detail and material, as it is explained in section 2 and is illustrated in Figure 2.10 [Correia, 2014].

5.3.1 Uniaxial Fatigue Stress Analysis

Fatigue design philosophy has evolved from fatigue limit and infinite life criteria to approaches based on finite life behaviour [Basquin, 1910] [Correia, 2014]. The local approaches use fatigue damage parameters to evaluate fatigue test results, especially for crack initiation life.

As mentioned before, for the fatigue life prediction in high-cycle regimes (HCF), the relation between stress amplitude, σ_a , and the number of cycles to failure, N_f , can be expressed by Basquin law.

Leite et al. [2018] suggested a methodology to perform the fatigue analysis based on Basquin law for a structural connection of a metallic bridge, using global-local numerical modelling. According to their scientific work, the steps were the following ones:

1. Global analysis of the structure:
 - (a) Global modelling;
 - (b) Loads application on the structure;
 - (c) Selection of the critical component and node of the bridge structure;
2. Local node analysis:
 - (a) Simplified continuous local model;

- (b) Detailed/advanced local models;
- (c) Analysis of the advanced local models;
- 3. Fatigue damage analysis in order to predict the crack initiation based on the Basquin fatigue curve for the metallic material;
- 4. Evaluation of the fatigue damage accumulation for the critical detail.

5.3.2 Multiaxial Fatigue Stress Analysis

The Findley multiaxial fatigue model is best known for being the older plane model and leads to satisfactory results. Takahashi [2014] proposed a multiaxial fatigue methodology based on the finite element method and using the Findley criterion for structural components under variable amplitude loading, which can be summarized in the following steps:

1. Choose an exterior node for analysis, n_i . For each node, n_i , perform the following steps:
 - (a) Considerate the notch effect by calculating the 6 stress tensor components ($\sigma_x, \sigma_y, \sigma_z, \tau_{xy}, \tau_{yz}, \tau_{xz}$) for each step time, through the following equations:

$$\sigma_x = \frac{\sigma_x^e}{n_K} \quad (5.3)$$

$$\sigma_y = \frac{\sigma_y^e}{n_K} \quad (5.4)$$

$$\sigma_z = \frac{\sigma_z^e}{n_K} \quad (5.5)$$

$$\tau_{xy} = \frac{\tau_{xy}^e}{n_K} \quad (5.6)$$

$$\tau_{yz} = \frac{\tau_{yz}^e}{n_K} \quad (5.7)$$

$$\tau_{xz} = \frac{\tau_{xz}^e}{n_K} \quad (5.8)$$

- (b) Run a multiaxial rainflow method and obtain the results in n_i node;
- (c) Choose a shear plan for analysis, titled Plan $\Delta_q(\theta_q, \phi_q)$. For each Plan $\Delta_q(\theta_q, \phi_q)$, perform the following steps (for each row j of the Rainflow Table):
 - i. Calculate the 6 stress tensor components ($\sigma'_x, \sigma'_y, \sigma'_z, \tau'_{xy}, \tau'_{yz}, \tau'_{xz}$) for each step time;
 - ii. Calculate Findley damage parameter(f);
 - iii. Estimate the number of cycles to failure N_f by comparing the value of Findley parameter obtained with the material fatigue curve;
 - iv. Calcule the damage, D_j .
- (d) Assess all rows in the Rainflow Table for the analysed shear plane $\Delta_q(\theta_q, \phi_q)$, in order to determine the total damage for this plane $D_{i,q}$.

2. Evaluate and compare the damage D_i of each node n_i of the finite element model. The node with the highest damage value is named critical point.

Other multiaxial fatigue model can be used in the sub-step c. proposed by Takahashi [2014] with the aim of evaluating the fatigue damage accumulation of critical points at the structural components.

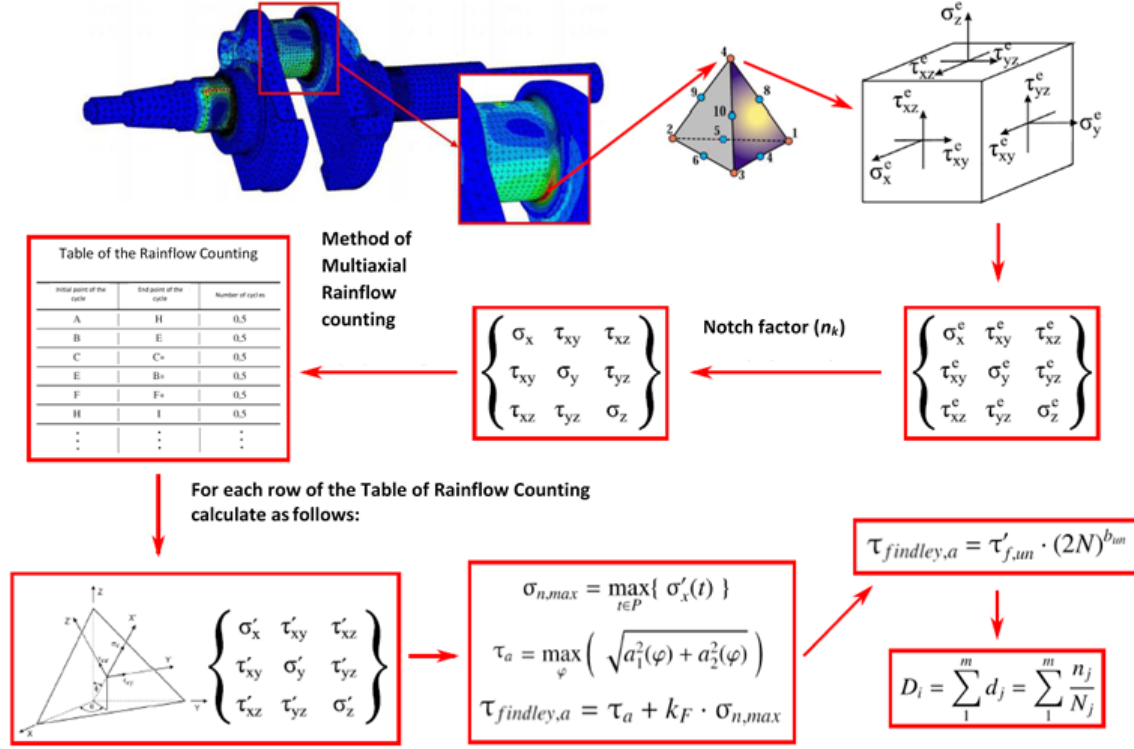


Figure 5.9: Multiaxial fatigue stress assessment based on Findley criterion and finite element method proposed by Takahashi [2014]

5.3.3 Proposed Approaches for Fatigue Life Prediction of Structural Components

In this study, a fatigue life prediction, based on two types of analysis: uniaxial and multi-axial, is presented, with the aim of performing a estimation of fatigue curve for the gusset plate bolted connection.

The first analysis is conducted using the experimental uniaxial fatigue data of S355J2 steel and applying the formulation proposed by Basquin [1910]. For that reason, the values of maximum stresses, present on the connection numerical model described in section 5.1.1, are required. Thus, for each loading condition imposed to the connection and respective nominal stress range, the number of cycles until failure are determined through the local uniaxial stress criteria. This methodology based on Basquin law can be divided into the following steps:

1. Experimental fatigue tests of S355J2 steel under uniaxial tensile loading;
2. Evaluation of the mean fatigue curve based on Basquin formulation for the metallic material through the experimental fatigue results of step 1.;
3. Numerical modelling of the gusset plate bolted connection;

4. Application of loads through the actuator displacements (see Fig. 5.2) for values around the yield region;
5. Identification of the critical point and maximum principal stress value in that point;
6. Identification of the critical cross-section;
7. Estimation of the number of cycles until failure, N_f , using the maximum stress computed in the numerical simulation and based on Basquin fatigue curve determined in step 2;
8. Determination of nominal stress range level, $\Delta\sigma$, in the critical cross-section for each actuator displacement applied to the brace (see Figure 5.2);
9. Establishment of the relation between nominal stress range level, $\Delta\sigma$, calculated in step 8., and number of cycles until failure, N_f , estimated in step 7.. Finally, an estimation of numerical fatigue curve for the connection under consideration is proposed.

The second analysis applied is based on the experimental multiaxial fatigue data available for S355J2 steel and using a multiaxial fatigue model for the high-cycle fatigue regime [Öztürk et al., 2016], [You and Lee, 1996]. The fatigue life prediction of the connection under consideration is also supported by a finite element modelling, in order to compute the stress tensor in critical point and, then, evaluate a selected damage model. In this way, the number of cycles is estimated based on a multiaxial fatigue damage model previously selected (see section 4) . Furthermore, each nominal stress range level can be correlated with the respective number of cycles until failure. This methodology for fatigue life prediction of a multiaxial stress state can be divided into the following steps:

1. Experimental fatigue tests for S355J2 steel under multiaxial loading;
2. Evaluation of the mean fatigue curve based on a multiaxial fatigue damage model (e.g. Findley, Sines, McDiarmid, Dang Van, etc.) for the material and through the experimental fatigue results obtained in step 1;
3. Numerical modelling of the gusset plate bolted connection;
4. Application of loads around the yield region and through the actuator imposed displacements (see Fig. 5.2),
5. Identification of the critical point and 6 stress tensor components ($\sigma_x, \sigma_y, \sigma_z, \tau_{xy}, \tau_{yz}, \tau_{xz}$) for each imposed displacement;
6. Identification of the critical cross-section;
7. Estimation of the number of cycles until failure, N_f , using a multiaxial fatigue damage model selected and estimated in step 2., and based on stress tensor components obtained in step 5.;
8. Determination of the nominal stress range level, $\Delta\sigma$, in the critical cross-section, for each actuator displacement applied to the brace of the connection under consideration (see Fig. 5.2);
9. Establishment of the relation between nominal stress range level, $\Delta\sigma$, step 8., an the number of cycles until failure, N_f , estimated in step 7.. Finally, an estimation of the numerical fatigue curve for the connection under consideration is proposed.

5.4 Linear Elastic Stress Analysis

In order to evaluate the fatigue life prediction of the gusset plate bolted connection (see Figure 5.1), a numerical modelling based on linear-elastic stress analysis was conducted. The finite element model presented in sections 5.1 and 5.2 was used to perform this study. The analysis type is ABAQUS/explicit dynamic and the loading is applied in two steps, as it is described in section 5.2.

During this analysis, eight different displacements were applied to the brace extremity, in order to compute the stress tensor components at the critical point of both gusset plate and brace. In Tables 5.3 and 5.4, the cross-section stress levels for each displacement and the geometric properties are listed for the gusset and brace, respectively.

In Figure 5.10, the von Mises stresses (σ_{VM}) on the connection for an displacement of 20mm ($F = 32356N$) are depicted, while in figure 5.11 are portrayed the principal stresses for the same displacement.

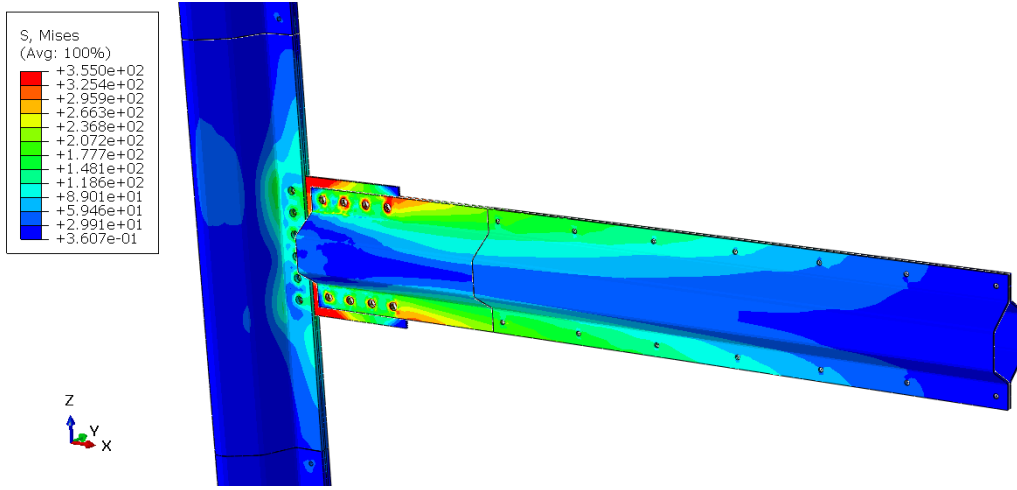


Figure 5.10: Overview of von Mises stress for a displacement of 20mm

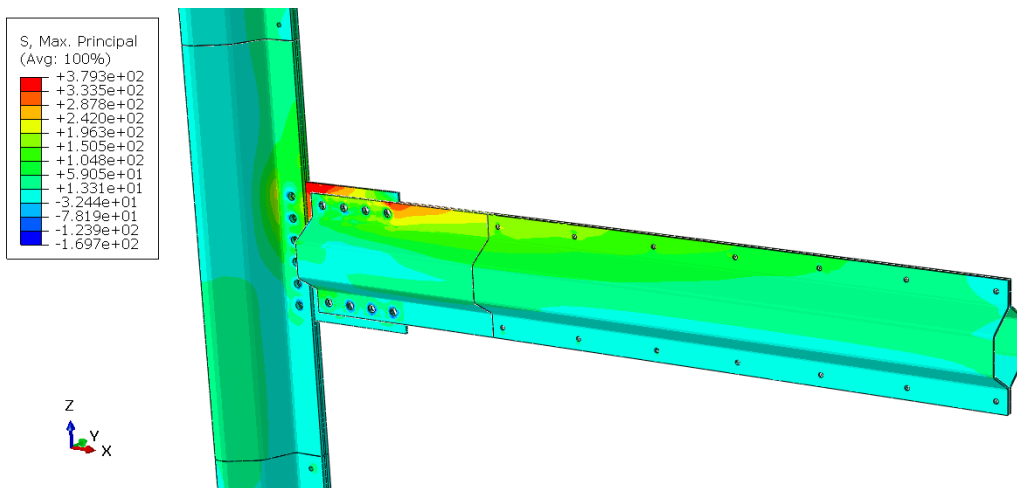


Figure 5.11: Overview of maximum principal stress for a displacement of 20mm

The stress tensor components ($\sigma_{11}, \sigma_{22}, \sigma_{33}, \tau_{12}, \tau_{13}, \tau_{23}$) on gusset plate and brace member for an displacement of 20mm ($F = 32356N$) are illustrated in more detail from figure

5.12 to 5.23.

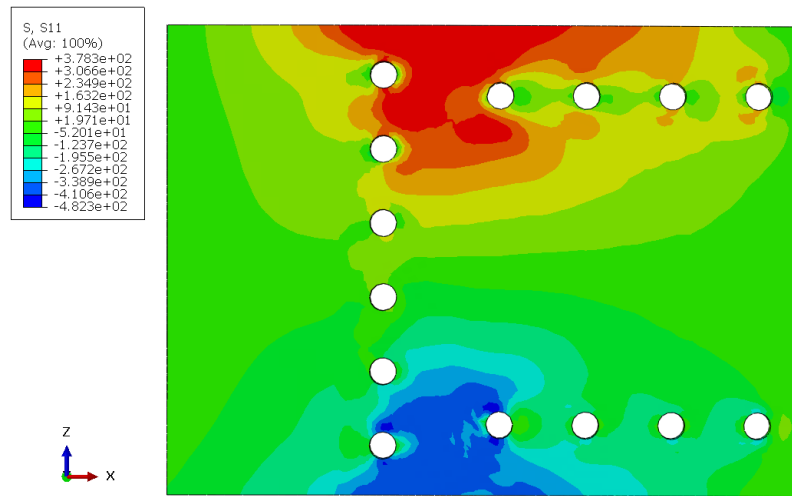


Figure 5.12: σ_{11} on the gusset plate for a displacement of 20mm

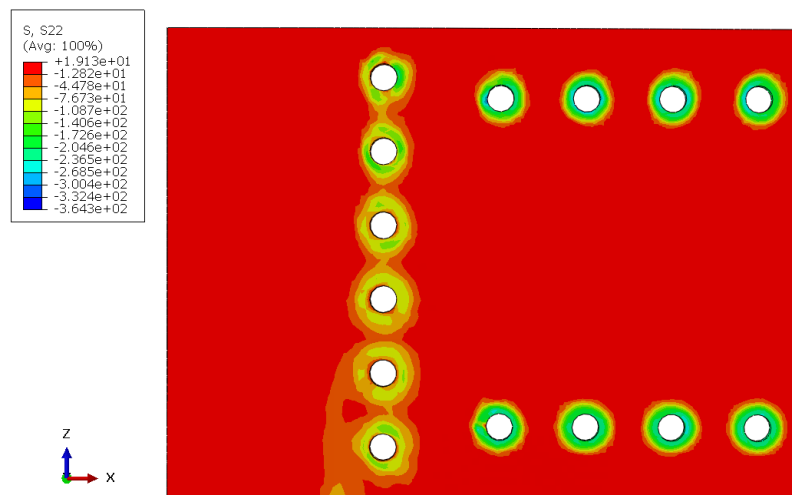


Figure 5.13: σ_{22} on gusset plate for a displacement of 20mm

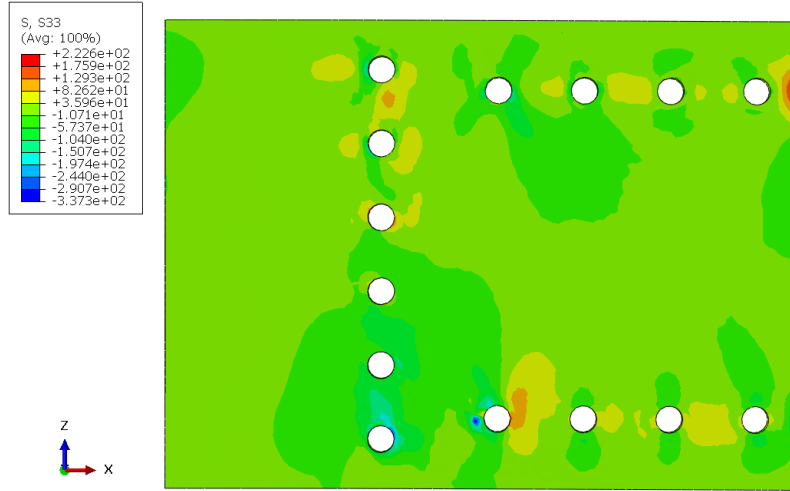


Figure 5.14: σ_{33} on the gusset plate for a displacement of 20mm

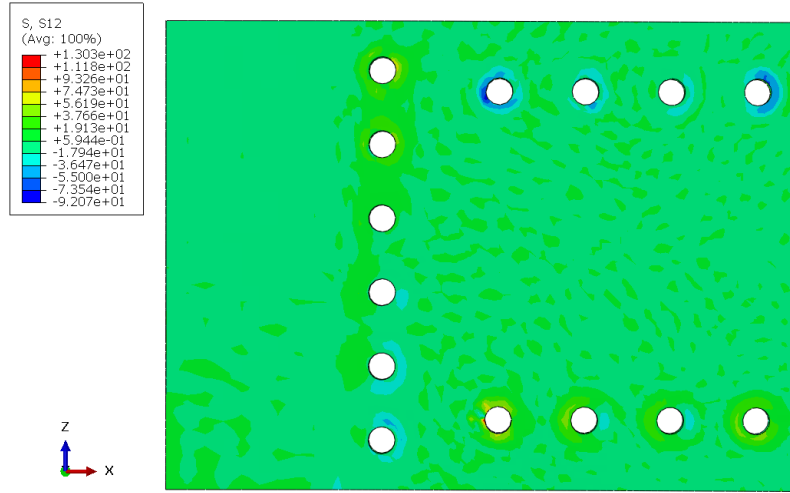


Figure 5.15: τ_{12} on the gusset plate for a displacement of 20mm

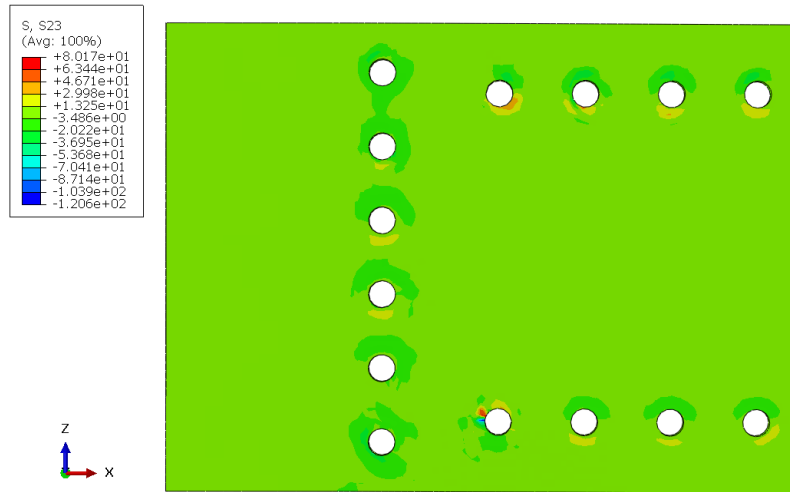


Figure 5.16: τ_{23} on the gusset plate for a displacement of 20mm

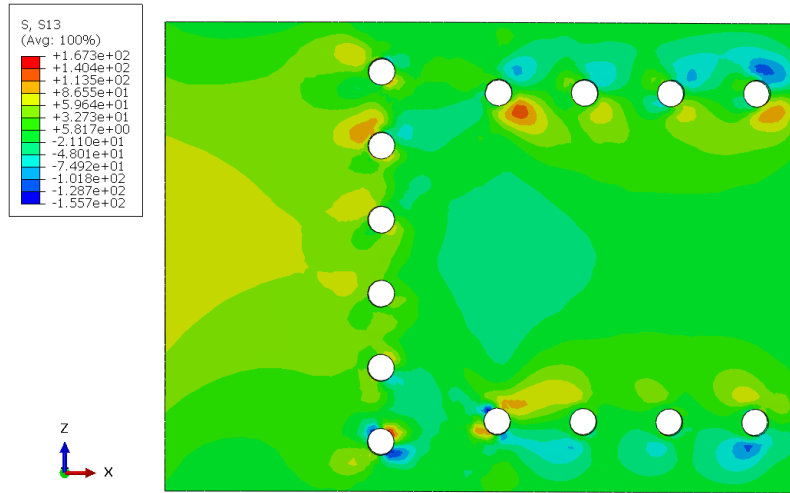


Figure 5.17: τ_{13} on the gusset plate for a displacement of 20mm

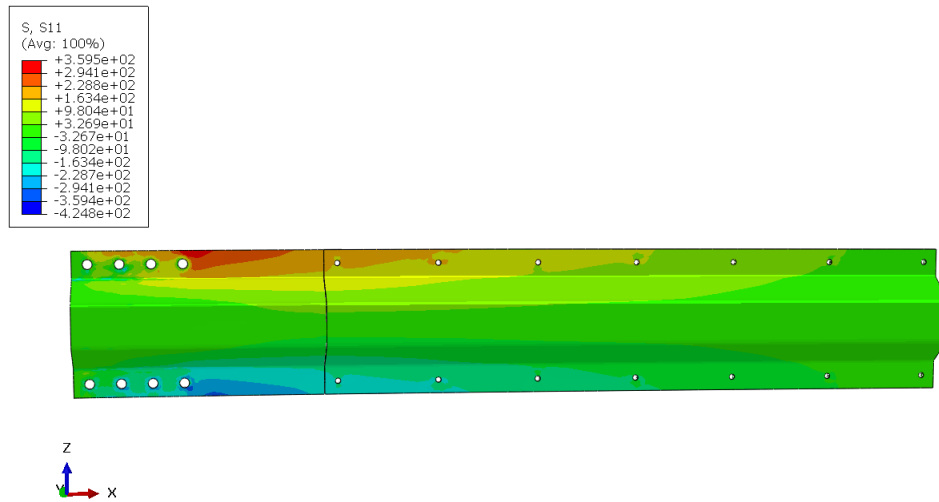


Figure 5.18: σ_{11} on brace for a displacement of 20mm

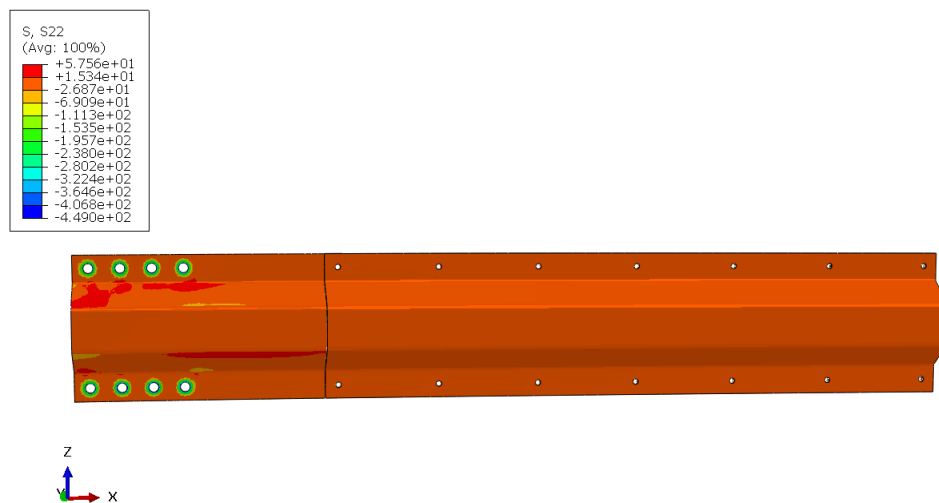


Figure 5.19: σ_{22} on the brace for a displacement of 20mm

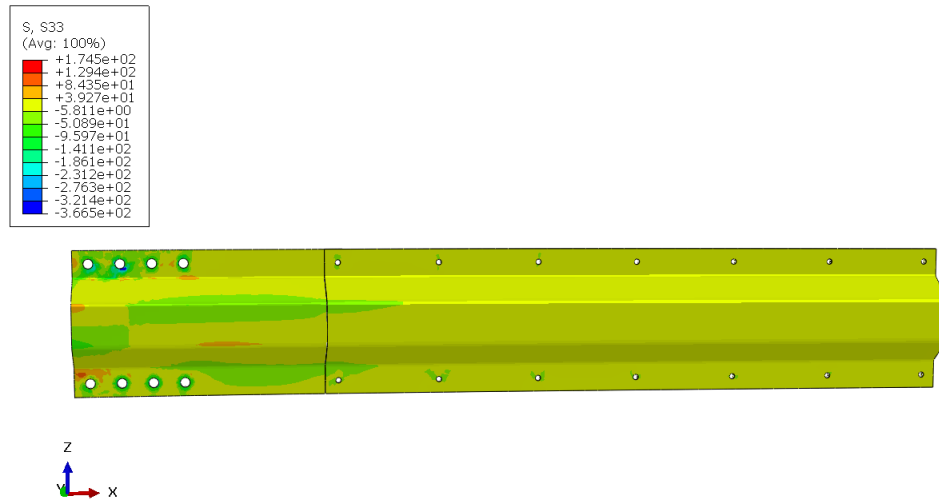


Figure 5.20: σ_{33} on the brace for a displacement of 20mm

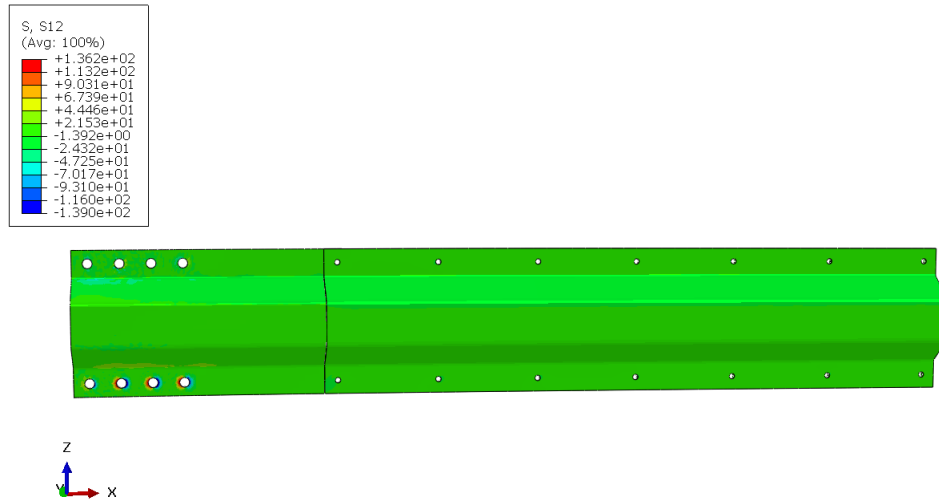


Figure 5.21: τ_{12} on the brace for a displacement of 20mm

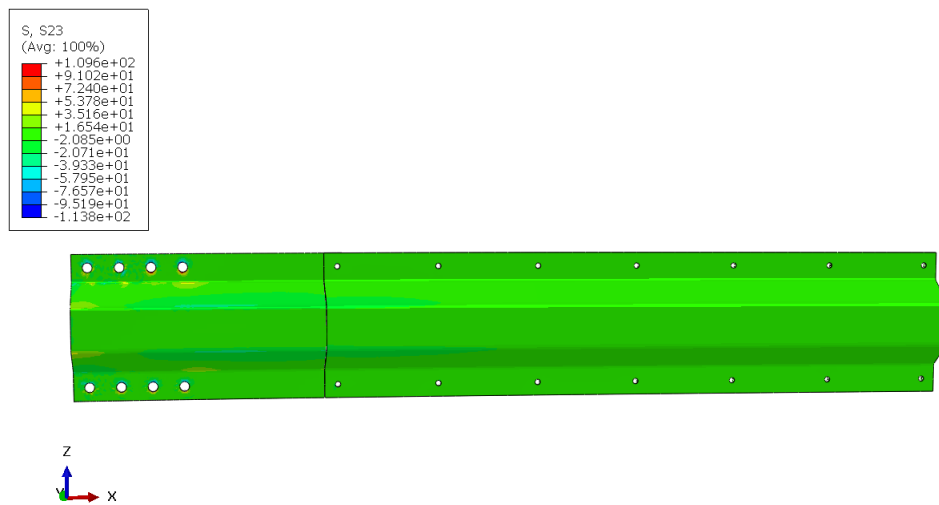
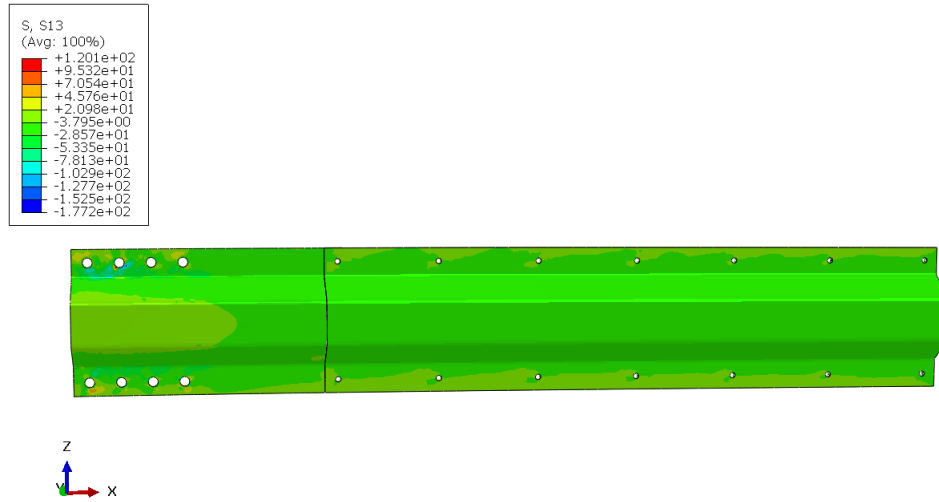


Figure 5.22: τ_{23} on the brace for a displacement of 20mm

Figure 5.23: σ_{13} on the brace for a displacement of $20mm$

The values of stress tensor components ($\sigma_{11}, \sigma_{22}, \sigma_{33}, \tau_{12}, \tau_{13}, \tau_{23}$) at the critical point of gusset plate and brace for eight values of displacement ($15mm, 17.5mm, 20mm, 25mm, 30mm, 35mm, 40mm$ and $45mm$) are listed in Table 5.5. These values are used during the application of methodologies described in section 5.3.3, in order to predict and assess the uniaxial and multiaxial fatigue life of a half-pipes bolted connection.

At this point of analysis, it is already predictable that the critical cross-section, where the fatigue failure will probably initiate, is located in the gusset plate, since it has the lowest section modulus and the largest distance from the load application point to the cross-section.

Table 5.3: Stress levels obtained for each displacement and cross-section properties of the gusset plate

Displacement <i>mm</i>	Force <i>N</i>	Distance <i>mm</i>	M <i>N.mm</i>	I <i>mm⁴</i>	w <i>mm³</i>	Stress level <i>MPa</i>
15	26069	2020	52659582	27436000	144400	365
17.5	29477	2020	59542732	27436000	144400	412
20	32356	2020	65359524	27436000	144400	453
25	36561	2020	73853220	27436000	144400	511
30	38234	2020	77232680	27436000	144400	535
35	38807	2020	78390140	27436000	144400	543
40	39253	2020	79291060	27436000	144400	549
45	39590	2020	79971800	27436000	144400	554

Table 5.4: Stress levels obtained for each displacement and cross-section properties of the brace

Displacement <i>mm</i>	Force <i>N</i>	Distance <i>mm</i>	M <i>N.mm</i>	I <i>mm⁴</i>	w <i>mm³</i>	Stress level <i>MPa</i>
15	26069	1755	45751271	27436000	144400	280
17.5	29477	1755	51731433	27436000	144400	317
20	32356	1755	56785131	26986014	163176	348
25	36561	1755	64164555	26986014	163176	393
30	38234	1755	67100670	26986014	163176	411
35	38807	1755	68106285	26986014	163176	417
40	39253	1755	68889015	26986014	163176	422
45	39590	1755	69480450	26986014	163176	425

Table 5.5: Stress tensor components in the critical point of the gusset plate and brace for each displacement

Member	Displacement <i>mm</i>	σ_{11} <i>MPa</i>	σ_{22} <i>MPa</i>	σ_{33} <i>MPa</i>	τ_{12} <i>MPa</i>	τ_{13} <i>MPa</i>	τ_{23} <i>MPa</i>
Gusset Plate	15	356	2	3	0.266	0.764	0.119
	17.5	371	3	38	0.346	-15	-2
	20	372	10	55	1	-7	-3
	25	390	-7	112	-2	11	0.717
	30	395	4	96	-0.772	-6	-0.038
	35	406	11	123	2	-1	2
	40	413	61	72	-2	-14	-0.563
	45	416	50	88	-0.714	-12	-0.095
Brace	15	304	-41	-6	-17	-2	-8
	17.5	345	0.310	-7	0.276	-11	-0.924
	20	354	-0.123	0.061	-0.729	-8	-0.912
	25	362	5	12	-0.493	-4	-0.268
	30	361	4	12	-0.015	-5	1
	35	335	-4	88	4	98	-3
	40	356	-13	53	6	-25	-13
	45	360	-11	56	6	24	-13

5.5 Results and Discussion

5.5.1 Uniaxial Fatigue Evaluation based on Basquin Law

In this section, a fatigue life prediction based on uniaxial Basquin criterion is carried out, following the methodology described in section 5.3. The Basquin fatigue curve for S355J2 steel tested under uniaxial loading with a stress ratio equal to 0, is presented in section 4.2 through the following equation:

$$\sigma_a = 274.49 N_f^{-0.024} \quad (5.9)$$

The maximum stresses(σ_{max}) on the gusset plate and brace determined in section 5.4, for each displacement (see Table 5.5), were evaluated and used to predict the numerical fatigue curves.

Then, the number of cycles until failure (N_f) was estimated by introducing the maximum tensile stress amplitude (Table 5.5), which were obtained for each force through the numerical simulation, in the Basquin fatigue curve for S355J2 steel tested under axial loading with $R = 0$ (Eq. (5.9)). Finally, the relation between the nominal stress range level ($\Delta\sigma$) in the critical cross-section, and the number of cycles until failure was estimated (Table 5.6).

Similarly to the experimental data analysis, there infinite life was also assumed for values above 5000000 number of cycles until failure and only the upper limit of infinite life was included in the graphic analysis. Besides, the numerical fatigue curve was only plotted for the gusset plate, since it is the member of joint where the critical section is verified.

Table 5.6: Values of Basquin law applied to the gusset plate and brace, for each displacement under consideration

Member	Displacement <i>mm</i>	σ_{max} <i>MPa</i>	σ_a <i>MPa</i>	N_f	$\Delta\sigma$ <i>MPa</i>
Gusset Plate	15	356	178	5000000(∞)	365
	17.5	371	186	5000000(∞)	412
	20	372	186	5000000(∞)	453
	25	390	195	1538733	511
	30	395	198	904988	535
	35	406	203	288140	543
	40	413	207	142775	549
	45	416	208	104544	554
Brace	15	304	152	5000000(∞)	280
	17.5	345	173	5000000(∞)	317
	20	354	177	5000000(∞)	348
	25	362	181	5000000(∞)	393
	30	361	181	5000000(∞)	411
	35	335	168	5000000(∞)	417
	40	356	178	5000000(∞)	422
	45	360	180	5000000(∞)	425

In Figure 5.24 is illustrated the numerical fatigue curve for the gusset plate, considering the uniaxial fatigue data of S355J2 steel. Thus, the uniaxial numerical curve for the connection under consideration is defined by the following equation:

$$\Delta\sigma = 963 \cdot N_f^{-0.046} \quad (5.10)$$

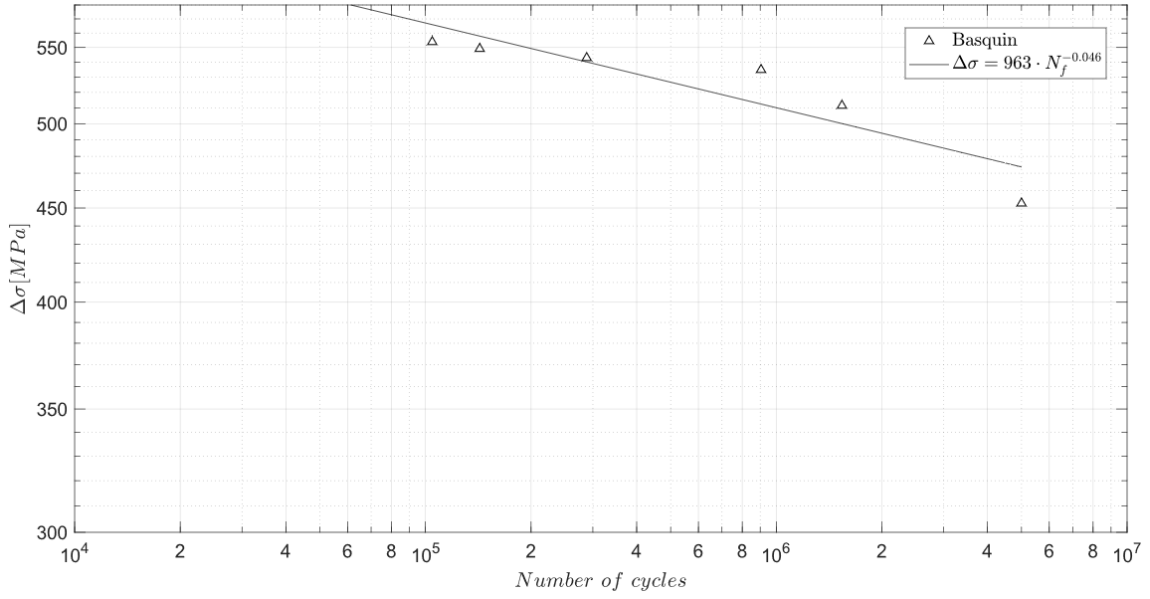


Figure 5.24: Numerical fatigue curve considering uniaxial fatigue data and applying the Basquin Law for high cycle regime

5.5.2 Multiaxial Fatigue Evaluation based on Dang Van Model

According to Eurocode 3 part 1-9, if the ratio between shear stresses, normal stresses and combination of normal stresses with shear stresses is lower than 15%, a uniaxial fatigue criterion can be used to assess fatigue life [European Committee for Standardization, 2010b].

For the case under study, the stress values on the gusset plate verify a ratio ($\frac{\sigma_{33}}{\sigma_{11}}$) around 15% or even slightly above, while on the brace this ratio is below 15%. Because of this, an evaluation of the fatigue life prediction based on multiaxial Dang Van model is carried out, as is described in section 5.3.

The Dang Van experimental fatigue curve obtained for S355J2 steel from multiaxial experimental data is defined in section 4.3.4 (Eq.(4.41)), through the following equation:

$$d = 297.41 N_f^{-0.037} \quad (5.11)$$

The equation above is used to calculate the number of cycles until failure for a certain value of Dang Van damage parameter. However, first of all, the Dang van damage parameter (d) (see Table 5.7), for each displacement, must be determined.

Therefore, a new field output, defined by the damage parameter (d) expression, was introduced in abaqus software, in order to calculate the damage parameter in all nodes of the numerical model. Then, in both the gusset plate and the brace, it was determined the node where occurs the maximum value of the field, as well as, that value itself.

Figures 5.25, 5.26 and 5.27 illustrate the Dang Van field on the connection.

After that, these parameters were introduced in Equation (5.11) and, subsequently, the number of cycles until failure (N_f) were estimated and presented in Table 5.7. Finally, the relation between the nominal stress range level ($\Delta\sigma$) in the critical cross-section and the number of cycles until failure (N_f) can be estimated.

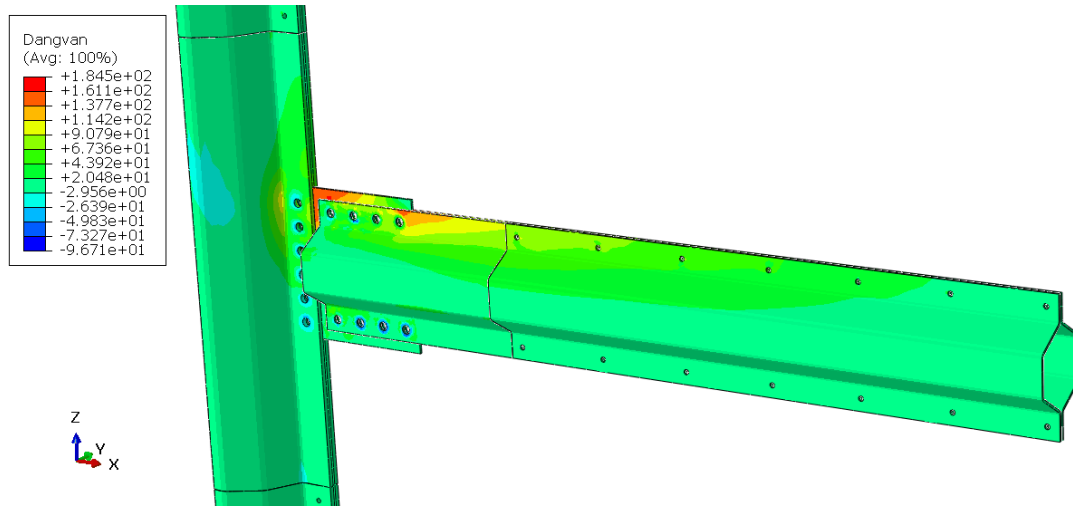


Figure 5.25: Overview of Dang Van damage parameter field for a displacement of 20mm

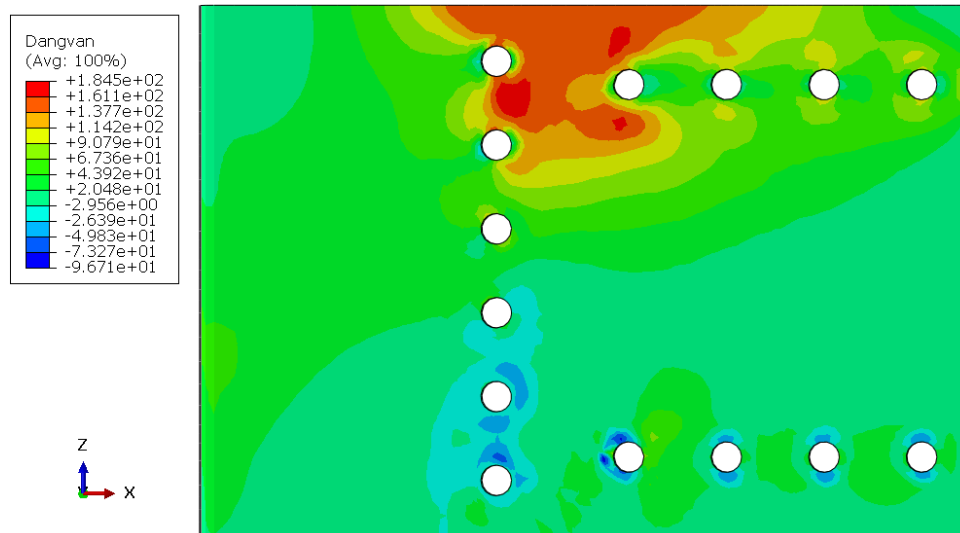


Figure 5.26: Dang Van damage parameter field on the gusset plate for a displacement of 20mm

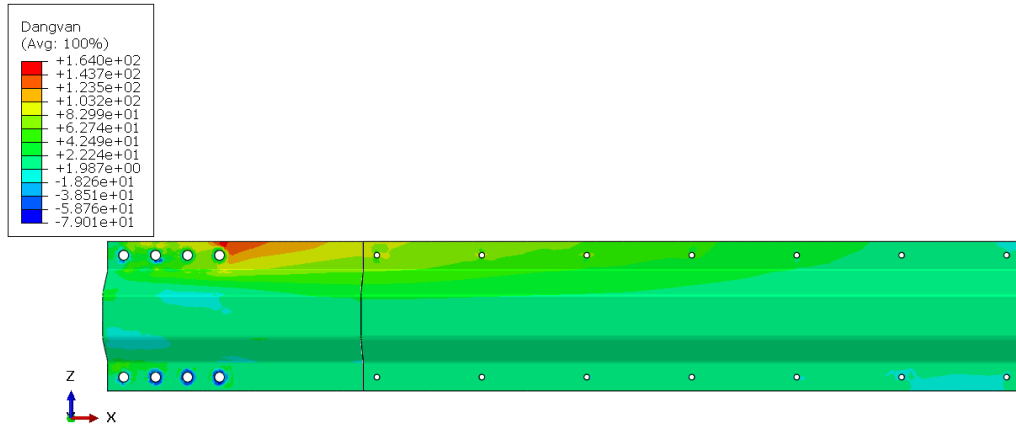


Figure 5.27: Dang Van damage parameter field on the brace for a displacement of 20mm

Looking at Table 5.7, it is clear, once again, that the gusset plate is the critical member, in other words, is responsible for the joint fatigue limit. Besides, for some applied displacements is achieved the low cycle region ($5 \cdot 10^4 \leq N_f$), which respective points (Number of cycles; stress range) will not be included in graphic analysis, since it is desired to assess high cycle fatigue region.

Table 5.7: Values of Dang Van model applied to the gusset place and brace for each displacement under consideration

Member	Displacement <i>mm</i>	<i>d</i> <i>MPa</i>	N_f	$\Delta\sigma$ <i>MPa</i>
Gusset Plate	15	170	3673199	365
	17.5	173	2289366	412
	20	185	373711	453
	25	196	78448	511
	30	198	59623	535
	35	207	17933	543
	40	211	102691	549
	45	213	8285	554
Brace	15	145	5000000(∞)	280
	17.5	153	5000000(∞)	317
	20	164	5000000(∞)	348
	25	164	5000000(∞)	393
	30	171	3134740	411
	35	174	1959127	417
	40	174	1959127	422
	45	175	1678023	425

Figure 2.17 illustrates the numerical fatigue curve for the gusset plate obtained by taking into account the biaxial fatigue data of S355J2 steel . Thus, the multiaxial numerical curve for the connection under consideration is defined by the following equation:

$$\Delta\sigma = 1925 \cdot N_f^{-0.081} \quad (5.12)$$

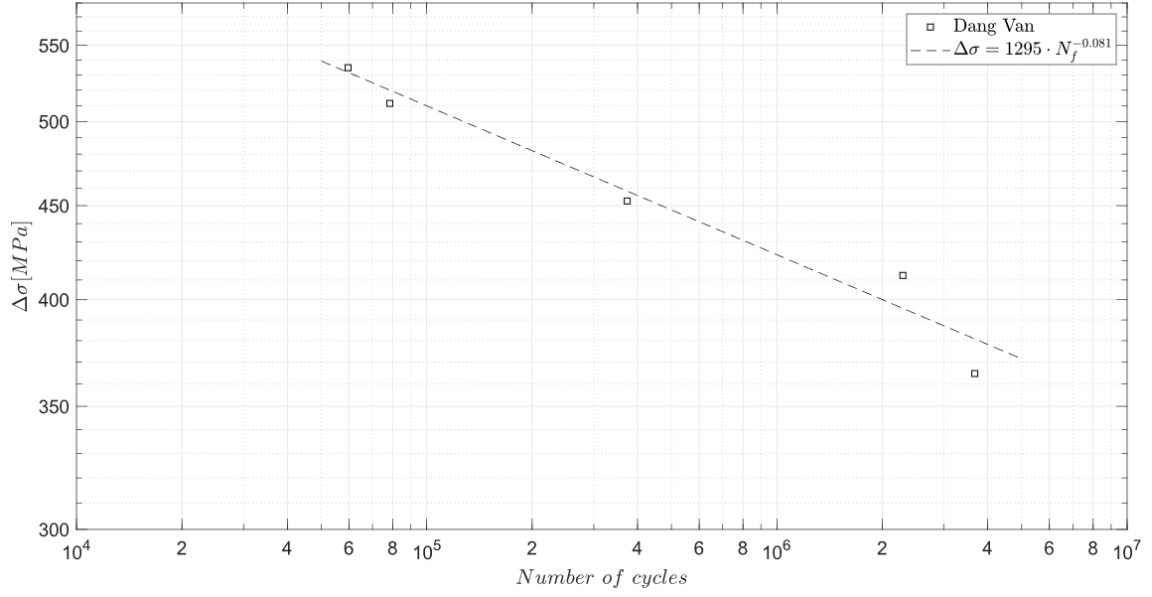


Figure 5.28: Numerical fatigue curve considering multiaxial fatigue data and applying the Dang van model for high cycle region

5.5.3 Multiaxial Fatigue Evaluation based on Findley Model

Besides Dang Van model, the Findley model was also applied, in order to assess the fatigue life of the bolted connection under a multiaxial stress state.

The experimental curve of Findley model for $R = 0$ had been previously studied and defined in Chapter 4 and is given by the following equation:

$$f = 303.78 N_f^{-0.039} \quad (5.13)$$

The methodology is similar to the one followed for Dang Van model, but the damage parameter of Findley model is defined and calculated in a different way. The computation of this model field is far more complex, because it requires the determination of a critical plane which depends on the value of the damage parameter. So, it was assumed that the node where is achieved the highest value of maximum principal stress is the critical one. Therefore, the local stresses in that node, collected from the numerical model, were used to calculate the shear stress amplitude and maximum normal stress on a θ plane through Morh's circle stress relations, as is described in chapter 4.

Then, the critical plane was determined, as well as, the Findley damage parameter(f) for each imposed displacement. The values of damage were applied to Equation (5.13), in order to estimate the respective number of cycles until failure. Last but not least, the relation between the nominal stress range and the number of cycles was proposed (Table 5.8).

Table 5.8: Values of Findley model applied to the gusset place and brace for each displacement under consideration

Member	Displacement <i>mm</i>	$\tau_{\theta,a}$ <i>MPa</i>	$\sigma_{\theta,max}$ <i>MPa</i>	k_f	f <i>MPa</i>	N_f	$\Delta\sigma$ <i>MPa</i>
Gusset Plate	15	75	272	0.304	158	5000000	365
	17.5	72	291	0.304	160	5000000	412
	20	68	296	0.304	158	5000000	453
	25	59	323	0.304	158	5000000	511
	30	64	323	0.304	163	5000000	535
	35	60	338	0.304	162	5000000	543
	40	59	323	0.304	158	5000000	549
	45	70	337	0.304	173	1907342	554
Brace	15	74	222	0.304	142	5000000	280
	17.5	75	261	0.304	155	5000000	317
	20	76	269	0.304	157	5000000	348
	25	75	278	0.304	159	5000000	393
	30	75	277	0.304	159	5000000	411
	35	67	294	0.304	167	4598683	417
	40	66	284	0.304	152	5000000	422
	45	66	288	0.304	153	5000000	425

Nevertheless, as can be seen in Table 5.8, the values obtained appear to suffer from the methodology lack of precision and rigour, since there are higher number of cycles for larger displacements. This occurs because when the node is selected based on maximum principal stress, the multiaxiality and effect of each kind of stress is not taken into account as in Findley model is done.

5.6 Conclusions

The numerical fatigue curves of the steel half bolted connection for high cycle regime, assuming a uniaxial or a multiaxial loading, were plotted on the same graph for comparison purpose (Fig. 5.29).

Thus, at looking for the graph below, it is clearly noticeable a large difference between both curves. By applying the Dang van model and, consequently, a multiaxial analysis the number of cycles until failure for a certain stress level is lower than the one obtained for the same level considering an uniaxial analysis.

Therefore, it is conclude that, for a fatigue analysis assessment and life estimation of this joint, a multiaxial analysis should be conducted. Thus, the numerical fatigue curve of the connection for S355 steel, was estimated through Dang van model.

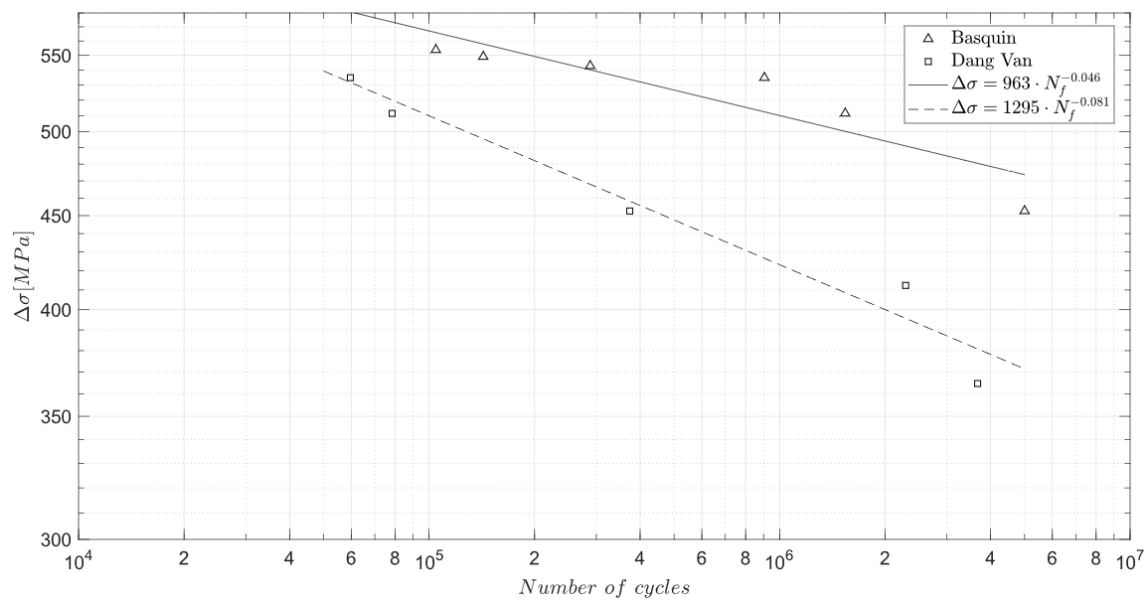


Figure 5.29: Comparison between numerical fatigue curves obtained considering uniaxial fatigue data (Basquin law) and multiaxial fatigue data (Dang van model)

Conclusion

6.1 Conclusions

Within the scope of this master thesis, uniaxial(axial) and biaxial(axial+torsional) fatigue tests were conducted and analysed for S355 J2 steel under different stress ratios.

The uniaxial fatigue design curves for axial, bending and torsional loadings were obtained for the high cycle region through the application of Basquin law. For the biaxial experimental fatigue data, four different multiaxial models(Findley, Dang Van, Sines and McDiarmid) were applied and evaluated, in order to estimate a fatigue design curve for high cycle region capable of evaluate a multiaxial fatigue state. Thus, it was conclude that the Dang Van model is the one which better describes the multiaxial fatigue phenomenon in S355 steel for high cycle region.

Fatigue crack growth rate tests were also conducted under pure mode I for different stress ratios. The constants of Paris law region were determined and compared to the experimental data previews obtained for mixed mode tests (mixed I+II).

From the experimental results for pure mode I, it is observed that the crack closure effect is not relevant for stress ratios between 0.1 and 0.7. In the case of a mixed mode (I+II), the fatigue damage is higher when the pure mode I is dominant. Besides, it was verified that all curves of fatigue crack growth rate as function of stress intensity factor for mode I equivalent stress intensity factor are distributed around a narrow region. Thus, for design purpose, in S355 steel, it is only required the evaluation of crack propagation under pure mode I.

Regarding the steel half-pipes bolted connections used on the lattice structure proposed by SHOWTIME project, uniaxial and multiaxial fatigue analyses were conducted. It was conclude, on both analysis, that the critical cross section is located in the gusset plate, because of the low inertia and distance to the loading application point. The number of cycles until failure, and even the global resistance of the connection, could be improved through the increase of gusset plate height, thickness or inertia.

Therefore, numerical fatigue curves were obtained, considering a uniaxial and a multiaxial fatigue state. For the uniaxial analysis was applied the Basquin law, while the multiaxial fatigue curve result from the application of Dang Van model.

The uniaxial and multiaxial numerical fatigue curves were compared, and it was conclude that a multiaxial fatigue analysis should be conducted, since it is observed a considerable difference between the curves. Thus, for design purpose of the half-pipes bolted connections, it should be considered the numerical curve obtained for the gusset plate, considering a multiaxial fatigue stress state.

6.2 Future Work

In order to improve the work developed during this master thesis elaboration, the following tasks are suggested :

- Perform additional fatigue tests for levels of loading already tested, with the aim of obtain at least three experimental points for each stress level. Besides, it would also be relevant to perform uniaxial tests for torsional loading.
- Extend the experimental fatigue programme to alternating amplitude and non proportional loads, as well as evaluate if Dang Van model is also a good choice for more complex loadings;
- Extend the experimental fatigue programme to the low cycle region;
- Conduct additional fatigue crack growth tests for mode I and mixed mode (II+I) under different stress ratios. Moreover, in the future, the crack closure effect should also be evaluated;
- Perform a probabilistic analysis for the experimental fatigue design curves estimated;
- Improve the material model used in the numerical connection model through the definition of a elastic plastic material model. Moreover, a cyclic loading should also be included in the numerical analysis, instead of the static analysis which was performed;
- Extend the numerical analysis to the fatigue crack propagation phase, through the introduction of a crack on the connection numerical model.

References

- Alvarez-Anton, L., Koob, M., Diaz, J., and Minnert, J. (2016). Optimization of a hybrid tower for onshore wind turbines by building information modeling and prefabrication techniques. *Visualization in Engineering*, 3:1–9.
- ASTM International (2013). ASTM 1823-13: Standard Terminology Relating to Fatigue and Fracture Testing. In *Annual book of ASTM standards*, pages 1–25. West Conshohocken, PA.
- ASTM International (2015). ASTM E647: Standard Method for Measurement of Fatigue Crack Growth Methods . In *Annual book of ASTM standards*, pages 1–49. West Conshohocken, PA.
- Basquin, O. H. (1910). *The exponential law of endurance tests*. American Society for Testing Materials.
- Bauer, Lucas and Matysik, Silvio (2019a). Nordex n43 lattice. accessed: august 2019. <https://www.wind-turbine-models.com/turbines/932-nordex-n43-lattice>.
- Bauer, Lucas and Matysik, Silvio (2019b). Vestas v90-3.0. accessed: august 2019. <https://en.wind-turbine-models.com/turbines/603-vestas-v90-3.0>.
- Boardman, B., Deere, and Company (1990). Fatigue resistance of steels. In ASM Handbook Committee, editor, *Properties and Selection: Irons, Steels, and High-Performance Alloys*. ASM International.
- Correia, J. (2014). *An integral probabilistic approach for fatigue lifetime prediction of mechanical and structural components*. PhD thesis, University of Porto.
- Correia, J., de Jesus, A. M. P., Moreira, P. M. G. P., and Tavares, P. (2016). Crack closure effects on fatigue crack propagation rates: Application of a proposed theoretical model. *Advances in Material Science and Engineering*, 2016:1–11.
- Correia, J. A., de Jesus, A. M., Fernández-Canteli, A., and Calçada, R. A. (2015). Modelling probabilistic fatigue crack propagation rates for a mild structural steel. *Frattura ed Integrità Strutturale*, 31:80–96.
- Dang-Van, K. (1994). Macro-micro approach in high- cycle multiaxial fatigue. In McDowell, D. and Ellis, R., editors, *STP1191-EB Advances in Multiaxial Fatigue*, pages 7–36. ASTM International, West Conshohocken, PA.
- Dang-Van, K. and Maitournam, M. H. (2003). Rolling contact in railways: modelling, simulation and damage prediction. *Fatigue and Fracture of Engineering Materials and Structures*, 26:939–948.

REFERENCES

- Desimone, H., Bernasconi, A., and Berreta, S. (2006). On the application of dang van criterion to rolling contact fatigue. *Wear* 260, pages 567–572.
- Ellyin, F. and Kujawski, D. (1993). A multiaxial fatigue criterion including mean-stress effect. In McDowell, D. and Ellis, R., editors, *STP1191-EB Advances in Multiaxial Fatigue*, pages 7–36. ASTM International, West Conshohocken, PA.
- European Committee for Standardization (2008). EN 1993-1-1 Eurocode 3: Design of Steel Structures – Part 1-8: General Rules and Rules for Buildings. In *European Standard*. CEN, Brussels, Belgium.
- European Committee for Standardization (2010a). EN 1993-1-8 Eurocode 3: Design of Steel Structures – Part 1-8: Design of Joints. In *European Standard*. CEN, Brussels, Belgium.
- European Committee for Standardization (2010b). EN 1993-1-9 Eurocode 3-Design of steel structures - Part 1-9: Fatigue. In *European Standard*, pages 1–45. CEN, Brussels, Belgium.
- Fernandes, A., de Castro, P., and Moura Branco, C. (1999). *Fadiga de Estruturas Soldadas*. Fundação Calouste Gulbenkian, Lisboa.
- Findley, W. N. (1958). *A theory for the effect of mean stress on fatigue of metals under combined torsion and axial load or bending*. [Providence] Engineering Materials Research Laboratory, Division of Engineering, Brown University.
- Global Wind Energy Council (GWEC) (2018). Global Wind Energy Report: Annual Market Update 2017. page 72.
- Guimarães, R. C. and Cabral, J. A. S. (1997). *Estatística*. McGraw-Hill, Portugal.
- Hibbit, D.K.B. and Karlsson, B.I. and Sorenson, P. (2001). *User's Manual I-III, version 6.3*. Hibbit, Karlsoon and Sorenson Inc.
- Institute for Sustainability and Innovation in Structural Engineering (2018). SHOWTIME: Steel Hybrid Onshore Wind Towers Installed with Minimal Effort. accessed: august 2019. <https://isise.net/site/index.php?module=publicProject&target=detailsid=93>.
- Jovasevic, S., Correia, J., Pavlovic, M., Dantas, R., Rebelo, C., Veljkovic, M., and de Jesus, A. (2019). Alternative steel lattice structures for wind energy converters. *International Journal of Structural Integrity*.
- Kallmeyer, A. R., Krgo, A., and Kurath, P. (2002). Evaluation of HCF Multiaxial Fatigue Life Prediction Methodologies for Ti-6Al-4V. *Journal of Engineering Materials and Technology*, 124(2):1–12.
- Kamal, M. and Rahman, M. M. (2018). Advances in fatigue life modeling: A review. *Renewable and Sustainable Energy Reviews*, 82(October 2017):940–949.
- Lee, Y.-L., Barkey, M. E., and Kang, H.-T. (2012). *Metal Fatigue Analysis Handbook - Practical Problem-Solving Techniques for Computer-Aided Engineering*. Elsevier.
- Leite, R., de Jesus, A., Correia, J. and Raposo, P., Jorge, R., Parente, M., and Calçada, R. (2018). A methodology for a global-local fatigue analysis of ancient riveted metallic bridges. *International Journal of Structural Integrity*, 9(3):355–380.

- Letcher, T. M. (2017). Why wind energy. In Letcher, T. M., editor, *Wind Energy Engineering: a Handbook for onshore and offshore Wind Turbines*, pages 3–13. Academic Press, India.
- Maktouf, W., Ammar, K., Naceur, I. B., and Saï, K. (2016). Multiaxial high-cycle fatigue criteria and life prediction: Application to gas turbine blade. *International Journal of Fatigue*, 92:25–35.
- Margetin, M., Ďurka, R., and Chmelko, V. (2016). Multiaxial fatigue criterion based on parameters from torsion and axial S-N curve. 10(37):146–152.
- McDiarmid, D. (1991). A general criterion for high cycle multiaxial fatigue failure. *Fatigue and Fracture of Engineering Materials and Structures*, 14(4):429–253.
- McDiarmid, D. (1994). A shear stress based critical-plane criterion of multiaxial fatigue failure for design and life prediction. *Fatigue and Fracture of Engineering Materials and Structures*, 17(12):1475–1484.
- McDowell, D. and Ellis, J. (1994). Overview. In McDowell, D. and Ellis, R., editors, *Advances in Multiaxial Fatigue*, pages 1–4. ASTM International, West Conshohocken, PA.
- Muskulus, M. (2012). The full-height lattice tower concept. *Energy Procedia*, 24:371–377.
- Navigant Consulting, I. (2012). Offshore wind market and economic analysis: Annual market assessment.
- North American Windpower (2019). Suzlon secures maiden order for new s111 hybrid wind turbine. accessed: august 2019. <https://nawindpower.com/suzlon-secures-maiden-order-new-s111-hybrid-wind-turbine>.
- Öztürk, F., Correia, J., Rebelo, C., De Jesus, A., and Simões da Silva, L. (2016). Fatigue assessment of steel half-pipes bolted connections using local approaches. *Procedia Structural Integrity*, 1:118–125.
- Richard, H. (1985). *Bruchvorhersagen bei überlagerter Normal- und Schubbeanspruchung sowie reiner Schubbelastung von Rissen*. VDI-Verl., Dusseldorf. (in German).
- Richard, H. and Benitz, K. (1983). A loading device for the creation of mixed mode in fracture mechanics. *Integrity journal of fracture*, pages 55–58.
- Rozumek, D., Marciniak, Z., Lesiuk, G., Correia, J., and de Jesus, A. (2018). Experimental and numerical investigation of mixed mode i+ii and i+iii fatigue crack growth in s355j0 steel. *International Journal of Fatigue*, pages 160–170.
- Rozumek, D. and Pawliczek, R. (2004). *Opis rozwoju pęknięć i zmęczenia materiałów w ujęciu energetycznym. Wieloosiowe zmęczenie losowe elementów maszyn i konstrukcji cz. VII*. Wydawnictwo Politechniki Opolskiej, Opole. (in Polish).
- Schijve, J. (2001). *Fatigue of Structures and Materials*. Kluwer Academic Publishers, United States of America.
- Schütz, W. (1996). A history of fatigue. *Engineering Fracture Mechanics*, 54:263–300.
- SHOWTIME (2014). EC-RFSR-CT-2015-00021-SHOWTIME – Steel hybrid Onshore wind towers installed with minimal effort. Project Proposal report, European Union.

REFERENCES

- SHOWTIME (2018). EC-RFSR-CT-2015-00021-SHOWTIME – Steel hybrid Onshore wind towers installed with minimal effort. First Annual Report, University of Coimbra (coordinator), 56 pages.
- Sines, G. (1955). Failure of materials under combined repeated stresses with superimposed static stresses. *National Advisory Committee for Aeronautics*.
- Sines, G. (1959). Behavior of metals under complex static and alternating stresses. In Sines, G. and Waisman, J. L., editors, *Metal Fatigue*, page 145–169. McGraw-Hill, New York.
- Socie, D. (1993). Critical plane approaches for multiaxial fatigue damage assessment. In McDowell, D. and Ellis, R., editors, *STP1191-EB Advances in Multiaxial Fatigue*, pages 7–36. ASTM International, West Conshohocken, PA.
- Socie, D. (2018). Multiaxial stress-life technical background. accessed: june 2019. <https://www.efatigue.com/multiaxial/background/stresslife.html>.
- Suresh, S. (1998). *Fatigue of Materials*. Cambridge University Press, New York.
- Takahashi, B. (2014). *Modern methodology for finite element based fatigue analysis of components subjected to uni and multiaxial fatigue*. PhD thesis, University of S. Paulo (Brazil). in Portuguese.
- van Lieshout, P., den Besten, J., and Kaminski, M. (2017). Validation of the corrected dang van multiaxial fatigue criterion applied to turret bearings of fpso offloading buoys. *Ships and Offshore Structures*, 12(12):521–529.
- Vestas Wind Systems A/S (2013). New tower enables increased power production at low wind sites. accessed: august 2019. https://www.vestas.com/en/media/_media/92670482644d4e5bb751ff6bd6f66a43.ashx.
- WindEurope (2018). Wind energy in Europe in 2018:Trends and statistics.
- You, B. and Lee, S. (1996). A critical review on multiaxial fatigue assessments of metals. *International Journal of Fatigue*, 18(4):235–244.

Experimental Fatigue Data

Table A.1: Fatigue data for pure torsion [Rozumek and Pawliczek, 2004]

Specimen Number	Ratio	τ_a	τ_{max}	τ_{min}	Number of cycles
-	-	<i>MPa</i>	<i>MPa</i>	<i>MPa</i>	-
1	-1	224	224	-224	240896
2	-1	224	224	-224	287584
3	-1	224	224	-224	307160
4	-1	197	197	-197	643378
5	-1	197	197	-197	832899
6	-1	197	197	-197	791741
7	-1	185	185	-185	2339531
8	-1	185	185	-185	3201723
9	-1	185	185	-185	4315280
10	-0.5	176	235	-117	158654
11	-0.5	176	235	-117	233059
12	-0.5	152	203	-101	550643
13	-0.5	152	203	-101	684452
14	-0.5	152	203	-101	640830
15	-0.5	139	185	-93	2233660
16	-0.5	139	185	-93	1056184
17	0	139	185	-93	3264627
18	0	138	276	0	357490
19	0	138	276	0	535925
20	0	136	272	0	725014
21	0	136	272	0	861084
22	0	132	264	0	1146944
23	0	132	264	0	1538050

Table A.2: Fatigue data for pure bending [Rozumek and Pawliczek, 2004]

Specimen Number	Ratio	σ_a	σ_{max}	σ_{min}	Number of cycles
-	-	<i>MPa</i>	<i>MPa</i>	<i>MPa</i>	-
19	-1	275	275	-275	3317086
20	-1	275	275	-275	2891788
21	-1	263	263	-263	404634
22	-1	263	263	-263	376679
23	-1	263	263	-263	334277
24	-1	397	397	-397	166734
25	-1	397	397	-397	154291
26	-1	397	397	-397	128240
27	-1	275	275	-275	1269204
9	-0.5	366	488	-244	57548
10	-0.5	366	488	-244	65619
11	-0.5	366	488	-244	72623
12	-0.5	297	396	-198	131641
13	-0.5	297	396	-198	169125
14	-0.5	297	396	-198	180616
15	-0.5	269	359	-179	593557
16	-0.5	269	359	-179	676729
17	-0.5	248	331	165	978181
18	-0.5	248	331	165	1341950
1	0	288	576	0	95689
2	0	288	576	0	131274
3	0	267	534	0	153110
4	0	273	546	0	169836
5	0	256	512	0	244293
6	0	256	512	0	420508
7	0	235	470	0	874345
8	0	235	470	0	1058257

Table A.3: Fatigue data for bending combined with torsion [Rozumek and Pawliczek, 2004]

Specimen Number	Ratio	σ_a	σ_{max}	σ_{min}	τ_a	τ_{max}	τ_{min}	Number of cycles
-	-	<i>MPa</i>	<i>MPa</i>	<i>MPa</i>	<i>MPa</i>	<i>MPa</i>	<i>MPa</i>	-
19	-1	200	200	-200	200	200	-200	170348
20	-1	200	200	-200	200	200	-200	193511
21	-1	200	200	-200	200	200	-200	230254
22	-1	179	179	-179	179	179	-179	630976
23	-1	179	179	-179	179	179	-179	642041
24	-1	179	179	-179	179	179	-179	764044
25	-1	164	164	-164	164	164	-164	1357916
26	-1	164	164	-164	164	164	-164	1455705
27	-1	164	164	-164	164	164	-164	2171604
10	-0.5	118	157	-79	118	157	-79	3196388
11	-0.5	118	157	-79	118	157	-79	2405950
12	-0.5	121	161	-81	121	161	-81	1543957
13	-0.5	121	161	-81	121	161	-81	1457029
14	-0.5	130	173	-87	130	173	-87	427168
15	-0.5	130	173	-87	130	173	-87	389342
16	-0.5	147	196	-98	147	196	-98	125274
17	-0.5	147	196	-98	147	196	-98	93750
18	-0.5	147	196	-98	147	196	-98	89503
1	0	118	236	0	118	236	0	1227659
2	0	121	242	0	121	242	0	840091
3	0	121	242	0	121	242	0	701517
4	0	123	246	0	123	246	0	376016
5	0	123	246	0	123	246	0	259500
6	0	129	258	0	129	258	0	234992
7	0	129	258	0	129	258	0	214236
8	0	139	278	0	139	278	0	141477
9	0	139	278	0	139	278	0	118901

Table A.4: Fatigue data for pure axial loading

Specimen Number	Ratio	σ_a	σ_{max}	σ_{min}	Number of cycles
-	-	<i>MPa</i>	<i>MPa</i>	<i>MPa</i>	-
1	0.01	168	340	3.40	5000000(∞)
6	0.01	182	368	3.68	5000000(∞)
7	0.01	188	379	3.79	5000000(∞)
8	0.01	190	385	3.85	5000000(∞)
9	0.01	193	390	3.90	5000000(∞)
4	0.01	196	396	3.96	324373
5	0.01	196	396	3.96	281589
11	0.01	202	407	4.07	621182
12	0.01	202	407	4.07	131064
21	0.01	207	419	4.19	247161
22	0.01	207	419	4.19	315639
19	0.01	216	436	4.36	122047
20	0.01	216	436	4.36	76082
18	-1	232	232	-232	5000000(∞)
17	-1	232	232	-232	2147377
14	-1	249	249	-249	561786
16	-1	249	249	-249	406826
13	-1	272	272	-272	157983
15	-1	272	272	-272	98626

Table A.5: Fatigue data for axial combined with torsional loading

Specimen Number	Ratio	σ_a	σ_{max}	σ_{min}	τ_a	τ_{max}	τ_{min}	Number of cycles
-	-	<i>MPa</i>	<i>MPa</i>	<i>MPa</i>	<i>MPa</i>	<i>MPa</i>	<i>MPa</i>	-
3	0.01	151	306	3.06	75	152	1.52	5000000(∞)
5	0.01	160	323	3.23	79	161	1061	5000000(∞)
6	0.01	165	334	3.34	82	166	1.66	5000000(∞)
1	0.01	168	340	3.40	84	169	1.69	332151
2	0.01	168	340	3.40	84	169	1.69	256955
7	0.01	174	351	3.51	87	175	1.75	313815
8	0.01	174	351	3.51	87	175	1.75	656534
9	0.01	174	351	3.51	87	175	1.75	181536
12	-1	164	164	-164	82	82	-82	5000000(∞)
13	-1	181	181	-181	90	90	-90	5000000(∞)
14	-1	194	194	-181	99	99	-99	2546156
15	-1	194	194	-194	99	99	-99	2040566
10	-1	204	204	-204	104	104	-104	133962
11	-1	204	204	-204	104	104	-104	835602
16	-1	204	204	-204	104	104	-104	390101
17	-1	204	204	-204	104	104	-104	383422
18	-1	164	164	-164	164	164	-164	88165
19	-1	164	164	-164	164	164	-164	44152

Appendix B

Damage Parameters of Sines, Findley, McDiarmid and Dang Van models

Table B.1: Sines damage parameter for pure axial loading and axial combined with torsional loading (for $k_s = 0.125$)

Specimen Number	Loading	Ratio	σ_a	τ_a	s
-	-	-	<i>MPa</i>	<i>MPa</i>	-
4-5	Axial	0.01	196	-	117
9	Axial	0.01	193	-	115
11-12	Axial	0.01	202	-	120
19-20	Axial	0.01	216	-	129
21-22	Axial	0.01	207	-	124
13-15	Axial	-1	272	-	128
14-16	Axial	-1	249	-	117
17-18	Axial	-1	232	-	109
1-2	Axial+torsion	0.01	168	84	126
6	Axial+torsion	0.01	165	82	123
7-8-9	Axial+torsion	0.01	174	87	130
10-11-16-17	Axial+torsion	-1	204	104	128
13	Axial+torsion	-1	181	90	113
14-15	Axial+torsion	-1	194	99	122
18-19	Axial+torsion	-1	164	164	155

Table B.2: Sines damage parameter for pure torsion, pure bending and torsion combined with bending (for $k_s = 0.125$)

Specimen Number	Loading	Ratio	σ_a	τ_a	s
-	-	-	MPa	MPa	-
1-2	Bending	0	288	-	171
3	Bending	0	267	-	158
4	Bending	0	273	-	162
5-6	Bending	0	256	-	152
7-8	Bending	0	235	-	140
9-10-11	Bending	-0.5	366	-	187
12-13-14	Bending	-0.5	297	-	152
15-16	Bending	-0.5	269	-	138
17-18	Bending	-0.5	248	-	127
19-20-27	Bending	-1	275	-	130
21-22-23	Bending	-1	263	-	171
24-25-26	Bending	-1	397	-	187
18-19	Torsion	0		138	103
20-21	Torsion	0		136	101
22-23	Torsion	0	-	132	99
10-11	Torsion	-0.5	-	176	131
12-13-14	Torsion	-0.5	-	152	113
15-16-17	Torsion	-0.5	-	139	104
1-2-3	Torsion	-1	-	224	167
4-5-6	Torsion	-1	-	197	147
7-8-9	Torsion	-1	-	185	138
1	Bending+torsion	0	118	118	125
2-3	Bending+torsion	0	121	121	129
4-5	Bending+torsion	0	123	123	131
6-7	Bending+torsion	0	129	129	137
8-9	Bending+torsion	0	139	139	148
10-11	Bending+torsion	-0.5	118	118	116
12-13	Bending+torsion	-0.5	121	121	119
14-15	Bending+torsion	-0.5	130	130	128
16-17-18	Bending+torsion	-0.5	147	147	144
19-20-21	Bending+torsion	-1	200	200	189
22-23-24	Bending+torsion	-1	179	179	169
25-26-27	Bending+torsion	-1	164	164	154

Table B.3: Findley damage parameter for pure axial loading and axial combined with torsional loading (for $k_f = 0.304$)

Specimen Number	Loading	Ratio	σ_a <i>MPa</i>	τ_a <i>MPa</i>	f	2θ <i>°</i>
-	-	-	-	-	-	-
4-5	Axial	0.01	196	-	175	302
9	Axial	0.01	193	-	173	302
11-12	Axial	0.01	202	-	180	302
19-20	Axial	0.01	216	-	193	302
21-22	Axial	0.01	207	-	185	302
13-15	Axial	-1	272	-	183	287
14-16	Axial	-1	249	-	168	287
17-18	Axial	-1	232	-	157	287
1-2	Axial+torsion	0.01	168	84	191	347
6	Axial+torsion	0.01	165	82	188	347
7-8-9	Axial+torsion	0.01	174	87	197	347
10-11-16-17	Axial+torsion	-1	204	104	183	333
13	Axial+torsion	-1	181	90	161	333
14-15	Axial+torsion	-1	194	99	174	333
18-19	Axial+torsion	-1	164	164	217	351

Table B.4: Findley damage parameter for pure torsion, pure bending and torsion combined with bending (for $k_f = 0.304$)

Specimen Number	Loading	Ratio	σ_a	τ_a	f	2θ
-	-	-	<i>MPa</i>	<i>MPa</i>	-	$^\circ$
1-2	Bending	0	288	-	256	302
3	Bending	0	267	-	237	302
4	Bending	0	273	-	243	302
5-6	Bending	0	256	-	227	302
7-8	Bending	0	235	-	209	302
9-10-11	Bending	-0.5	366	-	272	292
12-13-14	Bending	-0.5	297	-	220	292
15-16	Bending	-0.5	269	-	199	292
17-18	Bending	-0.5	248	-	184	292
19-20-27	Bending	-1	275	-	186	287
21-22-23	Bending	-1	263	-	245	287
24-25-26	Bending	-1	397	-	268	287
18-19	Torsion	0	-	138	145	32
20-21	Torsion	0	-	136	142	32
22-23	Torsion	0	-	132	138	32
10-11	Torsion	-0.5	-	176	184	22
12-13-14	Torsion	-0.5	-	152	159	22
15-16-17	Torsion	-0.5	-	139	145	22
1-2-3	Torsion	-1	-	224	234	17
4-5-6	Torsion	-1	-	197	206	17
7-8-9	Torsion	-1	-	185	193	17
1	Bending+torsion	0	118	118	190	5
2-3	Bending+torsion	0	121	121	195	5
4-5	Bending+torsion	0	123	123	198	5
6-7	Bending+torsion	0	129	129	208	5
8-9	Bending+torsion	0	139	139	224	5
10-11	Bending+torsion	-0.5	118	118	166	356
12-13	Bending+torsion	-0.5	121	121	170	356
14-15	Bending+torsion	-0.5	130	130	183	356
16-17-18	Bending+torsion	-0.5	147	147	207	356
19-20-21	Bending+torsion	-1	200	200	264	351
22-23-24	Bending+torsion	-1	179	179	236	351
25-26-27	Bending+torsion	-1	164	164	217	351

Table B.5: McDiarmid damage parameter for pure axial loading and axial combined with torsional loading

Specimen Number	Loading	Ratio	σ_a	τ_a	m
-	-	-	<i>MPa</i>	<i>MPa</i>	-
4-5	Axial	0.01	196	-	128
9	Axial	0.01	193	-	126
11-12	Axial	0.01	202	-	132
19-20	Axial	0.01	216	-	141
21-22	Axial	0.01	207	-	135
13-15	Axial	-1	272	-	156
14-16	Axial	-1	249	-	143
17-18	Axial	-1	232	-	134
1-2	Axial+torsion	0.01	168	84	144
6	Axial+torsion	0.01	165	82	142
7-8-9	Axial+torsion	0.01	174	87	149
10-11-16-17	Axial+torsion	-1	204	104	161
13	Axial+torsion	-1	181	90	141
14-15	Axial+torsion	-1	194	99	153
18-19	Axial+torsion	-1	164	164	196

Table B.6: McDiarmid damage parameter for pure torsion, pure bending and torsion combined with bending

Specimen Number	Loading	Ratio	σ_a	τ_a	m
-	-	-	<i>MPa</i>	<i>MPa</i>	-
1-2	Bending	0	288	-	188
3	Bending	0	267	-	174
4	Bending	0	273	-	178
5-6	Bending	0	256	-	167
7-8	Bending	0	235	-	153
9-10-11	Bending	-0.5	366	-	220
12-13-14	Bending	-0.5	297	-	179
15-16	Bending	-0.5	269	-	162
17-18	Bending	-0.5	248	-	149
19-20-27	Bending	-1	275	-	158
21-22-23	Bending	-1	263	-	151
24-25-26	Bending	-1	397	-	229
18-19	Torsion	0	-	138	138
20-21	Torsion	0	-	136	136
22-23	Torsion	0	-	132	132
10-11	Torsion	-0.5	-	176	176
12-13-14	Torsion	-0.5	-	152	152
15-16-17	Torsion	-0.5	-	139	139
1-2-3	Torsion	-1	-	224	224
4-5-6	Torsion	-1	-	197	197
7-8-9	Torsion	-1	-	185	185
1	Bending+torsion	0	118	118	150
2-3	Bending+torsion	0	121	121	154
4-5	Bending+torsion	0	123	123	156
6-7	Bending+torsion	0	129	129	164
8-9	Bending+torsion	0	139	139	177
10-11	Bending+torsion	-0.5	118	118	144
12-13	Bending+torsion	-0.5	121	121	148
14-15	Bending+torsion	-0.5	130	130	159
16-17-18	Bending+torsion	-0.5	147	147	179
19-20-21	Bending+torsion	-1	200	200	239
22-23-24	Bending+torsion	-1	179	179	214
25-26-27	Bending+torsion	-1	164	164	196

Table B.7: Dang Van damage parameter for pure axial loading and axial combined with torsional loading

Specimen Number	Loading	Ratio	σ_a	τ_a	d
-	-	-	<i>MPa</i>	<i>MPa</i>	-
4-5	Axial	0.01	196	-	176
9	Axial	0.01	193	-	173
11-12	Axial	0.01	202	-	181
19-20	Axial	0.01	216	-	193
21-22	Axial	0.01	207	-	186
13-15	Axial	-1	272	-	189
14-16	Axial	-1	249	-	173
17-18	Axial	-1	232	-	161
1-2	Axial+torsion	0.01	168	84	185
6	Axial+torsion	0.01	165	82	182
7-8-9	Axial+torsion	0.01	174	87	191
10-11-16-17	Axial+torsion	-1	204	104	185
13	Axial+torsion	-1	181	90	163
14-15	Axial+torsion	-1	194	99	176
18-19	Axial+torsion	-1	164	164	216

Table B.8: Dang Van damage parameter for pure torsion, pure bending and torsion combined with bending

Specimen Number	Loading	Ratio	σ_a	τ_a	d
-	-	-	<i>MPa</i>	<i>MPa</i>	-
1-2	Bending	0	288	-	257
3	Bending	0	267	-	238
4	Bending	0	273	-	244
5-6	Bending	0	256	-	228
7-8	Bending	0	235	-	210
9-10-11	Bending	-0.5	366	-	279
12-13-14	Bending	-0.5	297	-	226
15-16	Bending	-0.5	269	-	204
17-18	Bending	-0.5	248	-	189
19-20-27	Bending	-1	275	-	192
21-22-23	Bending	-1	263	-	253
24-25-26	Bending	-1	397	-	276
18-19	Torsion	0	-	138	138
20-21	Torsion	0	-	136	136
22-23	Torsion	0	-	132	132
10-11	Torsion	-0.5	-	176	176
12-13-14	Torsion	-0.5	-	152	152
15-16-17	Torsion	-0.5	-	139	139
1-2-3	Torsion	-1	-	224	224
4-5-6	Torsion	-1	-	197	197
7-8-9	Torsion	-1	-	185	185
1	Bending+torsion	0	118	118	178
2-3	Bending+torsion	0	121	121	183
4-5	Bending+torsion	0	123	123	186
6-7	Bending+torsion	0	129	129	195
8-9	Bending+torsion	0	139	139	210
10-11	Bending+torsion	-0.5	118	118	163
12-13	Bending+torsion	-0.5	121	121	167
14-15	Bending+torsion	-0.5	130	130	179
16-17-18	Bending+torsion	-0.5	147	147	202
19-20-21	Bending+torsion	-1	200	200	263
22-23-24	Bending+torsion	-1	179	179	236
25-26-27	Bending+torsion	-1	164	164	215

Appendix C

Publications

Evaluation of biaxial (axial+torsional) high-cycle fatigue behaviour of S355 structural steel

R. Dantas ^{a*}, J.A.F.O. Correia ^a, G. Lesiuk ^b, S. Jovašević ^c, D. Rozumek ^d, C. Rebelo ^c, W. Wisniewski ^b, A.M.P. De Jesus ^a

^a *CONSTRUCT & INEGI, Faculty of Engineering, University of Porto, Portugal*

^b *Department of Mechanics, Materials Science and Engineering, Wrocław University of Science and Technology, Poland*

^c *Department of Civil Engineering, University of Coimbra, Portugal*

^d *Department of Mechanics and Machine Design, Opole University of Technology, Poland*

*Corresponding author: up201403351@fe.up.pt

Keywords: Multiaxial fatigue; High-cycle fatigue, S355; structural steel

ABSTRACT

There are countless structural engineering applications where a multiaxial fatigue state can be identified. As it is well known, a multiaxial stress state is more critical and undesirable for any kind of structural element than a uniaxial stress state and, as such, it requires a special attention and evaluation of material behaviour.

In order to fulfil this idea, an experimental campaign was elaborated with the aim to test and evaluate biaxial high-cycle fatigue behaviour of S355 steel. This steel is mostly used in structural applications, such as wind turbine towers and bridges [1][2]. The most relevant mechanic properties of this steel can be found in Table 1, which is based on [3], and where E is young modulus, f_y is yield strength and f_u is tensile strength.

Table 1. S355 steel properties[3]

E [GPa]	f_y [MPa]	f_u [MPa]
211.60	422.00	744.80

This work aims to obtain experimental fatigue curves for different stress ratios (R), as well as, calculate a multiaxial fatigue damage parameter for a high cycle fatigue domain. The influence of a biaxial state and different kinds of loads (axial and torsional) in fatigue life will also be evaluated. Besides, experimental tests are carried out for various stress ratios to demonstrate and analyse how this parameter affects fatigue life. The impact of shear stress on fatigue behaviour of S355 steel is a relevant topic and it will also be a matter of study.

There were conducted two different tests: axial and biaxial (axial and torsional loads). An hourglass shape specimen with a minimum section area of 44.18 mm² was chosen for both axial and biaxial tests (Fig. 1). Experimental tests were carried out in force control, since it is desired to assess high-cycle fatigue domain. Besides, sinusoidal loads were applied with a frequency of 10Hz. For biaxial tests it is important to highlight that shear stress and normal stress signals are in phase, which, in other words, means that loading is proportional. Moreover, until now, shear stress value has been defined as half of normal stress value. The axial and biaxial tests were performed by MTS 810 testing system, which is characterized by a maximum capacity of 100 kN, and MTS 809 Axial/torsional test system with an axial maximum capacity of 50kN and torsional maximum capacity of 0.5 kN.m, respectively.

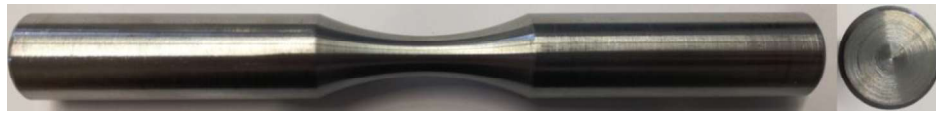


Fig. 1. Specimen used in uniaxial and biaxial fatigue tests

Experimental tests are still ongoing, and results obtained until now can be found in Table 2, where σ_a is normal stress amplitude and τ_a is shear stress amplitude. In this way, it is expected to perform these experiments for other stress ratios as well as to change reason between shear stress and normal stress in order to assess impact of these parameters on fatigue behaviour of S355 steel. After that, a multiaxial fatigue damage parameter will be calculated based on a suitable high cycle fatigue criterion [4]. A deterministic curve and experimental results will be presented, and a finite element model will be developed with the aim of determine the maximum local stress state.

Table 2 Results obtained until now from biaxial (torsional+axial) and uniaxial (axial) tests

Loading	Ratio	σ_a [MPa]	τ_a [MPa]	Number of Cycles
Axial+Torsional	0.01	174	87	313815
Axial+Torsional	0.01	174	87	656534
Axial+Torsional	0.01	174	87	181536
Axial+Torsional	0.01	168	84	332151
Axial+Torsional	0.01	168	84	256955
Axial+Torsional	0.01	165	82	5000000
Axial+Torsional	-1	340	169	3945
Axial+Torsional	-1	204	104	133962
Axial	0.01	224	-	136289
Axial	0.01	224	-	116342
Axial	0.01	196	-	324373
Axial	0.01	196	-	281589
Axial	0.01	193	-	5000000

REFERENCES

- [1] S. Jovašević *et al.*, “Global Fatigue Life Modelling of Steel Half-pipes Bolted Connections,” *Procedia Eng.*, vol. 160, no. 1cmfm Xviii, pp. 278–284, 2016.
- [2] M. Veljkovic, L. Simões da Silva, B. F. C. Fontoura, A. M. P. de Jesus, R. Matos, and C. Rebelo, “A comparison of the fatigue behavior between S355 and S690 steel grades,” *J. Constr. Steel Res.*, vol. 79, p. 2012, 2012.
- [3] J. A. F. O. Correia, A. M. P. de Jesus, A. Fernández-Canteli, and R. A. B. Calçada, “Modelling probabilistic fatigue crack propagation rates for a mild structural steel,” *Frat. ed Integrita Strutt.*, vol. 31, pp. 80–96, 2015.
- [4] F. Öztürk, J. A. F. O. Correia, C. Rebelo, A. M. P. De Jesus, and L. Simões da Silva, “Fatigue assessment of steel half-pipes bolted connections using local approaches,” *Procedia Struct. Integr.*, vol. 1, pp. 118–125, 2016.

ACKNOWLEDGMENTS

The authors acknowledge with thanks the support of the European Commission’s Framework Program “Horizon 2020”, through the Marie Skłodowska-Curie Innovative Training Networks (ITN) “AEOLUS4FUTURE – Efficient harvesting of the wind energy” (H2020-MSCA-ITN-2014: Grant agreement no. 643167) to the present research project.

Alternative steel lattice structures for wind energy converters

Wind energy
converters

Slobodanka Jovasevic

Faculty of Science and Technology, University of Coimbra, Coimbra, Portugal

José Correia

*Department of Civil Engineering, Faculty of Engineering,
University of Porto, Porto, Portugal*

Marko Pavlovic

Delft University of Technology, Delft, The Netherlands

Rita Dantas

Department of Mechanical Engineering, University of Porto, Porto, Portugal

Carlos Rebelo

Faculty of Science and Technology, University of Coimbra, Coimbra, Portugal

Milan Veljkovic

Delft University of Technology, Delft, The Netherlands, and

Abilio M.P. de Jesus

Department of Mechanical Engineering, University of Porto, Porto, Portugal

Received 1 May 2019
Revised 9 August 2019
Accepted 10 August 2019

Abstract

Purpose – In the last decades, the demand and use of renewable energies have been increasing. The increase in renewable energies, particularly wind energy, leads to the development and innovation of powerful wind energy converters as well as increased production requirements. Hence, a higher supporting structure is required to achieve higher wind speed with less turbulence. To date, the onshore wind towers with tubular connections are the most used. The maximum diameter of this type of tower is limited by transportation logistics. The purpose of this paper is to propose an alternative wind turbine lattice structure based on half-pipe steel connections.

Design/methodology/approach – In this study, a new concept of steel hybrid tower has been proposed. The focus of this work is the development of a lattice structure. Therefore, the geometry of the lattice part of the tower is assessed to decrease the number of joints and bolts. The sections used in the lattice structure are constructed in a polygonal shape. The elements are obtained by cold forming and bolted along the length. The members are connected by gusset plates and preloaded bolts. A numerical investigation of joints is carried out using the finite element (FE) software ABAQUS.

Findings – Based on the proposed study, the six “legs” solution with K braces under 45° angle and height/spread ratio of 4/1 and 5/1 provides the most suitable balance between the weight of the supporting structure, number of bolts in joints and reaction forces in the foundations, when compared with four “legs” solution.

Originality/value – In this investigation, the failure modes of elements and joints of an alternative wind turbine lattice structures, as well as the rotation stiffness of the joints, are determined. The FE results show good agreement with the analytical calculation proposed by EC3-1-8 standard.

Keywords Built-up polygonal sections, Preloaded gusset-plate connections, Steel hybrid towers, Tower geometry

Paper type Research paper

The authors acknowledge the support of the European Commission's Framework Programmes “Horizon 2020” programme through the Marie Skłodowska-Curie Innovative Training Networks (ITN) “AEOLUS4FUTURE – Efficient Harvesting of the Wind Energy” (H2020-MSCA-ITN-2014: Grant Agreement No. 643167) and RFCS – Research Fund for Coal and Steel programme through the Grant Agreement RFSR-CT-2015-00021-SHOWTIME.



International Journal of Structural
Integrity
© Emerald Publishing Limited
1757-9864
DOI 10.1108/IJSI-05-2019-0042

1. Introduction

Nowadays, global warming is one of the main concerns of our society and, as such, there is an increasing need to change the behaviours that are causing it. The principal activities responsible for the emission of greenhouse gases are energy production and industry. In 2014, the energy obtained from fossil fuels represented 81 per cent of world energy production (Letcher, 2017).

However, in 2014, the European Union aimed to have at least 27 per cent of the total energy consumption covered from the renewable energy sources (EWEA, 2017). Onshore wind energy as a renewable energy source represents a very competitive alternative to fossil fuels. By the end of 2015, the installed capacity of renewable wind energy was more than 141 GW in Europe (EWEA, 2015). The construction of more powerful wind energy converters (WEC) is required due to the increasing demand for renewable energies. The power produced by a wind turbine highly depends on the wind velocity. In this way, higher wind turbine towers are fundamental to reach zones with the less turbulent and faster wind, thus obtaining more power (Figure 1) (Letcher, 2017; Heistermann, 2011).

Up to 30 per cent of the total WEC cost is due to tower construction. The tower height increase leads to more difficult and more expensive transportation, assembly, erection and maintenance (Hau, 2006). However, as stated before, with the height increase, the generated energy increases as well.

In this way, several scientific and technical events have been organized with the purpose of generating scientific knowledge related to wind energy technology. In 2017, Winercost event (International Conference on Wind Energy Harvesting) brought together the present expertise on the built-environment wind energy technology in order to investigate smart cities methodologies and discussed a variety of topics, such as wind characteristics and loads; structures, materials and dynamics; grid integration, operations and control; markets, strategies, policies and socio-economics smart cities; and environmental aspects (Rebelo *et al.*, 2018).

Nowadays, the most frequently used tower types for WEC are steel, concrete or hybrid tubular towers. One of the tallest steel tubular towers installed is Vestas 3 MW wind turbine with 166 m hub height (Figure 2(a)). The diameter of this WEC tower model reaches 6.5 m in the base, which implies that base segments are made of several pieces to satisfy public road transport limitations. However, this has resulted in transportation and installation cost increase (Vestas Wind Systems A/S, 2016).

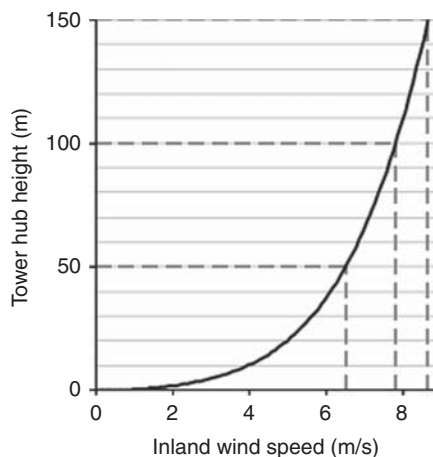
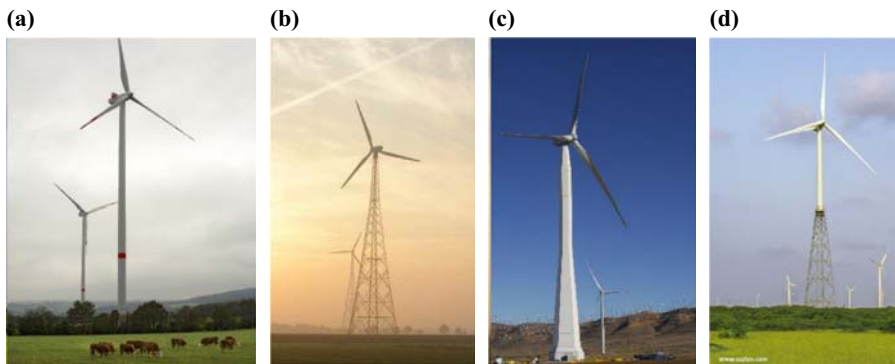


Figure 1.
Inland wind speed
increasing with
hub height

Source: Heistermann (2011)



Wind energy
converters

Figure 2.
Types of wind
turbine towers

Notes: (a) RUUKKI lattice tower; (b) GE space frame lattice tower; (c) Suzlon hybrid tower; (d) Vestas LDST tubular tower

In the beginning, the design and optimization of lattice structures by using tubular joint were studied in the offshore field, because these platforms are formed by a jacket structure (Duthoit and Falzarano, 2018). Gong (Gong, 2011) suggested a design and an analysis of two different types of transition piece models under different load conditions applied to wind turbine support structures. A design concept for wind turbine towers, which aims to replace the traditional support structures by simple lattice support structures, was proposed by Muskulus (2012). Moreover, Muskulus and Schafhirt (2014) presented a review on the design optimization of wind turbine support structures, where the challenges and possible approaches for structural optimization are highlighted as well as design recommendations are suggested.

Therefore, many works have been developed to replace traditional onshore wind turbine towers by hybrid structures (tubular + lattice tower). As previously mentioned, this modification allows higher towers, and consequently, more wind energy can be produced. Thus, there are many topics related to structural design, such as static and dynamic behaviour, fatigue analysis, wind loads, stability, structural integrity, efficiency, economic variables and security, that have been studied (Américo *et al.*, 2014; Alvarez-Anton *et al.*, 2016; Seidel *et al.*, 2016; Wang *et al.*, 2016).

Recently, a few other concepts have been developed. Ruukki (2011) used a lattice structure for 2.5 MW turbine to reach 160 m height (Figure 2(b)). For heights beyond 130 m, General Electric – Renewable Energy (2014) proposed a new enclosed lattice space frame assembled on-site (Figure 2(c)). This new solution makes the tower cost-effective and utilizes standard logistic (General Electric – Renewable Energy, 2014). Moreover, Suzlon Energy Limited (2016) designed a 120 m hybrid wind turbine tower with 2.1 MW rated power and a four-legged lattice structure with “L” shaped cross-sections. The instability of compressed members is overcome using intermediate struts (Figure 2(d)). Besides, Ruukki proposed a new type of open six-corner polygonal sections to improve the stability of members in lattice towers.

The lattice tower structure is an interesting solution to overcome transportation restrictions of public roads and achieve lighter structures (Gencturk *et al.*, 2012; Mohammadi *et al.*, 2018). Besides, these structures are characterized by large-based areas capable of better withstanding lateral loads applied and by a design that reduces wind loads (Gencturk *et al.*, 2014). However, the assembly task, as well as the maintenance of bolted connections, is more arduous and difficult. Fatigue loads are also a relevant issue to be aware of lattice towers (Gencturk *et al.*, 2012). Recently, Nunez-Casado *et al.* (2017) developed assembly strategies of wind turbine towers with the aim to minimize the fatigue damage. Other studies on the fatigue design of transition piece for onshore hybrid wind turbines, considering the multi-axial fatigue damage criterion, have been proposed (Farhan *et al.*, 2018).

Therefore, a hybrid tower design approach is being developed within the SHOWTIME (2014) project (Steel Hybrid Onshore Wind Towers Installed with Minimal Effort), where the lattice structure is used as the lower part of the tower and the tubular tower structure as the upper part. These two parts are connected by a transition piece. With this approach, the base diameter is reduced, hence facilitating the tower transportation. Additionally, optimized technology for steel tubular towers is being used for the upper portion of the tower, whereas the expression in the height is being achieved with lattice structure (Hau, 2006; Figueiredo and Carlos, 2013). Another advantage is that high cranes for tower installation can be avoided by using a lattice structure for a tubular tower and turbine installation. Several types of support structures for wind energy towers, particularly structures with tubular elements, have been proposed. One of the main goals of this research project is to use the new types of bolted polygonal cross-sections introduced by Ruukki (2011). In this type of structure, members are composed of built-up open cross-sections connected with preloaded bolts (Figure 3).

These section segments are manufactured by cold forming, so that the members are very thin and have a quite large diameter in comparison with their thickness. Therefore, resistance to global member buckling is increased. Local buckling can, however, be expected before section yielding due to the slenderness of cold-formed member. For this particular case, coupon tests on individual cold-formed section parts were performed by (Garzon, 2013). The results have shown that, due to cold forming, the yield strength for the section bent with 110° increases by about 29 per cent compared to the virgin plates.

Several studies were made to establish a comparison of polygonal and circular cross-sections for different slenderness ratios of D/t . Very thin-walled slender tubes with a ratio of the flat width and thickness b/t between 63 and 630 were tested by Bulson (1969). His results for tubes up to 18 sides showed a linear relationship between maximum strength and the number of sides. The polygonal sections with more than 22 sides collapse in the same mode as the circular tube. Therefore, after 22 sides, the polygonal tube did not have any structural advantage. Garzon's (2013) study showed a good agreement with Bulson's results for polygonal cross-sections with a b/t ratio between 69 and 191, but not for the polygonal tube with b/t ratio between 18 and 39. For these ratios (18 and 39), the maximal strength capacity under compression is reached for polygonal tubes with 16 sides. A small difference is observed in the resistance for the tubes with 12 sides. After 16 sides, the polygonal tube had no longer structural advantage over the circular tube. Therefore, polygonal sections with a number of sides lower than 12 were chosen for the members of the lattice structure.

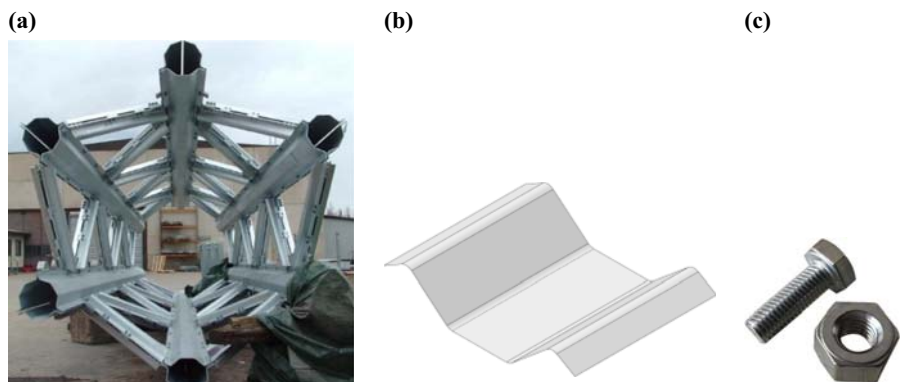


Figure 3.
Lattice structure for a
tubular tower and
turbine installation

Notes: (a) Lattice tower with built-up polygonal sections; (b) polygonal section segment; (c) preloaded bolts details

One of the important parameters in global structural behaviour is the behaviour of joints in a structure. Currently, codes use the effective length method to assess the stability of structures (Webber *et al.*, 2015). The effective length of compressed members (both pylon and brace members) is calculated considering non-linear moment–rotation characteristics of joints. An extensive study has been carried out due to the lack of this information in the current design codes (Webber *et al.*, 2015).

The main objective of this work is the optimization and detailed design of connections between polygonal members built on-site using preloaded bolts. The geometry of the lattice structure part and cross-sections of the members were determined from the parametric study. An optimization study for 120 m lattice structure models was made considering the number of “legs” and lattice structure height/spread (H/S) ratio, where the weight and the number of joints were discussed and taken into account in the analysis. Furthermore, finite element (FE) models of connections between polygonal built-up members were developed to determine resistance and moment–rotation characteristics. The numerical simulation of the half-pipe steel connections, consisting of a pylon and a secondary bracing, was based on two steps to simulate the bolt preload (the first step – using thermal contraction) and actuator loading (the second step – using displacement in vertical direction applied to the secondary bracing). In this study, two types of half-pipes steel connections were studied – the vertical element called pylon and the secondary element with horizontal or 45° angle bracing. These analyses were conducted considering two types of joints, bolted and welded joints, between the pylon and gusset plate linking to bracing. A quasi-static analysis was used.

2. Lattice geometry

A batch of different lattice structure geometries is designed for ultimate limit state. An iterative design approach is used. The ASHES aeroelastic and SAP2000 structural analysis software are used (Jovašević *et al.*, 2017). The parameters used in this study are targeting the ratio between the height of the tubular and lattice structure, the H/S ratio of lattice structure and the number of joints/bolts in the structure. The following parameters are defined for case studies:

- wind turbine power: 5 MW;
- tubular segment height: 100 m;
- lattice structure height: 120 m;
- number of “legs”: four and six; and
- lattice structure H/S ratio = 1/1; 2/1; 3/1; 4/1; 5/1; 6/1.

The most advantageous geometry of the lattice structure face was determined to compare four different solutions (Figure 4). For each proposed solution, the brace angle was varied with the 5° increment between 30° and 50° for four “legs” towers and 35° and 55° for six “legs” towers.

In this analysis, the used optimization criterion evaluated in terms of mass and number of joints. The evaluation of four “legs” lattice structures in terms of mass and number of joints of the lattice structure is represented in Figure 5(a). In the plot of this figure, it can be observed that the optimal solution is achieved for the second bracing layout with a brace angle of 45° ; therefore, this solution will be used for further study. In the same way, six “legs” structures were compared in Figure 5(b). Also, two solutions were assessed: one chosen from four “legs” lattice structure study and another one with K bracing layout (Figure 4). As an optimal solution, K -braced structure was selected. Furthermore, for both structures, with four and six “legs”, further parametric study was performed for a 45° brace angle.

For the next stage of the analysis, a 3D model of the lattice structure was created by varying braces’ cross-section along the height, while the columns’ cross-section was considered constant.

Figure 4.
Parametric study –
brace geometry

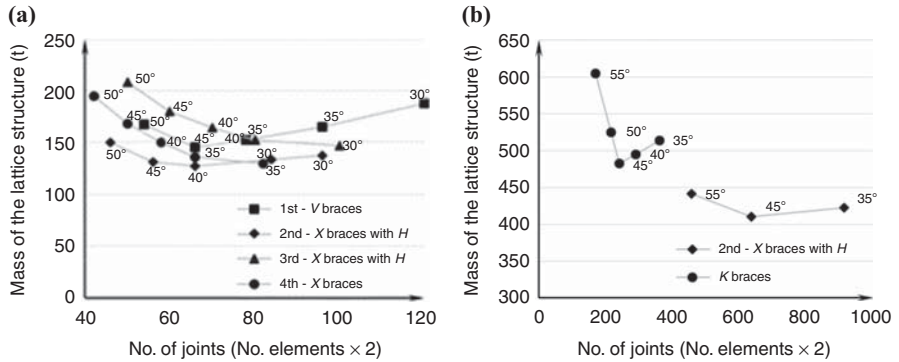
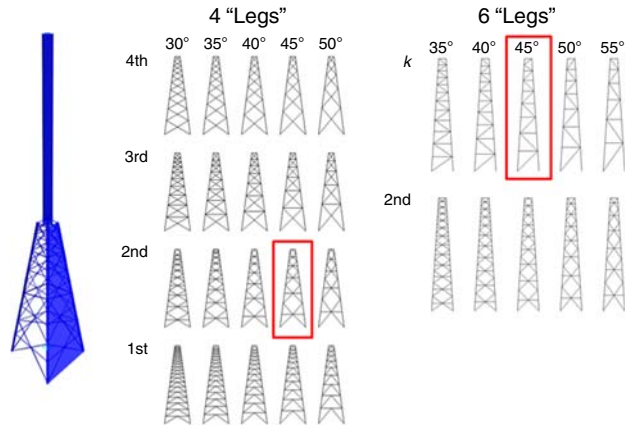


Figure 5.
Comparison of
2D models

Notes: (a) Four-legged lattice structures; (b) six-legged lattice structures. structures are shown in Figure 4

The braces angles are equal to 0° and 45° , respectively, for the welded and bolted joints under consideration. The weight and the number of joints of 120 m lattice models were compared for different H/S ratios of four “legs” and six “legs” lattice structures in Figure 6.

The comparison between suggested solutions is based on the following parameters:

- lattice structure weight;
- number of joints in the structure;
- estimated number of bolts (for N_{Ed} in brace elements); and
- foundation reaction force.

The results of the parametric study for four “legs” and six “legs” structures are demonstrated in Figure 6. The comparison is represented as a dependency of the structure mass and the number of joints (estimated number of the bolts). At this stage, presented in Figure 6(a), the only mass of lattice portion of the tower was accounted for. Four “legs” and six “legs” structures with the lowest mass were checked for H/S ratios of 5/1 and 3/1. Hence, these three solutions were used for further study related with the estimated number of bolts (Figure 6(b)).

In the further study, the entire tower was analyzed (including a tubular portion of the tower). The number of bolts was calculated for each solution according to EC 3 Part 1-8. The design of connections has shown that six “legs” lattice structure with K braces (without horizontals) requires the lowest number of bolts.

The height overspread (H/S) ratios of 3/1, 4/1 and 5/1 show more promising results; therefore, further analysis is performed on 120 m lattice with the mentioned H/S ratio.

The six “legs” lattice structure without horizontal braces (called H in Figures 5–7) was investigated. The four “legs” design optimization without horizontal bracing was not considered, as the elimination of any horizontal bracing causes an out of plane deformation at X -braces cross-points. To compare the six-legged structures with and without horizontals and the four-legged lattice structure, the same set of results were obtained and compared for all the designed structures. Moreover, the mass and estimated number of bolts for four- and six-legged structures with and without horizontal bracing are compared in Figure 6(b). For these cases, the cost of material for lattice structure manufacturing was compared (Figure 7).

Furthermore, it can be seen in Table I that with the increase of the H/S ratio, the maximum tensile force in the foundation increases as well. This occurs due to the smaller lever arm at the ground level to resist the overturning moment. So, the structures with higher H/S ratios need heavier foundations to overcome the overturning phenomena. Besides, as expected, the tensile force at the ground for six “legs” lattice structure with H/S ratio of 4/1 and 5/1 is smaller than for the similar ratio in four “legs” lattice structure.

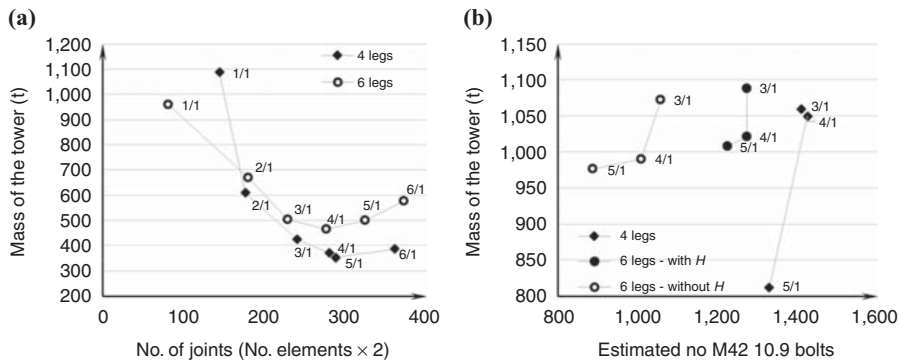


Figure 6.
The selected geometries for mass and (a) number of connections; (b) estimated number of bolts

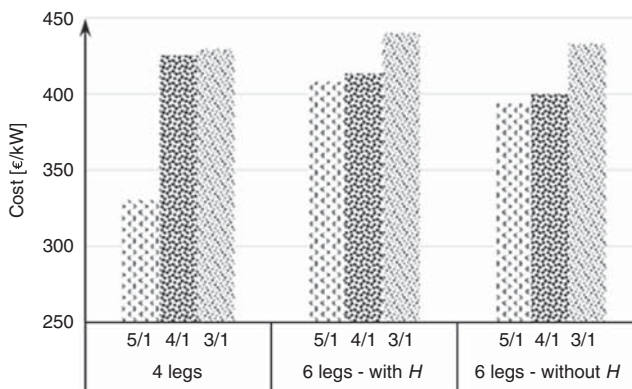


Figure 7.
Cost of material for lattice structure manufacturing

The four-legged tower with H/S ratio equal to 5/1 is the most economical solution when it comes to the weight of the steel structure being 16 per cent lighter than the 6-legged tower with the same H/S ratio. However, the reaction forces on foundations are higher, approximately 10 per cent. Regarding the estimated number of bolts, six-legged tower has 33 per cent fewer bolts compared to four-legged tower. Taking into account the fact that an increase in installed number of bolts increases the labour cost, the solution chosen to be more optimal is six-legged tower. Both H/S ratios, 4/1 and 5/1, should be investigated more in detail, taking into account labour and foundation costs.

3. Connection configuration

The joints analyzed in this work are depicted in Figure 8(a). The brace is the second member of the joint (horizontal or with 45° angle in Figure 8(b) and (c), respectively), and the pylon is the main member (vertical in Figure 8 (right)). Gusset-plate connections with preloaded bolts are used with the aim of maintaining the simplicity of the joint bolted *in situ*.

In this study, four case study joints were analyzed: B90, B45, W90 and W45. In these denominations, “B” and “W” represent bolted and welded pylon cross-section types (Figure 9), whereas “90” and “45” are the angles between pylon and brace element.

3.1 Cross-section type

Brace and pylon members of the lattice structure are composed by connecting cold-formed thin-walled open sections along the length with preloaded bolts in order to create a closed polygonal cross-section. The pylon is composed of three pieces bolted together along the length and forming a nine-sided polygonal cross-section. The brace is built out of two pieces bolted together along the length forming a hexagonal cross-section (Figure 9) (Jovašević *et al.*, 2017). Polygonal built-up sections are used instead of circular hollow sections due to higher ultimate strength. Additionally, polygonal members and connections between these members have a longer fatigue life as a result of the fatigue behaviour of preloaded high-strength bolted joints, which can bear higher fatigue loads than welded joints under shear or friction loads (Ozturk *et al.*, 2016; Jaspart and Weynand, 2016).

3.2 Dimensions

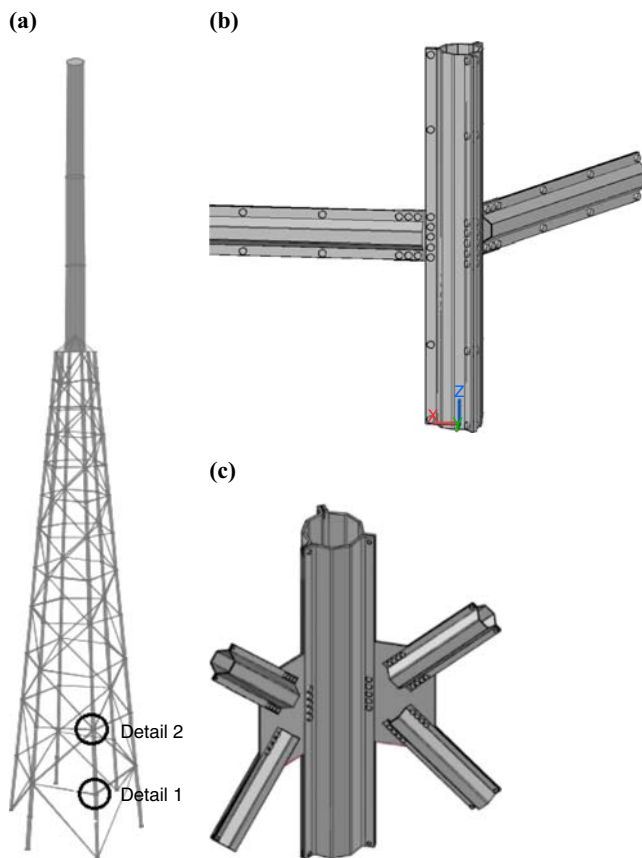
The characteristics of the joint (which is composed of the brace, the column and the gusset plate) are organized into two groups: dimensions (Table II) and mechanical properties (Table III):

(1) Dimensions:

- Column: column diameter (D_c), column thickness (t_c) and column bending radius (r_c).
- Brace: brace diameter (D_b), brace thickness (t_b) and brace bending radius (r_b).

Table I.
Maximal tensile force
in the foundation

H/S	R_3 (kN)
4 legs	
3/1	9,281
4/1	15,423
5/1	22,847
6 legs without H	
3/1	10,514
4/1	14,403
5/1	20,572



Notes: (a) Global structural model; (b) joint Detail 1; (c) joint Detail 2

Figure 8.
Joint between pylon
and brace members

Pylon members		Brace members	
Welded pylon		Bolted brace	
Joint detail	Cross-section	Joint detail	Cross-section
Bolted pylon			
Joint detail	Cross-section		

Figure 9.
Cross-sections
geometry and
joint details

IJSI	B90		B45		W90		W45		M20		M12	
	D_c	325	D_c	325	D_c	325	D_c	325	d_0	22	d_0	13
	t_c	12	t_c	12	t_c	20	t_c	12	d_b	20	d_b	12
	D_b	200	D_b	200	D_b	200	D_b	200	d_{nb}	25.4	d_{nb}	25.4
	t_b	5	t_b	10	t_b	5	t_b	5	t_{nb}	13	t_{nb}	8
	h_{gp}	380	h_{gp}	960	h_{gp}	380	h_{gp}	960	d_{hb}	25.4	d_{hb}	25.4
	t_{gp}	6	t_{gp}	8	t_{gp}	15	t_{gp}	10	t_{hb}	10	t_{hb}	16
	r_c	12	r_c	12	r_c	20	r_c	12	A_s	245	A_s	84.3
	r_b	5	r_b	10	r_b	5	r_b	5				
	r_{gp}	6	r_{gp}	8	r_{gp}	15	r_{gp}	10				
	Bolts	M20	Bolts	M20	Bolts	M20	Bolts	M12				
	$p_{2,cb}$	60	$p_{2,cb}$	110	$p_{1,bb}$	70	$p_{1,bb}$	35				
	$p_{1,bb}$	70	$p_{1,bb}$	70	$e_{1,bb}$	35	$e_{1,bb}$	20				
	$e_{1,bb}$	35	$e_{1,bb}$	35	$e_{2,bb}$	30	$e_{2,bb}$	20				
	$e_{2,bb}$	30	$e_{2,bb}$	30								
	$e_{1,cb}$	40	$e_{1,cb}$	40								
	$e_{2,cb}$	40	$e_{2,cb}$	40								

Table II.
Connections and bolts
dimensions (mm)

Table II.
Connections and bolts
dimensions (mm)

	Member		Bolt	
f_y		355	$f_{y,b}$	900
f_u		510	$f_{u,b}$	1,000

Table III.
Mechanical
properties (MPa)

- Gusset plate: gusset plate height (h_{gp}), gusset plate thickness (t_{gp}) and gusset plate bending radius (r_{gp}).
 - Bolts: distance between rows on column ($p_{x,cb}$), distance between bolt rows on brace ($p_{x,bb}$), edge distance ($e_{x,cb}$, $e_{x,bb}$), bolt head diameter (d_{hb}), bolt head thickness (t_{hb}), bolt hole clearance (d_0), nominal bolt diameter (d_b), nut diameter (d_{nb}), nut thickness (t_{nb}) and tensile stress area (A_s).
- (2) Mechanical properties:
- Brace, column and gusset plate: yield stress (f_y) and ultimate stress (f_u).
 - Bolts: ultimate stress ($f_{y,b}$) and yield stress ($f_{u,b}$).

4. Finite element model of the joint

In order to achieve the behaviour of the connection with a satisfactory level of accuracy, a large number of assumptions from a structural point of view and their application in the software need to be implemented. The numerical model used in this study was developed using ABAQUS/explicit dynamic solver (Dassault Systèmes, 2014). This solver was chosen over ABAQUS/Standard (Hibbit *et al.*, 2001) due to the usual convergence issues of the implicit solver. For an explicit dynamic solver, to be efficiently used for quasi-static analysis, the calculation speed needs to be increased artificially. This was achieved by mass scaling (Dassault Systèmes, 2014). Although in the short term, it implies that additional parameters should be tuned, in the long run, it creates a more stable model for manipulation.

4.1 Material models

The material model used for all joint elements (column, brace, gusset plate and bolts) is an elastic-perfectly plastic material model. For the end regions of members, elastic material model

was applied. The material used for column, brace and gusset plate is S355 steel grade with 355 MPa of yield stress and elastic modulus of 210 GPa. The bolts are 10.9 high-strength steel with a yield strength of 900 MPa, Young's modulus of 210 GPa and Poisson's ratio of 0.3.

4.2 Element types

In ABAQUS software, a wide range of elements is provided to be used for different geometry and analysis types. The solid elements in ABAQUS software can be used for linear analysis as well as for complex non-linear analyses, taking into account contact, plasticity, allowable penetration and large deformations.

In this model, different element types are used. It is assumed that the end regions of members (pylon and brace) can be used for dimensional reduction. Therefore, the whole model combines the reduced dimensional element type (continuum shell) with higher dimensional elements (solid elements).

It is very important to integrate into the analysis of appropriate coupling between different element types. Therefore, a simple FE model is created to compare three cases with different element types and to address the coupling technique. Models with solid element type, continuum shell element type and combination of solid and continuum shell were studied (ASCE, 2000). The shell-to-solid combination was implemented using a surface-based technique for coupling shell elements to solid elements available in ABAQUS software. The geometry and boundary conditions of the plate are given in Figure 10. The plate is 600 mm long, 100 mm wide and 10 mm thick.

Material properties used in this case are ideal plastic steel S355 with a yield point at $f_y = 355$ MPa, modulus of elasticity of $E = 210,000$ MPa and Poisson's ratio of $\nu = 0.3$. Elastic-perfectly plastic stress-strain curve is applied. Rigid-body constraint is defined at the end of the plate with the reference point (RP) in the centre of the cross-section. The load is applied in the RP in three steps, with each following the initial step. The loads applied are $N_z = -300$ kN, $M_y = 5$ kNm (major bending) and $M_x = 0.5$ kNm (minor bending).

Displacement at the end of the beam is compared between different element types for all three load cases and compared with analytical calculation as well (Table IV).

A good correlation between results is obtained. Therefore, for the further analysis, a combination of solid elements in the connection part tied with continuum elements at the end of the members is used.

Regarding the stress distribution, for minor bending loading and in the contact region between two element types, different stresses on the surface are observed (Figure 11).

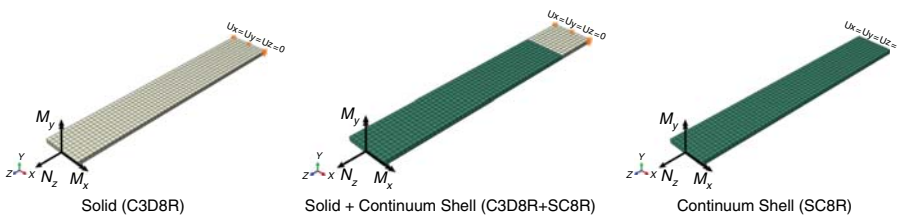


Figure 10.
Models with different
element types

	Analytical (mm)	Solid (mm)	Solid + CS (mm)	CS (mm)
Axial	0.857	0.853 (0.5%)	0.850 (0.8%)	0.848 (1.0%)
Major bending	5.143	5.181 (0.8%)	5.144 (0.0%)	5.104 (0.8%)
Minor bending	51.43	54.18 (5.3%)	51.83 (0.8%)	50.88 (1.1%)

Table IV.
Displacements at the
end of the plate

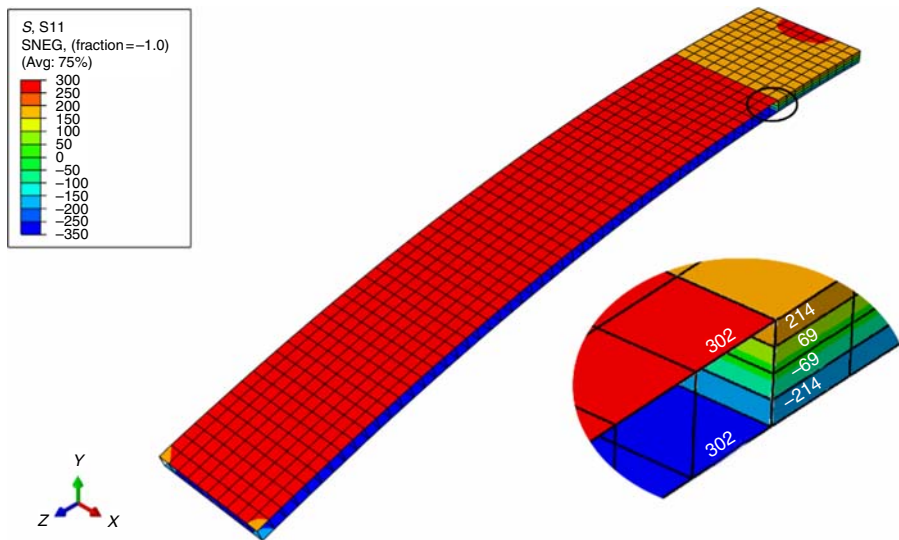


Figure 11.
Stress distribution at
the contact in the
solid + CS element
type models

This difference is due to the stresses that are computed at the element surface in the case of continuum shell elements and the stresses that are computed at the integration point, which is in the middle of the element for the C3D8R, in the case of the solid elements.

4.3 Interactions

FE models are considered and three types of interactions are implemented, which are described as follows:

- (1) Rigid-body constraint: it simulates the planar behaviour of a cross-section and integrates the global mechanic response (both in terms of kinematic and internal forces) of the whole section. Due to this type of constraint, it is possible to define RPs and apply the boundary condition of the entire section in these points (Figure 12).
- (2) Tie constraint: it connects two surfaces in a way that there is no relative displacement between them. It is used to simulate the weld connection between the gusset plate and the welded pylon. It was also used in bolted connections along with the elements outside of the connection. Moreover, this type of constraint was used to represent the contact between solid and continuum shell elements.
- (3) Contact interaction: it represents the interaction between surfaces, which is characterized by friction sliding without penetration. The “Coulomb friction” is used with the aim to represent tangential behaviour. In this analysis, the used friction coefficient takes the value of 0.4. To represent the normal behaviour, the “Hard contact” is used. This interaction must be applied to the surfaces of the bolt shank and hole; the surface of the bolt head and nut and the corresponding surfaces of the pylon, brace or gusset plate; and the surfaces in contact between gusset plate and pylon, brace or plate.

4.4 Boundary conditions, load application and analysis type

The analysis type is ABAQUS/explicit dynamic. It is carried out in two steps: clamping, in which bolt preload is applied, and monotonic load, with the final displacement (δ) taking the value of 200 mm in the vertical direction, as shown in Figure 12. The load is applied using

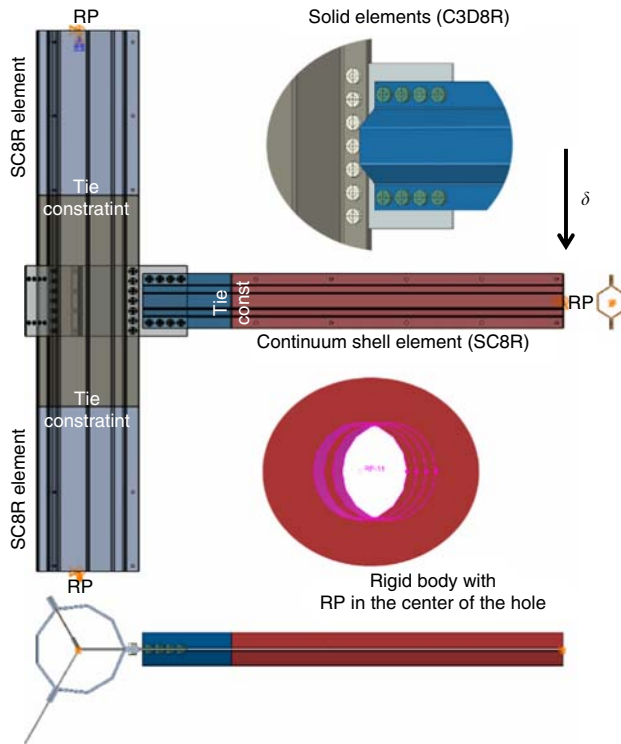


Figure 12.
Interactions and
boundary conditions

the “Explicit Dynamic” method including the non-linear effects of large displacements. Smooth amplitude functions are used for all loading steps, which change in boundary conditions, to withdraw impact behaviour and excitation of the model due to inertia forces.

4.4.1 Bolt preload model. Solid FEs, C3D8R, were used to model a simplified geometry of the bolts (Figure 13). The following simplifications are made:

- (1) the bolt shank is modelled as a cylinder with a diameter equal to the nominal diameter of the bolt (d_b);
- (2) in order to reduce the number of contact regions, washers are excluded; and
- (3) bolts along the elements are not modelled.

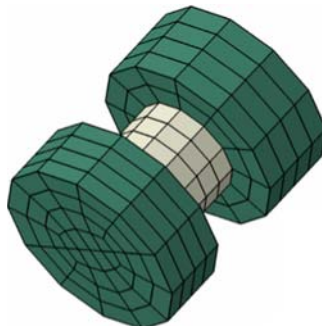


Figure 13.
Solid bolt model

For the tightening force of the bolts, a preload was applied as a thermal contraction of the bolt part that represents the shank. In the material properties of the bolt, shank expansion is defined as an orthotropic expansion, with $\alpha_{11} = \alpha_{22} = 0$ and $\alpha_{33} = \alpha$. The negative temperature is applied as a predefined field of the type temperature in the clamping step. The variation of the section is defined as constant through the region. The applied temperature is determined using the following relations:

$$\Delta T = \alpha \frac{\Delta l}{l_{shank}}, \quad (1)$$

$$\Delta l = \delta_{joint} \cdot F_{s.Rd}, \quad (2)$$

where α is the coefficient of thermal expansion, $F_{s.Rd}$ is the bolt preload force and δ_{joint} is elastic resistance of bolted connection (Pavlović *et al.*, 2015).

Elastic resistance of bolted connection is calculated according to the VDI Guideline (VDI – Association of German Engineers (2003)). It represents the sum of elastic resistance of the preloaded bolt δ_{bolt} and the elastic resistance of the clamping package (steel plates and bolt head and nut) δ_{cp} :

$$\delta_{joint} = \delta_{bolt} + \delta_{cp}. \quad (3)$$

According to VDI Guideline, the elastic resistance of preloaded bolt takes into elastic deformation within clamping length as well as the elastic deformations outside of the clamping length region that have an influence on the deformation behaviour of the bolt in the joint. The bolt model considered consists of three individual elements: the head, the shank and the nut. As in a bolt, the cylindrical elements are arranged in a row, the total resistance of a bolt is determined by adding the resistance of individual cylindrical elements within the clamp length and further deformation regions:

$$\delta_{bolt} = \delta_{head} + \delta_{shank} + \delta_{nut}, \quad (4)$$

where:

$$\delta_{head} = \frac{l_{head}}{E_{bolt} \cdot A_{nom}} \quad l_{head} = 0.5d \quad A_{nom} = \frac{\pi d^2}{4}, \quad (5)$$

$$\delta_{shank} = \frac{l_{cp}}{E_{bolt} \cdot A_{nom}} \quad l_{cp} = l_{shank}, \quad (6)$$

$$\delta_{nut} = \frac{l_{nut}}{E_{bolt} \cdot A_{nom}} \quad l_{head} = 0.5d. \quad (7)$$

For concentrically clamped bolted joint, the elastic resistance of clamped parts is calculated according to the following expression that is valid in the case of $D_A \geq D_{A,Gr}$:

$$\delta_{cp} = \frac{2 \ln \left[\left((d_w + d_0) \cdot (d_w + l_{cp} \cdot \tan \varphi - d_0) \right) / \left((d_w - d_0) \cdot (d_w + l_{cp} \cdot \tan \varphi + d_0) \right) \right]}{E_{cp} \cdot \pi \cdot d_h \cdot \tan \varphi}, \quad (8)$$

where d_w is the outside diameter of washer $= d_{nb} = d_{hb}$, l_{cp} is the clamping package length, φ is the deformation angle taken as $\varphi = 35^\circ$ and E_{cp} is clamping package Young's modulus (plates).

The preload force in the bolts obtained after applying the calculated temperature is lower than $F_{s,Rd}$. Therefore, the temperature must be calibrated (Liu *et al.*, 2019). Table V presents the temperatures that were calculated and calibrated, and the corresponding preloading forces for B90 case. The bolt diameter is M20 for which $F_{s,Rd} = 172$ kN, according to EN 1993-1-8. The preloading forces obtained in the first iteration, for calculated temperature, are 10 and 19 per cent lower than $F_{s,Rd}$ for brace and column bolts, respectively (Figure 14).

4.4.2 Load application. In the first step, a bolt load is applied through a thermal contraction with a duration of the 50 s. In the second step, the actuator displacement (δ) of 200 mm (vertical direction as shown in Figure 12) was applied over a period of 500 s. The displacement control loading is applied in a smooth manner, as shown in Figure 15, in order to diminish the inertia effects in quasi-static analysis using an explicit dynamic solver.

The maximum stable integration time increment for ABAQUS/explicit dynamic solver is obtained from the size of the smallest FE in the model divided by a wave propagation speed.

Clamping length (mm)	Calculated T (°C)	Preloading force (kN)	Calibrated temperature (°C)	Preloading force (kN)
16	-697	155 (10%)	-772	172
30	-494	139 (19%)	-608	172

Table V.
Applied temperature
and obtained
preloading force

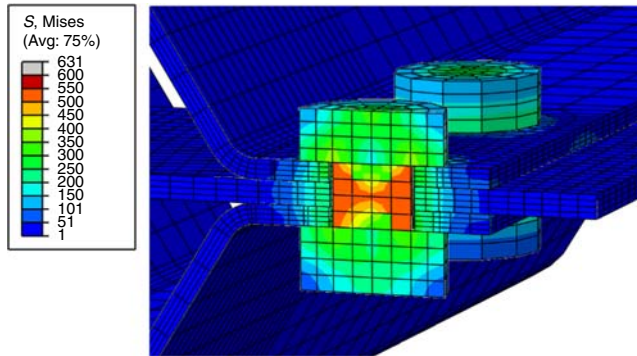


Figure 14.
Bolt model subjected
to thermal loading

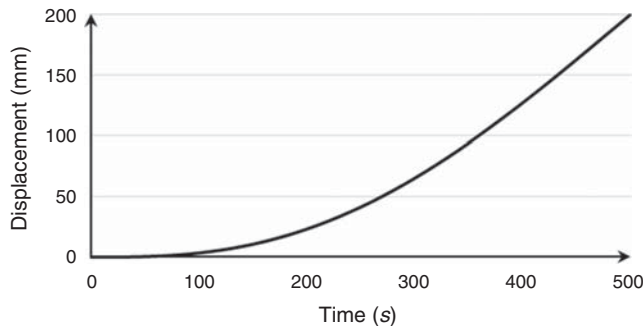


Figure 15.
Amplitude of
applied displacement

Hence, it can result in an inapplicable long computational time. The calculation speed can be increased using two methods: time scaling or mass scaling (Dassault Systèmes, 2014). Either of these methods can lead to an increase in inertia forces in the model, which might lead to meaningless results. Therefore, a compromise between the quality of results and acceptable computational time must be found. For these analyses, mass scaling with a time increment of 0.005 was applied. The FE masses are automatically increased, so their stable time increment matches the desired time increment (Dassault Systèmes, 2014). For these models, with a large range of element sizes, mass scaling is set to be variable (recomputed in every integration step) and non-uniform (different for each FE).

Mass scaling factor applied was obtained by matching input and output forces in a model for displacement controlled failure loading. Several analyses decreasing mass scaling factor were carried out, as shown in Figure 16. Linear matching curve without fluctuations for the smallest time increment ensures that no inertia effects govern the results (Figure 16).

The use of explicit solver in this study is for a quasi-static model. Therefore, it is critical to keep the kinetic energy to a minimum (KE/IE ratio less than 5–10 per cent). The energy ratio is presented in Figure 17. The kinematic energy is below 5 per cent of inertia energy through simulation; therefore, analysis can be considered quasi-static.

5. Resistance of connections

The moment–rotation curve is used to represent the connection behaviour. In this research, the moment–rotation curve was used with the aim of adjusting the FE model based on a comparison between the obtained ultimate resistance and the results obtained using EC3

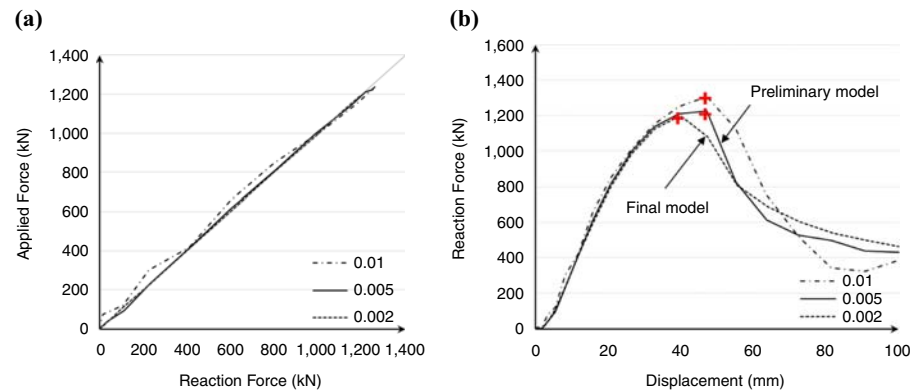


Figure 16. Mass scaling factor

Notes: (a) Applied force vs reaction force; (b) reaction force vs displacement

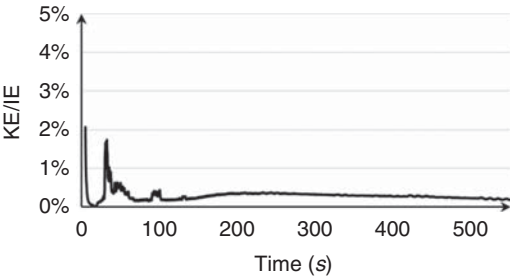


Figure 17. Quality of quasi-static solution

(European Committee for Standardisation, 2010). This curve is presented by the relationship between the bending moment ratio, M_j/M_y , and the corresponding rotation ratio, θ_j/θ_y . Bending moment, M_j , corresponds to the applied moment to a joint, whereas rotation, θ_j , is the rotation between the connected members. Bending moment, M_y , and rotation, θ_y , are, respectively, the plastic resistance of brace and the yield rotation of the brace determined according to FEMA 356 (ASCE, 2000):

$$\theta_y = \frac{W_{pl} \cdot f_y \cdot L_b}{6 \cdot E \cdot I_b}. \quad (9)$$

The bending moment of the connection corresponds to the applied load ($R3_{RP3}$) multiplied by the distance between the centre of the pylon and the end of the brace (L_{load}), as stated in the following relation:

$$M = R3_{RP3} \cdot L_{load}. \quad (10)$$

In Figure 18, the displacement values in the RPs (P_1 , P_2 , B_1 , B_2) are used to evaluate the rotational deformation of the joint:

$$\theta = \frac{u_{1(B1)} - u_{1(B2)}}{h_{br}} - \frac{u_{1(P1)} - u_{1(P2)}}{h_{gp}}, \quad (11)$$

where u_1 is the horizontal displacement, h_{br} is the distance between points B_1 and B_2 and h_{gp} is the distance between points P_1 and P_2 .

The results from FE models were compared with simplified design models based on EN 1993-1-8 rules. There are two main observations. First, the ultimate resistance from FE models is higher than from EC3, probably due to a more conservative approach of Eurocode. The second observation is that the failure modes suggested by von Mises plastic strain from finite element analysis (FEA) are correlated with EC3.

For B90, a gusset plate net-section failure was detected, as can be seen in Figure 19. Moreover, gusset plate bearing in the position of end pylon bolt was obtained both analytically and in FEA. Analytically, the lowest resistance was obtained for gusset plate bearing, and it is 4 per cent lower than for the gusset plate considering the net-section resistance. The ultimate resistance obtained analytically is 26 per cent lower than one obtained from FEA.

By its turn, B45 failure mode is gusset plate buckling (Figure 20). The same failure mode was obtained both analytically and in FEA. The ultimate resistance obtained analytically is 19 per cent lower than one from FEA.

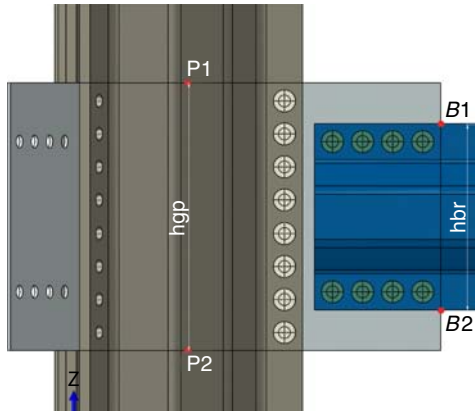


Figure 18.
Moment and rotation
calculation parameters

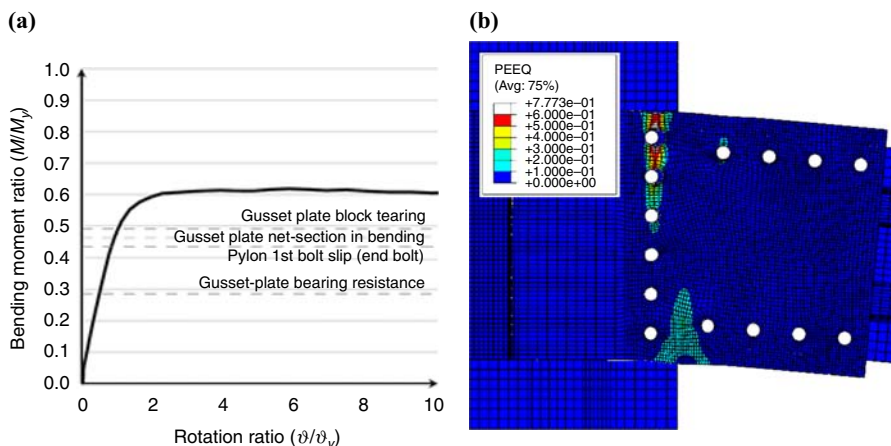


Figure 19.
B90 – gusset plate
net-section failure

Notes: (a) Moment–rotation curve; (b) FEM failure mode

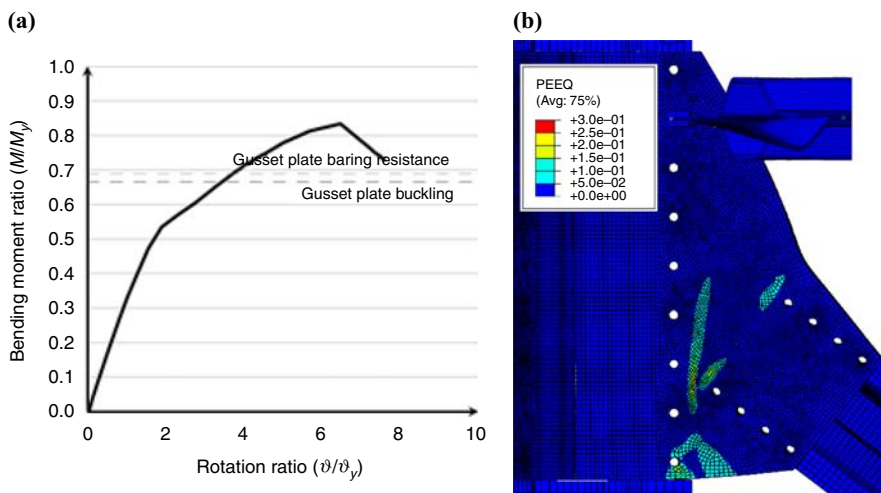


Figure 20.
B45 – gusset
plate buckling

Notes: (a) Moment–rotation curve; (b) FEM failure mode

In the W90 case, the observed failure was brace net-section failure combined with brace bearing resistance (Figure 21). The analytical result shows that brace net-section resistance is 8 per cent higher compared to brace bearing resistance. FEA ultimate resistance is equal to brace bearing resistance. Brace block tearing, whose resistance according to analytical calculation is 1 per cent higher than brace bearing resistance, was not observed in FEA.

Finally, in W45, brace block tearing was observed as failure mode both analytically and in FEA, with 38 per cent higher resistance obtained in FEA (Figure 22).

6. Conclusion

The work presented in this paper deals with the design of a hybrid lattice–tubular wind tower structure. A large set of different geometries was considered in order to achieve the

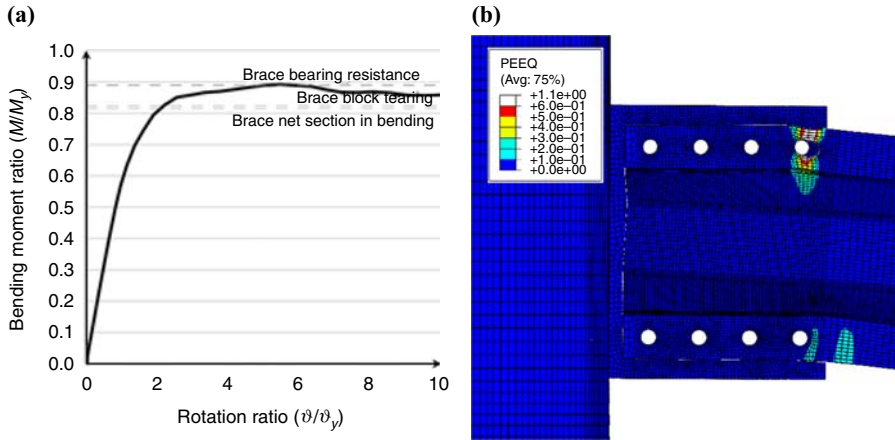


Figure 21.
W90 – brace net-
section failure

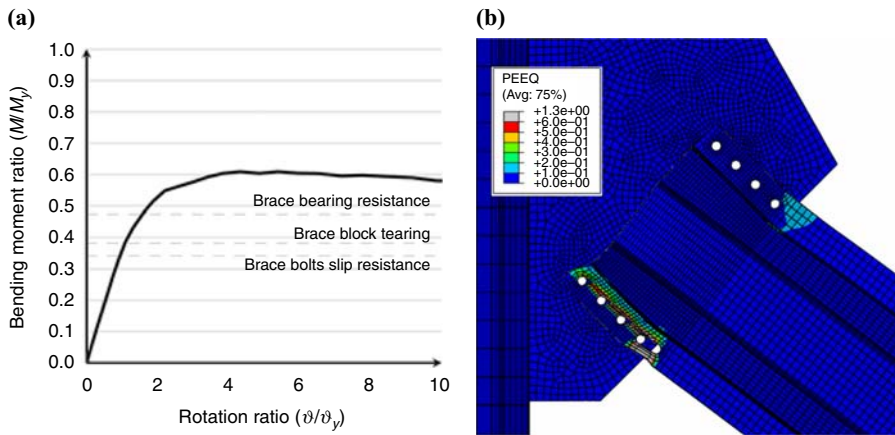


Figure 22.
W45 – brace
block tearing

lightest structure, considering also the minimal number of connections and bolts per connection. Based on results, it is possible to conclude that the six “legs” solution with K braces under 45° angle and H/S ratio of 4/1 and 5/1 provides the most suitable balance between the weight of the supporting structure, the number of bolts in joints and reaction forces in the foundations. The six-legged tower with $H/S=5/1$ has 33 per cent fewer bolts and 10 per cent lower reaction forces compared to the lightest solution (four-legged tower with $H/S=5/1$) whose structure is 16 per cent lighter.

Furthermore, a typical joint in this type of tower was investigated numerically in more detail. The 3D FE models were created. The analyses were carried out using ABAQUS/explicit dynamic solver in order to overcome convergence problems and decrease computational time.

Moreover, different types of elements were used: solid elements and continuum shell elements. For the rectangular cantilever beam, composed of solid, solid + CS and CS

elements, in axial, major and minor bending load case, the displacement at the end of the beam differs for up to 1.1 per cent compared to results obtained using elastic beam theory (except for solid elements model in minor bending where this difference is 5.3 per cent). Therefore, the solid + CS model was chosen for further study. For the tightening force of the bolts, the thermal contraction of the bolt shank was used. Analytical procedure was used to calculate applied temperate results in lower preload force than $F_{s,Rd}$. The difference for the studied case was up to 19 per cent, depending on clamping length. Therefore, the applied temperature must be calibrated in order to achieve $F_{s,Rd}$.

The FE results were compared with analytical calculation according to EC3-1-8. The comparison revealed that FE models are able to accurately predict the failure mode of the joint, while overestimating the design moment resistance for 26 per cent in case of gusset plate net-section failure, 19 per cent in case of gusset plate buckling, 8 per cent in case of brace net-section failure and 38 per cent in case of brace blocking failure. These differences can be attributed to a more conservative approach of Eurocode.

The experimental testing on joints will be carried out in the near future to validate the results obtained from FE models. The parametric study will follow, and hand calculation model that takes into account joint tolerances for assembly will be developed.

References

- ASCE (2000), "Prestandard and Commentary for the Seismic Rehabilitation of Buildings", FEMA-356, American Society of Civil Engineers, Washington, DC.
- Alvarez-Anton, L., Koob, M., Diaz, J. and Minnert, J. (2016), "Optimization of a hybrid tower for onshore wind turbines by building information modeling and prefabrication techniques", *Visualization in Engineering*, Vol. 4 No. 1, pp. 1-9.
- Américo, P., Magalhães Júnior, P.A.A., Rios, I.G., Ferreira, T.S., De Andrade Júnior, A.C., De Carvalho Filho, O.A. and Soares, P.H.D. (2014), "Design of lattice wind turbine towers with structural optimization", *International Journal of Engineering Research and Applications*, Vol. 4 No. 8, pp. 38-51.
- Bulson, P.S. (1969), "The strength of thin walled tubes formed from flat elements", *International Journal of Mechanical Sciences*, Vol. 11 No. 8, pp. 613-620.
- Dassault Systèmes (2014), "Abaqus Analysis User's Manual version 6.14".
- Duthoit, M. and Falzarano, J. (2018), "Assessment of the potential for the design of marine renewable energy systems", *Ocean Systems Engineering*, Vol. 8 No. 2, pp. 119-166.
- European Committee for Standardisation (2010), "EN 1993-1-8:2005 Eurocode 3: Design of Steel Structures – Part 1-8: Design of Joints", Vol. 3, Brussels.
- EWEA (2015), "The European offshore wind industry key 2015 trends and statistics", Brussels.
- EWEA (2017), "Wind energy in Europe: scenarios for 2030", European Wind Energy Association, Brussels.
- Farhan, M., Mohammadi, M.R.S., Correia, J.A. and Rebelo, C. (2018), "Transition piece design for an onshore hybrid wind turbine with multiaxial fatigue life estimation", *Wind Engineering*, Vol. 42 No. 4, pp. 286-303.
- Figueiredo, G. and Carlos, R. (2013), "Structural behaviour of hybrid lattice – tubular steel wind tower", Univesity of Coimbra, Coimbra.
- Garzon, O. (2013), "Resistance of Polygonal Cross-Sections – Application on Steel Towers for Wind Turbines", Luleå University of Technology, Lulea.
- Gencturk, B., Attar, A. and Tort, C. (2012), "Optimal design of lattice wind turbine towers", 15 WCEE, Lisbon.
- Gencturk, B., Attar, A. and Tort, C. (2014), "Selection of an optimal lattice wind turbine tower for a seismic region based on the Cost of Energy", *KSCE Journal of Civil Engineering*, Vol. 19 No. 7, pp. 2179-2190.

-
- General Electric – Renewable Energy (2014), “Space frame tower”, General Electric, Amsterdam, p. 2.
- Gong, W. (2011), “Lattice tower design of offshore wind turbine support structures”, master’s thesis, NTNU, Trondheim.
- Hau, E. (2006), *Wind Turbines: Fundamentals, Technologies, Application, Economics*, Springer, Berlin.
- Heistermann, C. (2011), “Behaviour of pretensioned bolts in friction connections”, Luleå University of Technology, Luleå.
- Hibbit, D.K.B., Karlsson, B.I. and Sorenson, P. (2001), “User’s Manual I-III, version 6.3”, *ABAQUS/Standard*, Hibbit, Karlsson and Sorenson.
- Jaspart, J.P. and Weynand, K. (2016), “Design of joints in steel and composite structures”, European Convention for Constructional Steelwork (ECCS), Brussels.
- Jovašević, S., Rebelo, C., Pavlović, M. and Veljković, M. (2017), “Numerical investigation of preloaded gusset plate connections between polygonal built-up members”, *Proceedings of Eurosteel*, pp. 292-297.
- Jovašević, S., Shah Mohammadi, M.R., Rebelo, C., Pavlović, M. and Veljkovic, M. (2017), “New Lattice-Tubular Tower for Onshore WEC – Part 1: structural optimization”, *Procedia Engineering*, Vol. 199, pp. 3236-3241.
- Letcher, T.M. (2017), “Why wind energy?”, in Letcher, T.M. (Ed.), *Wind Energy Engineering*, Academic Press, London, pp. 3-14.
- Liu, Z., Correia, J., Carvalho, H., Mourão, A., de Jesus, A., Calçada, R. and Berto, F. (2019), “Global-local fatigue assessment of an ancient riveted metallic bridge based on submodelling of the critical detail”, *Fatigue & Fracture of Engineering Materials & Structures*, Vol. 42 No. 2, pp. 546-560.
- Mohammadi, M.R.S., Richter, C., Pak, D., Rebelo, C. and Feldmann, M. (2018), “Steel Hybrid Onshore Wind Towers Installed with Minimal Effort: development of lifting process”, *Wind Engineering*, Vol. 42 No. 4, pp. 335-352.
- Muskulus, M. (2012), “The full-height lattice tower concept”, *Energy Procedia*, Vol. 24, January, pp. 371-377.
- Muskulus, M. and Schafhirt, S. (2014), “Design optimization of wind turbine support structures – a review”, *Journal of Ocean and Wind Energy*, Vol. 1 No. 1, pp. 12-22.
- Nunez-Casado, C., Lopez-Garcia, O., de las Heras, E.G., Cuerva-Tejero, A. and Gallego-Castillo, C. (2017), “Assembly strategies of wind turbine towers for minimum fatigue damage”, *Wind and Structures*, Vol. 25 No. 6, pp. 569-588.
- Ozturk, F., Rebelo, C. and Correia, J.A. (2016), “Finite element modelling of tubular bolted connection of a lattice wind tower for fatigue assessment”, University of Coimbra, Coimbra.
- Pavlović, M., Heistermann, C., Veljković, M., Pak, D., Feldmann, M., Rebelo, C. and Simões da Silva, L. (2015), “Connections in towers for wind converters, Part II: the friction connection behaviour”, *Journal of Constructional Steel Research*, Vol. 115, December, pp. 458-466.
- Rebelo, C., Correia, J., Baniotopoulos, C. and Jesus, A. De (2018), “Wind energy technology (WINERCOST)”, *Wind Engineering*, Vol. 42 No. 4, p. 267.
- Ruukki (2011), “Ruukki wind towers: reaching the heights with Ruukki”, Helsinki.
- Seidel, M., Voormeeren, S. and van der Steen, J.-B. (2016), “State-of-the-art design processes for offshore wind turbine support structures”, *Stahlbau*, Vol. 85 No. 9, pp. 583-590.
- SHOWTIME (2014), “EC-RFSR-CT-2015-00021-SHOWTIME – steel hybrid onshore wind towers installed with minimal effort”, Project proposal report, European Union.
- Suzlon Energy Limited (2016), *2.1 MW PLATFORM S97-S111*, Suzlon Group, pp. 1-12.
- VDI – Association of German Engineers (2003), “VDI Guideline – Part I, Systematic calculation of high duty bolted joints – Joints with one cylindrical bolt”.

- Vestas Wind Systems A/S (2016), "Large diameter steel flanges (LDST)", VESTAS, Aarhus, pp. 1-2.
- Wang, L., Kolios, A., Luengo, M.M. and Liu, X. (2016), "Structural optimisation of wind turbine towers based on finite element analysis and genetic algorithm", *Wind Energy Science Discussion*, Vol. 44, December, pp. 1-26.
- Webber, A., Orr, J.J., Shepherd, P. and Crothers, K. (2015), "The effective length of columns in multi-storey frames", *Engineering Structures Journal*, Vol. 102, pp. 132-143.

Corresponding author

José Correia can be contacted at: jacorreia@fe.up.pt